Surface Modification of Hydrophobic Polymer Films with Amphiphilic Molecules

COLIN PETER GIBSON

Surface Modification of Hydrophobic Polymer Films with Amphiphilic Molecules

Colin Gibson

Department of Chemistry

Durham University

2022

A thesis presented for the degree of Doctor of Philosophy

Abstract

The surface segregation of additive molecules within hydrophobic polymers is of great importance to a range of industrial systems. This thesis specifically addresses the segregation of surfactants within hydrophobic polymer films similar to those used in the babycare and feminine hygiene industry. The aims are to identify the key drivers of surface segregation, and be able to predict this behaviour.

Pentaethylene glycol monododecylether ($C_{12}E_5$) exhibits surface segregation in both crystalline and amorphous polymers, with the degree of matrix crystallinity shown to significantly influence surfactant segregation. Greater crystallinity has been shown to reduce the surface enrichment of these films which was attributed to the inhibition of movement of surfactant by the highly ordered crystalline domains. The surfactant layers also display different temperature and water resistance depending on the matrix, with the surface layer on amorphous polymers appearing to be more resistant to loss. However, both sample types appear to show two types of surfactant structures on the surface, with some surfactant appearing to remain anchored to the surface while the remaining surfactant is lost.

Nanometre scale strands were found on $C_{12}E_5$-containing films which were resistant to temperature elevation and water exposure. These were not seen in dodecyldimethylamine oxide (DDAO) / LDPE films. Instead small islands were seen but these islands show little surface activity.

The effect of surfactant hydrophilicity on surface segregation has also been studied by comparing $C_{12}E_3$ and $C_{12}E_5$ in polymer matrices. A larger head group size has been shown to produce a larger surface excess on the surface and this has been related to the greater compatibility of surfactants with a smaller hydrophilic head group.

Initial exploration of the influence of shear stress on interfacial segregation has shown that $C_{12}E_5$ segregates to the interface under shear and quiescent conditions. The lack of any strong influence of shear rate or temperature suggests that additive chemistry and matrix crystallinity are the most important factors in promoting surface modification with surfactant additives.

Contents

Statement of Copyright

Dedication

To Mum and Dad

I wish you could have seen this Dad.

Acknowledgements

"We don't make mistakes, just happy little accidents."

— Bob Ross

Firstly, my greatest thanks go to my supervisor, Dr Richard Thompson. Without his continuous support and advice, I could simply not have completed this project. I must also thank Dr Jan Claussen, my industrial supervisor at P&G for his useful direction in the project.

I must also thank all the instrument scientists at ISIS for their invaluable help in collecting NR data: Max Skoda, Becky Welbourn and Andrew Caruana. A special thanks must go to Christy Kinane and Stephen Hall who had to change samples for me at awful times thanks to the COVID pandemic. Thank you to Matt, Ophelie, Rebecca, Callum and James for their help at beamtimes. Thanks must also go to Doug Carswell for his help in running DSC measurements at Durham.

I would like to thank all members of the Thompson group, past, present and honorary for their helpful thoughts, questions and entertaining conversations. Thanks to everyone in the office who has had to put up with me! #TGOT Thank you to Matt and Caitlin for listening to who knows how many of my many gripes!

Thank you to all of my friends who have supported me through my PhD, particularly Dan, Vanessa, Chloe, Lucas, Rachel and Jack. And finally, thank you to my Mum, Rachael and of course Chris and Nicola for always being there to help me out whenever I've needed it.

List of Symbols and Abbreviations

α	Lattice site nearest neighbours
Γ	Area per adsorbed molecule
γ	Surface tension
δ	Phase angle
δ_{thick}	Thickness variation
θ	contact angle
λ	Wavelength
ρ	Density
ϕ_i	Volume fraction
χ	Flory-Huggins interaction parameter
ω	oscillatory frequency
A	Area
ATR-FTIR	Attenuated total reflectance Fourier-transform infrared spectroscopy
AFM	Atomic force microscopy
b_i	Scattering length
$C_{12}E_3$	Triethylene glycol monododecyl ether
$C_{12}E_4$	Tetraethylene glycol monododecyl ether
$C_{12}E_5$	Pentaethylene glycol monododecyl ether
CA	Contact angle
CMC	Critical micelle concentration
c	Concentration

D	Diffusion coefficient
DDAO	*N,N*-dimethyldodecylamine *N*-oxide
DSC	Differential scanning calorimetry
d_i	thickness of layer i
ΔG	Gibbs free energy change
E	Ion energy
E_A	Activation energy
ETC	Environmental test chamber
G'	Storage modulus
G''	Loss modulus
G^*	Complex modulus
HDPE	High density polyethylene
HLB	Hydrophilic-lipophilic balance
h	Planck constant
hPBd	hydrogenated poly(butadiene)
ΔH_{fusion}	Enthalpy change of fusion
IBA	Ion beam analysis
J	Diffusant flux
K_e	Molecular exchange rate
k_b	Boltzmann constant
$\vec{k_i}$	Momentum transfer vector
L	total film thickness
LDPE	Low density poly(ethylene)
$\mathbf{M}$	Optical matrix
M_n	Number-average molecular weight
M_v	Viscosity-average molecular weight
M_w	Weight-average molecular weight
m	mass
N_b	Scattering length density (Chapter 3)
N_i	Degree of polymerisation

NR	Neutron reflectometry
NRA	Nuclear reaction analysis
n	Refractive index
P	Pressure
P_e	Péclet number
PC	Polycarbonate
PEO	Poly(ethylene oxide)
PI	Poly(isoprene)
PMMA	Poly(methyl methacrylate)
PS	Poly(styrene)
PVA	Poly(vinyl alcohol)
PVAc	Poly(vinyl acetate)
Q	Momentum transfer vector
QNM	Quantitative nanomechanical mapping
R	Molar gas constant
$R(Q)$	Reflectivity
$R_{\max}$	Maximum roughness
R_q	Root mean squae roughness
R_{SA}	Surface area ratio
r_{ij}	Fresnel coefficient
S	Stopping power (chapter 3)
ΔS	Entropy change
SANS	Small-angle neutron scattering
SAXS	Small-angle x-ray scattering
SDS	Sodium dodecyl sulphate
SLD	Scattering length density
T	Temperature
T_c	Crystallisation temperature
T_g	Glass transition temperature
T_m	Melting temperature

TTS	Time-temperature superposition
t	Time
U	Internal energy
u_{ij}	interaction energy
vGP	van Gurp-Palmen
V	Volume
V_{lat}	Lattice site volume
v	Velocity
WAXS	Wide-angle x-ray scattering
WCA	Water contact angle
w	Mole fraction
x	diffusion distance
z	Depth
z^*	Surface excess

Chapter 1

Overview

The migration and segregation behaviour of additive molecules within hydrophobic polymers is of great commercial importance in the formulation of products with modified surface and processing behaviours. In particular, the inclusion of small molecules such as surfactants to impart hydrophilicity to polymer surfaces is highly relevant to the manufacture of non-woven layers of both babycare and feminine hygiene products. Successful formulations require the surfactant to segregate to the surface to modify it and any surfactant remaining within the bulk material has little effect.

Commercially manufactured products containing polyolefins and surfactants are often produced by injection moulding and extrusion. These techniques often require the blend to be at high temperatures to melt the polymer and undergo a wide range of shear rates when processed through an extrusion die. Furthermore, during use these products often come into contact with water-based fluids. Therefore, the successful exploitation of the properties imparted by the surfactant requires a surfactant-enriched layer to present itself on the surface after the blend is subject to the processing conditions. It is also necessary for the surfactant-enriched layer to remain present during use.

The aims of this work are to understand the key drivers of surface segregation within hydrophobic polymers. This understanding can be applied to computational and theoretical models to ultimately predict segregation in a wide range of

blends in order to provide a more heuristic approach to product formulation.

The compatibility of surfactants within polymers has previously been suggested to be a key driver in segregation. Therefore, within chapter 4, both DSC and rheometry have been probed as methods of investigating compatibility of non-ionic surfactants within both semi-crystalline and amorphous polymers. This will provide insight into the compatibility of the surfactant as a function of surfactant loading and comparison of different head group sizes.

Before investigating semi-crystalline polymers, it is necessary to explore the surfactant distribution of a surfactant, $C_{12}E_5$, within an amorphous polymer, *cis*-PI in chapter 5. Neutron reflectivity shall be used to investigate the depth profile of surfactant and work shall be performed to compare this to the surface properties of the films.

The behaviour of non-ionic surfactants within a more crystalline polymer, hydrogenated poly(butadiene), shall be probed within chapters 6 and 7. This will provide insight into the effect of crystallinity on the surfactant segregation. The distribution of $C_{12}E_3$ and $C_{12}E_5$ in a polymer film shall also be compared, allowing the effect of hydrophilic head group size on segregation and surface properties to be investigated.

A relatively novel technique, Rheo-NR, is explored in chapter 8 as a viable method for understanding the effect of shear forces on the surfactant distribution within a hydrophobic solvent. This shall be used to probe the effect of shear rate on surfactant distribution in order to understand how the blends behave during processing.

Finally, the key conclusions from each chapter shall be summarised in chapter 9 to provide an insight into the effect of both the additive and matrix properties as well as the processing conditions on the behaviour of surfactants within hydrophobic polymers. There will also be suggestions for future directions of work based on the results obtained in this thesis.

Chapter 2

Introduction

Polymers, particularly polyolefins have become a key component in the manufacture of many household items, with the annual global manufacturing capacity in the order of 100 Mt per year.[1] These polymers are selected for their excellent range of mechanical properties, chemical resistance and relatively low cost.[2] However, some modification of these properties can often be desirable and this is achieved by the incorporation of additives. These can be small molecules that can modify the surface and rheological properties of the polymer as well as the appearance and flame resistance of the material. However, these additives are not stationary within a polymer and can often migrate throughout the material, leading to additive-enriched regions and surface layers of additive. This process also presents the possibility of the loss of surfactant into any contacting materials, changing the properties of the polymer during storage or usage.

It is important to understand how the additives behave under different conditions as this may greatly impact the shelf life of the product and optimal storage conditions to maximise this. Furthermore, the understanding of the behaviour of the additives in a polymer matrix may allow the development of improved production methods that lead to reduced costs and waste: if an additive is designed to modify surface properties, it only has any effect at the surface and any additive remaining in the bulk polymer is superfluous. Therefore, the ideal behaviour of a surface-active additive will be for it to migrate to the surface during or shortly

after manufacture and for this to remain within the blend during use.

2.1 Polymers

2.1.1 Low-Density Polyethylene

Polyethylene is a simple, hydrophobic polyolefin. It is inexpensive, has excellent mechanical properties and good chemical resistance, making it a strong candidate for use in a wide range of commercial applications.

The structure of polyethylene is deceptively simple, consisting mainly of a chain of ethylene units covalently bonded together (Fig. 2.1). There are several approaches to synthesising polyethylene, two of the most common are radical polymerisation and metal-catalysed techniques.

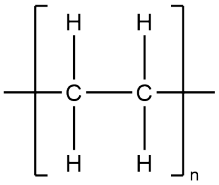

Figure 2.1: Structure of polyethylene.

Metal-catalysed polymerisation is a more modern approach to polymer synthesis and requires specific metal catalysts such as a Ziegler-Natta catalyst. These are commonly titanium and aluminium based compounds[3] which allow propagation of the polymer by insertion reactions into the monomer double bond. These catalysts give much greater control over the stereochemistry of the polymer and yield polymers with little branching.

Free-radical polymerisation is a much simpler synthesis technique, where the ethylene monomer and an initiator are mixed at high pressure and allowed to react.[4] Whilst this technique is fast and allows synthesis of large quantities of polyethylene, it gives little control over the structure of the resultant polymer. This often leads to large molecular weight distributions of the polymer chains and significant degrees of branching.[5]

The degree of branching within polyolefins significantly influences the properties of the polymer and polyethylenes with different amounts of branching can have a wide range of properties. More linear polyethylenes tend to have a much higher density due to the improved packing efficiency of the linear chain.[5] These polyethylenes are referred to as high-density polyethylenes (HDPEs). This improved packing efficiency also leads to a much higher degree of crystallinity, making it ideal for uses where high strength, good corrosion resistance and low flexibility are desired such as piping and chemical containers. Polyethylenes produced by free-radical polymerisation tend to be much more branched and thus have a lower density. These low density polyethylenes (LDPEs) are still fairly crystalline but tend to be more versatile for flexible items such as food packaging, plastic wraps and structural components of babycare and feminine hygiene products.[6]

2.1.2 *cis*-poly(isoprene)

Polyisoprene (PI) is a term used to encompass several polymers produced from isoprene, with varying structures depending on the reaction mechanism of polymerisation (Fig. 2.2). The polymerisation mechanism is dependent on the reaction conditions and catalyst used. Both the 3,4-addition and 1,2-addition isomers are produced where polymerisation occurs only through one double bond, leaving the second double bond remaining in the side group. This produces a much more complex polymer, with many chiral centres on the polymer backbone. These forms of polyisoprene can be produced in high yields using a MoO_2Cl_2 catalyst.[7]

Both *cis*- and *trans*-PI can be produced by metal-catalysed polymerisation techniques using a Ziegler-Natta catalyst. Furthermore, the catalyst chosen can influence the selectivity of the reaction. It has been shown that vanadium(III) chloride complexes can be used to produce *trans*-PI[8] and can be tuned to achieve > 99 % *trans*-1,4 addition.[9] *cis*-PI can be selectively produced by using a TiX_4 catalyst where X is a halide and an organoaluminium compound.[10]

Within this work, primarily *cis*-PI will be investigated. *cis*-PI is a hydrophobic, amorphous polymer which is commonly obtained from natural rubber or is

produced synthetically as discussed above.[11] It has a relatively low degree of crystallinity due to the rigid, bent backbone structure imposed by the double bond, which reduces the packing efficiency of the polymer. This is in contrast to *trans*-PI which has a much higher degree of crystallinity as the double bond locks the backbone in a relatively linear orientation.

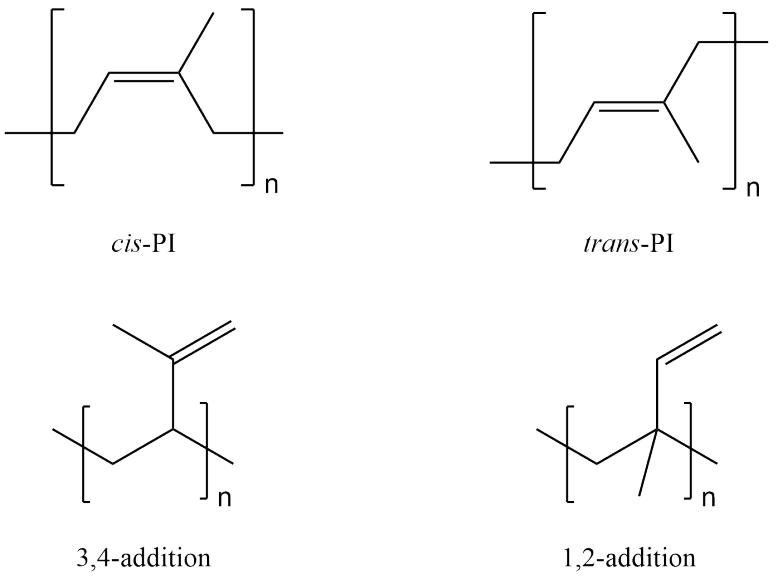

Figure 2.2: isomers of poly(isoprene). Different isomers are produced depending on the polymerisation mechanism.

2.2 Surfactants

Surfactants are amphiphilic molecules comprising a polar, hydrophilic moiety covalently bound to a non-polar hydrophobic group. Surfactants can broadly be divided into four categories: anionic, cationic, non-ionic and zwitterionic surfactants. These classifications are based on the nature of the hydrophilic head group. The primary focus of this work shall be non-ionic surfactants. However, a zwitterionic surfactant, dodecyldimethylamine oxide (DDAO) will also be compared to explore the impact of a surfactant structure with a much smaller polar head-group.

2.2.1 Polyoxyethylene alkyl ethers ($C_{12}E_x$)

Polyoxyethylene alkyl ethers (Fig. 2.3) are a family of amphiphilic molecules. These consist of a linear alkyl hydrophobic group and a hydrophilic head group comprising a chain of ethylene ether groups. Both the size of the head group and tail group can be varied in order to tailor the hydrophilicity of the amphiphile, with an increased number of ethyl ether groups giving a more hydrophilic molecule and a longer alkyl chain rendering the molecule less hydrophilic.

Figure 2.3: Generic structure of a $C_{12}E_x$ surfactant. The hydrophobic section is shown in red and the hydrophilic section is given in black.

2.2.2 Dodecyldimethylamine oxide (DDAO)

Dodecyldimethylamine oxide (DDAO) is an amine oxide based zwitterionic surfactant (Fig. 2.4). DDAO has been previously used in commercial products which are superabsorbent between 0 and 5 % wt.,[12] making it an ideal surfactant to compare to the results seen in the $C_{12}E_x$ series. This surfactant has also been shown to exhibit antimicrobial properties.[13]

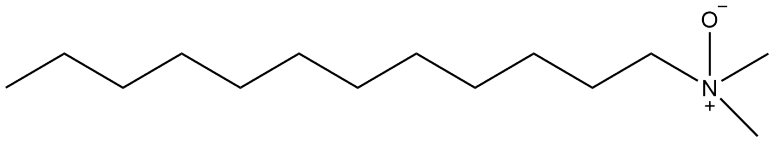

Figure 2.4: Structure of a DDAO molecule.

2.2.3 Amphiphile Self-Assembly

Due to their amphiphilic nature, surfactant molecules commonly form highly ordered structures within solution. One of the more simple structures formed are micelles: a spherical structure, which when the solvent is aqueous, allows the

hydrophilic groups to remain in contact with the water whilst shielding the tail groups within a hydrophobic core. An entropy increase is a key driving force for the formation of these micelles, which occurs as the hydrophobic tail is shielded from the aqueous environment.[14] Entropic effects arise from the organisation of water molecules in the presence of hydrophobic groups to preserve hydrogen bonding. These are referred to as hydrophobic interactions. Furthermore, the non-polar tails are not capable of hydrogen bonding, rendering them fairly insoluble. This allows them to form aggregate structures with other non-polar molecules. In a non-polar solvent, micelles still form but have the opposite structure, with a hydrophilic core of head groups. These are referred to as inverse micelles.[15] The thermodynamics for the formation of these micelles is distinct from those discussed above as there is no solvent hydrogen bonding network to be preserved. For ionic surfactants, the formation of these micelles becomes less likely with increasing head group charge, due to the increased electrostatic charges between the head groups in close proximity to each other.

The formation of micelles occurs at a specific concentration, known as the critical micelle concentration (CMC). Below this surfactant concentration, surfactant will enrich the surface. At the CMC, additional surfactant will form micelles within the bulk solution. Non-ionic surfactants tend to have a lower CMC than ionic and zwitterionic surfactants. Additionally, surfactants with a longer hydrophobic group also have a lower CMC.[16]

Whilst micelles are a common form of self-assembled structure, there are many others which can form. Israelachvili *et al.*[17] related the curvature of self-organised structures to the relative sizes of head and tail groups. This work demonstrated that curvature can be imparted into organised structures through the repulsive forces between surfactant head groups and can account for the formation of rod-shaped micelles and tubular bilayers. Another structure that may be particularly important in the case of surface segregation is surfactant lamellae. These are sheets of surfactant in which the molecules are aligned to form layers of heads and tail groups. It is also possible for multilamellar structures to form, where sheets are successively stacked together, giving a structure with alternating hydrophilic

and hydrophobic sheets. $C_{12}E_5$, a surfactant used within this thesis has been shown to be able to form lamellar structures within water[18] and these structures have been observed to be thermally responsive, with a transition between micellar and lamellar structures occurring as temperature is varied.

2.3 Thermodynamics of Polymers, Mixtures and Molecular Migration

Any spontaneous process is driven by a decrease in free energy. The change in free energy, in this case the Gibbs free energy, G, at constant pressure and volume can be given as a function of internal energy, U, temperature, T, and entropy, S, as:

$$\Delta G = \Delta U - T\Delta S \tag{2.1}$$

The theories below are applications of this thermodynamic relation to a molecular system. One of the most commonly used theories to describe the mixing of polymers is Flory-Huggins theory.

2.3.1 Flory-Huggins Theory

Flory-Huggins theory is a thermodynamic theory that was originally created to describe the mixing of a polymer and solvent and the statistical thermodynamics of the resulting system.[19] The theory is based on earlier work by Meyer[20] which treats space as a lattice in which sites are occupied by components of the system. It is important to note that in this model, no sites can be empty. One important issue to consider in this model is the difference in molecular weight between the polymer and solvent. This is accounted for by defining a volume, V_{lat}, and setting this as the volume of each lattice site. The model assumes that a polymer chain can be considered to consist of connected segments of V_{lat} as shown in Fig. 2.5. The lack of empty sites within this model is important as this describes the incompressibility of the system.

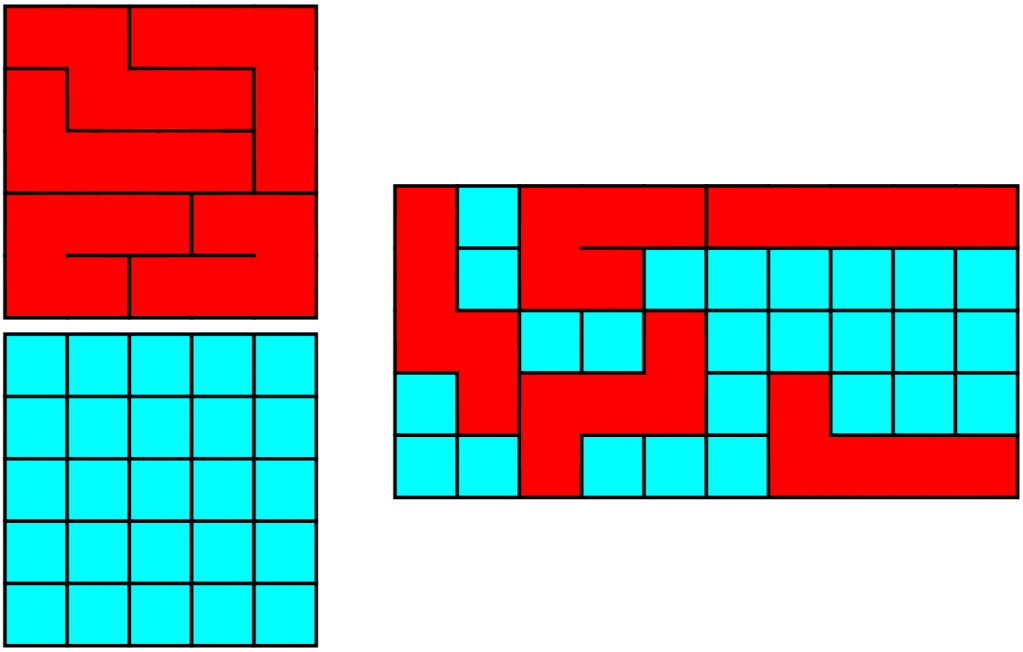

Figure 2.5: Illustration of a lattice model in 2 dimensions for a polymer and solvent mixing. The polymer is represented in red and the solvent in blue.

2.3.2 Application of Flory-Huggins Theory to Polymer-Polymer Mixtures

Whilst Flory-Huggins theory describes polymer-solvent mixing, it can be modified to model the mixing of two different polymers instead (illustrated in Fig. 2.6). For a binary polymer mixture, the system can be described in terms of the volume fraction of polymer A, ϕ_A, and the volume fraction of the polymer B, ϕ_B. Each of these polymers has a degree of polymerisation, N_A and N_B respectively. For an ideal mixture, at constant pressure the energy of mixing will be purely entropic and can be expressed as:[21]

$$\frac{\Delta G_{mix}}{k_B T} = \frac{\phi_A \ln \phi_A}{N_A} + \frac{(1-\phi_A)\ln(1-\phi_A)}{N_B} \tag{2.2}$$

where k_B is the Boltzmann constant and ϕ_A is the volume fraction of polymer A. As the system contains only 2 components, the volume fraction of B can be defined as $1 - \phi_A$.

Many systems are not ideal and thus more complexity is introduced. Interactions are required between the two polymers and can be described as either attractive or repulsive. This introduces an enthalpic term into the equation. As this is the Gibbs free energy, enthalpic contributions are captured in the internal energy and it is possible to describe the change in internal energy change of mixing per lattice site:

$$\Delta \bar{U}_{\text{mix}} = \frac{\alpha}{2}\phi_1(1-\phi_1)(2u_{AB} - u_{AA} - u_{BB}) \tag{2.3}$$

where α is the number of nearest neighbours of a lattice site, u_{AB} is the interaction energy between polymers A and B and u_{AA} and u_{BB} are the interaction energies of A and B with themselves respectively.

In order to simplify the equations, the Flory-Huggins interaction parameter, χ, as:[22]

$$\chi = \frac{\alpha}{2}\frac{2u_{AB} - u_{AA} - u_{BB}}{k_b T}. \tag{2.4}$$

This can then be substituted into equation 2.3 to give

$$\Delta \bar{U}_{\text{mix}} = \chi \phi_A (1-\phi_A) k_B T. \tag{2.5}$$

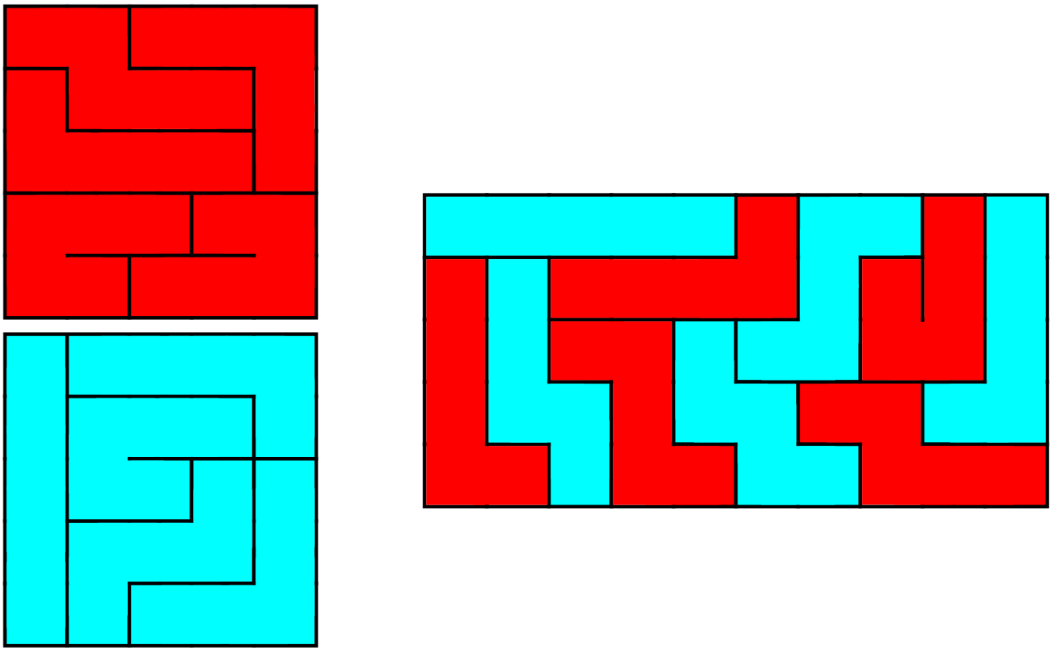

Figure 2.6: Illustration of a lattice model in 2 dimensions for two homopolymers mixing. Polymer A is represented in red and polymer B in blue.

Finally, it is possible to substitute the above equation into the Gibbs free energy equation (equation 2.1) to give

$$\frac{\Delta G_{mix}}{k_B T} = \frac{\phi_A \ln \phi_A}{N_A} + \frac{(1-\phi_A)\ln(1-\phi_A)}{N_B} + \chi\phi_A(1-\phi_A) \tag{2.6}$$

The free energy density can then be written by introducing V_A and V_A terms, defined as the volume of a repeat unit of polymer A and B respectively:[19,23]

$$\frac{\Delta G_{mix}}{k_b T} = \frac{\phi_A \ln \phi_A}{N_A V_A} + \frac{(1-\phi_A)\ln(1-\phi_A)}{N_B V_B} + (1-\phi_A)\phi_A\chi(V_A V_B)^{-0.5}. \tag{2.7}$$

It can be concluded from this work that the Flory-Huggins interaction parameter is intrinsic to a specific system and will be affected by the chemical interactions of the components of the system. In the case of a polymer and surfactant, the size and chemistry of the head and tail groups would affect this value considerably.

If the free energy of mixing is positive at all compositions, a mixed state is not thermodynamically stable and so the system will tend to phase separate over time. It may be possible to apply some of this theory to a system that contains both a polymer and a surfactant component. However, this theory does have limitations, particularly when considering a system where components have regions of varying polarity. Flory-Huggins theory treats all interactions as isotropic. Whilst this can be valid in a polymer mixture, the structure of surfactants and the tendency of these molecules to self-assemble means that interactions are directional and violates the underlying assumption that components are randomly distributed. Furthermore, as Flory-Huggins theory is intended to model polymer blend behaviour and, whilst the surfactants can be considered to be short chained block copolymers, the increased number of chain ends may produce invalid results from Flory-Huggins theory. These chain ends affect the compressibility of the system,[24] rendering the assumption that the system is incompressible invalid. Whilst Flory-Huggins theory may not accurately represent a non-polar polymer and a non-ionic surfactant, such as the system to be studied, it may be used to infer some basic predictions. It can be expected that if the head group of the surfactant is too large, u_{AB} will increase as the interactions will be greater, increasing χ. This means the system will phase separate in order to minimise the interactions and achieve a conformation with the minimal free energy.[25]

More complex models have been developed such as the work by Higgins *et al.*[26] that has been shown to work well for polymers and can take into account compressibility. However, these models require precise thermodynamic data on the compressibility of the polymers and mixtures are difficult to implement. Recent work by Patyukova *et al.*[27] has shown promise in handling polymer / surfactant mixures and should be applicable to non-polymer mixtures.

2.3.3 Spinodal Decomposition

If the free energy of the mixture changes from negative to positive, the mixture becomes thermodynamically unstable and may decompose into a phase-separated system of lower free energy. The mechanism of this is commonly spinodal decomposition[28] and is spontaneous when the second derivative of free energy density of mixing with respect to volume fraction is negative. The spontaneous nature of this process arises because any composition fluctuations away from that mixed state will necessarily have a lower free energy. During this process, a continuous morphology develops from fluctuations with randomly directed wave vectors. This leads to an isotropic structure due to the symmetry of the system. However, if a surface is present, asymmetry is produced in the system and this can lead to surface-directed spinodal decomposition.[28,29] The formation of a surface layer as decomposition waves propagate with vectors oriented normal to the surface can therefore occur.[28] This surface layer is enriched in one component relative to the other, with models also predicting self-organisation of the materials within the layer, including the formation of alternating layers.[30]

The formation of a surface layer can be understood in terms of Flory-Huggins theory. If the components do not mix, the system undergoes a rearrangement in order to form a configuration with the smallest interfacial area. This minimises the interfacial energy of the system, yielding a more stable structure. If one of the components has a lower surface energy then it will tend to be present in slight excess at the surface. Should this system undergo spinodal decomposition, then this excess will direct the process such that the concentration gradient grows with

time.

2.3.4 Entropy Effects

Another motivation for the migration of surfactant to the surface of the polymer is that it is an entropic effect rather than a product of the incompatibility of the components. It has been suggested that the configurational entropy per segment of a polymer chain at the surface is significantly lower than that in the bulk.[31,32] Simulations have indicated that as the polymer chains approach the surface, the polymer is compressed towards a single layer,[33] reducing the number of possible conformations that can occur.[34] This lower number of possible conformations leads to a significantly lower conformational entropy and this decrease in entropy is much more significant for the longer chained molecules. This means that it is more favourable for the shorter chained components such as oligomers and monomers to be found at the surface[31] as well as the polymer chain ends.

If two components are incompatible, these will not necessarily segregate to form a distinct layer of one additive on the surface of the film. Sakellariou observed that poly(methyl methacrylate) (PMMA) and poly(ethylene oxide) (PEO), two partially incompatible polymers, did not show any noticeable enrichment of either component on the surface.[35] It would be expected that the lower surface energy component, PMMA, would migrate to the surface to minimise surface energy. Whilst this does not occur in this work, Mayes *et al.*[36] did find surface enrichment of PMMA with a PEO-depleted layer 50 Å thick. However, this was only after annealing to 190 °C, above the glass transition temperature, T_g, of both components. This work was conducted on films on a silicon wafer and it must be noted that PMMA adheres strongly to the wafer.[37] Therefore it is possible that the initial composition is dominated by PMMA at the wafer surface, leaving PEO on the surface. This suggests that the kinetics of migration may be important or that whilst the surface layer may be the optimal structure, there can be a significant inhibitor to the formation of this.

2.4 Diffusion Within Polymers

Whilst thermodynamics may indicate whether an additive and polymer will tend to segregate, it cannot indicate the time scale on which this occurs. If the time an additive requires to segregate to a structure, which will impact product performance, is orders of magnitude greater than the expected lifetime of a product, this segregation will have little effect and can be considered negligible. Therefore, the dynamics of additive diffusion and segregation must be considered.

2.4.1 Activation Energy

As with most kinetic processes, there is an energy barrier to diffusion of migrants and this will affect whether or not migration occurs at all. Many processes with energy barriers can be modelled by an Arrhenius relationship and diffusion has been modelled this way:[38]

$$\ln D = \ln D_0 - \frac{E_A}{RT} \tag{2.8}$$

where D is the diffusion coefficient in a polymer matrix, D_0 is a pre-exponential factor, E_A is the activation energy of diffusion, R is the molar gas constant and T is temperature. Furthermore, molecular dynamics simulations have been performed by Wang *et al.*,[39] which gave predicted diffusion coefficients and activation energies that were in good agreement with experimental results at 293 and 313 K. However, the diffusion coefficients began to deviate from experimental results at higher temperatures, suggesting that there are effects other than those modelled at elevated temperatures.

2.4.2 Fickian and non-Fickian Diffusion

The movement of an additive can be a diffusive process. One key law describing diffusion is Fick's law. Equation 2.9 shows Fick's first law, where J is the diffusion flux, D is the diffusion coefficient of the diffusant, c is the diffusant concentration and x_i is the the distance in direction i.

$$J = -D\frac{dc}{dx_i} \tag{2.9}$$

This equation shows that the flux is positive when migration is down the concentration gradient and thus the migrant moves towards areas of lower concentration, eventually equalising the concentrations, leading to a concentration gradient of zero. This diffusion coefficent becomes negative during spinodal decomposition.

$$\frac{\partial c}{\partial t} = D\frac{\partial^2 c}{\partial x_i^2}. \tag{2.10}$$

Equation 2.10 shows Fick's second law, which describes the concentration change over time due to diffusion, where t is time, x_i is the distance, c is diffusant concentration and D is diffusion coefficient of the diffusant.[40] This second equation shows that concentration of migrant increases over time when the second derivative of the concentration gradient is positive. Fick's law has previously been applied to migration of additives out of non-swellable polymer matrices, with the loss of additive described by:[41]

$$m_t = 2c_0\rho\left(\frac{Dt}{\pi}\right) \tag{2.11}$$

where m_t is the total mass of migrant lost at time, t, c_0 is the initial migrant concentration in the polymer, ρ is the polymer density and D is the diffusion coefficient.

However, not all diffusion obeys Fick's law. This is described as non-Fickian diffusion and exhibits significantly different behaviours. This non-Fickian diffusion can be caused by swelling of the polymer matrix by the penetrant. Equation 2.10 for Fickian diffusion assumes that D has no concentration dependence. For systems studied in this work, the additives may have a plasticising effect, changing the matrix with increasing concentration, leading to a different diffusion mechanism. One form of non-Fickian behaviour that arises from this is commonly referred to as case-II diffusion.[42,43] The type of diffusion that is observed can be determined by its time dependence, denoted by t^n where n is a constant. Case-II diffusion has a time dependence where $n = 1$, whereas for Fickian diffusion, $n = 1/2$. There are additional forms of diffusion behaviours where n is a value between these values which are referred to as anomalous diffusion.[44] Case-II diffusion is characterised by a front of diffusing material which propagates linearly with time.[42]

2.5 Migration to the Surface in Polymers

Previous work has shown that additives can migrate from the bulk to the surface[45] within poly(vinyl alcohol) (PVA) films. This form of migration shall be defined as z-migration, where the migration is in the z-direction as defined in Fig. 2.7. This migration has been investigated in a range of systems, including polar polymer matrices and ionic surfactants. It is therefore important to consider the factors that affect migration in this work.

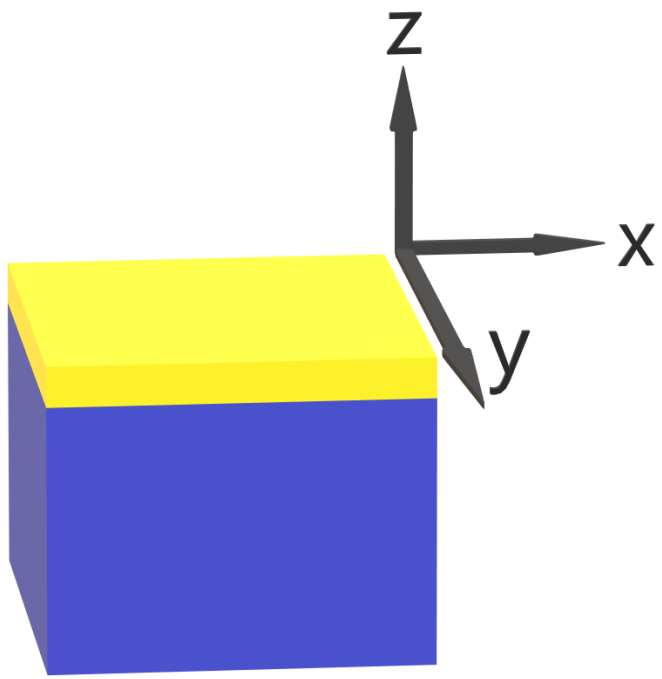

Figure 2.7: Schematic of a polymer film with the polymer bulk shown in blue and the surface layer shown in yellow. The x, y and z directions have been defined.

2.5.1 Effect of Matrix Crystallinity

Many commercially relevant polymers are semi-crystalline, meaning that they contain at least some regions of ordering dispersed throughout an amorphous network. Several factors affect the degree of polymer crystallinity and these include chemical regularity, whether all repeat units contain the same structural formula, and stereoregularity, whether the chain can achieve a conformation with translational

symmetry through bond rotation.[46] Furthermore, chain branching can also affect the crystallinity of polymers. Both Satti *et al.*[47] and Xu *et al.*[48] demonstrated that short chain branching could have a significant effect on the crystallinity of ethylene-propylene and ethylene-butene copolymers respectively. This also applies to polyethylene,[49] where the more linear chains can form lamellar crystalline structures. The introduction of branching causes the width of these lamellar crystallites to decrease, showing that these branches lower the crystallinity, melting temperature and melting enthalpy of the polymer. This increased crystallinity also tends to lead to an increase in polymer density and thus more linear polymers tend to be found in HDPE compared to LDPE.

This matrix crystallinity has been shown to affect additive migration and mobility. Marcato *et al.*[50] studied the diffusion of additives in HDPE, ethylene-propylene copolymer and polypropylene. The investigation was performed by exposing polymer blends containing antioxidants to oils for various amounts of time. High-performance liquid chromatography was then used to determine the amount of remaining antioxidant. It was shown that the largest quantity of antioxidant transferred to the contact medium was from ethylene-propylene copolymer and the smallest quantity was transferred from HDPE. The copolymer had a crystalline fraction of 30 % whereas HDPE is 70 % crystalline and it was concluded that this increased crystallinity decreased the rate of migration and the loss of additive from the polymer.

The decreased migration in highly crystalline polymers can be rationalised by understanding the path a migrant must take through a polymer. Mahlman[51] observed by X-ray diffraction that non-crystallising material is rejected from polymer spherulite structures as they form. Instead, it is propelled in a wave away from the spherulite, meaning that higher concentrations are found at the crystal boundaries. Furthermore, it was observed that migration of a polysiloxane additive occurred preferentially along the low density, disorganised crystal boundaries using atomic force microscopy (AFM) by Mäkpirtti.[52] Therefore, the path that the additive takes to migrate to the surface is no longer linear, thus the path is longer and causes migration to be much slower.

2.5.2 Additive Structure

The migration of an additive in a polymer is dependent on the physical properties of the additive as well as the matrix. The migration of Irganox 1010 and Irgafos 168 antioxidants (Fig. 2.8) has been compared within polyolefins.[50] It was shown that the larger molecular weight Irganox 1010 migrated out of the polyolefin much more slowly than Irgafos 168. However, this study did not attempt to understand whether molecular weight or the molecular volume is the key parameter affecting migration. Al-Malaika *et al.*[53] concluded that, for UV stabilisers within polyethylene, there was no clear correlation between molecular weight and diffusion coefficients, except for when the alkyl chain length is varied. This indicated that the diffusion coefficient depended much more on the additive shape and chemical structure rather than its mass alone.

Raynier *et al.*[54] related the diffusion process of additives to their geometric parameters such as their size and flexibility. Two main mechanisms were identified, a crawling motion (reptation) and a jumping mechanism. The reptation mechanism was common to highly mobile, flexible additives that commonly contain long alkyl chains. The jump mode is frequently seen in the case of more rigid molecules such as heterocycles and involves the movement of a molecule from one free volume to another. This supports the reasoning of Wang *et al.*[39] who propose that the diffusion of larger molecules occurs much slower as fewer free volume holes that are large enough to fit the molecule inside them will be produced by random polymer chain movement. It can therefore be concluded that the geometry of the migrating molecule will significantly affect diffusion.

2.5.3 Blend Storage Temperature and Aging

The storage conditions of these blends at elevated temperatures can impart significant changes to the distribution of the additive. Samples of polypropylene, a crystalline, non-polar polymer, containing alkyl sulfonates and fluorocarbon surfactants showed a large decrease in surface energy when aged at 45 °C for over 10 days.[55] However, samples containing the same quantities of additives aged at

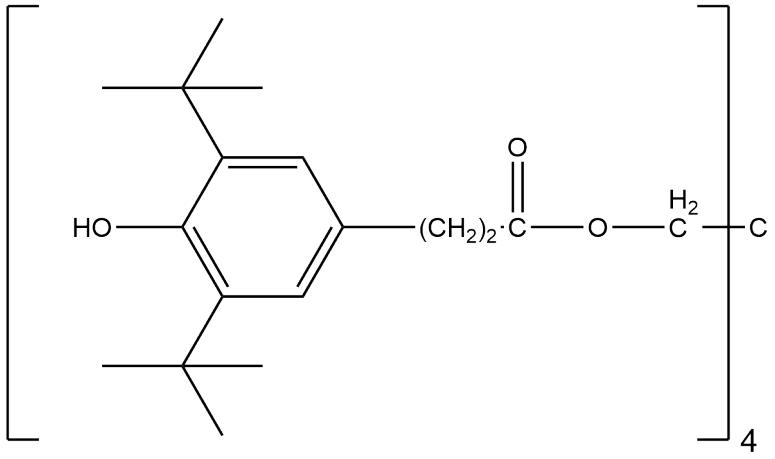

Irganox 1010

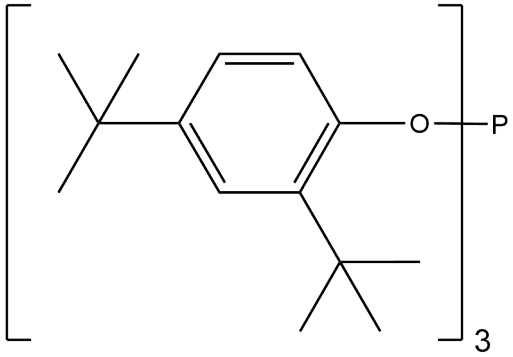

Irgafos 168

Figure 2.8: Chemical structure of Irganox 1010 and Irgafos 168.

5 °C showed much smaller decreases in surface energy. The T_g is similar to the lower temperature[56] (-10 °C) and so it is likely that the mobility through the amorphous region of the material changes enormously in this temperature range. If this is considered to be a kinetic effect, it can be explained by referring back to equation 2.8: at higher temperatures, the RT term is larger, meaning that more molecules have the required activation energy to diffuse and so the diffusion coefficient increases. Furthermore, the free volume of the polymer increases with temperature[57] and is strongly related to T_g. This means that there will be more available space within the polymer that the additive can migrate through, potentially allowing more channels for migration to the surface. This would also agree with Wang *et al.*[39] as at higher temperatures, more movement occurs and so larger holes can appear.

2.5.4 Additive Loss

A significant concern when studying the migration of an additive to the surface of a polymer is the loss of the additive. For small molecules, this commonly occurs by evaporation. Calvert and Billingham[58] proposed a theoretical model for this loss of additive. The model consisted of 3 key factors: the evaporation rate, the diffusion coefficient and the solubility of the additive. Firstly, if the additive was not above the saturation solubility, blooming of the additive to the surface did not occur and so the rate of additive loss is determined by whether the rate of volatilisation or diffusion dominates.

Work by Smith *et al.*[59] shows that the most significant factor affecting the loss of volatile plasticisers within a semi-crystalline polymer is not the diffusion coefficient but is instead the evaporation rate. Neutron reflectivity profiles of a polyester-polyurethane film with a plasticiser blend showed that the plasticiser concentration could equalise itself throughout the film before significant plasticiser loss. This showed that diffusion occurs much faster than evaporation and thus evaporation is the rate-limiting step of additive loss. However, this is not comparable to the systems studied within this work as the additives are not polar,

meaning that they are likely more compatible with the matrix than surfactants are, meaning that the only driver towards the surface is diffusion rather than compatibility.

There has also been significant interest in the loss of additives in the case of food packaging, where migration of additives out of the packaging into food is highly undesirable.[60–62] Schwope *et al.*[60] probed the migration of butylated hydroxytoluene and Irganox 1010 from LDPE into both solid foods and food-simulating liquids. The work showed that the size of the molecule played a key role in the migration, with the migration of larger molecules occurring more slowly than that of small molecules. Furthermore, it was shown that where additive loss is not caused by evaporation, the rate of diffusion alone controlled the loss of the additive into food, with the quantity lost correlating to $t^{1/2}$. This time relation is indicative of Fickian diffusion (section 2.4.2).

2.6 Relationship of Surfactant Surface Migration and Surface Energy

As surfactants segregate to and enrich the surface, the surface energy will change, leading to a change in the contact angle between a liquid and the surface. Young[63] demonstrated this and this work led to the development of the Young equation (equation 3.18), where the interfacial tensions are defined in Fig. 2.9. This model is relatively simple and relies on the assumptions that the surface is perfectly smooth and that the properties of the contacting fluid and the surface are unaffected by each other. This is not always valid as surfaces often have significant roughness and, in the case of a surfactant laden surface, surfactant may migrate from the surface to the probe liquid. Furthermore, there has also been work which has revealed that a droplet can have some effect on the surface below, with pH-buffered solutions shown to promote surface segregation of polar functional groups in carboxylic acid functionalised polystyrene.[64]

This change in free energy is also a key driver in the migration of additives to

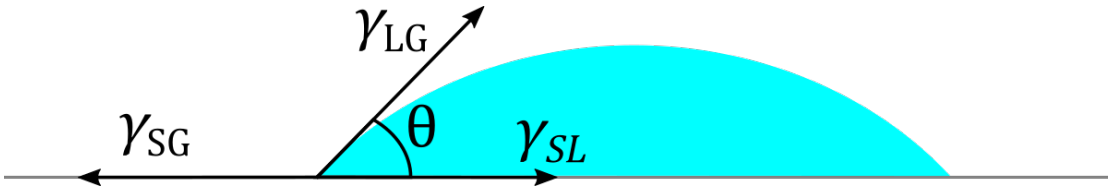

Figure 2.9: Schematic of a droplet of a probe liquid on a surface displaying the contact angle (θ), solid-liquid (γ_{SL}), solid-gas (γ_{SG}) and liquid-gas (γ_{LG}) surface energies.

the surface. The component with the lowest surface energy would be expected to migrate to the surface, lowering the free energy of the system.[14]

Surface energy difference has been demonstrated to be a key driver in migration by Lee and Archer.[32] This work featured the segregation of polystyrene-*b*-poly(dimethyl siloxane) in polystyrene. Furthermore, other copolymer additives with fluorinated groups have been shown to migrate to the surface of polymer blends. The low surface energy of these fluorinated additives was shown to be a key driver for the surface enrichment of these copolymers.[65]

2.7 Structure of the Surface Excess

There has been some work performed that has identified that enriched surface layer can form complex structures after the additive has migrated to the surface. Firstly, lateral migration can also occur and it has been shown that disk-like structures of additive have been observed on the surface of polyisoprene when oligo-isobutylene is included as an additive.[66] It was also noted that these islands coarsen slowly over time when the sample is annealed at a temperature above the T_g of the samples.[67]

More exotic structures can be formed when additional additives are incorporated. Briddick *et al.*[68] noted that lamellar structures can form in ternary blends. In the example, glycerol (a common plasticiser) and sodium dodecyl sulphate (SDS, an anionic surfactant) were observed to form a multilayer lamellar structure in PVA. This lamellar structure is the product of interactions between

these two additives. As the surfactant is ionic, there are repulsive interactions between the head groups. However, glycerol sits in a layer between the head groups, screening these charges from each other which allows a more favourable structure to form. It is also proposed that hydrogen bonding contributes to the structure of this layer: glycerol has three OH groups which allow it to hydrogen bond to the charged head group of SDS. This work implies that several components in a system can behave in a cooperative manner, allowing self-assembly of structures which may not be able to form without a specific component. Within industrial formulations, a wide range of additives can be incorporated into a single blend. This means that there could be significant interactions between additives within these samples which would produce much more complex structures than those seen within model systems.

2.8 Summary

Migration has been identified as a complex process that frequently occurs in industrially and commercially relevant materials. This process can be distinct from phase separation: whilst phase separation is the result of incompatibility, migration can have other drivers such as surface energy differences. Furthermore, the kinetics of migration can also introduce additional complexity to migration behaviour.

Previous work has discussed the thermodynamics of phase separation and segregation using Flory-Huggins theory. However, Flory-Huggins theory has limited effectiveness when modelling the behaviour of smaller molecules such as surfactants within a polymer matrix. This is due to the presence of both hydrophilic and hydrophobic groups which introduce directionality to the forces between the surfactant and polymer as well as the increased number of chain ends produced by the smaller molecules.

The kinetics of migration have also been discussed. Several forms of diffusion have been considered: Fickian, Case-II and anomalous diffusion. These have been shown to exhibit different time dependencies and thus different movement mech-

anisms occur. As migration involves the movement of small molecules through a polymer, it is expected that they may obey laws of diffusion and thus kinetics must be considered to assess whether any distributions observed are in equilibrium. However, the polymer matrix can also affect the kinetics of migration and so crystallinity is also an important factor to consider when assessing segregation of surfactants.

It has been shown that a wide range of factors affect migration and the formation of an enriched surface layer. These include the sample temperature and aging time, matrix crystallinity and the amount of surfactant present. Furthermore, lateral migration has also been discussed, this allows the formation of more complex surface structures. This appears to be relatively poorly understood and may have a significant performance of any product containing polymer and surfactant based materials.

The aims of this work will be to investigate the key factors affecting the migration of a non-ionic surfactant in non-polar matrices. To represent this, a model system consisting of a hydrophobic polymer with a single surfactant shall be considered. This is a suitable model system as many commercially relevant polymers are hydrophobic, such as LDPE and polyisoprene. Only very limited research, usually involving less well-defined commercial additives[50,60,69] has addressed this behaviour until now. In order to characterise a system suitable to test new computational approaches, a better defined model is required. A single surfactant in each sample will be used in order to assess the migration without the additional complexities of interactions between additives. The use of a surfactant series such as $C_{12}E_x$ gives scope for the adjustment of the head group size in order to assess how the surfactant hydrophilicity affects migration.

Initial investigations must also be conducted in order to determine the compatibility of the polymer and additive: this will indicate whether compatibility plays a role within surface segregation. It is also necessary to investigate how the surfactant is distributed initially within the sample in order to determine if migration has occurred when the sample is exposed to different conditions.

These products are commonly processed and extruded at high temperatures.

Therefore, it is important to assess the effect that both processing temperature has on the surface enrichment as well as the effect of shear forces. As many applications of these systems are in non-perishable products that may come into contact with water, the effects of water exposure must also be assessed and so it will be necessary to probe the resistance of any surface layers of surfactant to loss into the contacting water medium.

Chapter 3 describes the experimental methods used in this investigation of the bulk and surface properties of blended films. In chapter 4 the compatibility of additives within polymer matrices is investigated and the results from this underpin the analysis of the depth distribution of surfactant in amorphous polymer films in chapter 5. Chapter 6 examines the surfactant segregation behaviour in more crystalline polymers and compares this to results in previous chapters and chapter 5 to identify how the introduction of crystallinity to the matrix influences segregation. The influence of the head group size on segregation is investigated in chapter 7 and chapter 8 probes how surfactants segregate under shear forces similar to those experienced during processing using Rheo-NR.

Chapter 3

Experimental

3.1 Materials

A selection of polymers and surfactants were used in this project to create a model system designed to imitate the behaviour seen in commercial systems. The suppliers of each material is given in Table 3.1 and the molecular weights of polymers used can be found in Table 3.2. In this work, an analogue of LDPE has been used, hydrogenated poly(butadiene) (hPBd). This was necessary to facilitate the spin-coating of hydrophobic films. Due to the high crystallinity of LDPE, the films produced are often too rough to be measured by neutron reflectivity (NR). It must be noted, however, that whilst hPBd is considered to be a form of polyethylene, it is synthesised by a different route to commercial polyethylenes. Industrial polyethylenes are produced from the polymerisation of ethylene gas, which is obtained from petrochemicals. However, hPBd is synthesised from the hydrogenation of 1,4-polybutadiene produced by living ionic polymerisation (Fig. 3.1). This different synthesis technique does not produce perfect polyethylene, with some 1,2-addition occurring, leaving some ethyl side groups on the polymer chain after reduction.

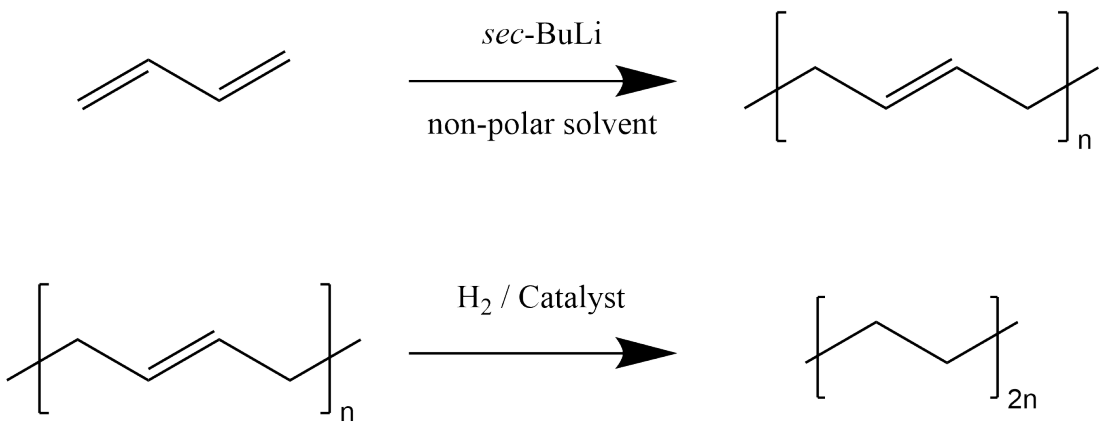

Figure 3.1: Reaction scheme of the synthesis of hPBd from 1,4-butadiene. The first step shows the polymerisation and the second step shows the hydrogenation of the polymer.

3.2 Sample Preparation

3.2.1 Polymer Solutions

cis-PI was dissolved in toluene or xylene with stirring to create 4 % wt. solutions. It was possible to dissolve *cis*-PI at room temperature. However, LDPE was dissolved in xylene, which required heating to 80 °C.[70] Similar toluene and xylene solutions of surfactants were also prepared at 4 % wt. These solutions were then combined in the relevant proportions to produce solutions with the desired surfactant to polymer ratio.

3.2.2 Spin Coating of Thin Films

Many of the experiments conducted within this thesis were performed on spin cast films of *cis*-polyisoprene or polyethylene and additives. Spin-coating is an effective technique for producing thin layers of polymer film.[71,72] For most experiments, films were prepared by spin casting samples from toluene solutions onto silicon wafer.

Solutions were spin cast on to 0.75 mm thick silicon wafers (for AFM, contact angle analysis or ion beam analysis) or 55 mm diameter, 5 mm thick silicon blocks

Table 3.1: Materials used within this thesis and the suppliers of each

Material	Supplier
cis-PI-01	Sigma-Aldrich
cis-PI-02	Sigma-Aldrich
hPBd	Polymer Source
LDPE	Sigma-Aldrich
Dodecane	Sigma-Aldrich
h-DDAO	Sigma-Aldrich
h-$C_{12}E_5$	Sigma-Aldrich
h-$C_{12}E_4$	Sigma-Aldrich
h-$C_{12}E_3$	Tokyo Chemical Industry UK
d_{25}-$C_{12}E_5$	Rutherford Appleton Laboratories
d_{25}-$C_{12}E_3$	Rutherford Appleton Laboratories
d_{25}-DDAO	Rutherford Appleton Laboratories
Toluene	Fisher
Xylenes	Fisher

(for neutron reflectometry). For both wafers and blocks, the crystal orientation used for spin casting was 100. Silicon blocks were cleaned with permanganic acid and then acetone prior to spin casting to remove any impurities to both aid in film wetting and ensure film consistency. Silicon wafers were cleaned with acetone and dried prior to spin casting.

Solutions were spin-cast using a Laurell spin coater model WS-650MZ-23NPP using a rotational speed of 3000 rpm for 45 s during drying. For polyethylene samples, the solution and substrate were heated to approximately 80 °C to prevent precipitation of the polymer at lower temperatures.

3.2.3 Melt Pressed Films

Thicker films for use in rheometry were prepared by melt pressing films. Solutions were first prepared as described above to ensure thorough mixing of components.

Table 3.2: Molecular weight distributions of polymers where M_n is the number-average molecular weight and M_w is the weight-average molecular weight.

Polymer	M_n / g mol^{-1}	M_w / g mol^{-1}	Dispersity
cis-PI–01	-	420,000	-
cis-PI–02	-	35,000	-
hPBd	380,000	532,000	1.4
LDPE	7,700	35,000	4.6

These solutions were then dried in a fume cupboard at 60 °C for 24 hours. Once all solvent was removed, the blend was then melt pressed into discs with a diameter of 25 mm or 40 mm and a thickness of 1 mm under 10 tonnes pressure. These sizes were selected to match the rheometer geometry used. The polymer was melt pressed at 120 °C, above the melting point of the polyethylene used, and the sample was held at this temperature for 30 minutes.

3.3 Differential Scanning Calorimetry

Differential Scanning Calorimetry (DSC) is a technique which can be used to quantify thermal transitions such as the melting point (T_m) and glass transition point (T_g).[73,74]

Solutions containing the materials to be investigated were placed into standard aluminium DSC pans and the solvent was evaporated by heating the pan to 80 °C. More solution was added and evaporation repeated if required until approximately 10 mg of the dry blend remained in the pan. This pan was then heated alongside an empty pan at a constant rate. The difference between the empty pan and the pan containing the sample was measured. Measurements were collected using a Perkin Elmer DSC 8000 by Douglas Carswell at the thermal analysis service, Department of Chemistry, Durham University. Measurements were collected at a heating and cooling rate of 10 °C per min. The calorimeter was calibrated using indium and tin reference samples. A baseline correction has also been applied

to some data. This involves the calculation of the gradient of the heat flow as temperature is ramped and this is then subtracted from the data to give a flat baseline.

3.4 Oscillatory Rheometry

Oscillatory rheometry is a method of rotational rheometry which is useful for probing the viscoelastic properties of a material. The storage and loss moduli (G' and G" respectively) are measured whilst an oscillating shear force is applied to the sample.[75]

Samples containing *cis*-PI–02 and an additive ($C_{12}E_5$ or dodecane) were prepared by manually mixing the components of the sample together. This method was chosen to prevent the inclusion of any residual solvent which may affect the rheological properties of the mixture. However, *cis*-PI–01 is not a viscous liquid at ambient temperatures and thus cannot be manually mixed. Therefore these blends were prepared as outlined in subsection 3.2.3. Samples were then investigated using a TA AR2000 rheometer with thermal control of the sample provided through a peltier plate. The samples were placed within a 40 mm diameter smooth parallel plate geometry with a gap of 0.5 mm. A strain sweep was performed at 0.1 rad s^{-1}, shown in Fig. 3.2. It can be seen from this figure that at higher strain rates, G' and G'' remain constant, indicating that for all strains tested, the sample is within the linear regime. In order to conduct successful measurements, a strain should be selected that is within the linear regime but is above the torque limit of the instrument. The oscillation torque is plotted against strain in Fig. 3.3, with the lower torque limit of the rheometer shown in red. From this data, a strain of 7.5 % was selected to ensure that measurements were above the torque limit but still within the linear regime. The angular frequency was varied between 0.01 and 100 rad s^{-1}. Several samples were also probed using thermal control delivered through an environmental test chamber (ETC), fitted to the rheometer. This allows a wider range of temperatures to be attained through the use of additional insulation and improved heating as well as liquid nitrogen cooling for sub-ambient

temperatures. Samples studied with the ETC were probed using a 25 mm diameter smooth parallel plate geometry, the maximum size capable of fitting within the ETC.

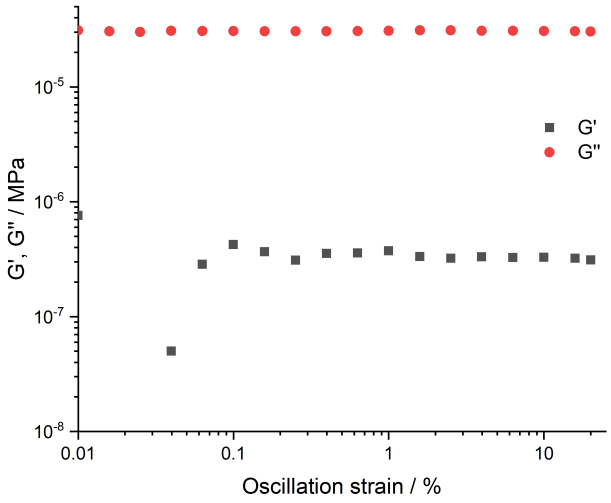

Figure 3.2: Strain sweep of *cis*-PI–02, showing how both G' and G" are both constant at 7.5% strain, indicating that the sample is still in the linear viscoelatic range.

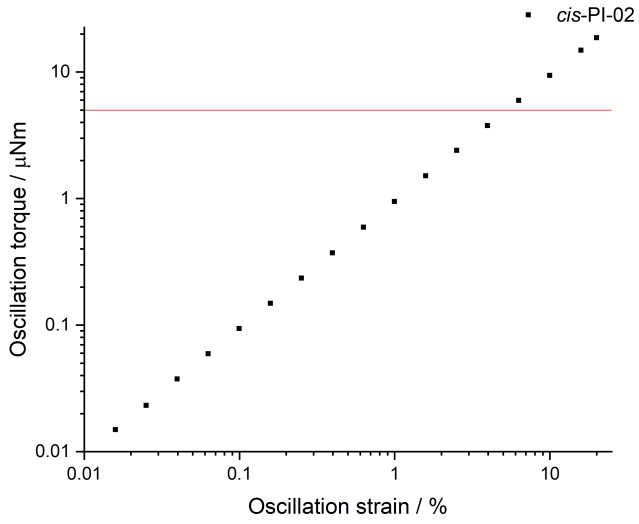

Figure 3.3: *cis*-PI–02 torque / strain plot. The torque limit on the instrument is shown by the red line, strain values where the torque falls below this line cannot be used for measurements.

3.5 Neutron Reflectivity

Neutron reflectometry (NR) is a surface-sensitive depth profiling technique. It is a powerful technique for probing the distribution of components in soft matter systems. Neutrons behave with both the properties of a particle and a wave (wave-particle duality) and therefore have a wavelength, λ, given by the de Broglie equation:

$$\lambda = \frac{h}{mv} \tag{3.1}$$

where h is the Planck constant, m and v are the mass and velocity of the particle respectively.

Neutrons interact with the nuclei of atoms and any unpaired electrons in the surrounding orbitals,[76] both of which cause scattering to occur. However, within this work, only the scattering from the nucleus is studied.

Neutrons are capable of both reflection and refraction when incident upon an interface. In specular NR, the angles of incidence and reflection are equal, allowing only the variation in scattering length density normal to the interface

to be measured. An important quantity in neutron reflection is the momentum transfer vector, $\vec{Q}$, which can be given by

$$\vec{Q} = \vec{k_f} - \vec{k_i} \tag{3.2}$$

where $\vec{k_i}$ and $\vec{k_f}$ are the momentum vectors of the incident and reflected wave respectively (Fig. 3.4). As specular NR by definition requires the incidence and reflected angle to be equal ($\theta_i = \theta_f$), the modulus of the incident and reflected wavevector are equal and can be given as

$$|\vec{k_i}| = |\vec{k_f}| = \frac{2\pi}{\lambda} \tag{3.3}$$

for neutrons with wavelength λ.[77]

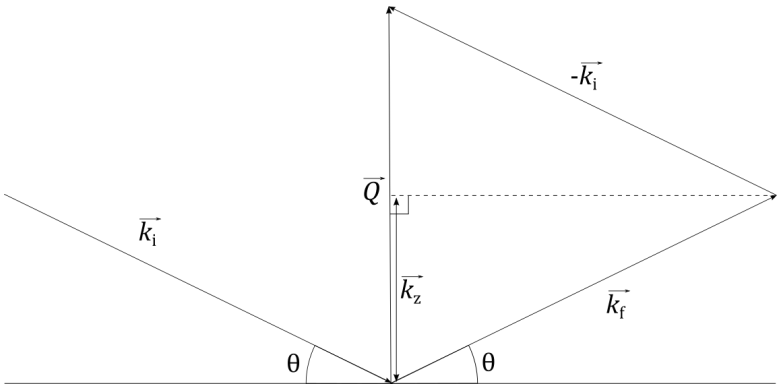

Figure 3.4: Schematic showing how the momentum transfer vector relates to the momentum vectors in elastic scattering

By combining equations 3.2 and 3.3, it is possible to define the modulus of the momentum transfer vector, Q, as[78]

$$Q = |\vec{k_f} - \vec{k_i}| = \sqrt{|\vec{k_f}|^2 + |\vec{k_i}|^2 - 2\cos(2\theta)} = \frac{4\pi}{\lambda}\sin\theta \tag{3.4}$$

giving Q which is only determined by λ and θ.

When there is usually a wide angle between incident and scattered waves, the Born approximation can be applied.[79] This ignores interference between incident and scattered waves, allowing specular reflectivity, $R(Q)$ to be defined as[80]

$$R(Q) = \frac{16\pi^2}{Q^4}|N_b'(Q)|^2 \tag{3.5}$$

with $N_b'(Q)$ defined by[78]

$$N_b'(Q) = \int_{-\infty}^{\infty} e^{iQ} \frac{\mathrm{d}N_b}{\mathrm{d}z} \mathrm{d}z \tag{3.6}$$

where N_b is the scattering length density (SLD) and z is the depth within the film. SLD is dependent on the density and isotopic composition of the molecules within the sample, with each isotope giving different scattering length contributions or scattering lengths (b_i).[81] This difference in scattering length between isotopes allows isotopic labelling to be used to produce contrast within systems containing hydrocarbon components. This can be achieved by substituting hydrogen atoms for deuterium within hydrocarbons. The SLD is calculated using equation 3.7 where V_m is the unit cell volume.

$$N_b = \frac{\sum_{i=1}^{N} b_i}{V_m} \tag{3.7}$$

The SLDs of relevant materials have been calculated using equation 3.7 and the scattering lengths listed in table 3.3 and can be found in table 3.4.

Table 3.3: Scattering lengths of elements of interest

Element	b_i / 10^{-15} m
H	-3.746
D	6.671
C	6.646
N	9.360
O	5.803
Si	4.149

If equation 3.5 is applied to a single interface, $R(Q)$ becomes

$$R(Q) = \frac{16\pi^2}{Q^4} \Delta N_b^2 \tag{3.8}$$

However, in many systems there is more than one single interface and so the reflectivity becomes more complicated. The Fresnel equation can be used to describe the reflection of neutrons at a single interface between two materials,[80]

$$R(Q) = \left| \frac{n_0 \sin\theta_0 - n_1 \sin\theta_1}{n_0 \sin\theta_0 + n_1 \sin\theta_1} \right|^2 \tag{3.9}$$

Table 3.4: Scattering length densities of relevant materials

Material	SLD / 10^{-6}Å^{-2}
d_{25}-$C_{12}E_3$	4.58
d_{25}-$C_{12}E_5$	3.81
d-hexadecane	6.79
$C_{12}E_5$	0.124
cis-PI	0.26
d-DDAO	5.95
LDPE	-0.36
Si	2.07
SiO	3.47

For a multilayer structure, with two interfaces 3.9 can be written:[80,82]

$$R(Q) = \left| \frac{r_{01} + r_{12}e^{2i\beta}}{1 + r_{01}r_{12}e^{2i\beta}} \right|^2 \tag{3.10}$$

where

$$r_{ij} = \frac{p_i - p_j}{p_i + p_j} \tag{3.11}$$

$$p_i = n_i \sin\theta \tag{3.12}$$

$$\beta_i = \frac{2\pi}{\lambda} n_i z_i \sin\theta_i \tag{3.13}$$

and θ_i is defined according to Fig. 3.5. r_{ij} in equation 3.11 can be referred to as the Fresnel coefficient of the interface between layers i and j and β_i is the optical path length through layer i. Few interfaces are perfectly smooth and so a roughness factor can be introduced to account for imperfections and diffuse surfaces.

$$r_{ij} = \frac{p_i - p_j}{p_i + p_j} e^{-0.5 q_i q_j <\sigma>^2} \tag{3.14}$$

where q_i and q_j are $4\pi \sin\theta_i/\lambda$ and $4\pi \sin\theta_j/\lambda$ respectively and $<\sigma>$ is the root mean square Gaussian roughness.[82]

To apply these Fresnel optical equations to multiple interfaces, the Abeles matrix formalism can be applied. Within this, a characteristic matrix, M_i, is

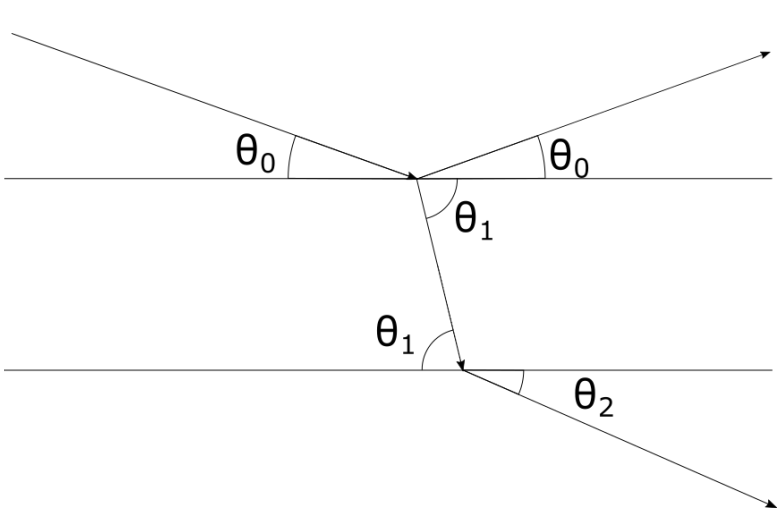

Figure 3.5: Refraction and reflection of neutrons showing how angles are defined within equation 3.10

created for each layer:[83]

$$\mathbf{M}_j = \begin{bmatrix} e^{i\beta_i} & r_{ij}e^{i\beta_i} \\ r_{ij}e^{-i\beta_i} & e^{-i\beta_i} \end{bmatrix} \tag{3.15}$$

where p_i is defined in equation 3.12. A matrix defining the reflectivity can then be obtained as the product of the characteristic matrix of each layer.

$$\mathbf{M} = \prod_{i=0}^{i} \mathbf{M_i} \tag{3.16}$$

which takes the form of a 2x2 matrix. The reflectivity can then be obtained as

$$R(Q) = \left| \frac{M_{10}}{M_{00}} \right|^2 \tag{3.17}$$

with M_{ij} corresponding to matrix elements in M.

Experimental Procedure

Specular neutron reflectometry was conducted using the INTER (for *cis*-PI-based samples) and POLREF (for hPBd-based samples) reflectometers at ISIS Neutron and Muon Source, UK.

Deuterium labelling is used to give a difference in scattering length density (SLD) of the components, providing the contrast required to identify the components.[84,85] Reflectivity profiles were collected using 2 or 3 incident angles (0.25°,

1.2° and 2.3°, with 1.2° omitted in 2 angle collections) to obtain a profile from critical edge to background. This gives a momentum transfer range of approximately $0.008 < Q/\text{Å}^{-1} < 0.5$. Depending on the instrument and number of angles used, collection times ranged between 1 and 2 hours per sample. Samples were placed in the path of the beam on a sample changer with 4 sample mounts; each sample mount could then be heated independently with a peltier stage beneath each mount. Fig. 3.6 shows a schematic of a sample mounted on the sample changer. Within this schematic, the four degrees of freedom which are varied during alignment are shown. Both ϕ and ψ are angles which are varied to give the maximum intensity of neutrons incident upon the detector, "trans" is the translational position, allowing changing of samples by moving them into the path of the beam and "h" is the height of the sample which is also used to adjust samples to account for variations in block and sample thickness. Measurements performed on LDPE samples were collected by Dr Christie Kinane, Dr Andrew Caruana and Dr Stephen Hall due to restricted access to the ISIS facilities.

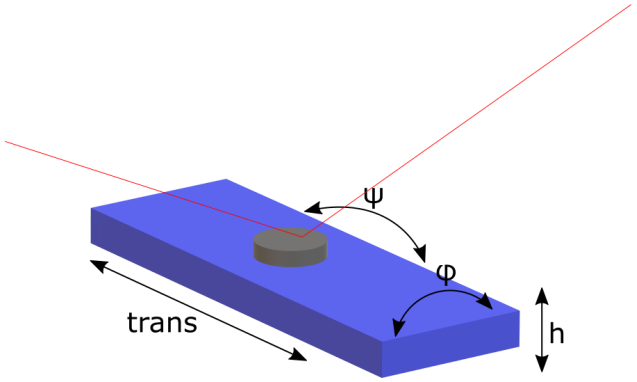

Figure 3.6: Schematic of sample changer used in NR measurements, showing the key degrees of freedom varied to align samples. The path of the neutron beam is shown in red.

3.5.1 Fitting Methods

Both the refnx[86] and MUSCtR[87] packages were used to both simulate reflectivity data using the Abeles matrix formalism discussed above and fit reflectivity data

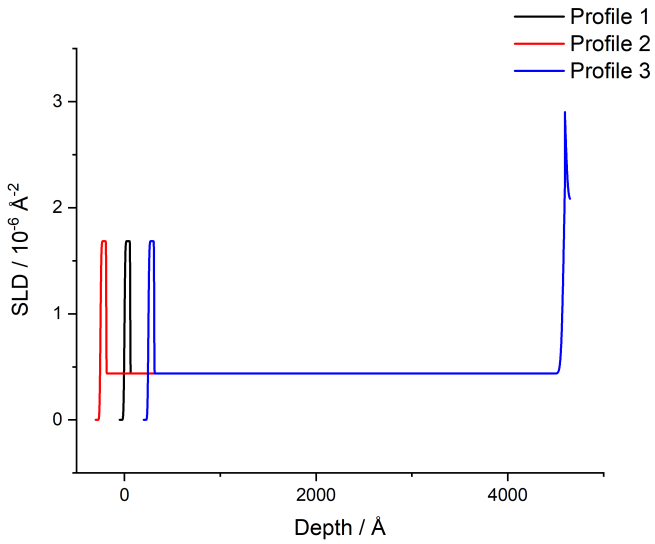

Figure 3.7: SLD profile demonstrating the model used by MUSCtR. The central profile (black) shows the test profile created by the user. Two other depth profiles are created from this by adding or decreasing the thickness of the bulk layer by a defined amount.

to SLD profiles, using a least-squares method to minimise the deviation of the fit.

The MUSCtR package is intended to fit reflectivity profiles from samples which have a undulating surface. These surface undulations have periodicities that are much larger than length scales which would contribute to the surface roughness in conventional fitting software. Instead, MUSCtR fits data with several reflectivity profiles which only differ in the thickness of a defined layer (in this work, the bulk layer). The additional profiles are generated by adding and subtracting a defined thickness, δ_{thick}, from the bulk thickness and this can then be fitted as a parameter. These profiles are then weighted with the central profile (profile 1 in Fig. 3.7) taking a larger weighting and are fitted to the reflectivity profile.

3.6 Contact Angle Analysis

Contact angle (CA) analysis is a technique used to investigate the wettability and surface energy of a surface through the use of a droplet of a probe liquid placed

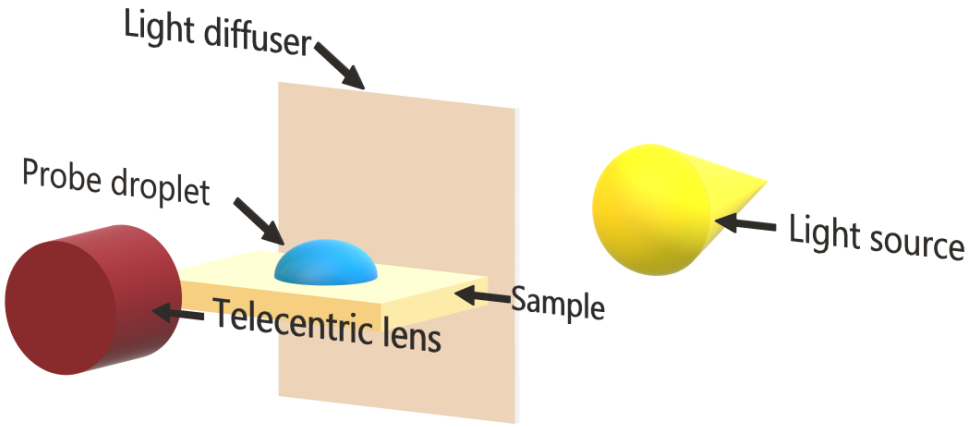

Figure 3.8: Schematic of contact angle analysis experimental setup, showing how a probe droplet is placed onto the sample, illuminated by a diffuse light source and recorded with a camera fitted with a telecentric lens

onto the surface.[88,89] The experimental setup is shown in Fig. 3.8. The spreading behaviour of this droplet is then analysed. Within this work, only water has been used as the probe liquid and shall therefore be referred to as water contact angle (WCA) analysis. The Young equation (equation 3.18) shows that the contact angle of the contacting droplet (θ_C) is related to the interfacial tension of the solid-gas (γ_{SG}), liquid-gas (γ_{LG}) and solid-liquid (γ_{SL}) interfaces.

$$\gamma_{SG} - \gamma_{SL} - \gamma_{LG} \cos\theta_C = 0 \tag{3.18}$$

The evolution of the droplet of probe liquid over time was captured using a camera equipped with a telecentric lens to give a longer focal field. Frames are then extracted from this video at regular time intervals and are then analysed using the DropSnake plug-in[90] for ImageJ.

3.7 Ion Beam Analysis

Ion beam analysis (IBA) encompasses a range of techniques that are used to provide quantitative elemental composition versus depth within a material. This

technique requires isotopic labelling of the component to be probed.

A beam of positive helium ions is produced from a stream of ^{3}He or ^{4}He gas which is fed into a radio frequency source chamber. A 6 kV potential is applied to the source and this propels the ions into a rubidium charge exchanger, producing negative He ions. These negative ions are then fed into a 1.7 MeV 5SDH pelletron accelerator (National Electrostatics Corp., Wisconsin, USA).

The negative ions are converted back into positive ions and are accelerated. The ions are then focussed by magnets into a 2 mm diameter beam, which is directed onto the sample within the end-station. The end-station is brought under high vacuum during analysis. To avoid evaporation of volatile components in samples within this high vacuum, samples are vitrified by plunging them into liquid nitrogen after spin coating.

Upon incidence with the sample, scattered ions, nuclear decay products, ejected ions and photons are produced and these are detected by a planar silicon detector and their energy spectra are analysed.

The depth distribution is determined from the relationship between the detected beam energy and the thickness of the sample. The beam will lose kinetic energy as it interacts with the sample and the stopping power, S, can be given as

$$S = -\frac{\mathrm{d}E}{\mathrm{d}z} \tag{3.19}$$

where E is the ion energy and z is the distance the beam has travelled through the sample.

IBA can have an elemental sensitivity on the order of parts per million and has a depth resolution on the order of tens of nanometres. Careful consideration must be given, however, to the irreversible damage caused to samples by the beam of ions. This means that the location of the beam print must be changed for each measurement and the beam charge incident on one location must be limited. To minimise the effects of sample damage, measurements are recorded at different locations on the sample which can then be added together to obtain statistically significant data.

Within this work, nuclear reaction analysis has mainly been used.

3.7.1 Nuclear Reaction Analysis

Nuclear reaction analysis (NRA) experiments involve a nuclear reaction within the sample. The most common reaction used is the reaction between deuterium in the isotopically labelled molecules and ^{3}He incident ions. A beam of 700 keV is used as the greatest probability of this reaction occurring is between 650 and 700 keV. The reaction can be shown as ^{2}H(^{3}He,^{1}H)^{4}He where ^{2}H and ^{3}He are the target and beam nuclei respectively and ^{1}H and ^{4}He are the product nuclei.[91] This reaction is also exothermic, with 18.352 MeV released.[92] Whilst both product ions can be detected, the proton is the ion which is more useful for depth profiling.[91,93]

An incident beam angle of between 70 and 80 ° was selected for these experiments and the beam charge per spot was 1 µC. Data collected at a specific incident angle in multiple locations on the same sample could be combined to give more accurate results, with typically 3 different locations used for each sample. Within this work, NRA was mainly used to support and validate neutron reflectometry depth profiles. NRA is highly advantageous as a complementary technique to NR as it is sensitive to deuterium regardless of lateral distribution within the film: whilst NR will only detect homogeneous layers, NRA is also capable of identifying inhomogeneous surface features.

3.7.2 Fitting Methods

All IBA data were analysed with the Surrey University DataFurnace[94] software (WiNDF v9.3.98 running NDF v9.6a) to calculate concentration versus depth profiles for the deuterated component within the sample.

DataFurnace is capable of fitting multiple spectra simultaneously, allowing data from multiple angles on a single sample to be used to produce a single depth profile. The fitting process is an iterative fitting algorithm which, from an estimated layer profile defined by the user, attempts to minimise the statistical quantity χ^2 based on the difference between the experimental data and the fit.

3.8 Atomic Force Microscopy

Atomic force microscopy probes the surface topography and mechanical properties of a sample by measuring the deflection of a cantilever as it moves across a surface. This technique gives detail of the surface properties at both the nano and micrometre scale. High precision movement of the cantilever both in the vertical and horizontal directions is achieved through use of piezoceramic actuators which, when a voltage is applied, expand or contract to move the sample relative to the cantilever. The deflection of the cantilever, caused by the surface of the sample, is then measured through the position of a laser reflected onto a photodiode from the cantilever (Fig. 3.9).

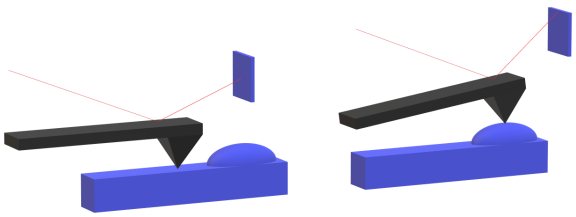

Figure 3.9: Schematic demonstrating how the movement of the laser position is caused by cantilever deflection. The position of the laser on the photodiode is measured and this is then used to determine the height of the surface feature

As the probe is rastered across the surface, a force distance curve is collected for each sample point. An example of this is shown in Fig. 3.10. As the probe approaches the surface, an attractive van der Waal's force is exerted on the probe, pulling the probe into contact with the surface. As the probe is then withdrawn from the surface, these van der Waal's forces adhere the probe to the surface, until the spring constant of the probe becomes larger than the van der Waal's forces and the probe returns to its resting position. If the spring constant of the probe is known, these adhesive forces can then be calculated for each sample point,

generating an adhesion map of the surface.[95]

Samples were prepared by spin coating solutions onto $\sim 1 \times 1$ cm^2 silicon substrates. This substrate was then fixed to a steel disk using double sided tape in order to allow the sample to be held inside the AFM with a magnet. A Bruker MM8 Multimode AFM was used with NuNano Scout 70R probes with a nominal spring contant of 2 N m^{-1}. For temperature controlled samples, the AFM is fitted with a NanoScope High Temperature Heater Controller. Analysis was performed in quantitative nanomechanical mapping (QNM) mode with a minimum of 512 samples per line. Images were analysed using Gwyddion v2.53 software. Within this thesis, both height and adhesion maps have been presented.

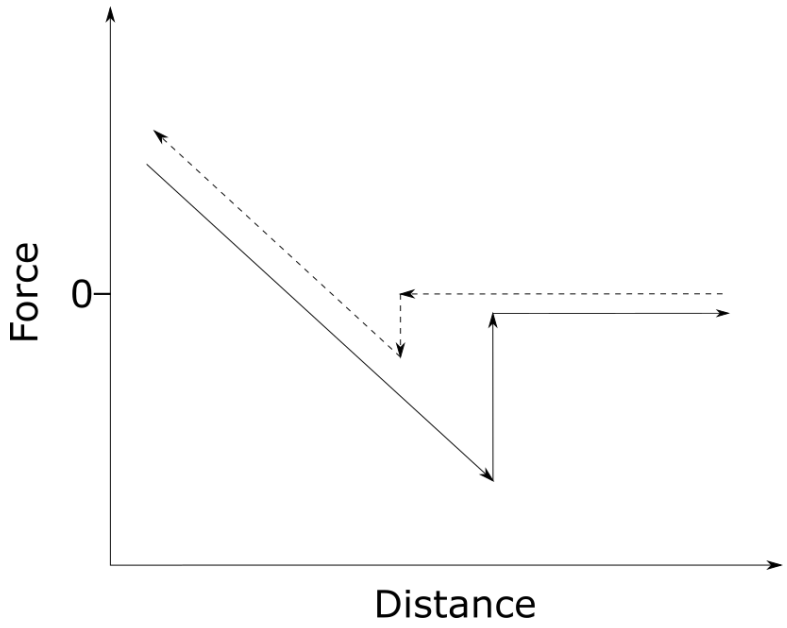

Figure 3.10: AFM force distance curve showing the adhesive force acting upon the probe as it is moved towards the surface (dashed) and then removed from the surface (solid).

Within this thesis, several parameters are calculated for each surface image. root mean square roughness, R_q, maximum roughness, R_{max}, and surface area ratio, R_{SA} have been used to compare the surfaces of samples.

The root mean square roughness, R_q indicates the standard deviation of the distribution of height values. This is given by Equation 3.8 where h is the height values for each point and N is the number of points.

$$R_q = \sqrt{\frac{\sum_{j=1}^{N}(h_j)^2}{h}} \tag{3.20}$$

The surface area ratio, R_{SA}, is defined by Equation 3.21 where A_P is the projected area and A_{SA} is the actual surface area.

$$R_{SA} = \frac{A_P}{A_{SA}} \tag{3.21}$$

Chapter 4

Compatibility studies of $C_{12}E_x$ surfactants in hydrophobic polymers

4.1 Chapter introduction

This chapter focusses on assessing the compatibility of a $C_{12}E_x$ surfactant (where $2 < x < 6$) in *cis*-PI and LDPE. This compatibility evaluation is required in further chapters to consider whether segregation is occurring due to the incompatibility of the additives or due to surface energy differences. Whilst the solution behaviour of individual components is well studied,[96–98] the behaviour of components in the absence of solvent is less often explored. Many commercial blends are prepared via melt processing,[99] meaning that solvent is absent. It is therefore important to consider the compatibility of surfactants within a polymer after it has been vitrified.

Whilst previous work studying the compatibility of small molecules in polymers has utilised cloud point analysis,[100] both *cis*-PI and LDPE are cloudy at room temperature, meaning that it is very difficult to discern whether the additive is compatible or not as this technique relies on a change from transparency (in mixed samples) to high turbidity in immiscible samples. Instead, alternative tech-

niques have been investigated that do not rely on visual methods of determining compatibility.

Within this chapter, two methods of assessing compatibility have been considered: assessment of the change in the polymer phase transitions via DSC and the change in rheological properties of a polymer / surfactant blend. Whilst work conducted in later chapters is centred on surfactant behaviour in thin polymer films, the compatibility analysis conducted here is carried out on bulk materials.

DSC has previously been used to assess the compatibility of additives and polymers. Daniels and Cabrera have shown that DSC is useful for measuring the compatibility of a plasticiser within poly(vinyl chloride).[101] The work demonstrates that the T_g of a polymer blend decreases as a compatible plasticiser is added. When the polymer and additive are compatible, the environment of the polymer changes with changing additive concentration. If this results in a change in free volume, the T_g will also be expected to change. This is also described by the Fox equation (4.1), which describes how the T_g of a binary mixture of compatible polymers, a and b, is proportional to the mole fraction of each component (w_i where i is a or b) and the glass transition temperature of each component ($T_{g,a}$ and $T_{g,b}$).

$$\frac{1}{T_g} = \frac{w_a}{T_{g,a}} + \frac{w_b}{T_{g,b}} \tag{4.1}$$

Whilst the additives in this case may not be polymers, the shift in T_g with changing weight fraction of additive may be expected to follow a similar trend.

There is significant precedent for the use of rheometry to assess the miscibility and compatibility in polymeric materials. Rheometry has previously been shown to be useful in assessing the compatibility of two polymers (poly (ethylene oxide) and poly(ϵ-caprolactone)) by Li *et al.*[102] Within this work, the phase-separation temperature of the mixture was identified from a change in the temperature dependence of G' through a plot of G' vs. T. This relationship between phase separation and a change in rheological behaviour has been widely studied.[103–105] Whilst much work focusses on the phase separation of polymer blends, an incompatible surfactant can produce microphases within the polymer. These will also

have distinctive rheological behaviour and so rheology can also be used to probe miscibility in these systems.

The Han plot has also been used as a tool for investigating thermally induced transitions within polymer blends.[106] This is a plot of $\log G'$ vs. $\log G''$ obtained from oscillatory rheometry. This technique has been applied to polymer blends such as polylactide / polyamide[107] and has shown that a compatible blend will show a linear relationship between $\log G'$ and $\log G''$ within the terminal region, where G'' exceeds G' at low frequency. This may be of particular use as the Han plot does not require temperature to be plotted on either axis, possibly providing a method to assess compatibility over a range of temperatures.

An alternative strategy for determining compatibility through rheometry, which is proposed in this work is facilitated by van Gurp-Palmen plots. These plots of δ vs. $\log G^*$ (where δ is the phase angle, Fig. 4.1, and G^* is the complex modulus) are primarily used to determine whether the Time-Temperature Superposition principle (TTS) holds for a polymer blend.[108] Within these plots, the TTS principle holds if the curves plotted for each temperature probed converge onto a single line. However, miscibility of components within polymer blends has also been investigated through the use of these plots.[109,110] The justification for this usage is that if the curves do not converge on a single line, and the TTS principle does not apply, a change in the properties of the material (such as a phase change) must occur as the temperature is changed.

4.2 Results

4.2.1 Assessing *cis*-PI / $C_{12}E_x$ Compatibility Using Thermal Analysis

Within this section, DSC results of mixtures of *cis*-PI and several additives shall be presented in order to assess both the value of DSC as a technique in determining compatibility of small molecules within polymers as well as understand the concentration dependence of the compatibility of these small molecules. Sam-

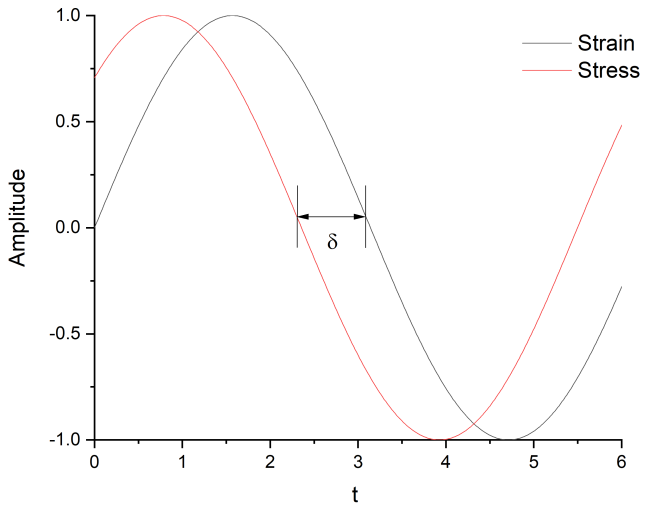

Figure 4.1: Stress and strain curves for a strain-controlled oscillatory rheometry experiment. The stress has a time lag behind the the strain, which is defined as the phase angle, δ.

ples of *cis*-PI–02 and surfactant were prepared as outlined in Section 3.3, with surfactant loading varying between 0 and 10 wt.%. All DSC measurements were performed with a heating and cooling rate of 10 °C per minute.

Figures 4.2 and 4.3 show the DSC thermograms of pure $C_{12}E_5$ and *cis*-PI respectively through both a heating and cooling step. Within Fig. 4.3 it is possible to observe a thermal event at approximately -65 °C in the heating step. This peak, accompanied by a change in baseline, is indicative of a glass transition. A demonstration of how T_g is obtained is shown in Fig. 4.4. This is much more difficult to observe within the cooling step. However, it is possible to identify a change in gradient, corresponding to the glass transition temperature. Fig. 4.2 shows the melting point of $C_{12}E_5$. As expected there is a difference between the temperature at which the melting peak (28 °C) and the crystallisation peak (5 °C) occur. However, these peaks shall be used to identify any pure, unmixed $C_{12}E_5$ present in blends below.

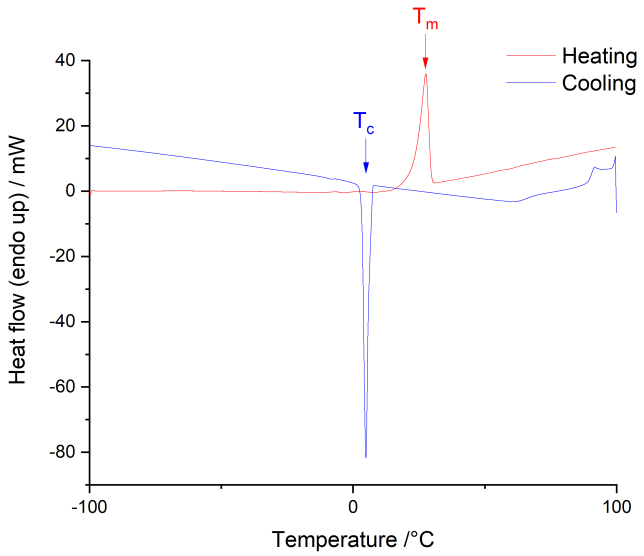

Figure 4.2: DSC thermogram of $C_{12}E_5$, collected with a ramp rate of 10 °C per minute. A baseline correction has been applied to the data. T_m and T_c have been labelled.

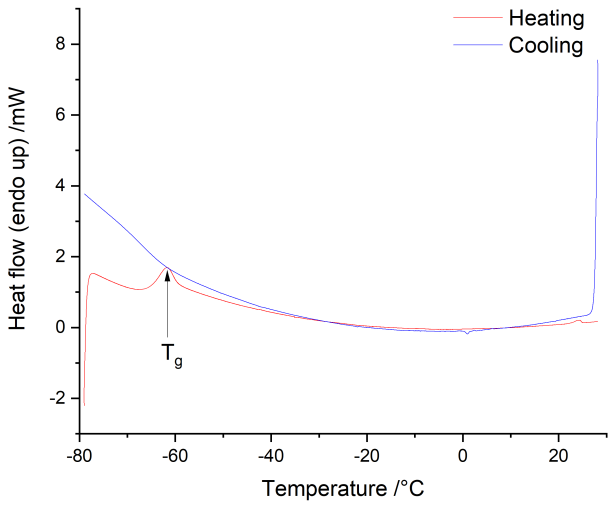

Figure 4.3: DSC thermogram of cis-PI, collected with a ramp rate of 10 °C per minute. A baseline correction has been applied to the data. The T_g has been labelled.

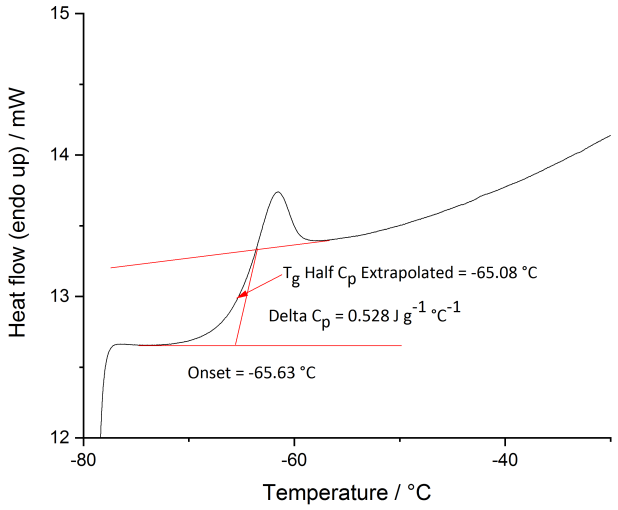

Figure 4.4: DSC thermogram of *cis*-PI demonstrating how the T_g is determined. The change in heat capacity is calculated and the temperature at which the C_p is half of this is given as the T_g

$C_{12}E_x$ / *cis*-PI DSC results

The DSC curves for the heating and cooling of $C_{12}E_3$ loadings between 1 and 10 % in *cis*-PI–02 have been plotted in Fig. 4.5. Within the heating curves, a clear T_g can be seen at all concentrations at approximately -60 °C which is consistent with literature results[111] (-67 °C). This transition does not change dramatically with changing composition. However, within the cooling curves, an exothermic peak can also be seen emerging near -25 °C, which becomes larger with increasing surfactant loading. A similar endothermic peak can also be seen in the heating curves above 0 °C. This corresponds to the crystallisation and melting of $C_{12}E_3$, suggesting that if there is a peak present, sufficiently large surfactant domains must be present to exhibit bulk properties. This is also seen in $C_{12}E_5$ samples (Fig. 4.6) at the melting point corresponding to $C_{12}E_5$, indicating that similar surfactant domains are also present in these samples with higher loadings.

The thermal behaviour of 10 % $C_{12}E_5$ in *cis*-PI–02 can be seen in Fig. 4.7. The measurements have been repeated on the same sample to determine whether the behaviour of the sample changes after heating or cooling. If no significant change

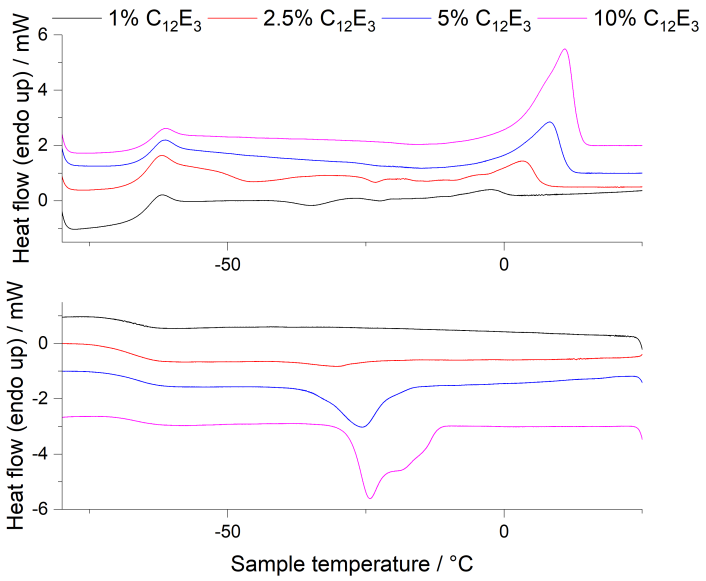

Figure 4.5: DSC heating (top) and cooling (bottom) curves of 1 – 10 % $C_{12}E_3$ in *cis*-PI–02. A baseline correction and offset has been applied to each set of data for clarity.

occurs, it can be assumed that the solution-cast films are a reasonable representation of melt-processed films. Within each cooling step, several exothermic peaks between -10 and -25 °C can be seen. These exothermic peaks tend to correspond to crystallisation events which, as this is a binary mixture where the polymer is already below T_m ($\sim$ 35 °C), can be attributed to the surfactant. The cooling step in Fig. 4.3 shows no noticeable peak event, with only a change in gradient observed at -60 °C, indicating that no polymer transition can be attributed to these peaks. Multiple peaks can be observed in liquid crystals,[112] which have previously been identified as crystallisation peaks between liquid crystalline phases. This is evidence of the presence of surfactant domains large enough to exhibit bulk properties: if the surfactant was fully mixed, crystallisation of the surfactant would not be possible, suggesting that a 10 % $C_{12}E_5$ loading is more incompatible with the matrix polymer. It has previously been shown that $C_{12}E_5$[113] and other surfactants of differing head and tail group length[114,115] can exhibit liquid crystalline behaviour within aqueous systems. This supports the hypothesis that these crystallisation peaks are caused by bulk surfactant within the polymer

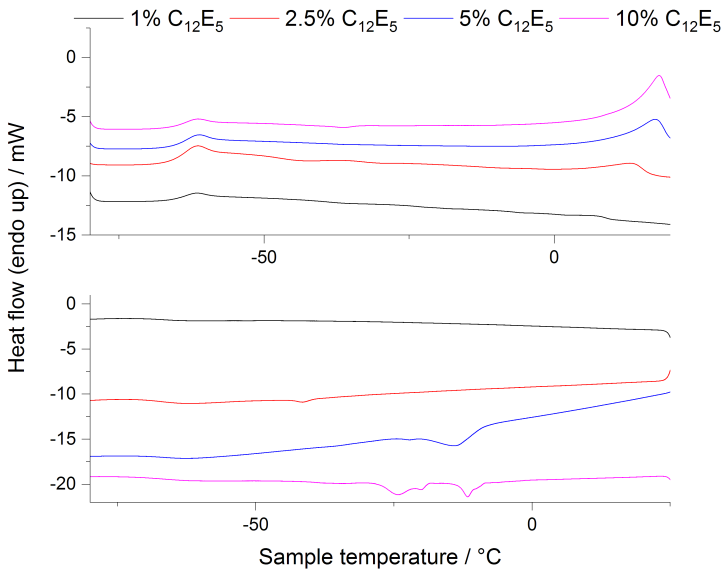

Figure 4.6: DSC curves of 1 – 10% $C_{12}E_5$ in *cis*-PI–02. Heating and cooling data have been plotted on separate axes with the same horizontal axis range. An offset has been applied to each set of data for clarity.

matrix. It is important to note, however, that the DSC thermogram of $C_{12}E_5$ (Fig. 4.2) does not show multiple crystallisation peaks and moreover crystallises at a significantly higher temperature. This suggests that $C_{12}E_5$ alone does not show this liquid crystalline behaviour and that the interaction with the polymer has some impact on the crystallisation behaviour of the surfactant. Tonegawa *et al.*[113] found that in water, $C_{12}E_5$ shows both lyotropic and thermotropic behaviour. Whilst the present work effectively uses a polymer as a solvent instead of water, it is possible that this thermotropic behaviour is also seen in *cis*-PI samples. These results suggest that the components are not highly compatible but do interact sufficiently to modify the behaviour of the pure components.

Further work has shown that $C_{12}E_3$ can also exhibit liquid crystalline behaviour in water.[116,117] $C_{12}E_3$ in water also shows thermotropic and lyotropic behaviour, with distinct lamellar surfactant and bulk water phases at low surfactant concentrations (<10 wt.%). To the author's knowledge, there is no comparable study of surfactants within a polymer, but the modification of thermal transitions of the additive could be consistent with liquid crystalline behaviour previously

reported of the surfactant in water.

Whilst it has previously been shown[118] that $C_{12}E_x$ surfactants with a longer ethylene oxide chain can display multiple peaks in the melting behaviour, the peaks seen are distinctly different from the observations in this work. Bouwstra *et al.* showed that these surfactants when hydrated could display multiple melting peaks[118] with a spacing of approximately 3 °C, presenting as a smaller shoulder on a larger peak.[119] However, the cooling exotherm peaks observed in Fig. 4.7 have a separation much larger than 3 °C and thus can be resolved into a distinct peak and a second lower temperature peak with a shoulder, suggesting that the structure of any surfactant domains may be different to those seen in water.

The presence of a single endotherm for the melting step suggests that the component that melts is all the same material. The multiple crystallisation exotherms may mean that this material adopts several morphologies as the sample is cooled to a final cold state, with an exothermic transition at each morphology change. An alternative possible hypothesis for the multiple exothermic peaks observed in the cooling step is that there is $C_{12}E_5$ in multiple environments. This may be, for example, in micelles of different structures or within both micellar and lamellar structures. The surfactant within these different environments would experience different interactions, affecting the melting point. Similar effects have been observed in polymers such as poly(ether ether ketone), where multiple peaks have been observed in the melting peak.[120] Supporting wide-angle X-ray scattering (WAXS) and small-angle x-ray scattering (SAXS) results[120] presented evidence of multiple crystal morphologies, similar to the possible different structures observed in the surfactant / polymer blend DSC curves.

Previous work by Chen and Wolcott has probed the miscibility of several polyethylenes and a smaller additive, paraffin.[121] Samples containing only PE and paraffin showed two distinct crystallisation peaks that cannot be attributed to the polymer. Therefore, these were both attributed to the paraffin, which was reasoned to be evidence of both bulk paraffin and paraffin-polymer blend. This could be a similar effect seen here, with several different surfactant-dominated compositions being observed in these higher concentration samples. Whilst it is

not possible to identify whether there is liquid crystalline behaviour or not within the bulk surfactant domains from these techniques, both possible reasons above support the hypothesis that there is surfactant domains within the polymer at higher concentrations.

In the heating steps, distinct endothermic events can be seen at -65 °C and 18 °C. These correspond to the glass transition of *cis*-PI–02 and the melting point of $C_{12}E_5$ respectively (Fig. 4.2 and 4.3). Whilst the glass transition is not an endothermic transition, a small endothermic peak is often present that is associated with an enthalpic overshoot. The presence of a surfactant melting peak again confirms the presence of some bulk $C_{12}E_5$, as large domains of surfactant would be required to exhibit a peak. This peak is also observed in $C_{12}E_3$ samples (Fig 4.5), suggesting that even with a smaller head group, the surfactant still forms some large domains within the sample, indicating limited compatibility between the surfactant and the polymer matrix.

The change in T_g of the polymer matrix as surfactant loading is varied is compared in Fig. 4.8. For each surfactant, data was gathered in a single series of measurements over a short period of time and so have a high degree of internal consistency. However, the instrumental drift between the time of measuring $C_{12}E_5$ and $C_{12}E_3$ may have been significant, precluding direct comparison between series. To explore this further, the measurements were repeated for 10 % $C_{12}E_5$ and 10 % $C_{12}E_3$ on the same day (triangles). These 10 % samples display that there is a significant difference between the values for $C_{12}E_5$ measured at different times, indicating significant drift. Therefore, whilst results can be compared within each series (i.e. different concentrations of the same surfactant), it is not possible to compare the different surfactants directly.

$C_{12}E_3$-containing samples show an initial decrease in T_g at low concentrations, followed by an increase above 1 % loadings, with the T_g rising above that of pure *cis*-PI-02 at 10 % loading. Both samples appear to show some impact of addition of surfactant on the *cis*-PI, suggesting that there is some mixing of the components[122] with the matrix. However, a key feature in the 10 % results is the lack of further increase in T_g at above 5 % loading in $C_{12}E_5$ samples, presenting

evidence of a limit in the miscibility of the surfactant between 5 and 10 %, with further surfactant no longer mixing with the matrix and thus not modifying the T_g of the polymer. This is not seen in $C_{12}E_3$, suggesting that the surfactant is more compatible across the concentration range investigated.

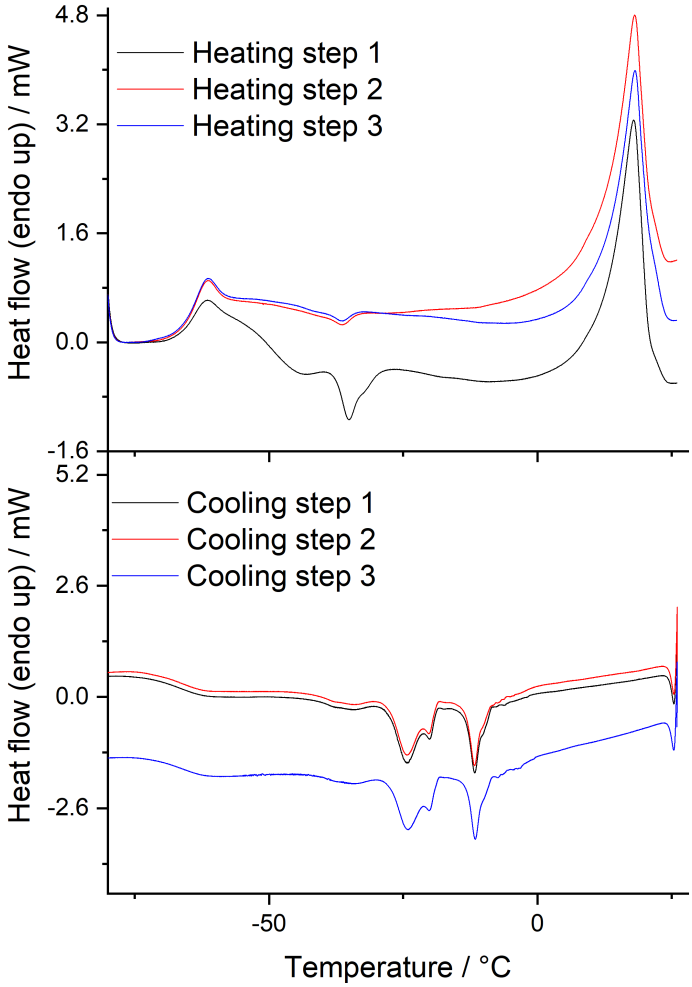

Figure 4.7: DSC curves of 10% $C_{12}E_5$ in *cis*-PI–02. Heating and cooling data have been plotted on separate axes with the same horizontal axis range.

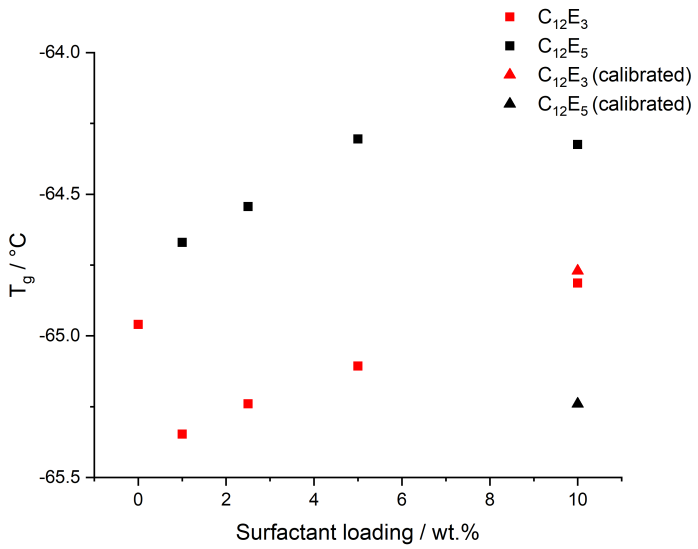

Figure 4.8: The variation in T_g with $C_{12}E_3$ and $C_{12}E_5$ loading in *cis*-PI-02.

4.2.2 Assessing LDPE / $C_{12}E_x$ Compatibility Using Thermal Analysis

The compatibility of surfactants within LDPE must also now be considered. Whilst the chemical structure of *cis*-PI and LDPE are similar, there is a significant difference in crystallinity between these two polymers: LDPE contains significant crystalline domains whereas *cis*-PI is amorphous. This could mean that the compatibility of the additive within the different polymer matrix may change.

This section involves the investigation of the compatibility of LDPE and surfactants through the use of DSC. However, LDPE does not have an easily distinguishable T_g due to the relatively low proportion of amorphous material, meaning that the same analysis technique as discussed in the previous section cannot be conducted. Instead, this work shall probe the melting transition of the blend, where it is expected that a decrease in T_m and crystallisation temperature, T_c, will be observed if the materials are compatible.

Whilst both T_m and T_c can be examined through this technique, it is more difficult within these samples to accurately identify T_m (Fig. 4.9). As there is also a change in heat capacity upon melting, shown by the change in gradient and step transition, it is not always possible to observe a distinct melting peak or accurately measure the enthalpy change of fusion, ΔH_{fusion}. However, it is much easier to reliably identify T_c and so this has been investigated. Fig. 4.9 also shows the significant difference in thermal behaviour of a sample between the first heating step and subsequent runs. This suggests that before the first melting process, there is a thermal history within the sample which is removed upon melting the polymer. Therefore, within measurements for these LDPE samples, only data from the first cooling step onwards are assessed. It is important to note that this thermal history may mean that the structure of solution cast films may be somewhat different to the structure of melt processed materials.

When measuring ΔH_{fusion}, it is also important to consider the baseline heat flow: as the area of the peak is calculated, a changing baseline heat flow may

have a significant effect on the area. As samples show a change in base heat flow during the crystallisation event, areas have been calculated with a sigmoidal baseline. this has been achieved by extrapolating the base heat flow before and after the event peak and applying a sigmoidal curve between the two extrapolated lines at the midpoint of the peak.

Dodecane / LDPE DSC results

As well as considering the compatibility of a surfactant molecule containing both a hydrophobic and hydrophilic region, it is prudent to consider the behaviour of a small molecule which would be expected to be compatible. In this case, dodecane has been selected for this purpose. Dodecane has the same structure as the hydrophobic group of a $C_{12}E_x$ surfactant (a 12 carbon linear hydrocarbon) and thus grants the ability to assess how a small molecule behaves without any hydrophilicity. Similar molecules are often used as plasticizers within polyolefin blends, including short chain oligomers[123,124] and solvents.[125] These plasticiser molecules, whilst often added to lower T_g can also have a significant effect on the T_m of the polymer, as was shown for PVA samples with glycerin.[126]

Figure 4.10 shows the variation of the melting and crystallisation point of LDPE as dodecane loading is increased. In both melting and crystallisation data, it is clear that at low dodecane loadings, the melting point initially increases slightly. However, above 2.5 % dodecane, T_m and T_c begin to decrease. Initially this is surprising as it would be expected that small molecules similar to solvents would increase the entropy of the melt, thus making crystallisation less thermodynamically favourable, lowering the T_m of the blend.[125] However, instead at low concentrations, an elevation in T_m is seen. This increase in T_m, however, is within error and so this effect is not a physical feature of the material.

The effect of a small molecule on T_c of a polymer can also be understood by considering the free energy change of melting. The presence of a small molecule will increase the entropy of the liquid phase. This makes the liquid phase more thermodynamically favourable, lowering the crystallisation and melting temperature.[127]

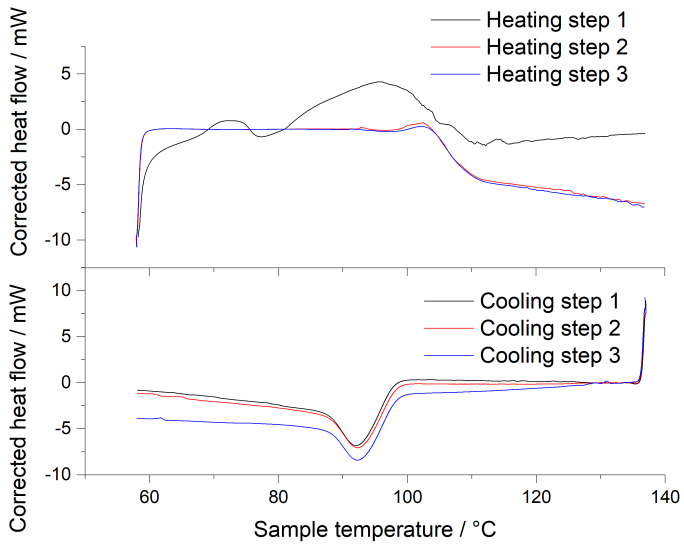

Figure 4.9: DSC thermogram of LDPE showing several successive repeated heating and cooling cycles on the same sample. Heating and cooling data are plotted on separate axes for clarity with the same horizontal axis range.

$C_{12}E_x$ / LDPE DSC results

The change in crystallisation temperature plotted against surfactant loading for $C_{12}E_3$, $C_{12}E_4$ and $C_{12}E_5$ is shown in Fig. 4.11. Interestingly, the 3 surfactants show distinctly different behaviour. $C_{12}E_5$ and $C_{12}E_4$ show a large ($\sim$ 6 °C) decrease in T_c even at 1 % loadings, whereas $C_{12}E_3$ shows only a modest decrease in T_c even at high loadings. The behaviour seen for $C_{12}E_4$ and $C_{12}E_5$ is consistent with a compatible additive that favours the molten state of the polymer. This is similar to the work of Wu *et al.*,[128] where a similar decrease in melting point can be seen. It must be noted, however, that the work by Wu *et al.* is based on PVA, which has only a moderate degree of crystallinity. This means that a T_g could still be measured and consider the plasticising effect of the additive. Whilst it is not possible to directly compare the degree of T_m decrease, the polymer used in the work by Wu *et al.* is PVA rather than a hydrophobic polymer, this is a good example of the effect of a plasticiser on the polymer melting point and illustrates a key difference between these surfactants and a conventional plasticizer. Whilst both $C_{12}E_5$ and $C_{12}E_3$ show an initial decrease in T_c, beyond 2.5 to 5 % surfactant

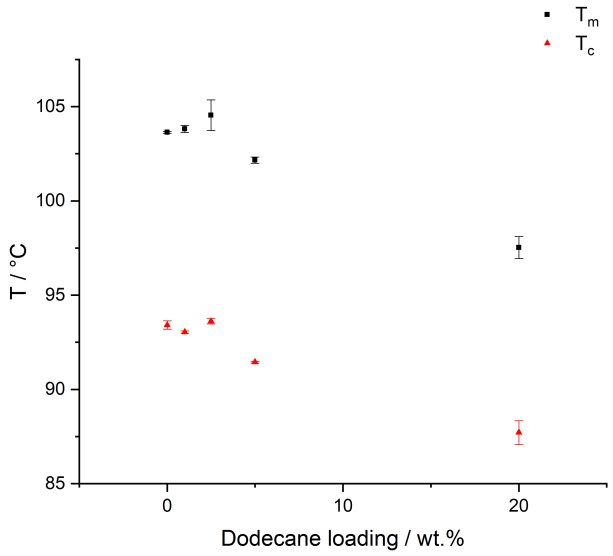

Figure 4.10: Melting and crystallisation temperatures of an LDPE / dodecane as a function of dodecane loading calculated from DSC data. Results have been plotted showing standard error based on 3 repeats.

loading, T_c no longer shows any decrease. This suggests that above this surfactant concentration, no more surfactant is compatible with the polymer and thus can cause no further decrease of T_c. The difference in behaviour between $C_{12}E_3$ and the two longer head group surfactants suggests that there is a change in compatibility between $C_{12}E_3$ and $C_{12}E_4$. However, it appears that the absolute value of T_m or T_c is not a reliable measure of compatibility.

An alternative parameter to consider is the ΔH_{fusion}. This is the energy change observed when the sample crystallises and is calculated from the area of the peak in the DSC thermogram. Fig. 4.12 shows ΔH_{fusion} plotted for several surfactants against surfactant loading. It is clear from these results that $C_{12}E_5$ shows a similar behaviour for ΔH_{fusion} as was seen for T_c, with an increase in magnitude seen as surfactant loading is increased. It is important to note that ΔH_{fusion} has been normalised by the LDPE concentration of the blend, meaning that this eliminates the decreasing polymer concentration as surfactant loading increases. As ΔH_{fusion} is the energy change associated with the melting of the polymer, this enthalpy change can be related to the degree of crystallinity, with more crystalline

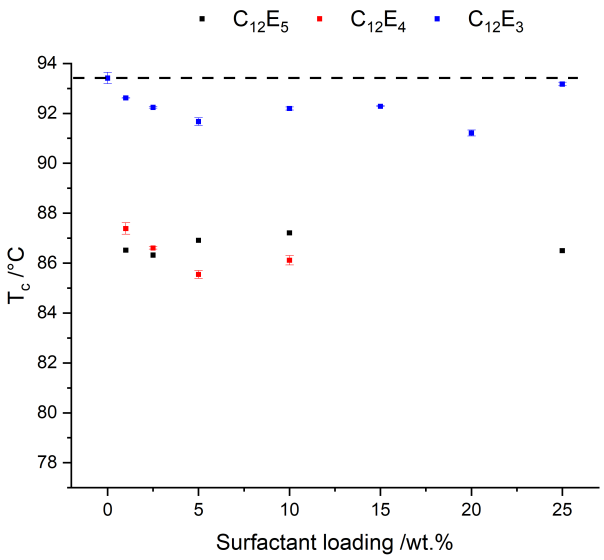

Figure 4.11: T_c vs. surfactant loading for LDPE / $C_{12}E_5$, $C_{12}E_4$ and $C_{12}E_3$. Results are obtained by measuring the position of the maximum point of the crystallisation peak for each sample using a sigmoidal baseline. The dotted line shows the T_c of unloaded LDPE.

samples showing a larger magnitude of ΔH_{fusion}.[129] This suggests that the $C_{12}E_5$ induces more crystallinity within the polymer. This is also observed to a more minor degree in low loadings of $C_{12}E_3$, with a much lower decrease in ΔH_{fusion} observed. This appears to present a conflicting description of the compatibility of the polymer and surfactants compared to the change in T_c. However, it should also be noted that the ΔH_{fusion} for LDPE of a similar molecular weight[130] ($M_v = 47,000$ g mol^{-1}) has been determined to be 149 J g^{-1}, meaning that as the sample in literature was found to have a degree of crystallinity of 0.50, the LDPE used in this work has a degree of crystallinity of 0.06. This is far lower than what is expected for LDPE and is unlikely to be the accurate degree of crystallinity. It is possible that the surfactant molecules disrupt the crystallisation structures of the polymer, producing a significantly different crystalline structure, with a different enthalpy of crystallisation. It therefore must be concluded that this is a poor method for determining compatibility with these materials.

From the thermodynamics of crystallisation, it is possible to infer the mole

fraction of solvent and therefore, with a knowledge of the mass fraction, it is possible to use this information to estimate the effective molecular weight or extent of aggregation of the solvent. Using the melting point of the blend T_m and the melting point of the pure polymer, T_m^0, it is possible to calculate the ratio of the molar volume of the polymer repeat unit, V_u, to molar volume of surfactant, V_1,[131,132] using equation 4.2. χ in this equation refers to the Flory-Huggins interaction parameter between the polymer and surfactant and ϕ_2 is the volume fraction of the polymer. As χ is expected to be low between a hydrophobic polymer and surfactant and ϕ_2 is high within the sample range measured, the $\chi(1-\phi_2)^2$ term can be ignored. ΔH_u is the enthalpy of fusion per polymer repeat unit, which is invariant with different diluents.[132] For polyethylene, ΔH_u has been reported as 4059 J mol^{-1}.[133,134]

$$\frac{1}{T_m} - \frac{1}{T_m^0} = \frac{R}{\Delta H_u}\left(\frac{V_1}{V_u}\right)^{-1}\left[(1-\phi_2) - \chi(1-\phi_2)^2\right] \tag{4.2}$$

Fig. 4.13 shows the $V1/Vu$ values for the 3 surfactant series. This data suggests that there is a significant change in behaviour between $C_{12}E_3$ and $C_{12}E_4$ / $C_{12}E_5$. This shows that at all loadings it appears that the shorter head group surfactant occupies a much larger volume per molecule than $C_{12}E_4$ and $C_{12}E_5$ within the polymer matrix. This again suggests a difference in compatibility between the surfactants, with $C_{12}E_3$ remaining mixed at all concentrations. However, the values of $V1/V_u$ are unfeasible: these values for $C_{12}E_4$ and $C_{12}E_5$ imply that the entire surfactant molecule has a comparable size to the C_2H_4 repeat unit of the polymer, strongly suggesting that the analysis cannot be relied upon. This also agrees with the observations from crystallisation enthalpy measurements that the crystallisation of LDPE and a surfactant is more complex than the polymer alone and may obey a different mechanism.

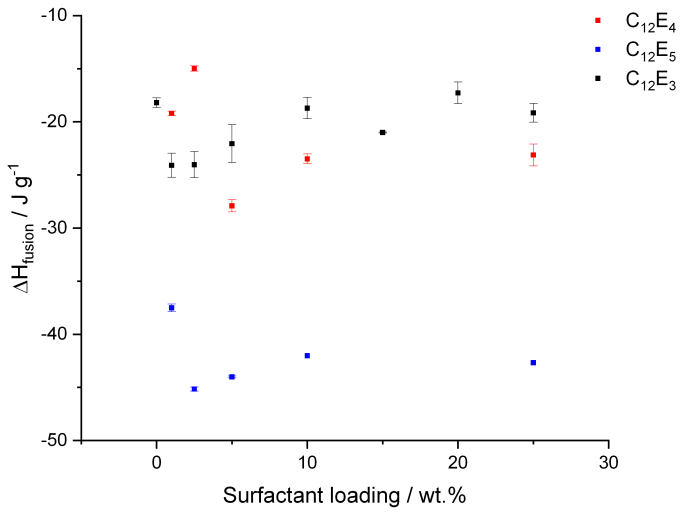

Figure 4.12: ΔH_{fusion} vs. surfactant loading for LDPE / $C_{12}E_x$ blends, ΔH_{fusion} has been normalised by the LDPE concentration.

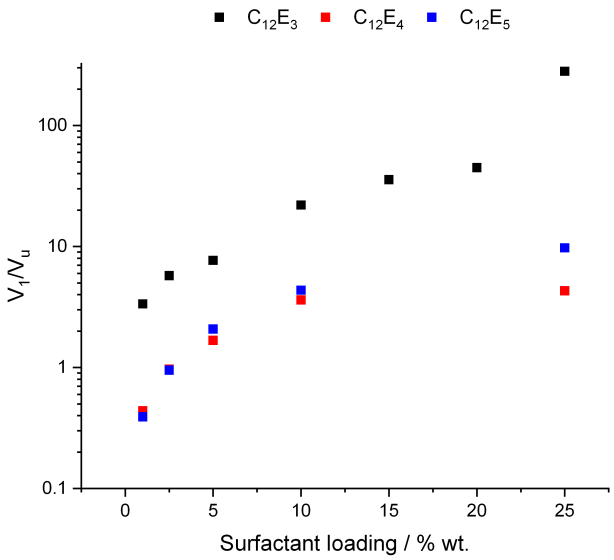

Figure 4.13: Ratio of surfactant molecular volume (V_1) to polymer repeat unit volume (V_u) for $C_{12}E_3$, $C_{12}E_4$ and $C_{12}E_5$ in LDPE as a function of surfactant loading.

4.2.3 Assessing *cis*-PI / $C_{12}E_x$ Compatibility Using Rheometry

Within this section, two samples of *cis*-PI have been assessed, *cis*-PI-01 and *cis*-PI-02. Figure 4.14 shows the storage and loss moduli of a blend containing *cis*-PI-01 and 1 % $C_{12}E_5$. Within the experimental region probed (0.1 – 100 rad s^{-1}), G' is larger than G", indicating that the blend is within the rubbery plateau region. To obtain rheometry measurements of this sample within the terminal regime, much lower frequencies would need to be probed. These measurements become impractical below 0.01 rad s^{-1} (where the time required to collect measurements extends beyond the order of hundreds of seconds) and so it is not possible to obtain the terminal region of these samples at the temperatures to be investigated. There are two possible ways to access the terminal region: either the temperature can be raised (assuming the TTS principle holds) and to use a lower molecular weight polymer.[75] There is limited scope to vary temperature within this experiment as at higher temperatures, *cis*-PI has a tendency to thermally oxidise and degrade.[135,136] Therefore, a lower molecular weight *cis*-PI shall be focussed on in this section. Fig. 4.16 shows the rheometry data for this lower molecular weight *cis*-PI and reveals that sample is within the terminal region at the temperatures and frequencies used in this experiment. This replacement of the polymer for a lower molecular weight analogue is acceptable here as Flory-Huggins theory indicates that the compatibility is independent of molecular weight if the polymer molecular weight remains much larger than that of the additive.

Figure 4.15 presents the behaviour of *cis*-PI and dodecane, a linear hydrocarbon. This hydrocarbon, lacking a hydrophilic group, is expected to be more compatible with the polymer matrix and is not expected to aggregate. The frequency sweep rheology for *cis*-PI containing 5 % dodecane (Fig. 4.15) appears to be quite similar to the corresponding sample without dodecane, Fig. 4.16, confirming this compatibility.

In order to assess whether any change which is observed at higher temperatures is reversible, samples were retested at 20 °C after being heated to 60 °C. The data

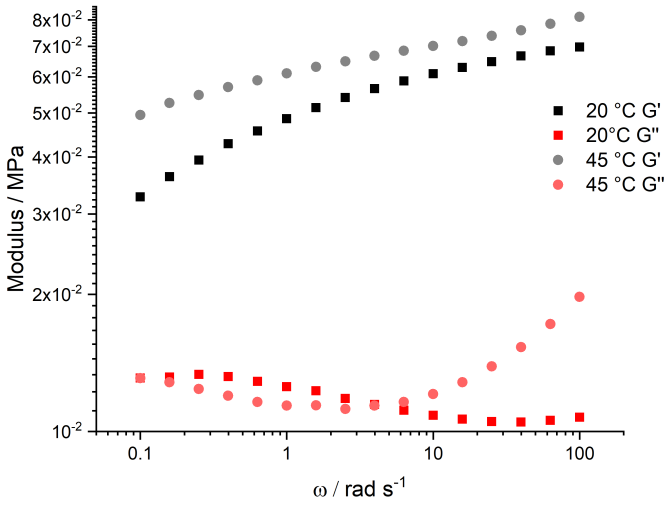

Figure 4.14: G' and G" of *cis*-PI-01 and 1% $C_{12}E_5$ obtained by oscillatory rheometry at 20 °C and 45 °C.

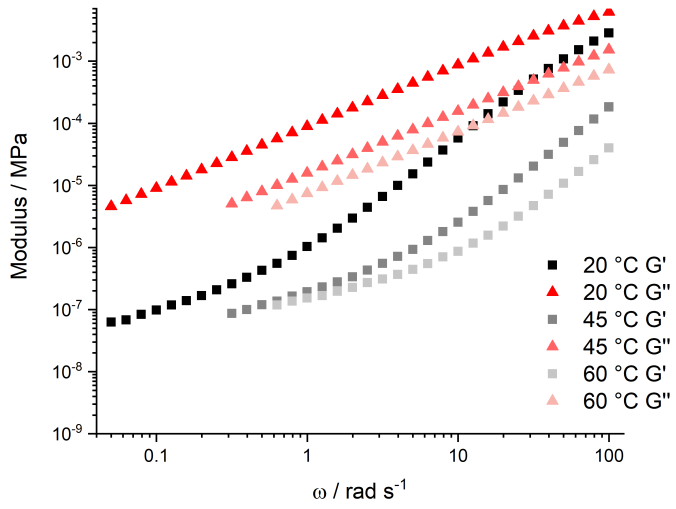

Figure 4.15: G' and G" of 35,000 g mol^{-1} *cis*-PI and 5 % wt. dodecane, a compatible hydrocarbon. Data below the torque limit of the instrument has been removed.

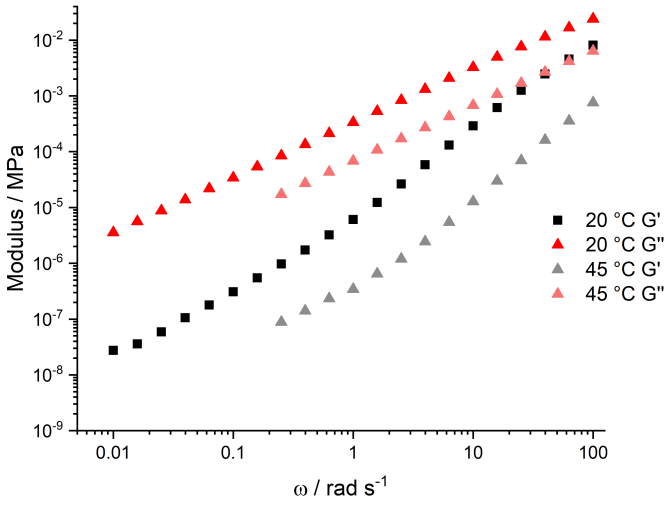

Figure 4.16: Storage and loss modulus of 35,000 g mo1^{-1} *cis*-PI. Data at 45 °C below the torque limit of the instrument (at low angular frequency) has been removed.

for *cis*-PI–02 / 5% wt. $C_{12}E_3$ samples at 20 °C before and after heating are shown in figure 4.17. From this figure, it is clear that there is very little change in G'' after heating and only a very small change is seen in G'.

Han plots

The Han plot of 5 % dodecane in *cis*-PI–02 has been plotted in Fig. 4.18, with the gradients for the linear portion of the data presented in table 4.1. These results show little change in gradient as temperature is varied. This is somewhat unsurprising, it is expected that dodecane would be compatible with the *cis*-PI polymer matrix, yielding a homogeneous blend. this would be expected to show little temperature dependence of the blend rheology[137] as observed.

Han plots for $C_{12}E_3$ and *cis*-PI–02 have been plotted in Fig. 4.19, with different temperatures of the same composition plotted on the same axes. The gradients for the linear region around $G' = 10^{-3} - 10^{-6}$ MPa for each temperature and composition have been calculated and plotted in table 4.2. The gradient of the Han plot for a mixed system would be expected to be 2,[138] with any lower gradient

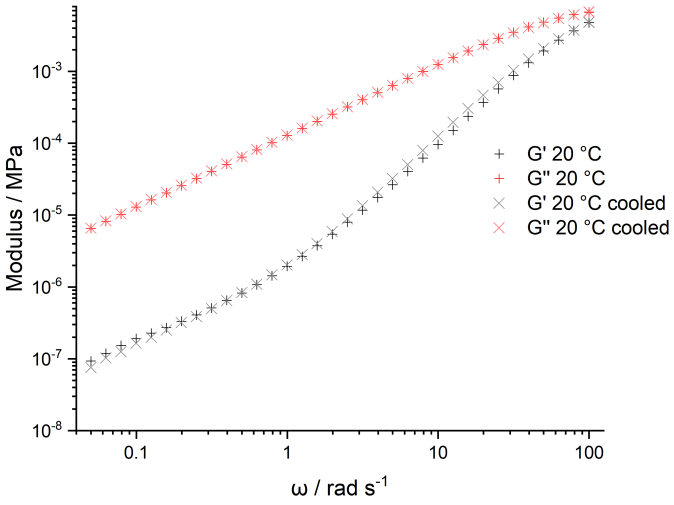

Figure 4.17: G' and G" of 5 % $C_{12}E_3$ in *cis*-PI–02 at 20 °C before and after being heated to 60 °C. To show overlapped data, the samples before heating are shown with plusses and the cooled samples have been shown with crosses. Note that there is very little difference in G" between the two tests.

expected to be caused by a two-phase morphology. It is believed that this lower gradient is an effect of the elastic contribution to G' of the interface between the two phases at high shear rates. However, it has also been noted that a lower gradient than 2 can be seen in polymer samples with significant polydispersity[139] and so this has not been considered an indication of compatibility within this work.

Upon inspection of Figs. 4.19, 4.20 and 4.21, it is clear that all surfactants show a curve indicative of G' increasing relative to G'' at lower ω. Similar curves have been seen in samples of nylon 12 containing maleic anhydride grafted styrene–ethylene/butylene–styrene (SEBS-*g*-MA).[140] This has been understood to be caused by the elastic nature of the interface between the additive and the matrix; G' characterises the elastic component of the modulus of a material and at low frequencies, the shear applied is at a sufficiently low rate to allow for both G' and G'' to respond to the stress. Furthermore, at lower shear rates, there is also sufficient time for the SEBS-*g*-MA to also respond.[140] It is likely that at low

frequencies, materials in a single phase can relax but if a permanent interface between incompatible phases is present, a contribution to G' becomes apparent. At higher frequencies, this becomes negligible compared to the modulus of the polymer.

Comparison of the Han plots of each surfactant shows that $C_{12}E_5$ shows the largest change in gradient with temperature increase. This suggests that this is more incompatible with the polymer than surfactants with shorter head groups, with a decrease in the elasticity associated with domains of separate compositions within the blend.[141] From Flory-Huggins theory (Eqn. 2.7), it can be inferred that a surfactant with a larger head group would be expected to be less compatible with the non-polar matrix.[22] It is also reported by Agrawal *et al.*[142] that two miscible materials would be expected to have curves on Han plots at different loadings that were able to superimpose. However, it is clear by inspection that the $C_{12}E_5$ samples show different shaped curves for different loadings at the same temperature, confirming that there is incompatibility.

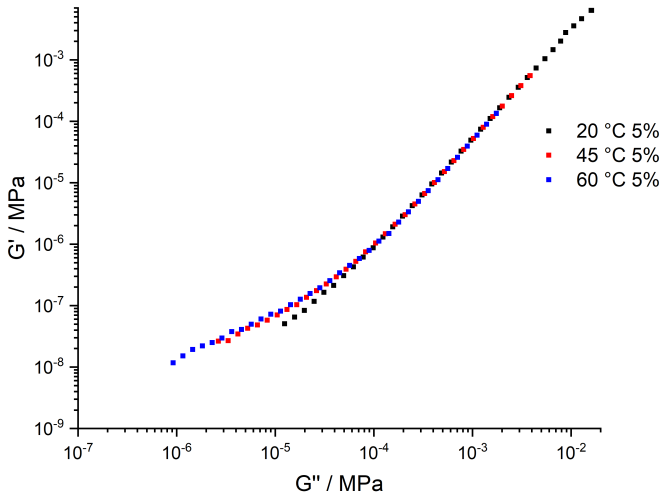

Figure 4.18: Han plot of *cis*-PI–02 with 5 % dodecane at 20, 45 and 60 °C

Table 4.1: Gradients of Han plots for 5 % dodecane in *cis*-PI-02 at 20, 45 and 60 °C given in fig. 4.18

Dodecane conc. / % wt.	$\frac{dG'}{dG''}$		
	20 °C	45 °C	60 °C
5	1.77	1.77	1.78

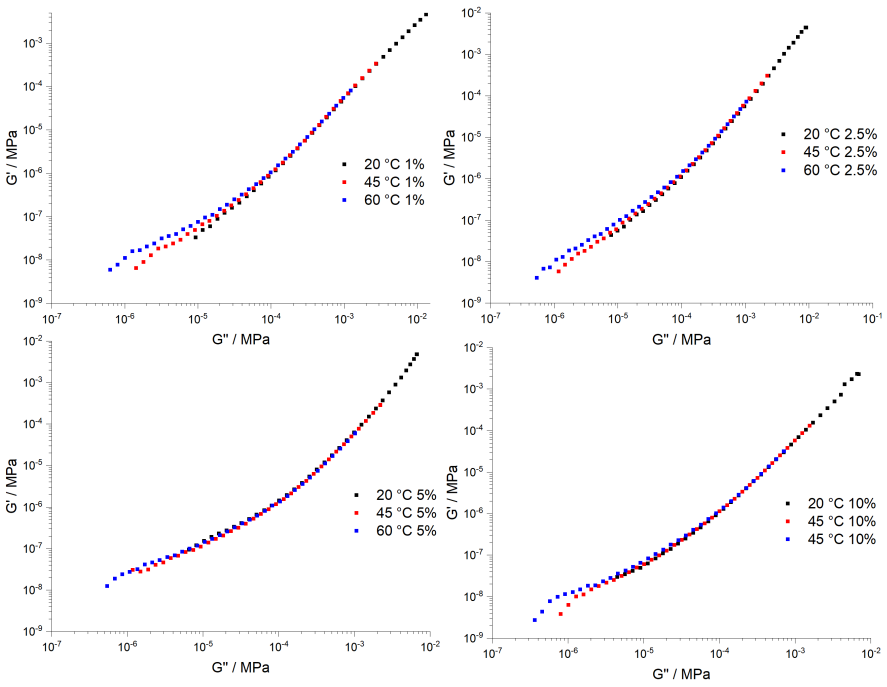

Figure 4.19: Han plot of 1% (top left), 2.5% (top right), 5% (bottom left) and 10% (bottom right) $C_{12}E_3$ in *cis*-PI–02

Table 4.2: Gradients of Han plots of $C_{12}E_3$ in *cis*-PI–02 shown in figure 4.19

$C_{12}E_3$ conc. / % wt.	$\frac{dG'}{dG''}$		
	20 °C	45 °C	60 °C
1	1.74	1.78	1.73
2.5	1.95	1.77	1.66
5	1.99	1.79	1.63
10	1.87	1.68	1.58

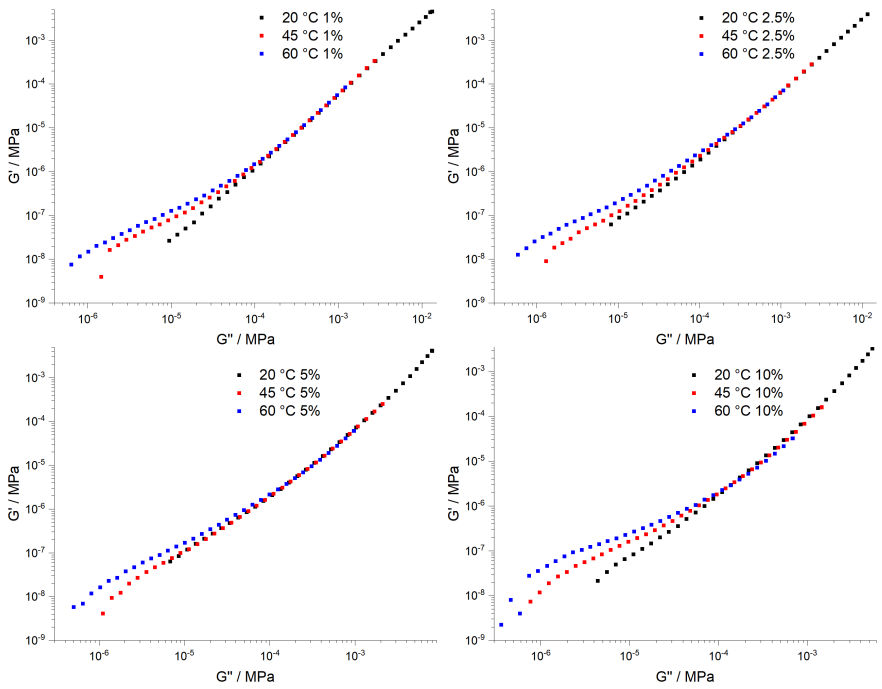

Figure 4.20: Han plot of 1% (top left), 2.5% (top right), 5% (bottom left) and 10% (bottom right) $C_{12}E_4$ in *cis*-PI–02.

Table 4.3: Gradients of Han plots for $C_{12}E_4$ in *cis*-PI-02 given in figure 4.20

$C_{12}E_3$ conc. / % wt.	$\frac{dG'}{dG''}$		
	20 °C	45 °C	60 °C
1	1.71	1.59	1.40
2.5	1.54	1.33	1.07
5	1.56	1.36	1.16
10	1.66	1.44	1.11

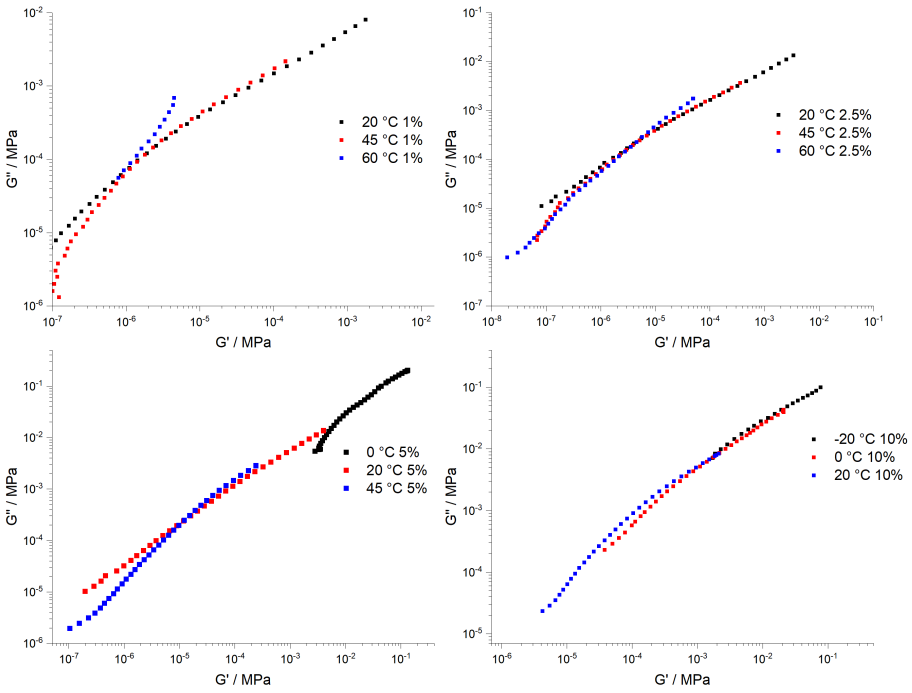

Figure 4.21: Han plot of 1% (top left), 2.5% (top right), 5% (bottom left) and 10% (bottom right) $C_{12}E_5$ in *cis*-PI–02.

Table 4.4: Gradients of Han plots for $C_{12}E_5$ in *cis*-PI-02 at 20, 45 and 60 °C given in fig. 4.21

$C_{12}E_5$ conc. / % wt.	$\frac{dG'}{dG''}$				
	-20 °C	0 °C	20 °C	45 °C	60 °C
1	-	-	1.71	1.50	0.82
2.5	-	-	1.69	1.19	1.01
5	-	1.53	1.49	1.28	-
10	1.67	1.41	1.41	-	-

van Gurp-Palmen Plots

The van Gurp-Palmen plot is commonly produced to assess the applicability of the TTS principle to a system. The failure of the TTS principle suggests that complex thermorheological behaviour occurs within the material probed: as temperature is varied, the sample has a different rheological response.[143] This can commonly be attributed to immiscibility of components of a blend or long-chain branching.

Before considering the behaviour of the surfactants, dodecane has again been considered. Inspecting the van Gurp-Palmen (vGP) plot for dodecane in *cis*-PI-02 (Fig. 4.22), it can be seen that there is very close overlap between the plots at different temperatures. Li *et al.*[144] observed that blends with droplet-matrix and co-continuous structures show different characteristic shapes in the vGP plot. As this is not seen within this vGP plot, it can be concluded that the dodecane fully mixes with the polymer, in agreement with the conclusions from the unchanging gradients in the Han plots seen in Fig 4.18.

Determining what is considered to be a deviation from overlapping data is also important before assessing samples as well as discussing any other possible causes for changes in the curve. Trinkle and Friedrich[145,146] noted that both dispersity and branching can have a significant effect on the vGP plot. It has been shown that, over several decades of G^*, linear samples show a characteristic curve with one minimum and one inflection point; the position of these features are affected significantly by both the molecular weight and dispersity of the polymer. As the samples used within this work are all produced using the same *cis*-PI, neither dispersity nor molecular weight should vary between samples, meaning any changes observed should be an effect of the inclusion of surfactant and not due to the polymer.

The vGP plots for *cis*-PI–02 with a range of $C_{12}E_3$ concentrations have been plotted in Fig. 4.23. All four compositions tested here show very good overlap of the curves for the three temperatures probed (20, 45 and 60 °C). This is similar to what is observed for dodecane (figure 4.22), suggesting that at all surfactant loadings investigated, the $C_{12}E_3$ is compatible with the matrix and no phase

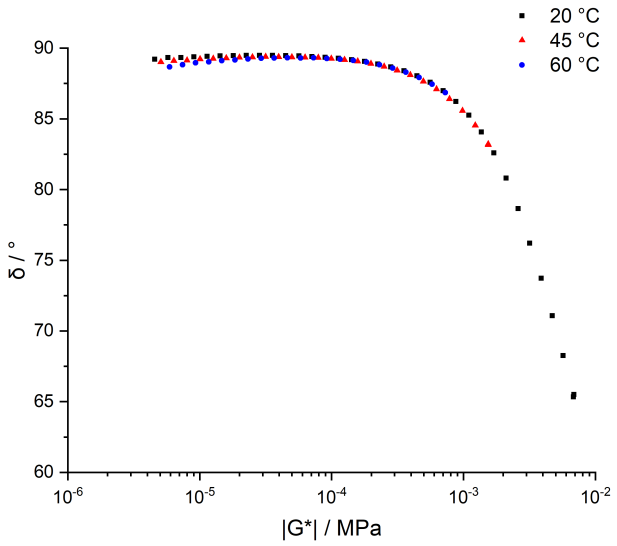

Figure 4.22: van Gurp-Palmen plot for *cis*-PI and 5% wt. dodecane at 20, 45 and 60 °C.

separation occurs over the temperature range investigated.

Comparing the van Gurp-Palmen plots for *cis*-PI–02 containing $C_{12}E_3$ to $C_{12}E_4$ (Figs. 4.23 and 4.24 respectively), there is a significant difference between the two sets of plots. Importantly, there is significantly poorer overlap between data at different temperatures for $C_{12}E_4$ than for $C_{12}E_3$, particularly at 60 °C. This indicates that there is a difference in behaviour between these two surfactants as temperature is varied. The reduced overlap shown in $C_{12}E_4$, particularly visible in the 10 % sample, suggests that as the temperature is elevated to above 45 °C, the structure of the blend changes. This is likely caused by separation of the two components. This phase separation would indicate a change in compatibility with changing temperature.[144] The increased compatibility of $C_{12}E_3$ compared to $C_{12}E_4$ is likely due to the smaller surfactant head group: this group is hydrophilic and thus a smaller head group would be expected to have the lowest driver to phase separate

$C_{12}E_5$ samples show much poorer overlap than any other surfactant, with higher loadings (5 and 10 %) exhibiting vastly different shapes to lower loadings. This is strong evidence that there is a decrease in miscibility of surfactants as the

head group size is increased. Zainal[147] *et al.* presented work showing the vGP plots of a blend of natural rubber graft polymer and PEO; the pure PEO samples show a similar shape to the data shown in lower loadings of $C_{12}E_3$ and $C_{12}E_4$ in *cis*-PI, suggesting that these surfactants show the behaviour expected for one phase. However, mixed samples show a significant curve on a vGP plot, commonly with a decrease in δ at low G^*. This was correlated to optical microscopy images which showed that blends with this different rheological behaviour also exhibited phase separated morphologies. This supports the assertion that high loadings of $C_{12}E_5$ are incompatible with the matrix as these vGP plots (Fig. 4.25) also show a similar decrease at low G^*.

Surprisingly little work has been conducted to study the rheological behaviour of amphiphilic additives within polymer matrices. However, work has been performed on immiscible blends of polymers.[148] This work is based on earlier work by Doi and Ohta[149] which discussed the rheology of systems containing interfaces within the bulk material. These interfaces present a mechanism of energy storage which is not present in a homogeneous system. Any interfaces between domains of different compositions will have an interfacial tension, which can crudely be considered to be the energy required to create more of this interface. Under shear flow, deformation of these domains can occur, a process requiring the creation of more interface.[149] This shift in G' relative to G'' means that the phase shift, δ has a different value for a given value of G^* than would be the case in the absence of this interface.

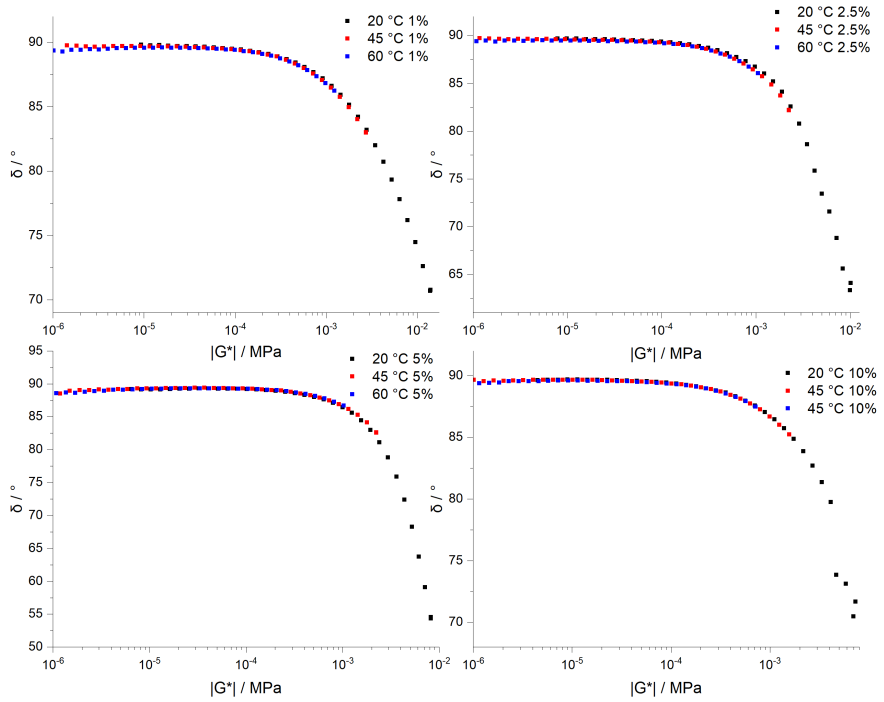

Figure 4.23: van Gurp-Palmen plot of 1% (top left), 2.5% (top right), 5% (bottom left) and 10% (bottom right) $C_{12}E_3$ in *cis*-PI–02.

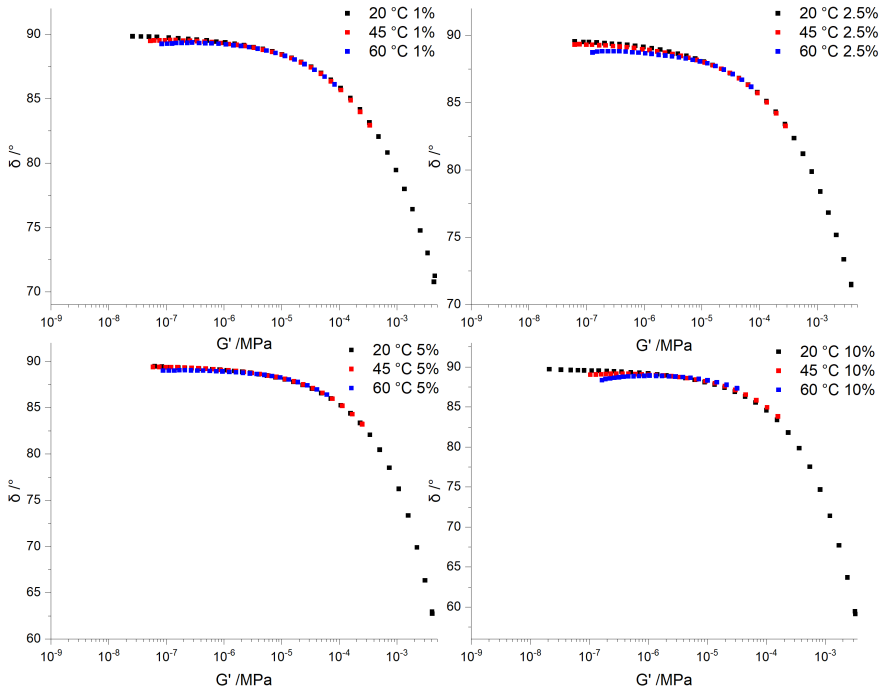

Figure 4.24: van Gurp-Palmen plot of 1% (top left), 2.5% (top right), 5% (bottom left) and 10% (bottom right) $C_{12}E_4$ in *cis*-PI–02

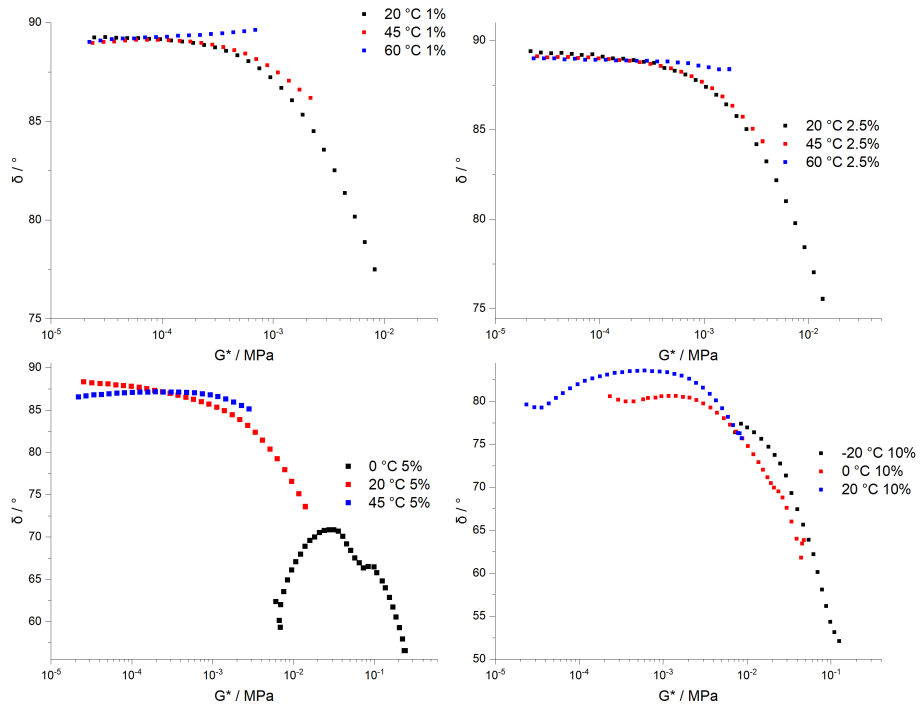

Figure 4.25: van Gurp-Palmen plot of 1% (top left), 2.5% (top right), 5% (bottom left) and 10% (bottom right) $C_{12}E_5$ in *cis*-PI–02

4.3 Chapter Conclusions

Within this chapter, both thermal analysis and rheological results have been presented in order to assess the compatibility of small molecule additives to both *cis*-PI and LDPE.

Thermal analysis has been used to probe the T_g change within *cis*-PI samples and the T_c change as well as any change in ΔH_{fusion} in LDPE samples. *cis*-PI samples have shown differing behaviour in the value of T_g when surfactants with different head group sizes are incorporated. Samples containing $C_{12}E_5$ and $C_{12}E_3$ showed a small peak in the DSC thermogram within the temperature range at which the respective surfactant melts, presenting evidence of the presence of bulk surfactant. This was also supported by the appearance of multiple crystallisation peaks which could not be assigned to the polymer. The multiple peaks have been

attributed to $C_{12}E_5$ in different environments, with different structures and interactions contributing to a small change in T_m for the surfactant. Whilst this was also observed for $C_{12}E_3$ systems, the multiple peaks were much less pronounced and could not be as easily distinguished.

It has been shown that the T_g of *cis*-PI is affected differently for each surfactant. *cis*-PI samples containing $C_{12}E_5$ showed an increase in T_g consistent with the surfactant having some antiplasticisation effect. However, T_g then became independent of $C_{12}E_5$ concentration above 5 % loading, suggesting that addition of further surfactant had little effect which may indicate that no more surfactant will mix with the polymer. $C_{12}E_3$ showed an initial small decrease in T_g, with a continually increasing T_g above 1 % loading. This is indicative of an initial plasticising effect, followed by a similar antiplasticisation to $C_{12}E_5$. However, the T_g in these samples continually increased as $C_{12}E_3$ loading was increased across the range measured, suggesting that even at 10 % loading, more surfactant could still be mixed with the polymer.

LDPE samples were also investigated using DSC, with the T_c and ΔH_{fusion} of the polymer / surfactant blend measured. The surfactants present did tend to reduce the crystallisation temperature, as would be consistent with an additive that is at least partially compatible with the polymer. However, attempts to infer molecular weight from the extent of T_m reduction led to unphysical results for $C_{12}E_5$ and $C_{12}E_4$.

However, a key limitation of thermal analysis in assessing compatibility is that the compatibility seen is only relevant for the temperature of the event examined. This means that it is not possible to assess the compatibility of two materials at a temperature where no thermal transition, such as a T_g, T_m or T_c, is present. This also prevents this technique from being useful in measuring how compatibility may change as temperature is varied.

Rheometry has been studied for *cis*-PI samples through the use of both Han and van Gurp-Palmen plots. From these results, it was clear that $C_{12}E_5$ was the least compatible surfactant with *cis*-PI, with vGP plots showing an inability to superimpose at different temperatures. This was accredited to a breakdown in the

TTS principle, often associated with distinct domains of phase separated material within the blend. Han plots also showed some ability to discern incompatible materials, with a larger deviation in $\frac{dG'}{dG''}$ seen for more incompatible materials.

Although there was insufficient time to attempt rheological analysis of compatibility for LDPE / surfactant mixtures, this could be a promising technique to measure compatibility at higher temperatures. However, at lower temperatures, the crystallinity of the polymer would prevent this kind of analysis from being used.

Chapter 5

$C_{12}E_5$ Distribution in *cis*-PI Films

Some of the work comprising this chapter has been published as: Gibson, C. P.; Litwinowicz, M. L.; Tellam, J.P.; Welbourn, R. J. L.; Skoda, M. W. A.; Claussen, J.; Thompson, R. L. "Water-Resistant Surface Modification of Hydrophobic Polymers with Water-Soluble Surfactant Additives", *Polymers*, 2021, **13**, *19*, 3407.

5.1 Chapter Introduction

For a surface-active additive in a polymer blend to be effective, it must be able to migrate to the surface,[99,150] with surfactant remaining in the bulk having little impact on the surface properties. It is therefore of great importance to understand how a surfactant behaves within hydrophobic polymers at a range of temperatures as well as to understand how the surfactant layer behaves when exposed to water. These conditions are intended to replicate the conditions that commercial samples containing similar materials may experience during manufacture and use.

Previous work has probed the behaviour of anionic surfactants within hydrophilic polymers and has shown that a surfactant-enriched layer can be detected at the surface.[45,68] However, little work has been performed on hydrophobic polymers with non-ionic surfactants. Some work has identified that similar surfactants

show surface enrichment on the surface of polypropylene films,[151] a polymer with a relatively high degree of crystallinity. Within this thesis, the influence of crystallinity on segregation is of interest and so far there has been no study of any non-crystalline system. This is interesting as the polypropylene system would be amorphous under processing conditions, but then become crystalline upon cooling. This leaves an open question as to whether the segregation observed arises during processing or as a result of crystallisation. Therefore, the study of an amorphous material would be a useful tool in understanding the segregation during product manufacture. Furthermore, little work has quantified the precise thickness of this enriched layer and few attempts have been made to relate this to surface structure or features.

Within this chapter the distribution of a non-ionic surfactant, $C_{12}E_5$, within *cis*-PI shall be investigated. $C_{12}E_5$ has been selected as a model surfactant owing to its similar structure to additives used commercially[99] and *cis*-PI has been selected due to the absence of crystallinity in the polymer. The lack of crystallinity will allow an understanding of the behaviour of a surfactant within a hydrophobic polymer before including the further complexity that these crystalline domains confer.

Using NR, the depth profile of $C_{12}E_5$ will be elucidated and the relationship between the surfactant loading and the depth distribution will be evaluated. This chapter will also probe how the surfactant distribution affects the surface properties of the film, using contact angle analysis to investigate any wettability changes arising from this. AFM will also be used to study any surface topography changes induced by surfactant presence and how these change with surfactant loading and sample history.

The effect of temperature elevation will also be studied, with NR again used to probe the depth profile at higher temperatures. Moreover, the effect of water exposure of films will be investigated, probing the surface hydrophilicity and any changes in surface topography caused by the water exposure in addition to the depth profile changes.

5.2 NR Fitting Strategy

Before assessing any NR results, it is necessary to understand the approach used to fit the reflectivity profiles. Within this section, the fitting program selection and the justification for including a surfactant-enriched layer at the surface will be explained through comparisons of NR profiles and simulated profiles. As deuterated surfactants are used in this film and these components have a higher SLD (table 3.4) than hydrogenous components, a surface layer will have a much higher SLD than the bulk layer containing the matrix polymer.

5.2.1 Use of MUSCtR

As discussed in section 3.5.1, MUSCtR has the capability to fit data with a compound reflectivity profile, generated by combining the multiple profiles with a specified difference in thickness of one layer in the model. In samples where there is a defined thin layer of surfactant, but a greater overall variation in film thickness, a single roughness parameter does not accurately describe the composition profile or the reflectivity.

The effect of introducing a variation in the bulk layer thickness is shown in Fig. 5.1. It can be clearly seen that the introduction of this thickness variation, simulating long range undulations, suppresses the appearance of Kiessig fringes arising from the thickness of the bulk layer. The removal of these Kiessig fringes at around $Q = 0.02$ Å^{-1} is justified upon inspection of the NR profiles obtained for samples of $C_{12}E_5$ and *cis*-PI–01 (Fig. 5.2): it is clear there are no Kiessig fringes in any of these profiles.

MUSCtR has previously been used to study PDMS films containing d_{25}-$C_{12}E_4$,[152] a homologue of $C_{12}E_5$. Within the work by Litwinowicz *et al.*, it was possible to resolve an enriched layer at the water-film interface. This was possible despite significant surface undulations by including a thickness variation in the fitting models, providing evidence for the effectiveness of MUSCtR in fitting undulating samples.

The absence of Kiessig fringes can also be caused by a much larger bulk layer

thickness, with much thicker samples no longer showing fringes. However, the thickness of the samples has been measured by using AFM to scan a scratch on the film. Fig. 5.3 shows an example of a cross-section of a 10 % $C_{12}E_5$ / *cis*-PI film; Fig. 5.3a shows a surface plot, with 10 sample lines collected with 1 µm spacing between each line. From this profile, each line is extracted as a cross-section (Fig. 5.3b). This cross-section shows the film on the left, with the scratch performed to reveal the bare silicon on the right. It is important to note that the large peak in the centre of the cross-section continues along the edge of the scratch and is likely caused by recoil of the film as it is removed. By comparing the height of the film to the height of the silicon block, it is possible to determine an average film thickness across all samples between 4500 Å and 6000 Å. The cross-section also shows the need for MUSCtR, with noticeable undulations seen on the film surface with lengths of several hundreds of nanometres to microns. Features of this size cannot be accounted for by roughness within each layer of the film, as the roughness cannot be attributed to a single layer in the film. These surface undulations may also give rise to the decrease in reflectivity seen in the critical edge of 10 % d_{25}-$C_{12}E_5$ samples. These surface features are of a comparable size to the neutron wavelength and therefore can scatter the reflected neutrons.

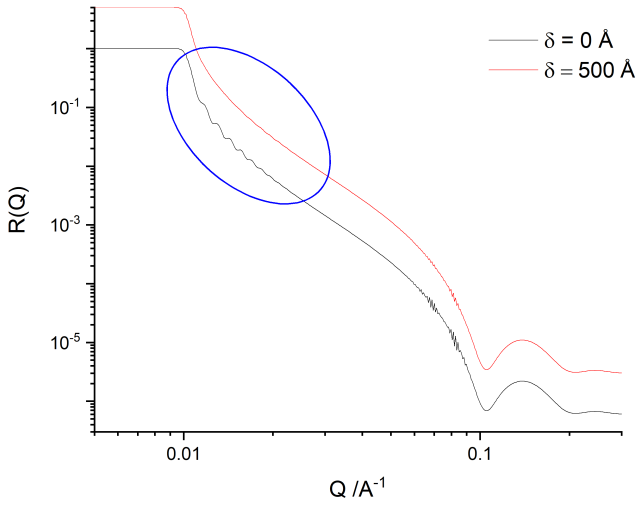

Figure 5.1: Comparison of $\delta = 500$ Å and $\delta = 0$ Å for a sample containing a surface layer and a bulk layer of 4500 Å. An offset has been applied to prevent overlap of profiles. The Kiessig fringes are circled in blue.

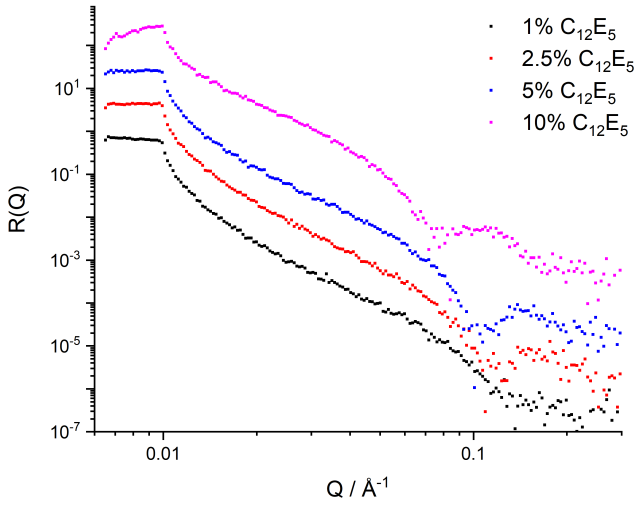

Figure 5.2: NR profiles of 1 – 10 % $C_{12}E_5$ in *cis*-PI-01 at 20 °C. an offset has been applied to the 2.5 – 10 % data sets. $R(Q)$ in the critical edge region ($Q < 0.01$ Å^{-1}) is expected to be 1.

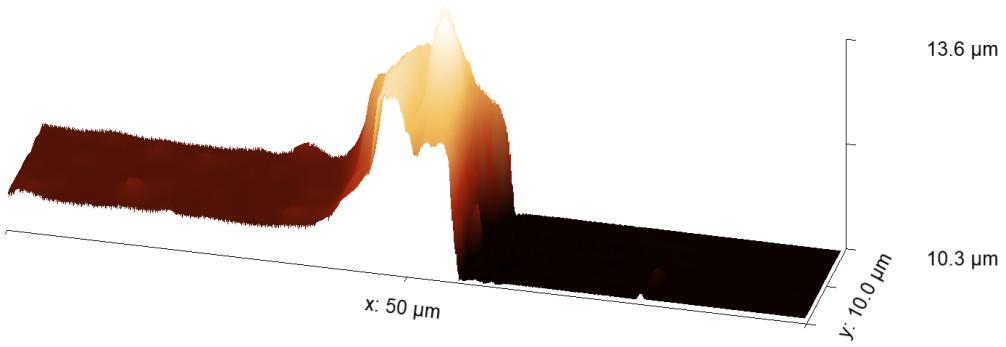

(a)

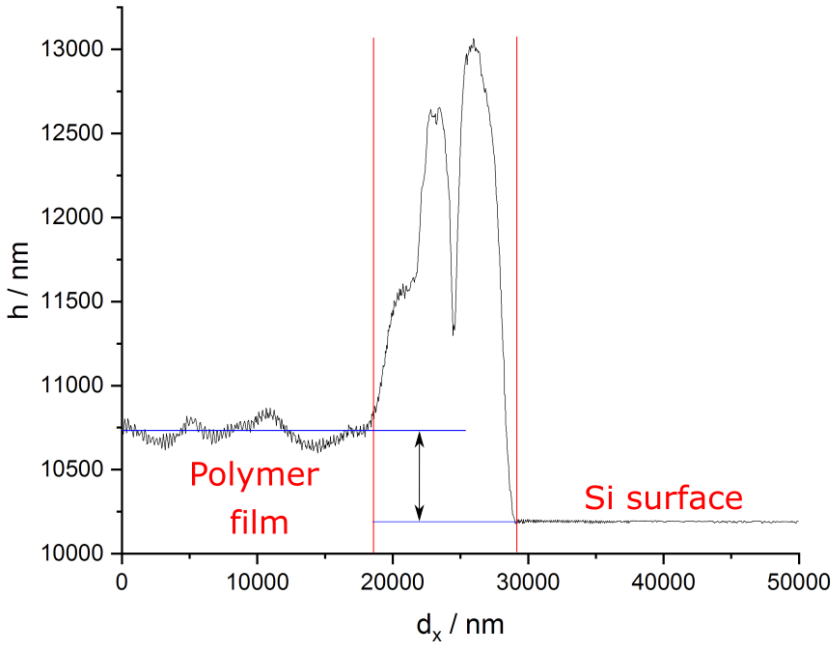

(b)

Figure 5.3: (a) 3D AFM surface plot of a 10 % $C_{12}E_5$ / *cis*-PI–01 film on a silicon block where the film has been removed on the right. (b) Cross-section of a 10 % $C_{12}E_5$ / *cis*-PI–01 film on a silicon block. The polymer film and silicon surface are annotated. The film thickness is also shown as the difference between the two blue lines where the left line represents the average film thickness and the right line represents the silicon surface. The large undulations that the left blue line intersect give rise to the requirement for MUSCtR. Note there is a significantly taller feature along the edge of the scratch.

5.2.2 Evidence for Surfactant Segregation at the *cis*-PI Film Surface

It is difficult to infer a composition profile directly from $R(Q)$, but there are features in the $R(Q)$ profile that can be related to composition profile features. Within this chapter, SLD profiles produced from reflectivity data will be discussed. These models have been generated using a layer model with each layer defined in Fig. 5.4. Fig. 5.5 shows simulated reflectivity profiles in which a surface excess layer, with a thickness d_1, is either absent ($d_1 = 0$ Å), thin ($d_1 = 60$ Å) or thicker ($d_1 = 120$ Å). It can be seen that without a surface layer, the reflectivity follows a smooth decay with no large fringes. As the surface layer is introduced and made thicker, a series of fringes become present at high Q, with the frequency increasing with thickness. The position of the first trough of the fringes also moves further towards low Q as the frequency increases, shown in Fig. 5.5. From inspection of the reflectivity profiles shown in Fig. 5.2, there is a fringe above 0.06 Å^{-1}, which is much more pronounced in higher concentration samples, justifying the presence of a surface layer. It must be noted that there appears to be an interference pattern found between 0.05 Å^{-1} and 0.1 Å^{-1} in all data presented in this figure, which is an artefact generated by the simulation of reflectivity.

Further inspection of the profiles in Fig. 5.2 reveals that Kiessig fringes corresponding to a layer with a thickness of $\sim 40 - 60$ Å. This is significantly thicker than the native oxide layer, which when grown naturally has a maximum thickness of approximately 20 Å.[153] Therefore, there must be a layer within the film with a thickness of $\sim 40 - 60$ Å which must have a different SLD from the bulk layer.

Another possible structure considered is a layered structure where there is a buried layer enriched in surfactant adjacent to the silicon oxide layer. If the buried layer had a sufficiently large SLD, it is possible that this layer could present as a single layer with a length scale similar to a surface layer seen in experimental NR results. A comparison of these two models, given in Fig 5.6, reveals that they both present distinctly different reflectivity profiles. Whilst both layers can

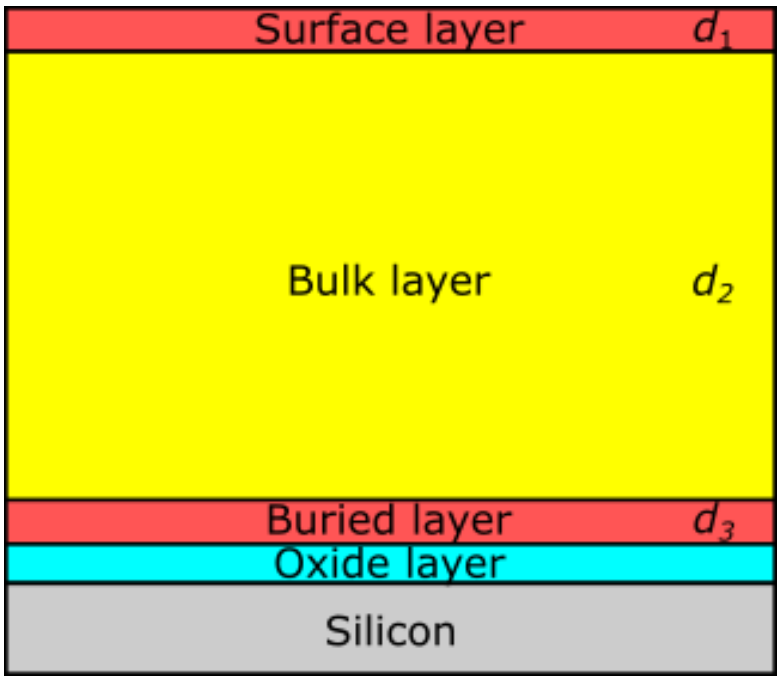

Figure 5.4: Schematic defining each layer within the model, including the buried layer where applicable.

produce fringes of a similar frequency, the buried layer does not display fringes with sufficient amplitude to accurately fit the results in Fig. 5.2. This is a result of a lack of sufficiently large SLD contrast between layers, confirming that there must be a layer at the surface, not at the oxide interface.

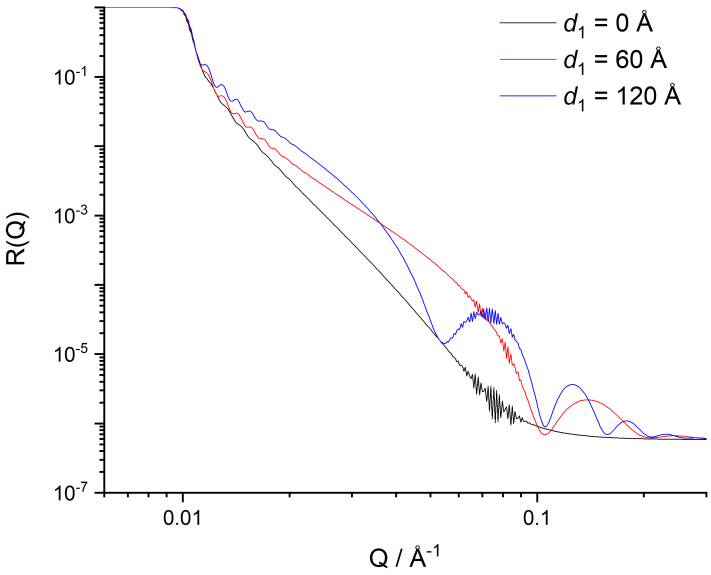

(a)

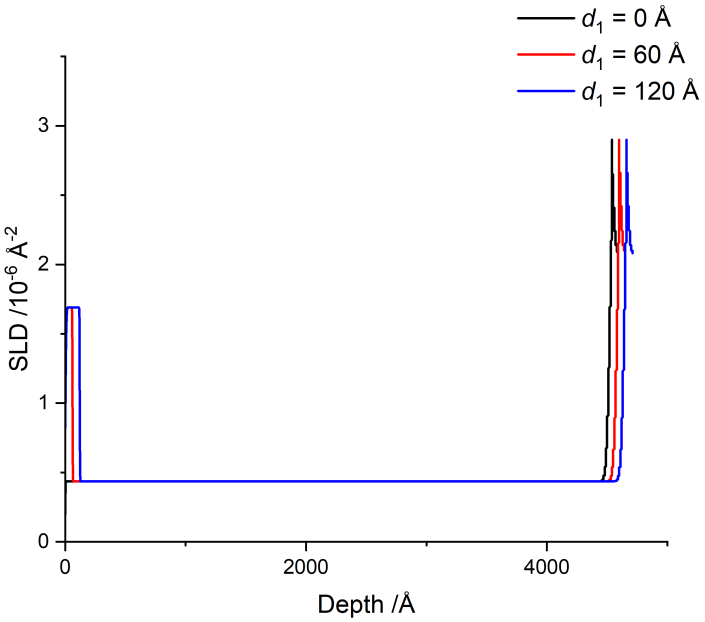

(b)

Figure 5.5: (a) NR profiles showing samples with a surface layer with an SLD of 1.69×10^{-6} Å^{-2} with thicknesses of 0, 60 and 120 Å. Note that in these samples, a thickness variation has not been applied to the bulk layer. (b) SLD of the simulated profiles used to generate the $R(Q)$ data above.

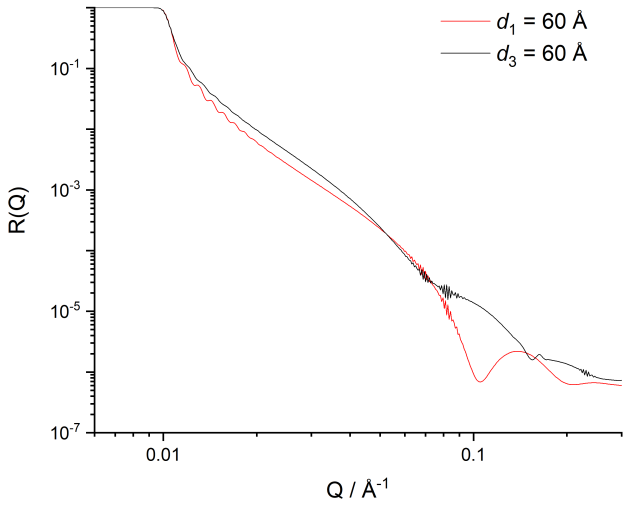

Figure 5.6: Comparison of a surface layer (red) and buried layer at the silicon oxide interface (black) in *cis*-PI. Whilst both layers are of the same thickness, the surface layer has an SLD of 1.69 Å^{-2} and the buried layer has an SLD of 3.00 Å^{-2}. Layers are defined in Fig. 5.4.

5.3 Results and Discussion

5.3.1 Initial Surfactant Distribution and Behaviour

Before the effects of temperature or water exposure can be considered, it is prudent to probe the initial surfactant distribution (after spin-casting) and how this varies with surfactant loading. This has been achieved by the collection and fitting of NR measurements as described in section 3.5. After fitting, it is possible to obtain a surface excess, z^*, from the composition versus depth profile, which is described by

$$z^* = \int_0^\infty \phi(z) - \phi_b \mathrm{d}z \tag{5.1}$$

where $\phi(z)$ is the surfactant fraction at depth z and ϕ_b is the bulk surfactant concentration. This surface excess is equivalent to the thickness of a pure layer of surfactant. z^* is also related to the area per adsorbed molecule which is more commonly used in the surfactant science literature, Γ, by

$$\Gamma = \frac{z^*}{V_{surf}} \tag{5.2}$$

where V_{surf} is the volume of the surfactant, 701 Å^3 for $C_{12}E_5$.

Initial inspection of the NR profiles (Fig. 5.7, inset), reveals a fringe at high Q (~ 0.1 Å^{-1}) with a long wavelength. As outlined in section 5.2, this presents evidence of a surface layer with a higher SLD than the bulk. The long wavelength of the fringes also indicates that the surface layer is relatively small, with a thickness below 100 Å. It can also be seen that the minimum near ~ 0.1 Å^{-1} moves to lower Q as the concentration increases, implying that the surface layer becomes thicker with increasing surfactant loading. An increased amplitude in the fringes also suggests that the surface layer has a larger SLD, this is particularly apparent in 10 % samples. From inspection of the SLD of the possible components of the film (Table 3.4), a larger SLD must be caused by a significantly larger concentration of d_{25}-$C_{12}E_5$ in the surface layer compared to the bulk.

Fig. 5.7 presents the concentration dependence of the surfactant in the near-surface region of the film. As discussed in section 5.2, the total film thickness

measured by AFM was 4500 – 6000 Å; therefore, too thick to characterise directly by NR. It must also be noted that concentration profiles also extend several thousand Å beyond that reported in Fig. 5.7; however, the bulk concentration remains constant to the oxide layer and has therefore been omitted. All samples present clear evidence of d_{25}-$C_{12}E_5$ blooming to the surface of PI films. Whilst the bulk shows a concentration consistent with the expected average surfactant loading, there is a much larger concentration present near the surface. As the average concentration increases, the surface layer also becomes thicker and more enriched. However, the maximum surface concentration of the surfactant is significantly less than 100 % and the surfactant instead presents as an enriched layer in the depth profile. This enriched layer is also confirmed in nuclear reaction analysis depth profiles, Fig. 5.8, where a layer of d_{25}-$C_{12}E_5$ is also clearly identifiable even at lower resolution.

Computational studies have calculated the length of a $C_{12}E_5$ molecule to be approximately 28 Å in a vacuum.[154] This measure is the longest possible representation of a molecule. Whilst this length can be decreased by folding or tilting of the molecule, it cannot exceed this value. It is clear that the adsorbed surface layer thickness exceeds the length of a single molecule, Fig. 5.7. Furthermore, samples of 10% surfactant loading show a surface excess of 36 Å, as calculated according to equation 5.1 (Table 5.1), which exceeds the maximum quantity of surfactant that could exist as a single layer. These results clearly show that while it is commonly the case that there is sufficient surfactant on the film surfaces to form a pure monolayer, it takes the form of multiple incomplete layers with a surface concentration for 60 % surfactant or less.

There are few literature examples of hydrophilic additives being used to modify non-polar polymers. Whilst Zhu and Hirt reported the formation of a surface layer of hydrophilic additives on a hydrophobic polypropylene film,[151] this work could not resolve the precise thickness of this surface layer because of the more limited depth resolution of attenuated total reflectance Fourier-transform infrared spectroscopy (ATR-FTIR), the technique used in the reported work. It should be noted that the films within this study were much thicker, with total film thick-

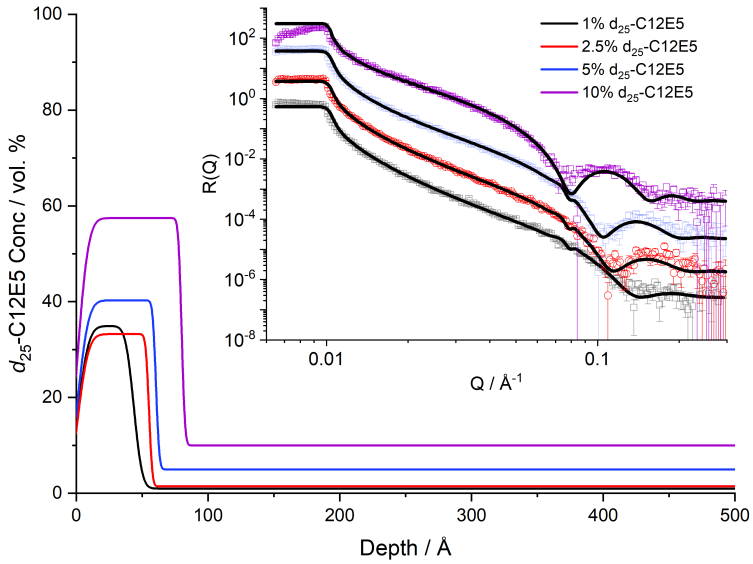

Figure 5.7: Near-surface concentration profiles of d_{25}-$C_{12}E_5$ in *cis*-PI-01 at 20 °C. Reflectivity data and fits are shown in the inset, offset for clarity.

nesses of ∼100 μm. Furthermore, ATR-FTIR could only probe the top 1.3 μm of film, with this defined as the surface layer. Whilst the surface concentration was not calculated, sufficient surfactant must be present within a layer this thick to produce a surfactant layer multiple layers thick. Nevertheless, it appears that hydrophilic modification is possible, not only in the melt-extruded films of Zhu and Hirt's study, but also in spin cast films that are presented here. This similarity suggests that the preparation technique and particularly the presence of solvent in sample preparation does not hinder the migration of an additive molecule.

Studies by Briddick *et al.*[45] in PVA showed surface layers of d_{25}-$C_{12}E_5$ present with a thickness that is comparable to the thicknesses reported in Fig. 5.7, suggesting that the initial surfactant segregation is similar in both PVA and *cis*-PI matrices. The surface segregation in *cis*-PI is much less expected than in PVA: the PVA films were spin-cast from water in which these surfactants are highly surface-active, but these PI films are spin-cast from toluene, with a low surface energy and so no surface activity of $C_{12}E_5$ is expected. Furthermore, the surface energy of PI (32 mN m^{-1})[155] is lower than that of PVA ($39-59$ mN m^{-1}),[156–158] again indicating a lower thermodynamic impetus for surface segregation.

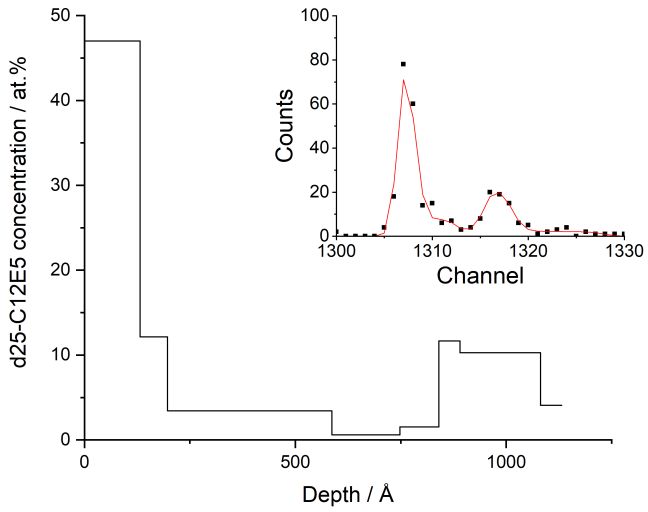

Figure 5.8: concentration profile of 10% d_{25}-$C_{12}E_5$ in *cis*-PI-01 determined from NRA. NRA data and fit is shown in the inset. Note that the film is much thinner than those examined in NR, but even so, some interfacial excess may be expected to be apparent from the NR experiments.

The thickness of the enriched surface layer is well-characterised by NR and presents evidence of a multilayer structure. Multiple (an even number) layers of surfactant would allow the surfactant to present the hydrophobic, low surface energy groups to both the hydrophobic polymer and the air. Whilst an even number of layers could present a low-energy surface to both the air and bulk polymer, only an odd number of layers would maintain the arrangement at the *cis*-PI whilst presenting a hydrophilic surface to a water interface. It is interesting to note that the smallest layer thickness observed is $\approx 40 - 50$ Å, corresponding to a bilayer structure, based on the surfactant molecule length noted above.[154] Furthermore, the 10 % sample shows a surface layer that is nearly 100 Å thick, corresponding closely to a 4-layer structure. No samples show a surface layer with a thickness between these values, supporting the hypothesis that a 3-layer structure would be unstable. Such a structure would have to present polar oxyethylene surfaces against the non-polar *cis*-PI or air, neither of which would be energetically favourable. The small discrepancy between the measured layer and an even

Table 5.1: Surface excess for samples at 20, 45 and 60 °C and after rinsing for 10 s and 20 s with deionised water. Surface excess has been calculated using equation 5.1.

$[d_{25}\text{-}C_{12}E_5]$ / wt.%	z^*/Å				
	20 °C	45 °C	60 °C	20 °C 10s rinse	20 °C 20s rinse
1	14	13	14	13	14
2.5	16	17	14	11	11
5	15	17	18	13	14
10	36	34	33	30	34

multiple of the extended surfactant chain length indicates some tilting of the surfactant molecule orientation with respect to the sample normal, or possible some overlap or interdigitation between layers.

The concentration-independence of z^* is unexpected for an incompatible surfactant that forms multilayers on the film surface. Previously, it has been observed that highly compatible amine oxide surfactants in PVA form a concentration-independent surface excess, but the segregation of other, less compatible surfactants is strongly dependent on concentration.[159] In the case of compatible mixtures, z^* and the thickness of the adsorbed layer corresponded closely to a surfactant monolayer. Here, however, the multilayer adsorbate is not consistent with a compatible surfactant and as such, it is expected that the amount of surfactant excluded to the surface would increase with increasing bulk concentration.

The fraction of surfactant within the entire film that appears as an enriched layer is also useful metric to assess because it provides a measure of the efficiency of surface modification. This fraction can be defined by equation 5.3, where ϕ_{surf} is the surface fraction, z^* is the surface excess and ϕ_{total} is the total amount of surfactant within the film of thickness L.

$$\phi_{surf} = \frac{z^*}{L\phi_{total}} \tag{5.3}$$

Throughout the composition range studied, the majority of the surfactant re-

Table 5.2: Surface fractions for *cis*-PI-01 / d_{25}-$C_{12}E_5$ at 20 °C

Film Surfactant Loading / wt.%	ϕ_{surf}
1	0.24
2.5	0.20
5	0.08
10	0.07

mains in the bulk of the film, Table 5.2. This new observation indicates that the surface modification is not very efficient at a molecular level for these materials and concentration and film thickness range. It also shows that the fraction of surfactant segregated to the surface decreases with increasing surfactant loading. This suggests that whilst there is an increase in surface excess, this surface excess is not proportional to surfactant loading. As the initial surfactant distribution in solution would be expected to uniform across the film, it may be possible that the driver for segregation is not sufficient to induce long range migration of surfactant and so only surfactant nearer to the surface is driven to form enriched surface layers. However, it does allow for the possibility that the remaining surfactant in the bulk could later be exploited to regenerate a hydrophilic surface. Such a process might be possible if further segregation could be triggered by some stimulus, such as heating.

5.3.2 Temperature Elevation Effect on Surface Layers

The experiments within this section involved the examination of *cis*-PI / $C_{12}E_5$ samples using NR whilst the samples were heated to elevated temperatures. This was performed by heating samples using a peltier stage as described in section 3.5.

Upon heating, the surface shows very little change, Table 5.1. The uncertainty of the surface excess measurements is $1 - 3$ Å,[159] thus there is no evidence for the surface excess measurements having any significant temperature dependence. The concentration profiles from which z^* values were derived are shown in Fig.

5.9. Although there appears to be some small variations in the calculated profiles, these are close to the limit of the precision of the measurement, and there is no systematic shift in the surface concentration or thickness of the adsorbed layer with changing temperature. It must also be noted that at this temperature, none of the film components are solid or glassy; therefore, samples should be relatively unhindered in approaching equilibrium.

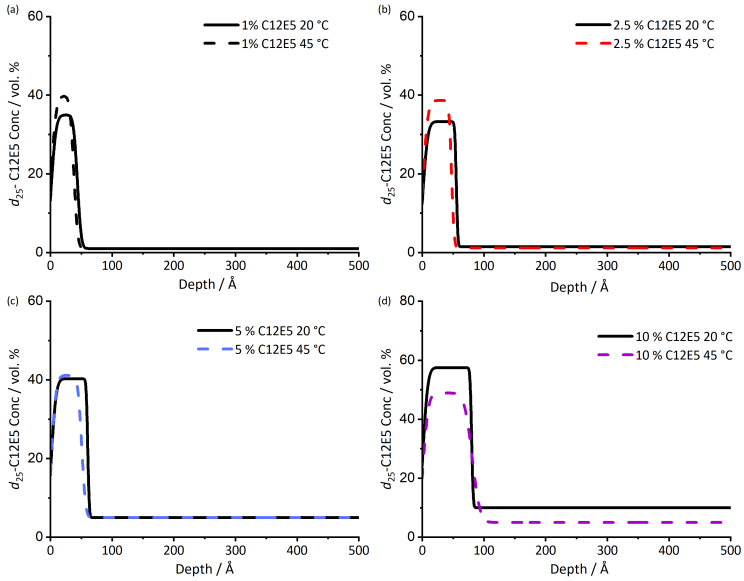

Figure 5.9: NR depth profiles for d_{25}-$C_{12}E_5$ in *cis*-PI–01 at 20 and 45 °C. The depth profiles are determined from the SLD profiles of films. Surfactant loadings are 1 % (a), 2.5 % (b), 5 % (c), 10 % (d).

Although the temperature dependence of surfactant segregation in polymers has received relatively little attention, it is possible to draw some useful comparisons between the experiments reported here and previous reports on the behaviour of plasticisers in polymers. Xie *et al.*[160] investigated the surface segregation of dioctyl phthalate to the surface of polystyrene (PS) films. This work revealed that heating samples after film preparation caused an increase in the surface dioctyl phthalate concentration up to 60 °C, after which surface concentrations decreased. Their samples were below the T_g of PS in this example and heating towards T_g likely favours the equilibration of the plasticiser, promoting segregation. However, because the *cis*-PI samples are far above their T_g,

heating has little effect on the vertical distribution. The absence of any strong temperature-dependence in these films suggests that heating has little impact on the thermodynamic favourability of adsorption over this range.

When considering the effect of temperature elevation, it is important to consider the effect of evaporation of the surfactant on the distribution. This is because the combination of a minute surfactant volume ($\sim$ 0.1 mg) with a macroscopic surface area ($\sim$ 10 cm^2) in these spin-cast films provides an ideal geometry to promote evaporation. In a similar thin-film geometry, Smith *et al.*[59] showed that for a small molecule (a plasticiser) in a polyester / polyurethane film, the rate of loss of the molecule is limited not by the rate of diffusion of the molecule in the film, but by the rate of evaporation of additive from the film. It must be noted for the work shown here that if the rate of evaporation were significant compared to the rate of diffusion within the film, then the near-surface region of the film would be depleted, rather than enriched in surfactant as has been observed. Furthermore, the experimental procedure requires equilibration of samples at 45 °C for approximately 8 hours. Following this, the changes in the composition profile are negligible; therefore, there is no evidence for evaporation during heating. However, the experiments conducted within this chapter do not present an opportunity to probe the effect of time upon the surface excess: whilst heating has been probed, no work has been conducted to understand if the length of time that the samples are aged for at a given temperature. As sample measurements require several hours of data collection, only longer scale ageing (weeks or months) experiments could be conducted which may present an opportunity for further study in future work.

5.3.3 Water Exposure Effect on Enriched Layers

The surface segregation of d_{25}-$C_{12}E_5$ was quantified at 45 °C and 60 °C and then after repeated 10 s rinses with ultrapure water and these surface excesses are summarised in Table 5.1. The change in depth profiles after a 10 s rinse is shown in Fig. 5.10. Rinsing once or even twice causes surprisingly little change in

surface excess: the largest change shown upon rinsing is in the 5% surfactant sample, with a decrease of ~ 27 % (between 60 °C and re-measured at 20 °C after a 10 s rinse). When compared to the uncertainty of these measurements, noting the slightly higher values recorded after a second rinse, there is again remarkably little change in surface excess concentration upon rinsing.

The significance of the resilience of the surface excess with respect to rinsing becomes apparent when the quantity and solubility of surfactant are considered. Wahlgren *et al.*[161] determined the solubility of $C_{12}E_5$ to be in excess of 10 w/v% based on cloud point. From this value, for a single rinse of approximately 10 mL of water, 1 g of $C_{12}E_5$ could be dissolved. Based on the surface excess thickness for 1% $C_{12}E_5$ loading, a 55 mm diameter silicon block will have 3.2 µg of surfactant at the surface. This would only require 32 nL of water to dissolve, meaning that there is over 300,000 times the amount of water required to remove all of the surface layer at equilibrium. If all of the surfactant was capable of moving from the film into the water, it would be reasonable to assume that all surfactant would be removed from the surface: the surface layer is thin and so there is little to prevent surfactant loss. However, the post-rinsing NR results for the surface excess, summarised in Table 5.1, indicate that the surfactant / polymer film is remarkably stable with respect to rinsing. Further rinsing for an additional 10 s appears to have no significant effect.

Given the remarkable stability of the thin surfactant layer on the *cis*-PI surface, it is interesting to consider its impact on surface properties such as wettability. WCA results show that significant levels of hydrophilicity are generated in films containing at least 5 % $C_{12}E_5$ surfactant in samples at 20 °C before exposure to water. It is expected that the hydrophilicity of the films will depend on the presence of $C_{12}E_5$ on the surface of *cis*-PI, which is otherwise hydrophobic. This is confirmed by the absence of any hydrophilicity in *cis*-PI films (Fig. 5.11) and the low contact angle of films containing 10 % $C_{12}E_5$. It is interesting to note that while the surface excess measured by NR at 5 % loading is similar to results for lower loadings of surfactant, there is a significant change in WCA over this range.

All contact angle measurements also display a decrease over time. This can be

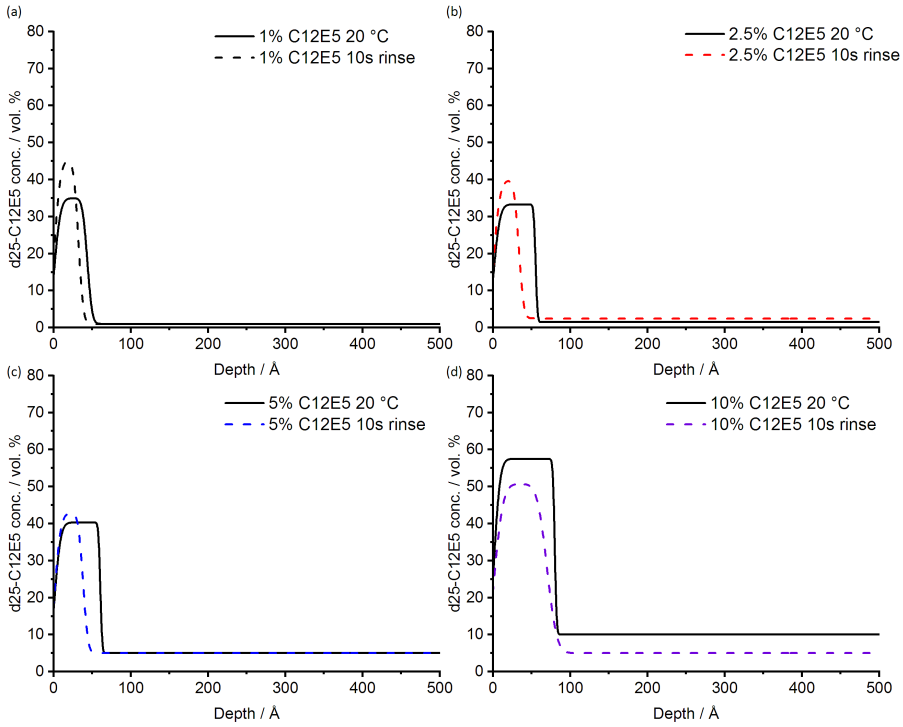

Figure 5.10: NR profiles of *cis*-PI-01 / d_{25}-$C_{12}E_5$ films at 20 °C and after a 10 s rinse with water. Surfactant loadings are (a) 1 %, (b) 2.5 %, (c) 5 and (d) 10 %. Whilst film thicknesses are significantly larger, only the first 500 Å from the surface have been shown.

caused by either a rearrangement of surfactant to provide a hydrophilic surface or evaporation of the probe droplet causing a receding contact angle. It is likely that the long time scales over which the contact angle decrease occurs in 1 % samples indicates that evaporation is the main cause of the decrease in those samples. At higher (5 %, 10 % $C_{12}E_5$) loadings, film surfaces are much more hydrophilic and contact angles decrease with time over short periods, likely caused by a rearrangement of the surfactant.

It should be noted that contact angle measurements show significant variation (several degrees, as demonstrated by Fig. 5.12) when repeat measurements are carried out, even when on nominally identical samples. Thus, individual profiles must be treated with caution, while noting the following points: in the as-made

samples, there is no significant surface modification at 1 % $C_{12}E_5$ compared to the 0 % control sample. After rinsing, the contact angles increase for all compositions, and in some cases (1 and 10 % $C_{12}E_5$) show contact angles greater than 90°. Whilst the NR data shows that the adsorbed surfactant is stable with respect to water exposure, the contact angle data presented in Fig. 5.11 presents equally clear evidence that the surface properties are dramatically modified by rinsing. There is also evidence for incomplete surface coverage: NR shows there is a layer enriched in surfactant for all samples, yet not all samples show wetting behaviour when water is placed on the surface. This is indicative of domains of surfactant on the surface with other regions of exposed *cis*-PI. If uniform surface coverage occurred, the same contact angle behaviour would be expected at all positions and any variation suggests that differences in local surfactant concentration are present.

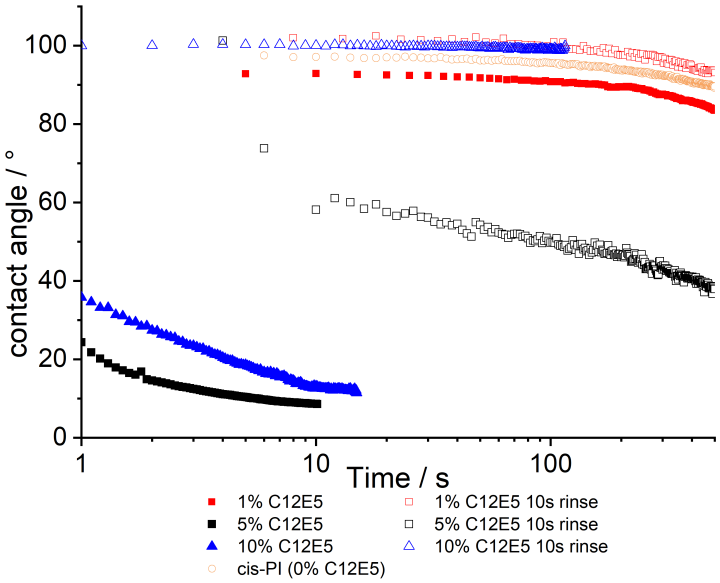

Figure 5.11: Contact angles for 1 – 10 % $C_{12}E_5$ in *cis*-PI-01 before and after a 10 s rinse with deionised water. The data are a function of time where 0 is the time that the probe droplet (water) is placed on to the surface. A *cis*-PI sample has also been shown in orange, showing 0% surfactant loading.

AFM measurements are shown in Figs. 5.13 – 5.15 with height and adhesion maps presented. The AFM images confirm the presence of gradual undulations

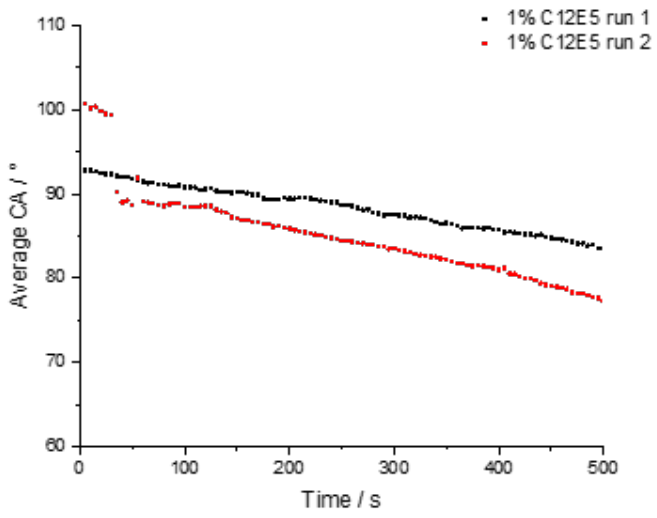

Figure 5.12: Successive measurements of contact angle on 2 distinct locations on a single 1 % $C_{12}E_5$ / *cis*-PI-01 sample, showing the variability of results even within identical films.

in film thickness, which necessitated multi-profile fitting of the NR data (section 5.2.1). Before rinsing, a small number of thread-like "strand" features were found on the surface. These strands are slightly raised with respect to the surface and correlate with regions of adhesion. In the absence of any variation in composition, raised features sometimes correlate with a reduction in adhesion due to the reduced contact area between the probe and the surface. Here, the increase in adhesion on these raised features indicates that the strands are of a different composition from the surrounding surface, most likely the surfactant.

These strands are not seen in samples containing no surfactant (Fig. 5.13), showing that the strands must be produced by the presence of surfactant. These strands become more apparent at higher concentrations, with strands appearing in the adhesion surface maps above 2.5 % before rinsing. The strands also become more pronounced after rinsing for 10 s, with more strands appearing on the surface after rinsing. It is important to note, however, that images do not show the same position on each sample. As the sample is removed from the AFM to be rinsed, it is not possible to return the sample to the same position upon reintroducing it to

the microscope. However, the trends observed are consistent across all samples.

The precise origin of the surface changes seen in Figs. 5.13 – 5.15 is unclear, but is consistent with some change in the organisation of the surfactant. While strand-like features of $C_{12}E_5$ adsorbed on mica surfaces under water have been reported by Dong and Mao,[162] those features, which are quite closely packed and aligned parallel to each other are very different from the more free-standing extended features that have been observed in these samples. There appears to be little if any work presenting similar behaviour of surfactant strands forming at the solid-air interface. In this work, the strands that are spontaneously formed are much longer than those previously reported on surfaces and are unusual that they are essentially free-standing and are not obviously altered by rinsing. It must be noted that although these surface features are much straighter, and possibly branched, their length is roughly consistent with the worm-like micelles of $C_{12}E_5$ found in solutions by light scattering studies.[163]

The results shown within this work show an interesting discrepancy between the surface excess measured by NR, which is remarkably stable with respect to rinsing and the wettability behaviour, which is altered by rinsing. The fact that repeated rinsing has no significant effect on the surface layer measured by NR suggests that it remains in place rather than is removed, then replaced from the bulk. Had the latter process occurred, it would be expected that with two rinses, there would be a systematic depletion in any regenerated surface layer. Overall, these results indicate that the resilient surface excess measured by NR is not entirely responsible for the observed wetting behaviour. Furthermore, the surface excess measured by NRA in Fig. 5.8, 69 Å, is almost twice the value measured by NR. It is postulated that this discrepancy arises because the film surface includes some $C_{12}E_5$ that is detected by NRA, but not NR, and it is this fraction of the segregated surfactant that is mainly responsible for the wettability phenomena. The contribution to the surface excess that is only detected by NRA is most likely to arise from the "strands" that are detected by AFM, and may also account for the anomalous concentration dependence of the surface excess noted earlier. These strands are relatively small (several microns) and are likely to be

smaller than the coherence length of the neutrons, meaning that very little of the NR profile observed arises from incoherent addition.

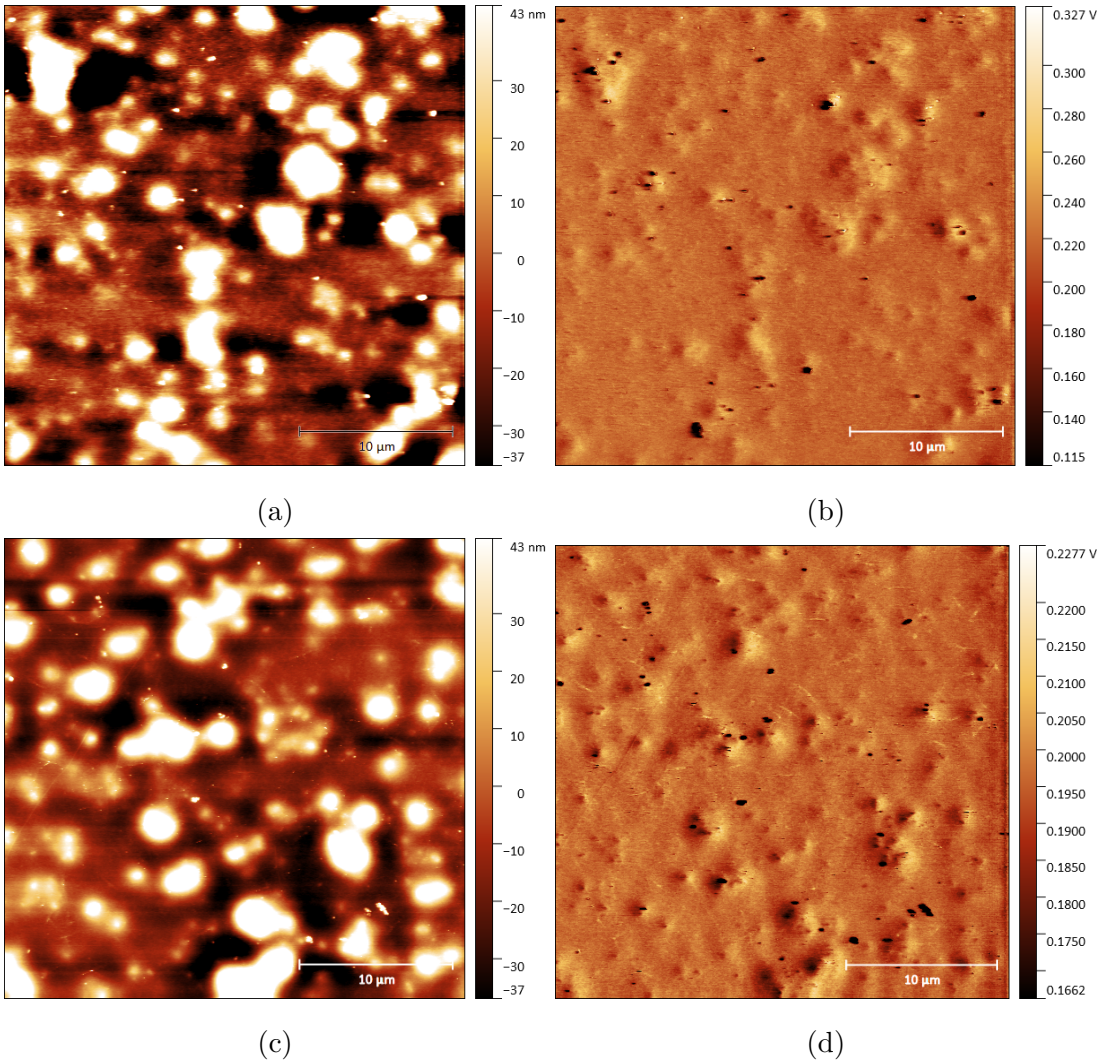

Figure 5.13: AFM height (a) and adhesion (b) maps of *cis*-PI-01 without and $C_{12}E_5$ for the same position of the same film; height (c) and adhesion (d) map of the same film shown in the top AFM images after a 10 s rinse. Height maps have been plotted on the same vertical scale.

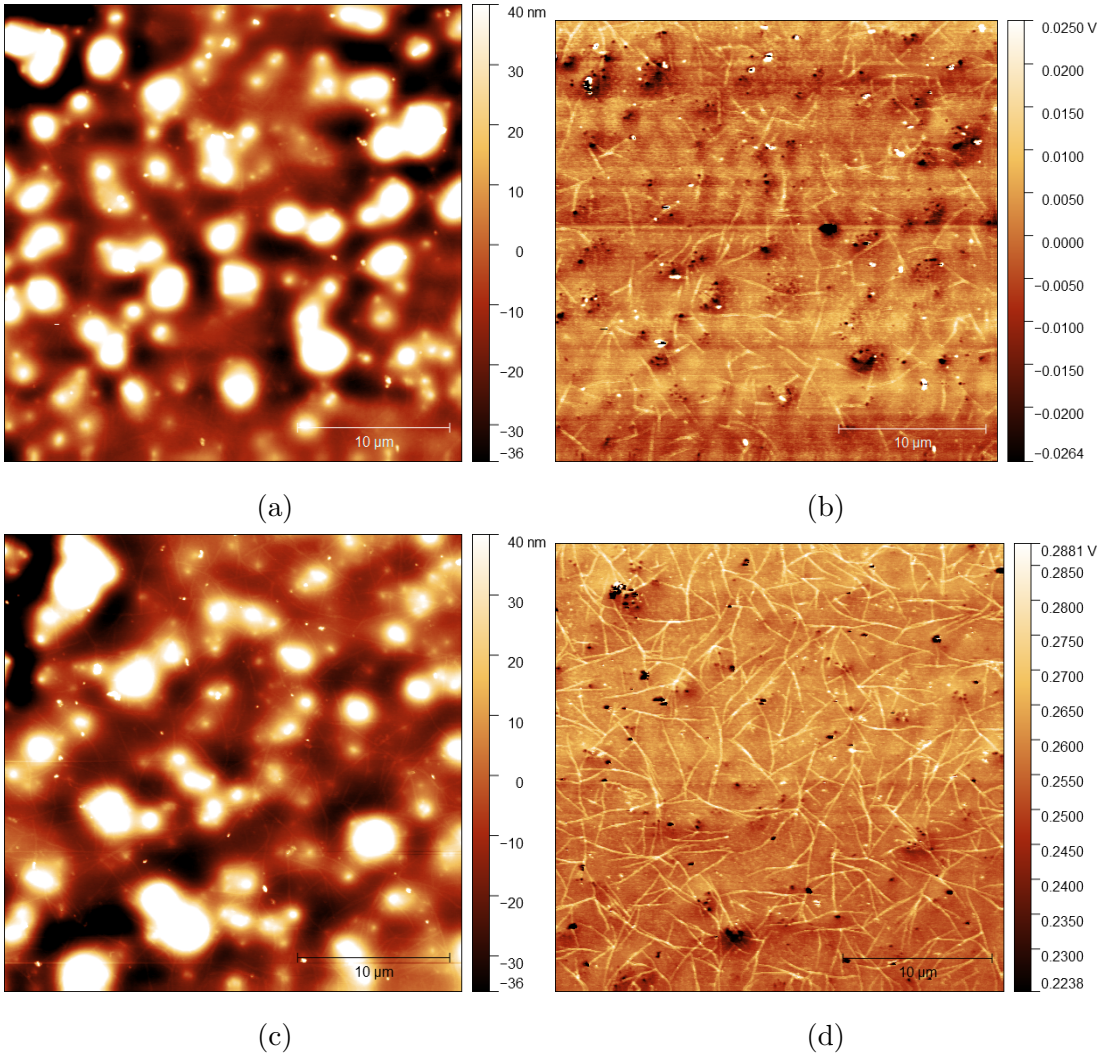

Figure 5.14: AFM height (a) and adhesion (b) maps of 2.5 % loading of $C_{12}E_5$ in *cis*-PI-01 for the same position of the same film; height (c) and adhesion (d) map of the same film shown in the top AFM images after a 10 s rinse. Height maps have been plotted on the same vertical scale.

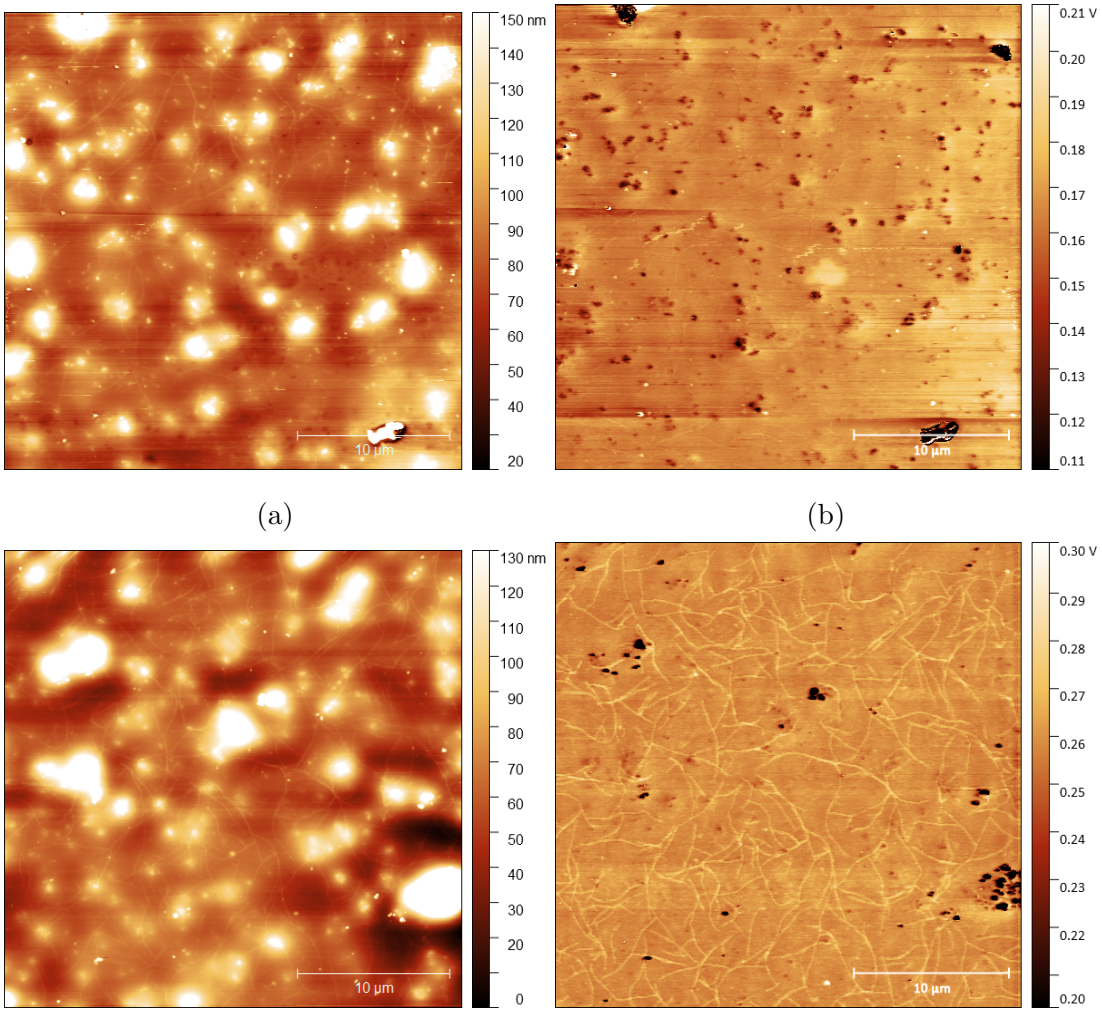

Figure 5.15: AFM height (a) and adhesion (b) maps of 10 % loading of $C_{12}E_5$ in *cis*-PI-01 for the same position of the same film; height (c) and adhesion (d) map of the same film shown in the top AFM images after a 10 s rinse. Height maps have been plotted on the same vertical scale.

5.4 Chapter Conclusions

Within this chapter, it has been shown that for spin-cast $C_{12}E_5$ / *cis*-PI blended films, a rich variety of complex and intriguing blooming behaviour is found. A clear surface excess of the amphiphile presents at the air interface, which is nearly invariant over a range of composition and temperature. There are few precedents for amphiphile segregation at hydrocarbon polymer surfaces[25,164,165] and neither concentration or temperature dependence of adsorbed nanostructures nor their stability with respect to rinsing have been reported. This work shows unexpected concentration dependence and resilience with respect to rinsing, which is important for applications based on this model system. Even when these blends are spin-cast from a low surface energy solvent, non-ionic surfactant adsorption is spontaneous, showing that this behaviour is more general than was previously known. It has also been demonstrated that the non-ionic surfactant, which adsorbs to the surface is resistant to evaporation, with a surface excess remaining after temperature elevation for several hours.

The NR depth profiles presented indicate that surface adsorption is persistent even after exposure to significantly more water than is required to remove the surfactant. However, the contact angle measurements of the films before and after rinsing indicate a change in the surface properties of the film, suggesting that there must be a structure change in the surfactant that occurs upon exposure to water. It is possible to resolve this difference in observations by recognising that NR is only sensitive to planar structures such as complete surface layers. Other surface features such as strings and droplets are not detected by specular NR, meaning that if these structure changes are induced upon water exposure, little evidence of these features may be seen in NR, even though NR provides a very precise characterisation of surfactant bloomed on polymer surfaces. These additional features, however, may be detected by NRA which is less sensitive to lateral variation. Only by a combination of techniques can an accurate picture of the blooming process be obtained, and it is apparent that this level of detail is needed in order to understand why such a complex relationship between surface

segregation and surface modification exists even for a very simple model.

Chapter 6

Effect of Polymer Crystallinity on Surfactant Distribution in Polymer Films

6.1 Chapter Introduction

Whilst many commercial products are produced from natural rubbers and other similar polymers, many products (including those that are industrially relevant within this work) are produced from more crystalline polyolefins such as polyethylene and poly(propylene). Thus it is now prudent to consider the introduction of crystallinity to the polymer matrix: the degree of crystallinity within these polymers is much greater and may have a significant impact on the segregation of surfactant within these blends.

Previous work has already identified that matrix crystallinity can have a large effect on the mobility and diffusion of small molecules. Goffri *et al.*[166] have previously demonstrated the segregation of a crystalline polymer with a crystallising additive polymer. This additive polymer was shown to segregate to the surface of cast films. This was not observed with the same additive polymer in amorphous polymers,[167] showing that the presence of crystallinity within the matrix polymer can induce surface segregation.

Surface segregation has also been observed for LDPE. Blends of LDPE in an ethylene-propylene-diene rubber were investigated by Bieliński *et al.* and exhibited a crystalline structure at the surface of the blend, demonstrating that the LDPE segregated to the surface.[168] This shows that surface segregation is possible within LDPE systems and that the crystallinity of this polymer can play a role in surface segregation.

Mäkipirtti *et al.* observed that within semi-crystalline polymer blends, non-crystallising additives are found in low concentrations within spherulite domains and are more abundant at crystal boundaries.[52] Moreover, it has also been observed that within crystalline polymers, the diffusivity and additive solubility within the amorphous regions decreased as crystallinity increases.[169] The paths molecules must take within crystalline polymers during diffusion also tend to be much more convoluted, with molecules moving along crystal boundaries where there is amorphous polymer.[169,170] This presents a reasonable possibility that the segregation of a surfactant within a semi-crystalline polymer may be quite different from that in a more amorphous polymer such as that studied in chapter 5, with this evidence supporting the hypothesis that the surfactant is incompatible with the crystalline regions.

The work presented in this chapter shall involve the comparison of the behaviour of $C_{12}E_5$ in hPBd and the same surfactant in the *cis*-PI films introduced in the previous chapter. These comparisons shall be made using NR, ion beam analysis, contact angle analysis and AFM. The distribution shall be assessed using NR, with surface excesses calculated from these depth profiles. The comparison of contact angles will show how the introduction of crystallinity affects the ability of surfactant to modify the surface properties of the polymer film. AFM images will also elucidate how the surfactant is distributed laterally across the surface in both polymers. hPBd has been selected as an analogue for LDPE in this work to facilitate the production of smooth films for NR experiments. As hPBd and *cis*-PI are non-polar and have similar surface energies, this presents an opportunity for the impact of crystallinity to be isolated as the main cause of any differences.

6.2 NR Fitting Strategy

The hPBd samples presented within this chapter are fitted using the refnx software. This fitting software was chosen as the undulation-fitting capabilities of MUSCtR were not required. The figure presented in chapter 5 (Fig. 5.1) shows how the implementation of a thickness variation removes the small Kiessig fringes seen between the critical edge and 0.08 Å. The reflectivity profiles for 1 – 10 % d_{25}-$C_{12}E_5$ in hPBd have been plotted in Fig. 6.1 as $R(Q)Q^4$ vs. Q; this plot removes the Q^4 decay from the data, making it much easier to identify any smaller features within the data. From these plots it is possible to identify small fringes between the critical edge and 0.03 $Å^{-1}$, particularly in the higher concentration samples. The presence of these fringes indicates that the film profile can be effectively described by a layer with a single, well-defined thickness.

At approximately 0.1 $Å^{-1}$ a broad bulge can be observed. This feature corresponds to a thin layer of increased SLD at the substrate interface. However, the Q-value of this fringe corresponds to a layer with a thickness of approximately 40 – 60 Å, significantly thicker than the maximum thickness of a native oxide layer.[153] Therefore, the data indicates that this is a buried layer within the film that is enriched in the deuterated surfactant.

Higher concentration samples in hPBd required a more complicated model in order to fit the reflectivity profile. Within this model, multiple layers are included at the silicon oxide interface. These layers are enriched in surfactant in a way that produces a gradient of surfactant concentration which increases towards the oxide layer and can be seen in Fig. 6.2. Without these additional layers, it is not possible to achieve a sufficiently low reflectivity between 0.03 and 0.1 Å to fit the experimental profile. This is shown in Fig. 6.3, revealing that with only an oxide layer the data cannot be accurately fitted.

The presence of a thin layer of slightly increased SLD at the surface is also justified in Fig. 6.2. An SLD depth profile and reflectivity profile are shown (top and bottom respectively) in red. It is clear that without this surface layer, the simulated profile is not capable of accurately capturing the Kiessig fringes at low

Q. Furthermore, the χ^2 value decreases from 981 to 428 upon addition of the surface layer, indicating that the quality of the fit has been improved.

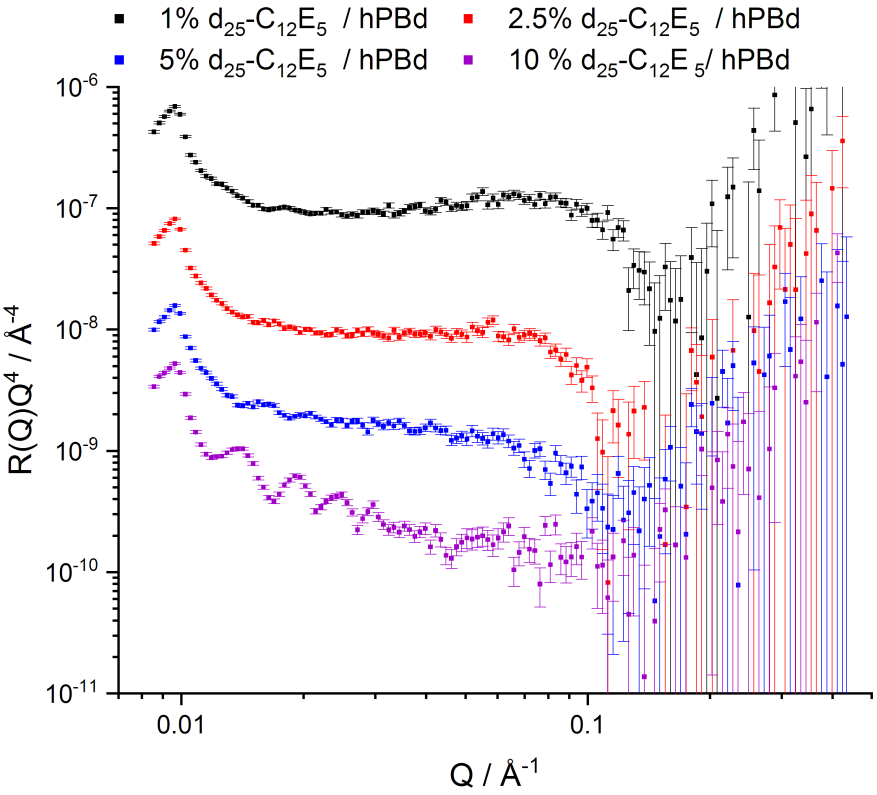

Figure 6.1: $R(Q)Q^4$ vs. Q for 1 – 10 % d_{25}-$C_{12}E_5$ in hPBd films. An offset has been applied to 1, 2.5 and 5 % loadings for clarity.

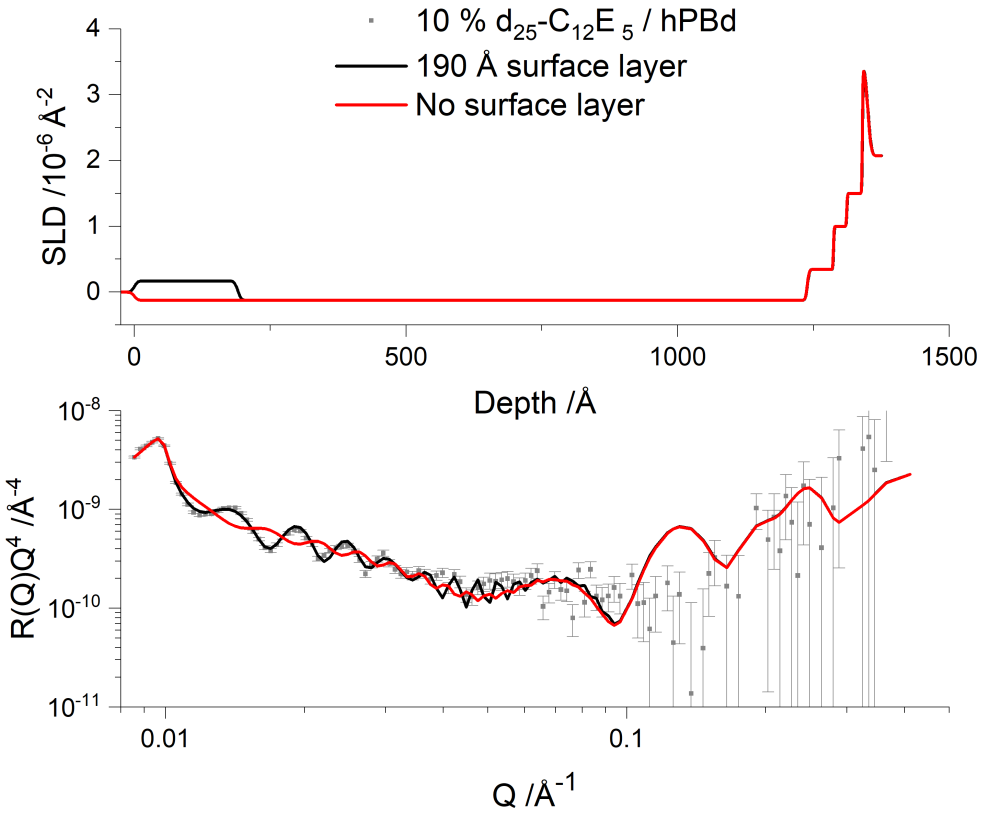

Figure 6.2: (Top) SLD profiles for simulated reflectivity profiles with no surface layer and a 190 Å surfactant-enriched layer. (Bottom) $R(Q)Q^4$ vs. Q for 10% d_{25}-$C_{12}E_5$ in hPBd showing fits with and without surface layer. NR data was collected using the POLREF reflectometer.

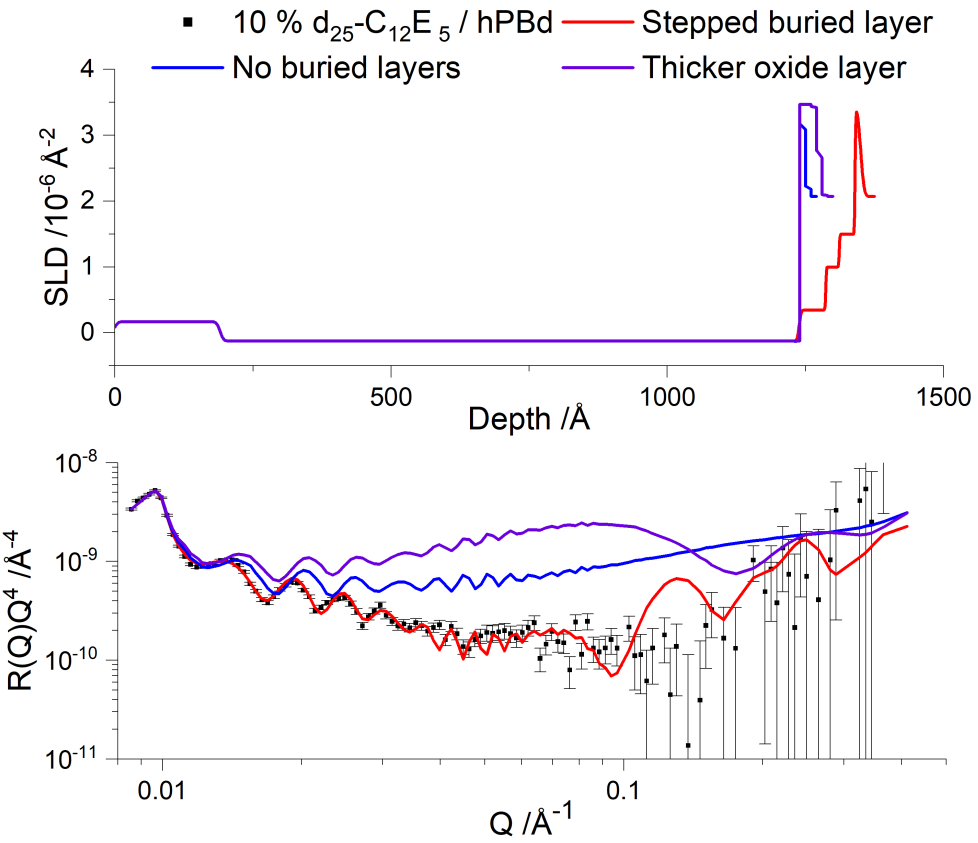

Figure 6.3: (Top) SLD profiles for simulated reflectivity profiles with and without a buried layer and a thicker oxide layer. (Bottom) $R(Q)Q^4$ vs. Q for 10 % d_{25}-$C_{12}E_5$ in hPBd showing fits corresponding to the SLD profiles shown in the top graph. NR data was collected using the POLREF reflectometer.

6.3 Results

6.3.1 Initial Surfactant Distribution

A key factor to assess when considering how the introduction of matrix crystallinity affects the behaviour of the surfactant within a polymer film is the surface excess (discussed in chapter 5), which is obtained from the surfactant depth profile. Thus, NR has been used in order to elucidate the surfactant distribution within the film.

Within this section, the NR depth profiles of d_{25}-$C_{12}E_5$ in hPBd films will be compared to those of d_{25}-$C_{12}E_5$ in *cis*-PI–01, providing an indication of how the introduction of crystallinity into the matrix influences initial segregation. Depth profiles of films with d_{25}-$C_{12}E_5$ after heating to above the T_m of hPBd will also be presented, demonstrating any differences in distribution change when the hPBd semi-crystalline domains are melted.

Initial inspection of the reflectivity spectra (Fig. 6.4) reveals two key features. Firstly, there is a minimum that can be seen between 0.1 and 0.2 $Å^{-1}$. This signifies a buried layer of surfactant, as discussed above. Secondly, at higher loadings, higher frequency Kiessig fringes can be identified, with these becoming most apparent at 10 % loading. This corresponds to a defined surface layer which is higher in SLD than the bulk, providing evidence of some surface enrichment. These Kiessig fringes can be seen more clearly in Fig. 6.2, where reflectivity is plotted as $R(Q)Q^4$ vs. Q, removing the Q^4 decay from the reflectivity. It can also be seen from this figure that the Kiessig fringe at high Q becomes less apparent at higher loadings. This appears initially surprising, the loss of this fringe suggests that the buried layer becomes less enriched with higher surfactant loading. It is important to note that the periodicity of these Kiessig fringes cannot correspond to the total film thickness, since this is of the order of 100 - 150 nm, much larger than the film thickness required to produce fringes with this periodicity.

These reflectivity profiles have been fitted according to the strategy outlined above and the fitted data can be seen in Fig. 6.5a. Some initial observations

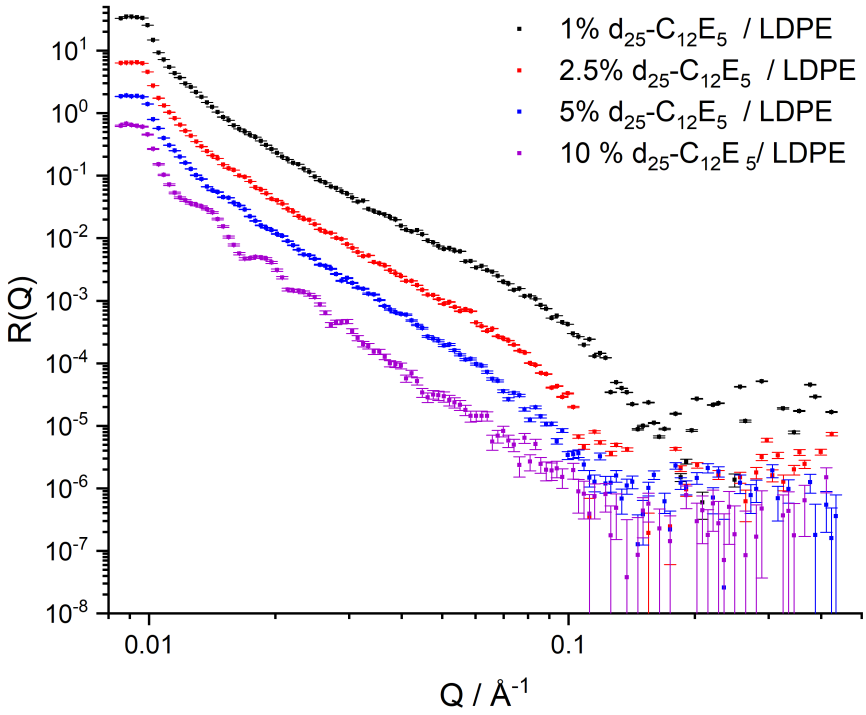

Figure 6.4: Reflectivity spectra of d_{25}-$C_{12}E_5$ in hPBd films for loadings between 1 and 10 % surfactant. An offset has been applied to each data set for clarity

can be made regarding the quality and accuracy of the fitted models. Firstly, it is clear that the fit follows the experimental data well at low Q values up to 0.03 Å^{-1}. This shows that there is strong evidence for the surface layer shown in the SLD profiles (Fig. 6.5b). The fit to the experimental data at higher values of Q is significantly poorer, with a feature that has a larger amplitude and shorter frequency (particularly at higher surfactant loadings) than the feature in the experimental data. However, the data quality at high Q is significantly poorer. This is because $R(Q)$ within this Q range is so low that it is not possible to collect data of good statistical quality within the timescales of an experiment. It is therefore preferable to fit the higher frequency fringes more accurately.

The SLD profiles of d_{25}-$C_{12}E_5$ in hPBd are given in Fig. 6.5b. From immediate inspection, it is clear that there is a significant range of thicknesses between samples which have been prepared in the same way. Since the experimental protocol

requires the substrate to be heated for spin-coating, but it is difficult to control the temperature accurately, this will have some effect on the solvent evaporation rate and therefore the final film thickness. Previous work has shown that the temperature of both the deposited solution and the substrate have a significant effect on film thickness, with higher temperatures giving thicker films.[171] It has also been well established that the evaporation rate of the solvent has a significant effect on film thickness,[172–174] which in the case of a volatile solvent such as the xylene used in these experiments will be greatly influenced by solution and substrate temperature.

From the profiles presented in Fig. 6.5b, it can be seen that the bulk film SLD is significantly lower than what would be expected for a layer with the initial surfactant loading specified. A comparison has therefore been made between a model with a bulk SLD corresponding to that of a 10 % d_{25}-$C_{12}E_5$ layer and one with the best possible fit obtained (Fig. 6.6). It is clear from this comparison that, whilst the 10 % layer gives a better fit towards high Q, the reflectivity profile is not capable of resolving the Kiessig fringes between 0.01 and 0.02 $Å^{-1}$ as accurately. Within previous chapters, it has been seen that it is much more difficult to determine an accurate bulk loading from NR: there is little change in the SLD within the range of loadings expected in the bulk, meaning that small variations in loading give little change in the reflectivity profile.

If the depth profile obtained by NR is compared to a depth profile obtained by NRA, Fig. 6.7, it is clear that the surface layer detected by NR is much less enriched than that seen in NRA. However, the layer thickness is comparable to those seen in NR. This appears to suggest that, similar to in *cis*-PI samples, there is some d_{25}-$C_{12}E_5$ that is invisible to NR. This may contribute to the discrepancy between the expected and measured average volume fraction in NR.

The surface excesses have been calculated and are given in Table 6.1. It is clear that for all samples, only a modest surface excess can be detected by NR. It appears that this surface excess remains relatively unchanged as the surfactant loading is increased from 1 to 5 %. However, the surface excess then increases significantly at 10 % loading. This is similar to the behaviour seen in *cis*-PI

samples, where a large increase is seen at the same loading.

The small surface excess is consistent with the WCA data presented in Fig. 6.8. Samples containing 1 – 5 % $C_{12}E_5$ show high contact angles, indicating a hydrophobic surface presented to the water droplet. It is interesting to note that there is little difference in initial contact angle between 1 and 5 %, reflecting the highly similar surface excess shown in table 6.1. Both of these loadings show a slight decrease in contact angle over time but this is likely caused by water evaporation from the droplet[175] Fig. 6.9 shows the contact angle of a hPBd film which illustrates how the water droplet contact angle decreases over time. However, 10 % $C_{12}E_5$ samples exhibit a much different behaviour. Initially the contact angle begins slightly above 60° and remains stable briefly but then rapidly drops to less than 20°. This rapid decrease is also shown in the images in Fig. 6.10, where it can be seen that the contact angle change is complete in less than 1 second. Previous work by Kumar *et al.* has shown that the placement of a droplet of water on a film comprising a hydrophobic matrix and a non-ionic surfactant can induce the assembly of surface layers of surfactants ahead of the droplet contact line.[176] Within this work, the surfactant was adsorbed to the surface and a droplet of water was then placed on the surface. These surfactant enriched regions were more hydrophilic than the surrounding surface and this was attributed to an "autophilic effect", in contrast to the autophobic effect observed in Cetrimonium bromide-silica systems. This is where self-assembly of surfactant ahead of the contact line reduces γ_{SG}, increasing the contact angle.[177] It is therefore possible that the rapid spreading seen in the 10 % $C_{12}E_5$ / hPBd samples may be caused by the induction of either further enrichment of the surface or a rearrangement of surfactant in response to the the probe droplet being placed onto the surface.

Comparing the surface excesses within *cis*-PI and hPBd, it is clear that a larger surface excess is seen in *cis*-PI at all loadings, with the largest surface excess seen in hPBd being comparable to the smallest in *cis*-PI. This presents the possibility that this reduced migration can be rationalised by several hypotheses. Firstly, it is unclear from these results whether this change is caused by a compatibility change or the reduced ability of the additive to migrate through the matrix.

Table 6.1: Surface excesses of d_{25}-$C_{12}E_5$ in both hPBd and *cis*-PI–01 films for loadings between 1 and 10 % surfactant. Surface excess has been calculated using equation 5.1. *cis*-PI–01 results are taken from chapter 5.

Matrix	z^*/Å			
polymer	1 % d_{25}-$C_{12}E_5$	2.5 % d_{25}-$C_{12}E_5$	5 % d_{25}-$C_{12}E_5$	10 % d_{25}-$C_{12}E_5$
cis-PI	14	16	15	36
hPBd	4	6	3	13

Lützow *et al.* observed that the mobility of a small molecule (in the literature work, toluene and n-heptane) within a polymer decreases as the crystallinity is increased.[169] This would mean that the small molecule within hPBd would be hindered from migrating to the surface due to the slower rate of movement caused by the more tortuous that the additive must travel along to the surface.[178] This has been illustrated in Fig. 6.11. Whilst both small molecules in the work by Lützow *et al.* are hydrophobic, similar effects have also been seen for hydrophilic alcohols in polyolefins.[179] Therefore, it is possible that the lack of distinct surface segregation may be the product of a lower equilibrium segregation of surfactant in a crystalline matrix or kinetic hindrance of surfactant segregation caused by the increased degree of crystallinity. Another hypothesis for this diminished surface segregation may be that the segregation takes a different form, with a greater proportion of the adsorbed surface surfactant in a structure that is invisible to neutrons.

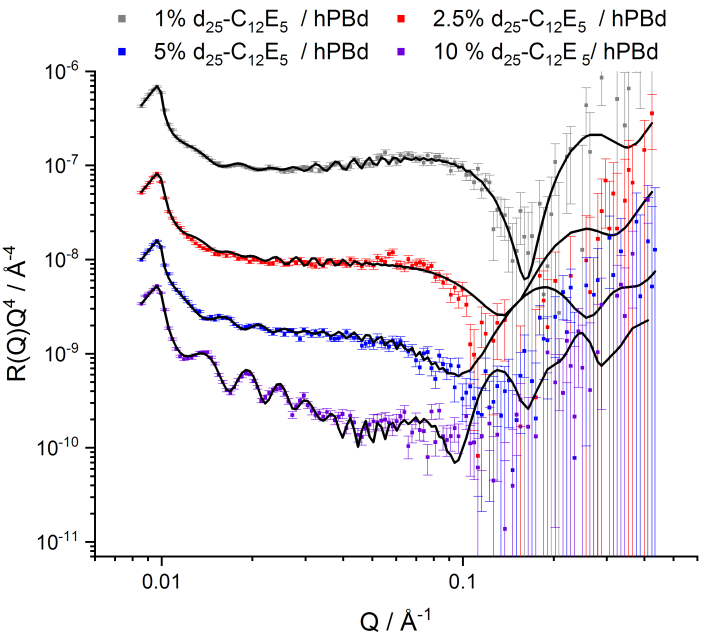

(a)

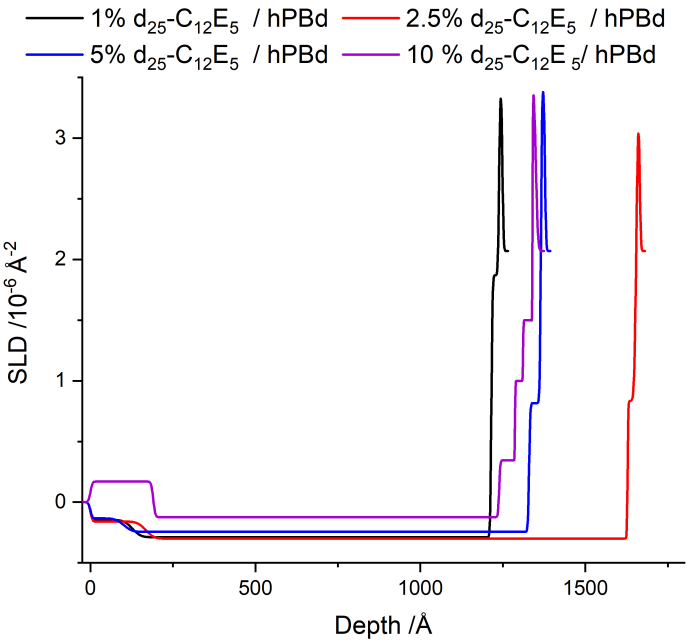

(b)

Figure 6.5: (a) Data and fits for the NR reflectivity of 1 – 10 % d_{25}-$C_{12}E_5$ / hPBd films. Data have been plotted as $R(Q)Q^4$ vs. Q and an offset has been applied to each data series. (b) SLD profiles of 1 – 10 % d_{25}-$C_{12}E_5$ in hPBd obtained from fitting experimental NR data.

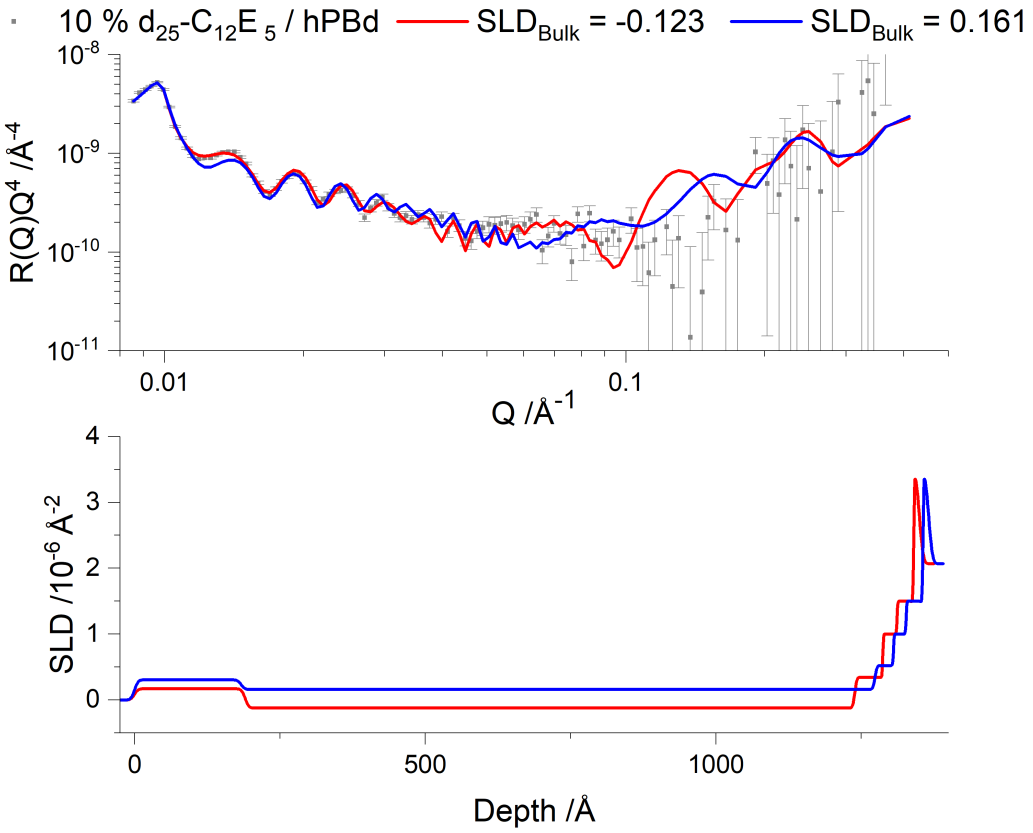

Figure 6.6: 10 % d_{25}-$C_{12}E_5$ / hPBd film SLD profile comparison for models with a bulk layer SLD of -0.123 (the best fit obtained by chi-squared minimisation) and 0.161 (the SLD of a 10 % d_{25}-$C_{12}E_5$ layer) (bottom) with experimental data and computational fits shown (top)

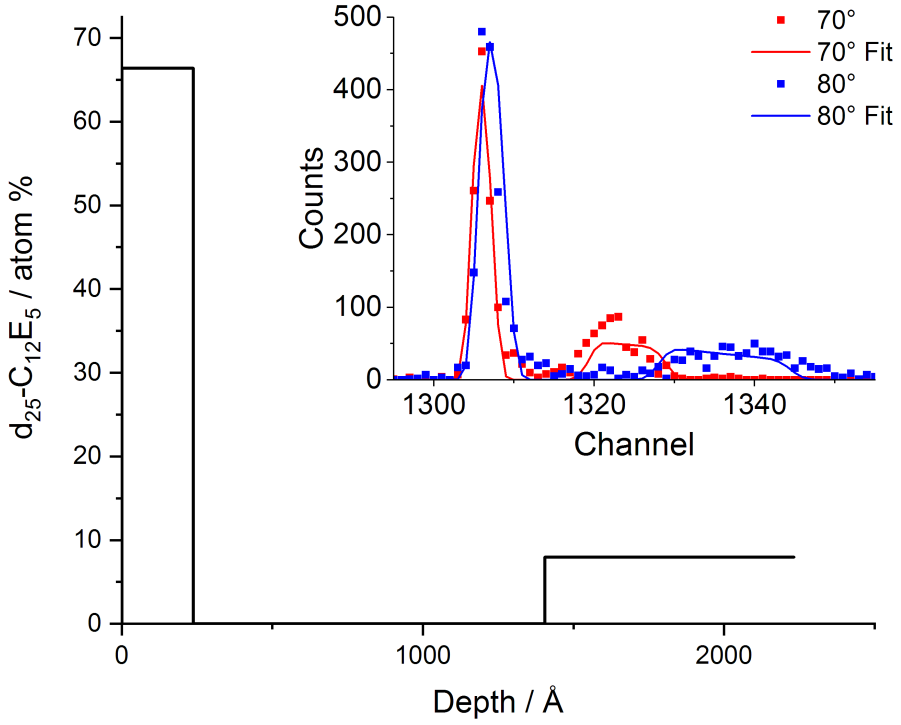

Figure 6.7: NRA depth profile of 10 % d_{25}-$C_{12}E_5$ in LDPE. Inset: NRA data and fits at 70° and 80° angles of incidence.

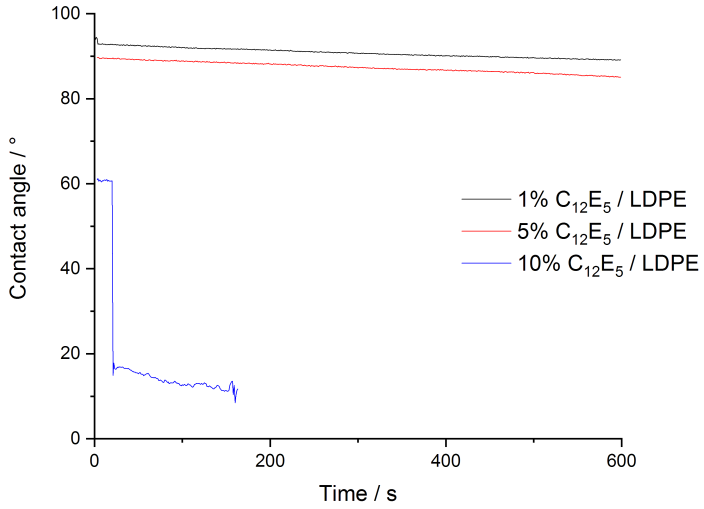

Figure 6.8: Water contact angles of spin-cast hPBd films containing 1 – 10% $C_{12}E_5$. A droplet has been placed on the surface and the contact angle has been recorded over time. Note that the 10% sample data ends much earlier than other loadings due to the difficulty in fitting droplets at low contact angles.

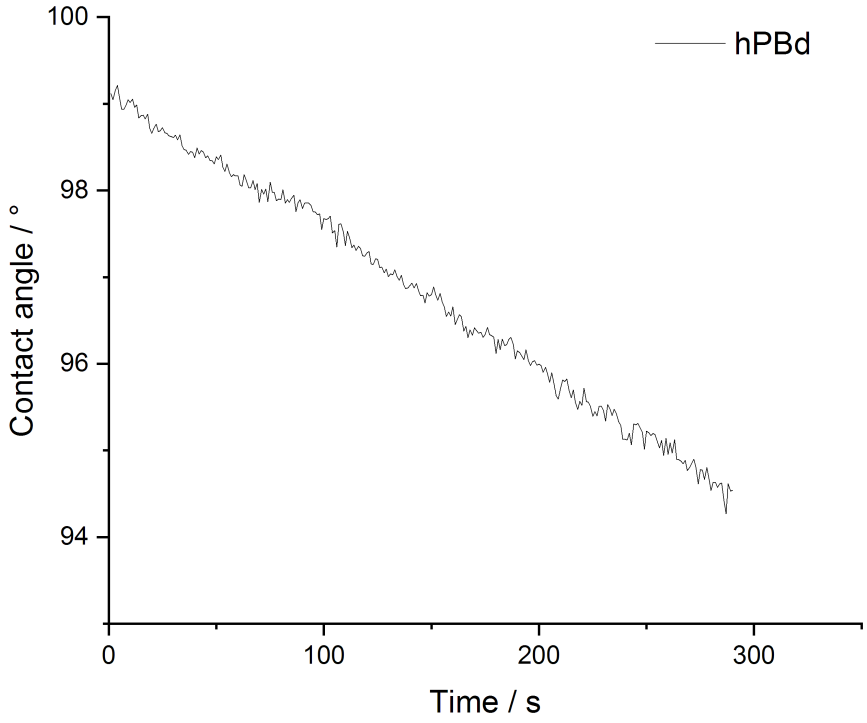

Figure 6.9: Contact angle measurements collected for a hPBd film.

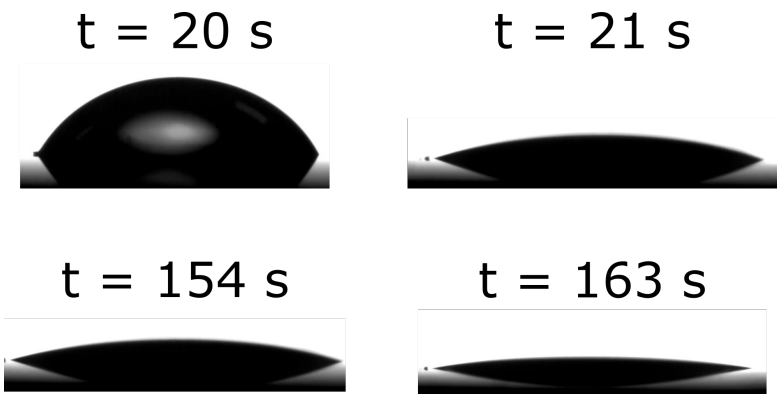

Figure 6.10: WCA droplet images for a droplet of water on a 10% $C_{12}E_5$ / hPBd film. The times shown are the rapid decrease in contact angle between 20 s and 30 s after droplet deposition and the slower, more subtle change seen between 154 s and 163 s.

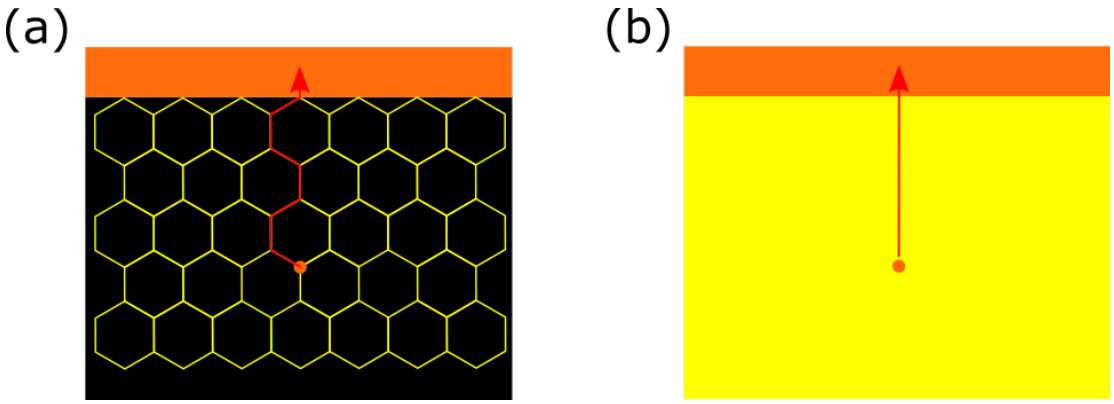

Figure 6.11: Schematic showing how crystallinity affects the diffusion path length. If the penetrant (shown as an orange circle) diffuses to the surface in a crystalline polymer (a), it must take a much longer pathway as it is excluded from the crystalline regions (crystalline boundaries shown as black lines). However, in an amorphous polymer (b), the path length is much shorter.

6.3.2 Influence of Melting Transition on Surfactant Segregation

While it is convenient to study the impact of crystallinity on surface segregation by comparing the behaviour in two different matrices, this introduces other complexities arising from the different chemistry. An alternative is to study the same matrix above and below its melting point. This has the effect of removing the crystallinity within the polymer as the crystalline domains melt. The melting of these domains reproduces some of the conditions in the processing of industrial samples; commonly polymers are extruded while molten and although the shear forces are not replicated in the experiments discussed in this section, these experiments make it possible to isolate the effect of temperature increase on surfactant distribution.

During the neutron experiments in this section, samples were heated to 125 °C, which is above the melting point (105 °C, from Fig. 4.9) of the polymer and held at that temperature for the duration of the experiment. This was not possible for the contact angle measurements shown: the melting point of the polymer is greater than the boiling point of the water. Instead, samples have been heated to 120 °C for 2 hours and have then been allowed to cool to room temperature. Whilst this will not reveal any changes which occur at higher temperature that are reversible when samples are cooled, it will elucidate any behaviour which occurs irreversibly upon heating.

Initial inspection of the NR profiles, Fig. 6.12a, shows that the large bulge that was attributed to the surfactant enriched layer in 55 °C samples (Fig. 6.5a) has become much less pronounced, suggesting that there is a significantly smaller contrast between layers within the sample. This is most likely caused by a decrease in the surfactant enrichment of this surface layer. Fitting these data yields the SLD profiles shown in Fig. 6.12b, which confirm the lower SLD of the surface layer compared to the surface layers in samples at 55 °C.

A comparison of the depth profiles for samples at 55 °C and 125 °C is given in Fig. 6.13. It can clearly be seen that the surface layer becomes less enriched at

higher temperatures, with 10 % samples showing the largest decrease. However, it should be noted that even at low loadings, some enrichment is still found at 125 °C. Surface excess values for the temperature dependence of segregation in hPBd are summarised in table 6.2. A comparison of these values with those for *cis*-PI samples shows that the surfactant loss in hPBd is much larger than the loss in a more amorphous matrix. While the *cis*-PI samples are not heated to the same temperature as the hPBd samples, if the same evaporation process occurred in both polymer matrices, a larger difference between z^* should be seen. Comparing the surface excesses above and below the T_m, it is clear that after heating there is little surface excess present in all samples, with even 10 % loading showing a z^* of less than 1 Å. This suggests that at temperatures above the melting point of hPBd, all surfactant is lost from the surface, which is not seen in the *cis*-PI matrix.

Contact angle analysis data has been reported in Fig. 6.14 for 1 and 10 % $C_{12}E_5$ in hPBd before and after heating to 125 °C. From this work, it can be seen that there is little difference in 1 % samples, confirming the observations from NR that little change appears to occur at low loading. However, at 10 % loadings, the behaviour drastically changes and a hydrophilic-hydrophobic switch is observed. It is likely that this caused by the evaporation of surfactant from the surface, leaving the hydrophobic hPBd remaining.

An alternative hypothesis for the decrease in surface excess and wettability upon heating at 10 % loading in hPBd is that a rearrangement of the surfactant occurs when the sample is heated. This may lead to a structure which is invisible to neutron reflectometry. Evidence of the presence of these invisible structures has been presented in Chapter 5. However, this large change is not seen upon heating in *cis*-PI samples, suggesting that there is some influence of the crystallinity that enables this rearrangement to occur in response to temperature change. These structures may also no longer promote wetting, which would be in agreement with the contact angle results.

It is somewhat surprising that the retention of a surface excess is seen in *cis*-PI but not hPBd. To understand this difference in behaviour, it is necessary to

Table 6.2: Surface excesses calculated from SLD profiles of d_{25}-$C_{12}E_5$ in hPBd and *cis*-PI at temperatures above and below the melting point of each polymer.

d_{25}-$C_{12}E_5$	z^* /Å			
loading /	hPBd		*cis*-PI	
wt.%	55 °C	125 °C	20 °C	60 °C
1	4	3	14	14
2.5	6	1	16	14
5	3	0.3	15	18
10	13	0.4	36	33

understand the process of surfactant loss. As a surfactant-enriched layer is formed spontaneously upon film formation, it is possible that the surfactant can also migrate from the bulk to the surface. Wei *et al.* showed that this process (in the loss of plasticiser from a polymer) is the product of two distinct steps: evaporation and diffusion.[180] Therefore, both the thermodynamic and kinetic elements of surface segregation must be considered.

Diffusion is a kinetic process and can either be described by Fick's second law (equation 2.10) if the surfactant does not swell the polymer[40] or Case-II diffusion if the matrix swells.[42] Furthermore, the rate of diffusion in Fickian diffusion is dependent on the diffusant concentration, whereas this relationship is not present in non-Fickian diffusion. However, determination of the diffusion mechanism is beyond the scope of the present work, with prolonged swelling experiments of thicker films in contact with fluid surfactants required to investigate this.

Evaporation is largely influenced by the vapour pressure of the evaporating molecule. Under equilibrium conditions, the molecular exchange rate (the rate at which molecules can move between liquid and gas phases), K_e can be described. Ward and Fang showed that K_e can be written as[181]

$$K_e = \frac{\eta P_\infty(T^L)}{\sqrt{2\pi m k_b T}} \tag{6.1}$$

where $P_\infty(T^L)$ is the saturation vapour pressure at the temperature T^L, m is the molecular mass of the evaporating molecule, k_b is the Boltzmann constant and η

is a distribution of the energies of the molecules defined as

$$\eta = e^{\frac{V_\infty^L}{k_b T^L}[P_e^L - P_\infty(T_L)]} \tag{6.2}$$

where V_∞^L is the specific volume of the saturated liquid phase and P_e^L is the equilibrium pressure in the liquid. Whilst this is initially intended for the evaporation from a liquid interface, this theory has been applied to the evaporation of solvent from phase separating polymer mixtures and has successfully been used to simulate the phase separation whilst drying. Importantly, the polymer structure or the viscosity of the mixture was not required in these simulations, suggesting that the matrix has little effect on the rate of evaporation of additives.

Whilst evaporation should not be influenced by the matrix polymer, it is possible that diffusion of surfactant to the surface may be impacted by the properties of the polymer. Below the melting point of the polymer, diffusion in hPBd would be expected to be hindered, with Schulz *et al.* showing that the diffusion coefficient of a penetrant can be affected by the crystallinity, with crystal structures resulting in a longer diffusion pathway and thus lower diffusion coefficient[178] as the penetrant is mostly excluded from the crystalline domains.[182] However, above the melting point, there are no longer any crystalline domains and thus there is no hindrance to diffusion.

Work by Cherdhirankorn *et al.* used fluorescence correlation spectroscopy to investigate the diffusion of probe molecules in molten polymers. These results suggested that a correlation could be seen between the diffusion coefficient of a penetrant and the T_g of the matrix polymer, with a higher T_g giving a smaller diffusion coefficient.[183] This is explained by the sensitivity of diffusion to the local segmental dynamics of the polymer chain. As shown in chapter 4 (Fig. 4.4), the T_g of *cis*-PI is -65 °C and the T_g of hPBd has been reported to be significantly lower at -100 °C.[184] This would indicate that the diffusion coefficient of the surfactant in hPBd would be larger than in *cis*-PI, meaning that it is expected that if the bulk surfactant was capable of replenishing the surface layer, samples where the matrix is hPBd would be more able to replenish the surface effectively.

To consider the thermodynamic components of the segregation in these sys-

tems, surface energy must be discussed. Firstly, there are two interfaces featuring the polymer / surfactant blend in this system: the buried layer and the surface layer. The buried layer present in the hPBd samples is not detected within *cis*-PI. Zhang *et al.*[185] discussed the role that surface energy plays in the crystallisation of polymer films during solution-coating. It was reported that a lower surface energy substrate led to a reduced nucleation penalty for crystallisation of the film. Within the present work, the substrate surface energy is not changed, but instead surfactant is present. If this surfactant can enrich the polymer-substrate interface, it will also lower the interfacial energy and thus decrease the nucleation penalty, making crystallisation of the surfactant more favourable. This may be a significant driver in the formation of an enriched buried layer which does not appear present in *cis*-PI, where crystallisation does not occur.

This interpretation can also be applied to the air-polymer interface. In this case, it is useful to compare the surface energy of *cis*-PI and a more crystalline polymer such as LDPE. Previous studies have shown that *cis*-PI has a higher surface energy (32 mJ m^{-2})[155] than LDPE (21.8 mJ m^{-2}).[186] This would mean that there is a larger motivation for segregation of surfactant to the surface of *cis*-PI in order to lower the surface energy than in LDPE. Furthermore, the surface energy of the silicon substrate,[187] 1240 mJ m^{-2}, is much larger than the surface energy of LDPE, meaning that the nucleation penalty at the interface is much larger than at the surface, leading to a much larger thermodynamic driver for segregation to the buried interface than to the film surface.

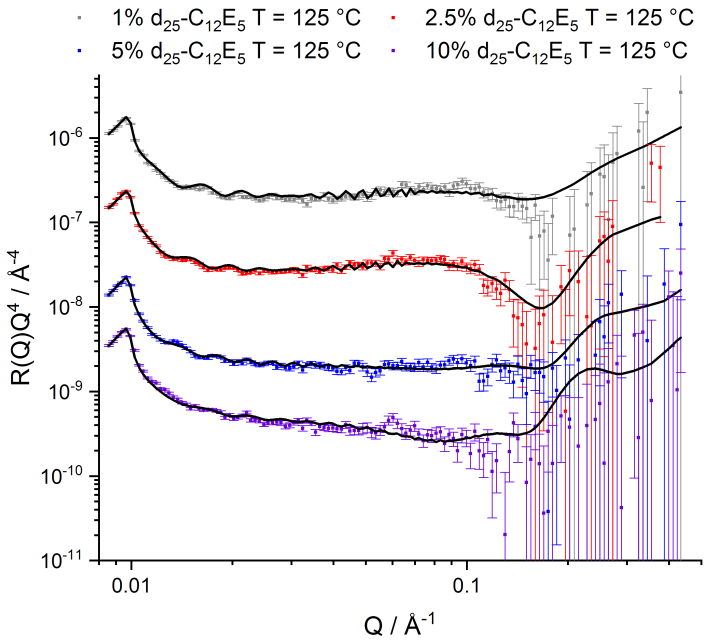

(a)

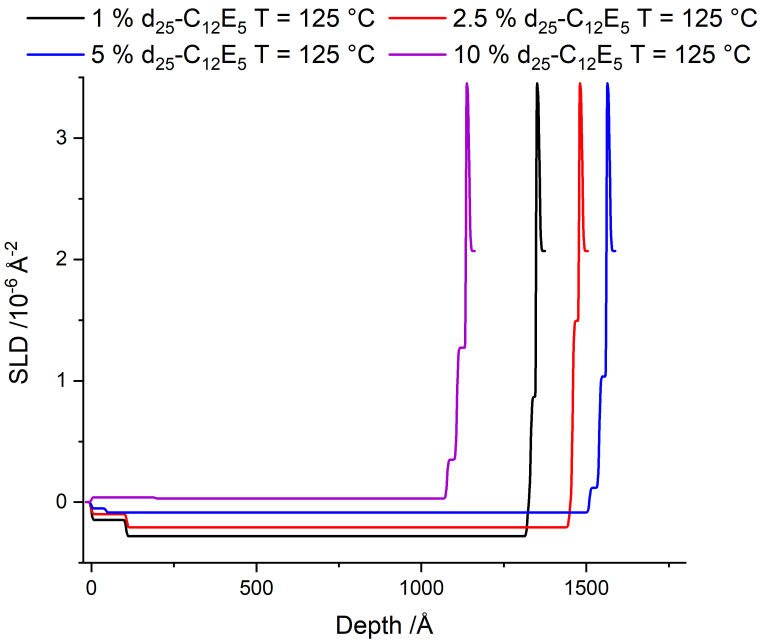

(b)

Figure 6.12: (a) Data and fits for the NR reflectivity of 1 – 10 % d_{25}-$C_{12}E_5$ / hPBd films at 125 °C. Data have been plotted as $R(Q)Q^4$ vs. Q and an offset has been applied to each data series. (b) SLD profiles of 1 – 10 % d_{25}-$C_{12}E_5$ in hPBd at 125 °C obtained from fitting experimental NR data shown above.

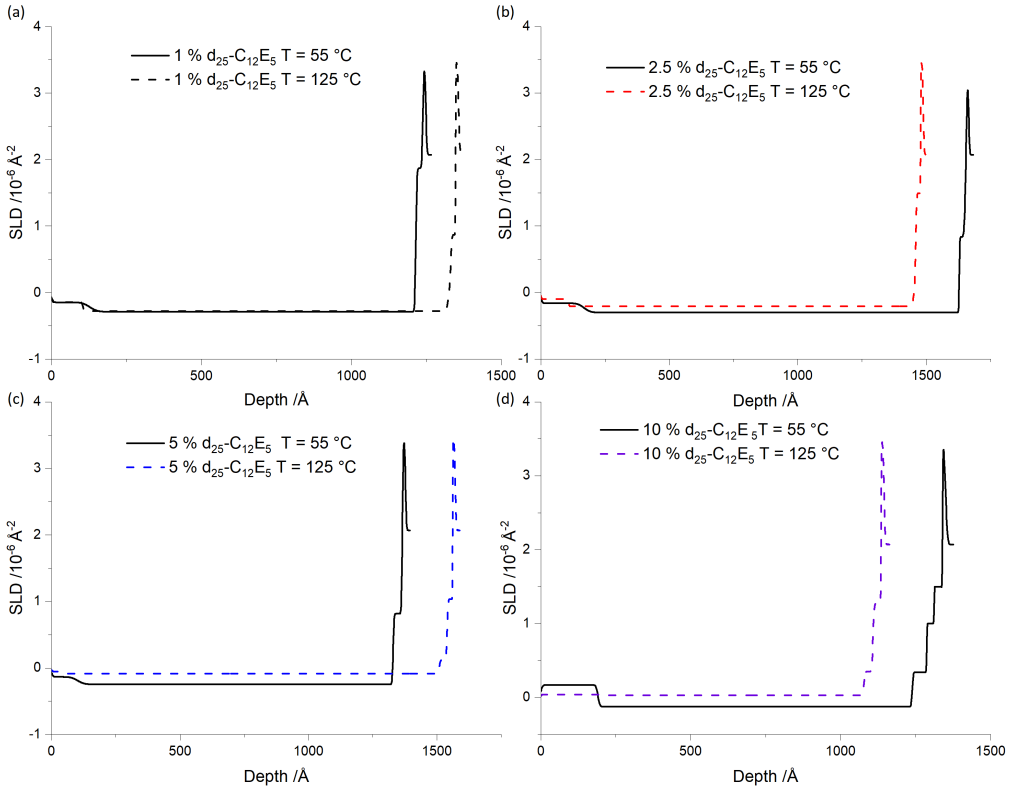

Figure 6.13: Comparison of concentration profiles for d_{25}-$C_{12}E_5$ in hPBd at 55 °C and 125 °C as obtained by NR. Surfactant loadings are 1% (a), 2.5% (b), 5% (c) and 10% (d)

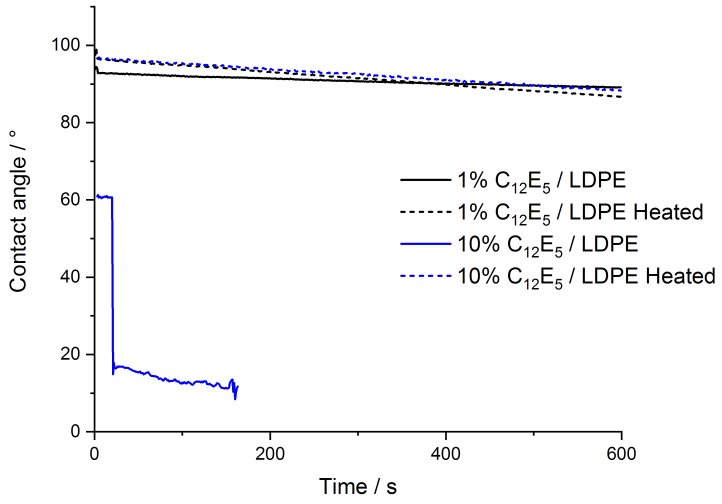

Figure 6.14: Water contact angles of 1 and 10 % $C_{12}E_5$ / hPBd films at before and after heating to 125 °C for 2 hours.

6.3.3 Effect of Crystallinity and Temperature Elevation on Surface Morphology

Crystalline polymers have a much more complex surface morphology than amorphous polymers with crystal features such as spherulites and other ordered structures on the surface.[188] It is therefore of great interest to probe how the surfactant loading affects the morphology of a crystalline film.

Firstly, Fig. 6.15 shows the surface of hPBd without any surfactant. It is clear that the surface has a significantly different morphology from that of *cis*-PI samples, Fig. 5.14. Within the surface height maps, the film surface is dominated by a crystalline structure, with crystalline domains bordered by crystal boundaries that are lower in height. The presence of these features in samples without surfactant show that this change in surface morphology is caused by the increased crystallinity of the polymer rather than any induction of a different structure of surface surfactant by the polymer. This surface morphology is consistent with surface structures observed by Hardman *et al.*[189] using the same instrument. Furthermore, these are reminiscent of the crystalline structures seen in similar work investigating LDPE surfaces.[190,191] LDPE and hPBd are much more crystalline than *cis*-PI and so it should be expected that the film would exhibit a much more structured surface.

The surface of 1 % $C_{12}E_5$ (Fig. 6.16a) show some small strand like features, similar to those seen in *cis*-PI samples, Fig. 5.14 and 5.15. The features on the surface of hPBd (table 6.3) are comparable in thickness to those on *cis*-PI(approximately 350 nm). Sections have been taken from the image across the strands and these have been plotted in Fig. 6.16b.

Comparison of the surface of 1 % and 10 % $C_{12}E_5$ (Fig. 6.16a and 6.17 respectively) in hPBd yields some interesting observations. Firstly, the height range between the highest points on each crystalline domain and the trough in the crystal boundaries is much lower for higher loadings. It is possible that these cracks seen on the samples are being filled with surfactant, which would reduce the depth of these features. However, the thickness of the enriched surface layer in the NR

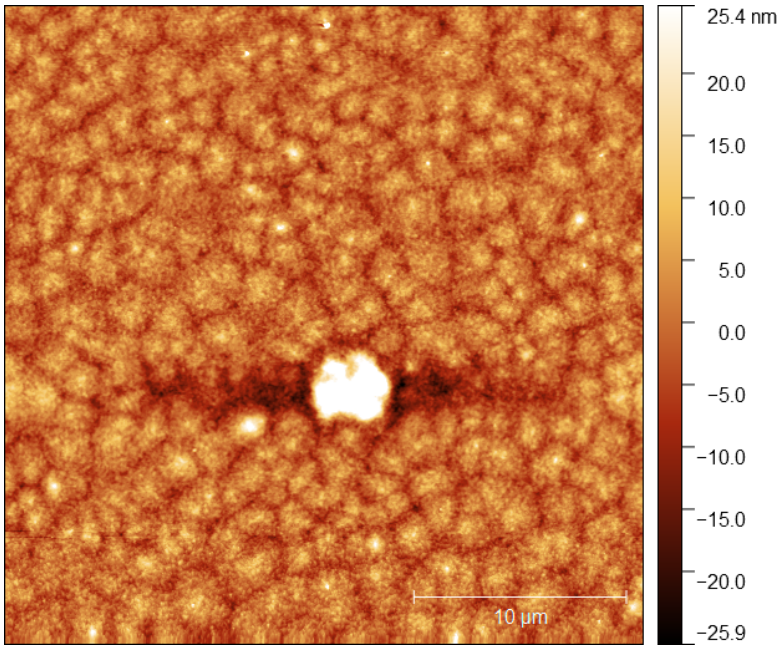

Figure 6.15: AFM image of hPBd surface at 20 °C.

Table 6.3: Strand height and width for 1% $C_{12}E_5$ / hPBd films at 20 °C and 60 °C determined from the cross-sections shown in Figures 6.16b and 6.18b.

1% $C_{12}E_5$ /	section number				
hPBd 20 °C	1	2	3	4	5
Strand height / nm	11.9	11.7	6.11	8.03	8.12
Strand width / nm	399	232	176	173	352
1% $C_{12}E_5$ / hPBd 60 °C					
Strand height /nm	6.02	10.3	7.47	12.9	5.47
Strand width / nm	170	459	335	464	177

depth profiles (Fig. 6.13) is significantly thicker than the depth of the features, suggesting that there must be additional surfactant at the surface of the film.

It is also possible to observe that there are no large strand-like features in 10 % samples like those seen in 2.5 % samples. Instead, it appears that the surface contains a large number of much smaller and thinner strands which can be seen on both the surface of crystalline domains and crystal boundaries. This may suggest that as the surface excess becomes larger, the surfactant begins to become more abundant on the surface and rather than form large, distinct strands it forms much smaller strands that cover more of the surface.

Whilst relatively little attention has been given to the surface topography of blends of surfactants and semi-crystalline polymers, recent work by Gubala *et al.* has investigated the behaviour of erucamide on polypropylene surfaces.[192] Within this work, AFM images showed that there was bilayer of erucamide formed at a lower loading than the loadings of surfactant in these experiments, with additional layers forming on top of this layer as isolated domains. This is unlikely to be similar to the phenomena shown here: whilst the surface layer thicknesses shown in Fig. 6.7 are comparable to the thicknesses given in the work by Gubala *et al.*, the surface excess is much smaller than what it required for complete bilayer formation, leading to the conclusion that complete surface coverage does not occur.

Samples have also been assessed using AFM at elevated temperatures, Figs. 6.18a and 6.19. However, whilst the melting temperature of hPBd is over 100 °C, it was not possible to elevate the samples to melt the polymer and collect high quality data. Above the melting point, the polymer becomes a viscous fluid, leading to the polymer adhering to the probe and being transferred around the sample as the probe moves. Instead, samples have been heated to temperatures below the melting point to assess how surface topography changes as the temperature is increased.

Comparing 1 % $C_{12}E_5$ samples at 20 °C and 60 °C (Fig. 6.18a), it initially appears that the surface profiles are quite similar. However, the height scales are significantly different, with the lower temperature samples exhibiting a much

Table 6.4: Statistical roughness quantities for 1 % $C_{12}E_5$ / hPBd films shown in Figs. 6.16a and 6.18a

Temperature / °C	R_q	$R_{\max}$	R_{SA}
20	14.75	11.37	0.9954
60	14.79	11.51	0.9971

more flat surface than samples at 60 °C. It must be noted that the same sample is used at each temperature, with only the position on the sample changed between measurements. This result is quite surprising: the samples are below the T_m and so the degree of crystallinity should not change, leading to little surface change. However, these features do not appear to be detected within statistical roughness quantities (table 6.4), with little difference in all values at different temperatures. These small differences of roughness may likely be caused by the expansion of the polymer at the increased temperature, with crystalline and amorphous domains expanding at different rates.[193]

The strands which are seen in the 1 % samples at 20 °C are still seen in 60 °C AFM images. If the heights and widths of the strands are compared at each temperature (table 6.3), it appears that whilst the height scale of the polymer surface changes, the strands seem to remain the same after heating. This initially appears to contrast with the results shown from NR, where the surface excess appears to be lost upon heating. However, there is a significant temperature difference between the conditions under which the NR and AFM measurements are collected and work in chapter 5 showed that at 60 °C little change in surface surfactant concentration was seen in *cis*-PI samples. It is also possible that, similar to *cis*-PI / $C_{12}E_5$ samples, there is some surfactant which is not detected by NR which remains present even after heating. Furthermore, it is also possible that this surfactant loss seen in NR only occurs when the matrix is melted (above the temperature that AFM measurements are conducted) and so less surfactant loss is seen at all temperatures up to 60 °C.

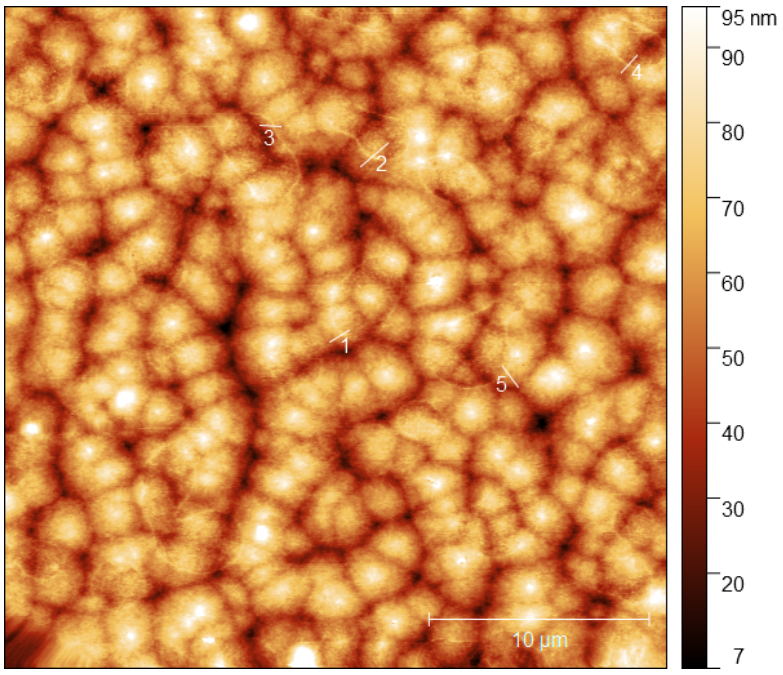

(a)

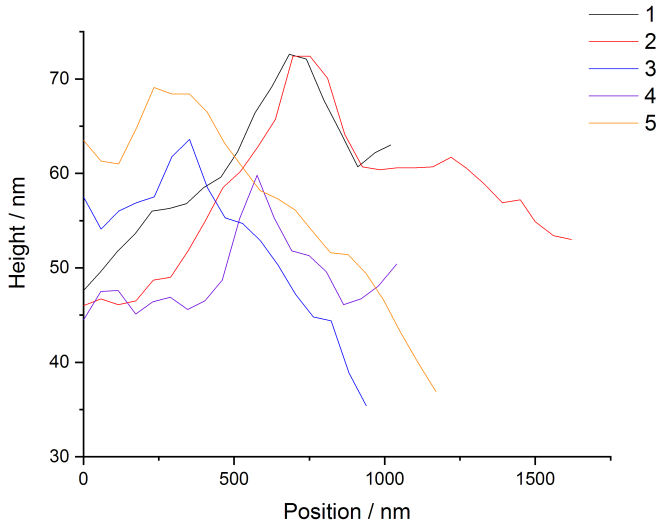

(b)

Figure 6.16: (a) AFM height image of 1% $C_{12}E_5$ in hPBd at 20 °C. Several sections of strand-like features have also been shown. (b) Cross-section of strands seen in AFM image above. Numbers correspond to the numbers labelled in the AFM image.

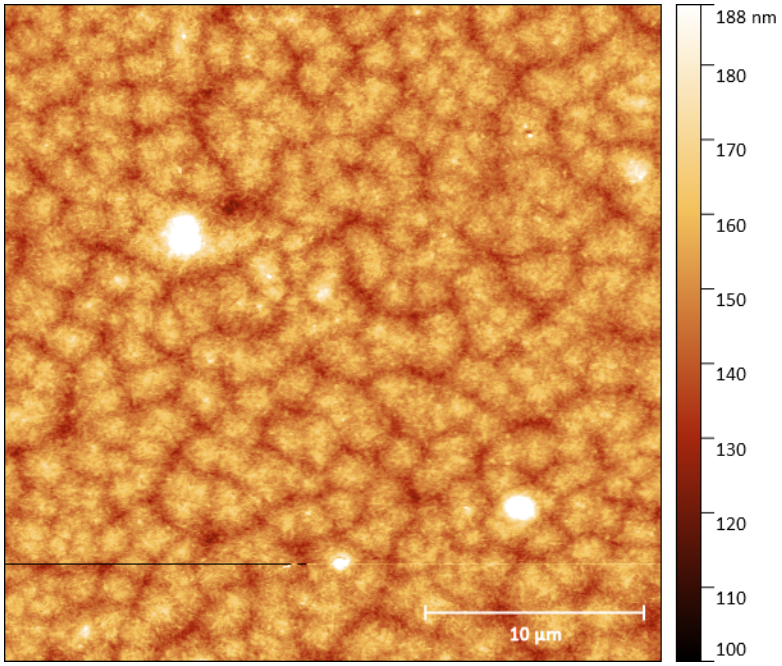

Figure 6.17: AFM height image of 10 % $C_{12}E_5$ in hPBd at 20 °C. The same scale range has been applied to this image as Fig. 6.16a.

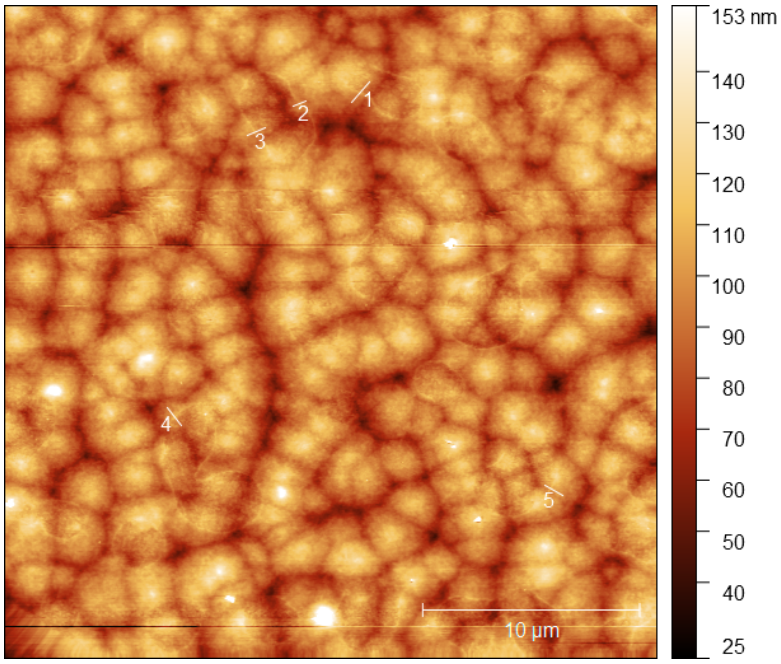

(a)

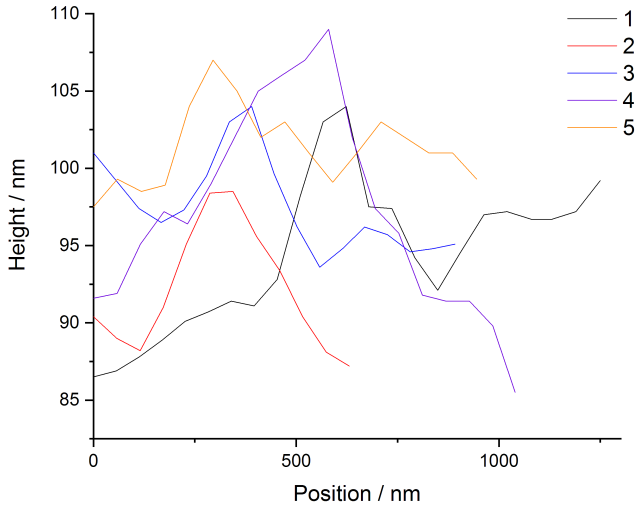

(b)

Figure 6.18: (a) AFM height map of 1 % $C_{12}E_5$ in hPBd at 60 °C. Sections of strands have been shown. (b) Cross-section of strands seen in AFM image above. Numbers correspond to the numbers labelled in the AFM image.

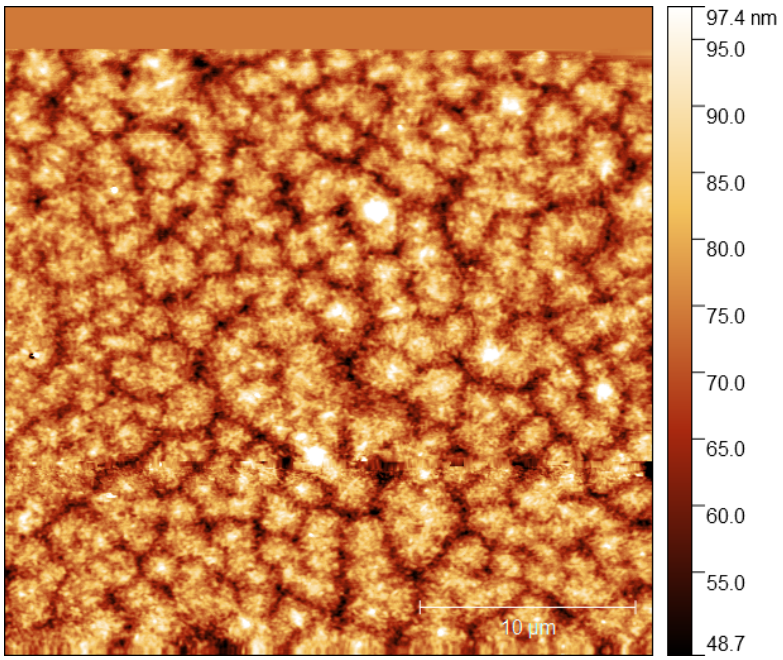

Figure 6.19: AFM height imange of 10 % $C_{12}E_5$ in hPBd at 60 ℃. Note that the top 2 μm have been omitted due to a tracking error during the collection.

6.4 Chapter Conclusions

This chapter has probed the distribution of $C_{12}E_5$ within hPBd films with respect to surfactant concentration using neutron reflectivity. This work has revealed that surfactant does segregate within hPBd films but only to a low degree, with small surface excesses being seen. Additionally, the surfactant depth profile has also been compared at temperatures above the melting point of the polymer to simulate the processing conditions of commercial samples. NR also suggested that heating may eliminate the surfactant from the surface, which is further supported by contact angle analysis measurements. The contact angle results are similar to those seen on *cis*-PI surfaces. However, the NR results show that whilst in *cis*-PI the surface excess remains, in hPBd samples the surface excess is lost. This again reinforces the hypothesis that the surface excess that is detected by NR is the primary source of surfactant that is responsible for surface modification.

It has been shown that whilst hPBd does show a surfactant-enriched layer at the surface, this is much lower in surfactant concentration than in *cis*-PI, with a maximum surface excess in 10 % samples that is comparable to the loadings in 1 % $C_{12}E_5$ / hPBd films. It has been suggested that this may be caused by the more difficult diffusion of molecules through semi-crystalline polymers, with small molecules unable to migrate to the surface after the film has been spin-cast and all solvent has evaporated.

As was observed for *cis*-PI samples in chapter 5, the surface excess measured by NR was significantly smaller than the surface layer of surfactant detected by NRA. This has again been attributed to two distinct types of surfactant layers, with one showing more uniform coverage and is therefore detectable by NR. After the sample is heated to above the melting point, NR reveals that this surface layer in samples with a lower loading is almost negligible. Contact angle analysis also shows that after heating, the surface in both 1 and 10 % samples becomes hydrophobic, suggesting that unlike in *cis*-PI matrices, surfactant in hPBd films does not remain present on the surface after heating. It is unclear whether this is caused by loss of all surfactant (including surfactant in the bulk) or whether bulk

surfactant is unable to migrate up to the surface to replenish the surface layer.

AFM images have shown that hPBd / $C_{12}E_5$ films also contain strands, with strands appearing more prominent at low surfactant loadings. Importantly, analysis of the width and height of these strands show little difference between 20 and 60 °C, suggesting that these strands are not affected by temperature elevation. This would appear to confirm that these strands cannot be attributed to the surfactant layer detectable by NR.

Chapter 7

Effect of Surfactant Head-Group Size on Surface Properties of Polymer Films

7.1 Chapter Introduction

Previous chapters have assessed the distribution of surfactant within a polymer as well as how crystallinity changes the surfactant segregation behaviour. Attention must now be given to the impact of the surfactant. The polyoxyethylene alkyl ether family of surfactants, as previously discussed, consist of an alkyl chain bonded to a chain of repeating ether units. This allows the length of the head and tail group to be varied to produce a range of surfactants with different hydrophilic-lipophilic balances (HLB).

This variation of head and tail group size can be used to tune the surfactant properties to suit the intended application, with commercial materials using a range of surfactants to impart hydrophilicity to different polyolefin fibres.[55,194] It would therefore be of significant interest to understand how changing the head group size influences the tendency of a surfactant to segregate to the surface and thus impart hydrophilicity to the polyolefin surface.

Previous studies of surfactant segregation has shown that increasing the in-

compatibility promotes greater surface segregation. Hu *et al.*[195] showed that surfactants with an enhanced hydrogen bonding capability (in the work of Hu *et al.*, ionic surfactants compared to non-ionic surfactants) were capable of greater hydrogen bonding capability with the water molecules in the subsurface, the layer of water molecules immediately below the surfactant layer (Fig. 7.1). This reduced the surface entropy of the water by creating an ordered water molecule structure, leading to a smaller decrease in surface tension by opposing the favourable enthalpic term. However, in a polyolefin matrix, increasing the incompatibility of the surfactant also increases the size of the high surface energy polar group, so it is not trivial to predict whether such a change would promote or inhibit surface segregation.

Within this chapter, the effect of the size of the hydrophilic head group will be on the distribution of the surfactant. $C_{12}E_3$, $C_{12}E_4$ and $C_{12}E_5$ shall be compared within an LDPE matrix as well as an amine oxide surfactant, DDAO. This shall be performed using NR to collect depth profiles of the surfactant within films. Surface properties will then be compared using contact angle analysis to understand how the wettability changes over time upon contact with water. AFM images shall also be used to enable comparison with the lateral structure of hPBd containing $C_{12}E_5$, which was studied in the previous chapter.

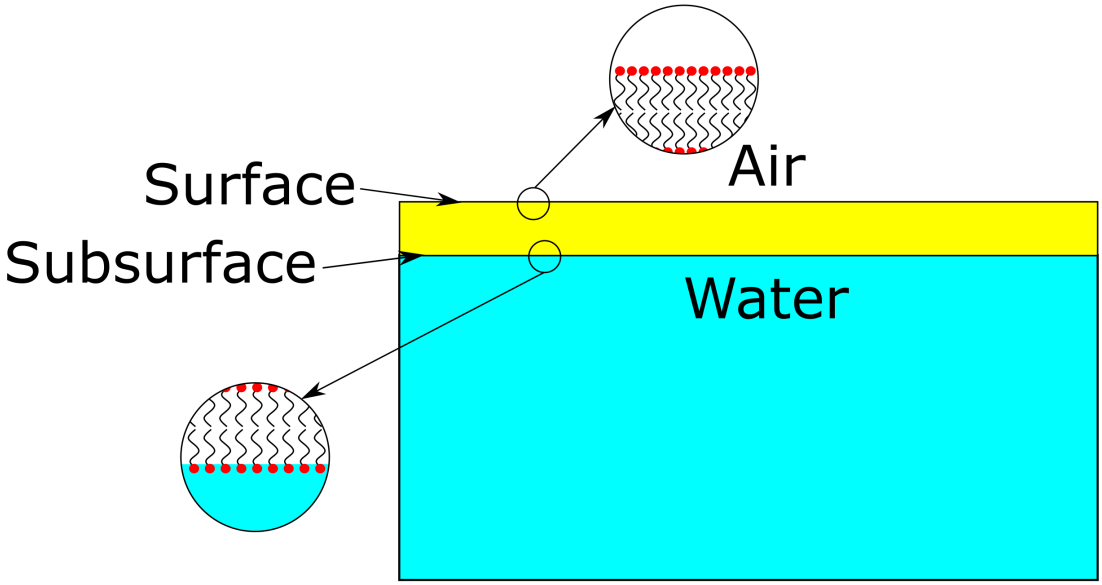

Figure 7.1: Diagram illustrating the surface and subsurface in the work by Ye *et al.*[196] The subsurface is the interface between the water and the bottom of the surfactant layer and the surface is the interface of the surfactant layer and the air.

7.2 Results and Discussion

7.2.1 Effect of Head-Group Size on Surfactant Distribution in hPBd Films

This section shall probe the surfactant distribution of a defined series of surfactants within hPBd films. This shall be performed using NR depth profiling and will present an opportunity to compare how surface enrichment changes with head group size.

Upon inspection of the NR profiles in Fig. 7.2a, it appears that there is little difference between the profiles at different $C_{12}E_3$ loadings. Furthermore, the fringes observed in d_{25}-$C_{12}E_3$ / hPBd samples are much smaller in amplitude than those seen in d_{25}-$C_{12}E_5$-containing samples (Fig. 7.3). This suggests that the contrast between the surface layer and the bulk is much smaller for d_{25}-$C_{12}E_3$ samples, which indicates that the surface layer is much less enriched in surfactant than in d_{25}-$C_{12}E_5$ samples. The concentration profile corresponding to the best fit of the data confirms that the surface excess of d_{25}-$C_{12}E_3$ is very small (Fig.7.2) and is much smaller than was previously found for d_{25}-$C_{12}E_5$ (Fig. 6.5b). Comparison of the profiles of the two surfactants at 1 – 5 % loadings reveal that the surface layers have very similar SLDs and thicknesses. The main difference between the two surfactants appears at 10 % loadings, where the SLD difference between the enriched layer and the bulk layer is much lower in d_{25}-$C_{12}E_3$ samples than d_{25}-$C_{12}E_5$ / hPBd films.

Whilst the surface enrichment of the surface in d_{25}-$C_{12}E_5$ samples is low compared to *cis*-PI samples, the thickness of the layer is in the range of 100 to 125 Å for all samples. The necessity of this layer is justified by Fig. 7.4, where a model without this layer is shown. This SLD profile is not able to accurately fit the fringes seen in the data, with the amplitude of fringes in the simulated profile appearing too large. This additional layer reduces this amplitude. The layer is several times thicker than the length of a surfactant molecule, again suggesting that rather than a complete layer of surfactant, a small proportion of the film is

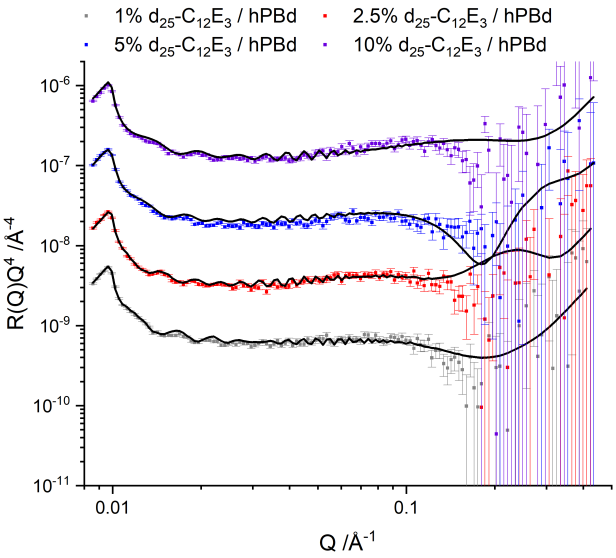

(a)

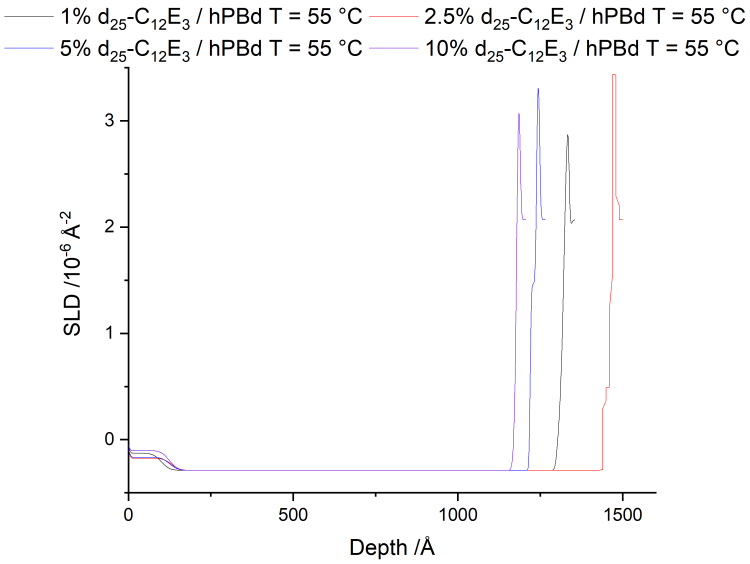

(b)

Figure 7.2: (a) Data and fits for the NR reflectivity of 1 – 10 % d_{25}-$C_{12}E_3$ / hPBd films at 55 °C. Data have been plotted as $R(Q)Q^4$ vs. Q and an offset has been applied to each data series. (b) Surfactant depth profiles of 1 – 10 % d_{25}-$C_{12}E_3$ in hPBd obtained from fitting experimental NR data.

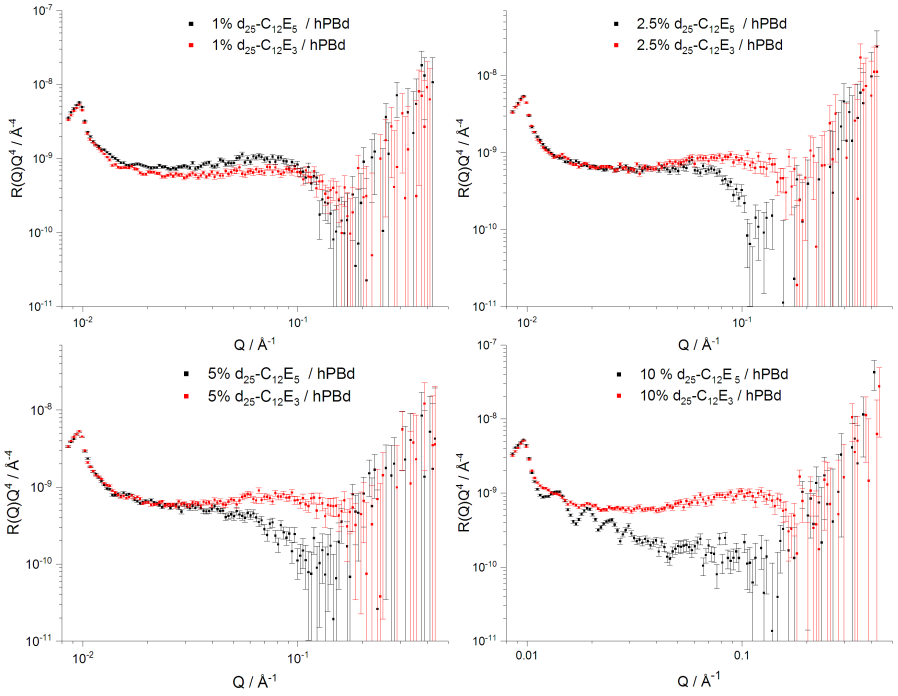

Figure 7.3: Comparison of $R(Q)Q^4$ vs. Q for d_{25}-$C_{12}E_5$ and d_{25}-$C_{12}E_3$ in hPBd at 55 °C at loadings between 1 and 10 % wt.

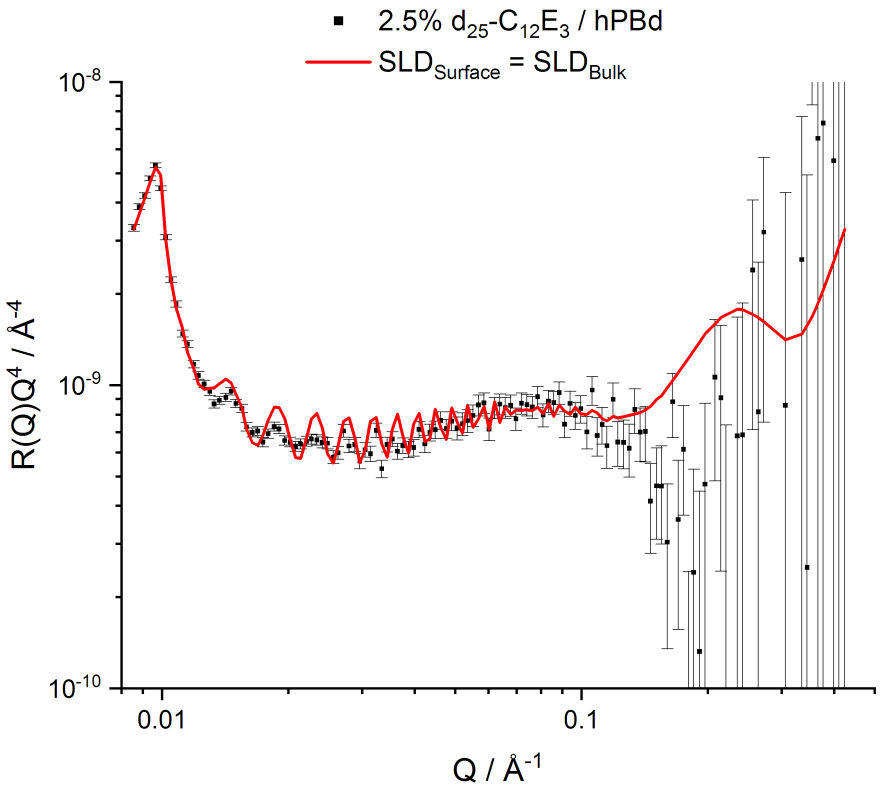

Figure 7.4: Reflectivity data for 2.5 % d_{25}-$C_{12}E_3$ in hPBd at 55 °C, fitted with a reflectivity profile simulated from an SLD profile with identical parameters as that in Fig. 7.2a except for the SLD of the surface layer is set to the same value as the bulk layer.

covered with a layer that consists of several layers of surfactant.

The surface excess values given in table 7.1 also confirm that there is little difference in the total amount of surfactant at the surface at all loadings. These surface excesses were determined from Fig. 7.5. Whilst there was a moderate increase in surface excess at 10 % d_{25}-$C_{12}E_5$, this is not seen for 10 % d_{25}-$C_{12}E_3$. This appears to suggest that, whilst at higher loadings surface enrichment is seen in d_{25}-$C_{12}E_5$ / hPBd films, the same does not occur for the surfactant with the smaller headgroup . Therefore it seems likely that there is some driver for segregation in d_{25}-$C_{12}E_5$ / hPBd films that is not present within d_{25}-$C_{12}E_3$ / hPBd films. This observation is consistent with the earlier analysis of compatibility obtained from DSC in chapter 4. The DSC results showed that $C_{12}E_3$ loadings between 1 and 10 % were equally compatible, thus surface segregation may be directed by surface energy difference, but is not likely to be promoted by incompatibility. It must also be noted that the 10 % $C_{12}E_5$ sample shown in Fig. 7.5 are distinctive as this is the only sample that a positive surface SLD is present, which suggests that there is a surface excess that cannot be determined as surface roughness.

The factors affecting the segregation of the surfactant can broadly classified as thermodynamic, where a driver such as surface energy difference or compatibility drives migration and kinetic, where the speed at which migration occurs may limit segregation.

Flory-Huggins theory introduced in chapter 2 can be used to consider the differences between these two surfactants. Within the Flory-Huggins equation (equation 2.7), at the same approximate volume fraction of each surfactant, the only difference will be the interaction parameter, χ. As χ is a factor of the interaction energy between the polymer and surfactant[22] (u_{AB}, equation 2.4), it would be expected that as this interaction becomes more positive, the possibility of the two components no longer mixing increases. This interaction will be largest where the head group is larger as this will have a more unfavourable interaction with the non-polar polymer matrix. However, Flory-Huggins theory does not specifically consider surface segregation. Instead, all that can be inferred from it is that $C_{12}E_5$ is more incompatible than $C_{12}E_3$ with the polymer matrix. The

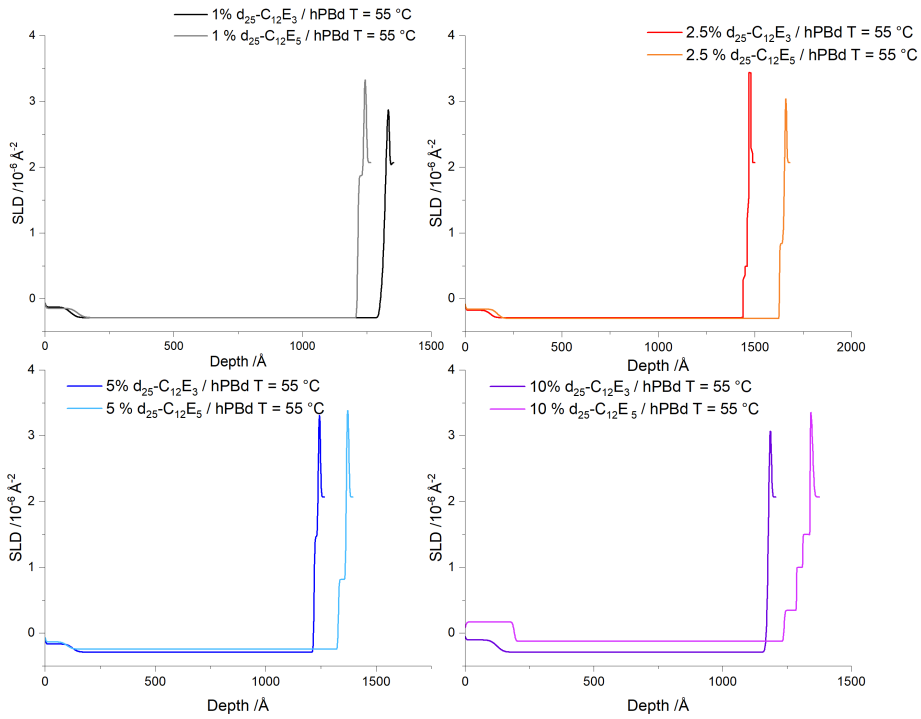

Figure 7.5: Comparison of SLD profiles of d_{25}-$C_{12}E_3$ and d_{25}-$C_{12}E_5$ in hPBd films at 55 °C calculated from NR.

observation that $C_{12}E_5$ has a greater surface excess, despite having the larger high surface energy group that may inhibit surface segregation, indicates that incompatibility may be the most important factor in driving surface segregation for polyoxyethylene alkyl ether surfactants.

The same pattern of compatibility behaviour was suggested by rheology results (chapter 4) in *cis*-PI, another non-polar matrix. These results showed that $C_{12}E_5$ was less compatible with the polymer matrix than $C_{12}E_3$. This supports the results from Flory-Huggins theory that $C_{12}E_5$ is likely to be less compatible in hPBd than $C_{12}E_3$.

Previous work has been conducted with much thicker extruded polypropylene films containing $C_{18}E_2$, $C_{18}E_4$ and $C_{18}E_6$ [164] and has considered the kinetic factors in segregation. This work demonstrated that an enriched layer of surfactant could be seen in all films. Moreover, it was observed that the surface enrichment was

greater with shorter head groups. This was accounted for by the potentially greater mobility of the smaller molecule ($C_{18}E_2$) within the polypropylene matrix. Whilst this is the opposite result of those seen in this work, it is important to note that there are several key differences between this work and the present results.

Firstly, poly(propylene) has a much higher degree of crystallinity than hPBd.[197] This higher crystallinity may cause a much greater hindrance to the mobility of the surfactant than hPBd does, which would mean that the shorter surfactant length of $C_{12}E_3$ would not have the same effect in hPBd as is seen in the work by Datla *et al.*[164]

The preparation technique is also different. Within the present work, samples are spin-cast from xylene whereas the films probed by Datla *et al.* are extruded. The presence of a solvent may influence the segregation of the surfactant. Ye *et al.* showed that the solvent used in spin-casting affected the segregation of different groups in a random copolymer of methyl methacrylate and 2-perfluorooctylethyl methacrylate.[196] It is therefore likely that the presence of solvent during film formation influences the segregation by allowing the polymer chains to swell, meaning that the surfactant is free to migrate to the surface, relatively unhindered unlike in extruded samples. However, there is a key difference between the present work and the work of Ye *et al.*, the surfactant in the work of Ye *et al.* is fluorinated, and would therefore be expected to be surface active in most organic solvents. This surface activity would not be expected in the case of the non-ionic surfactant in xylene as used in this work. Gundabala *et al.* showed that, for surfactants with low Péclet numbers, an enriched surface layer would be seen in drying latex films.[198] The Péclet number is defined as[199]

$$P_e = \frac{\text{advective transport rate}}{\text{diffusive transport rate}} = \frac{Lv}{D} \tag{7.1}$$

where L is the characteristic length of the system, u is the velocity of the flow field and D is the diffusion coefficient. It is expected that the diffusion coefficient would be larger for a smaller surfactant due to its shorter chain length,[164] giving $C_{12}E_3$ a lower Péclet number. This has also been confirmed by comparison of polyoxyethylene alkyl ether and longer polyoxypropylene-polyoxyethylene

(PO-EO) alkyl ether surfactants in water. Ye *et al.*[196] identified that there are two processes in surface enrichment: migration of the surfactant from the bulk to the bulk / surface layer interface (subsurface) and from the subsurface to the air / surfactant interface. Here, the rate of surface adsorption from the subsurface to the air / surfactant surface was found to be faster in shorter surfactants.[200] However, this work did note that the rate was faster from the bulk to the subsurface for the longer surfactant (Fig. 7.1). Ye *et al.* attributed this to the greater hydrophobicity of PO-EO alkyl ether surfactant, meaning that the surfactant was less compatible with the bulk water layer. Therefore, it is possible that the migration of the longer chained surfactant in the present work is more facile due to the greater incompatibility of the surfactant and polymer matrix.

While it is interesting to see that there is little surface excess, the NR data shows that the surfactants do accumulate at the buried interface between hPBd and the silicon substrate. This is evidenced by the observation that the polymer / silicon oxide interface is not a single step transition. Instead, several additional layers have been introduced into the model. These layers represent a surfactant enriched layer at the silicon oxide interface. The presence of this layer reveals that, whilst surfactant is capable of segregating to the air interface, it can also segregate to the buried surface. Fig. 7.5 shows that as concentration increases, the SLD and thickness of the buried layer also increases. Furthermore, the largest buried layer can be found at 10 % loadings of d_{25}-$C_{12}E_5$. This is also consistent with previous observations: d_{25}-$C_{12}E_5$ shows a larger surface layer than $C_{12}E_3$ and at 10 %, there is more surfactant within the film to migrate to the surface. It can therefore be inferred that the drivers for interfacial segregation are the same as surface segregation.

The d_{25}-$C_{12}E_3$ / hPBd films were also heated to 125 °C in the same way to d_{25}-$C_{12}E_5$ / hPBd films in chapter 6. The reflectivity profiles for samples at 125 °C have been plotted against the reflectivity profiles for samples at 55 °C in Fig. 7.6. From these profiles, it can be seen that there is very little difference between the samples at different temperatures. This is in agreement with previous measurements, where the key differences observed within d_{25}-$C_{12}E_5$ samples (Fig.

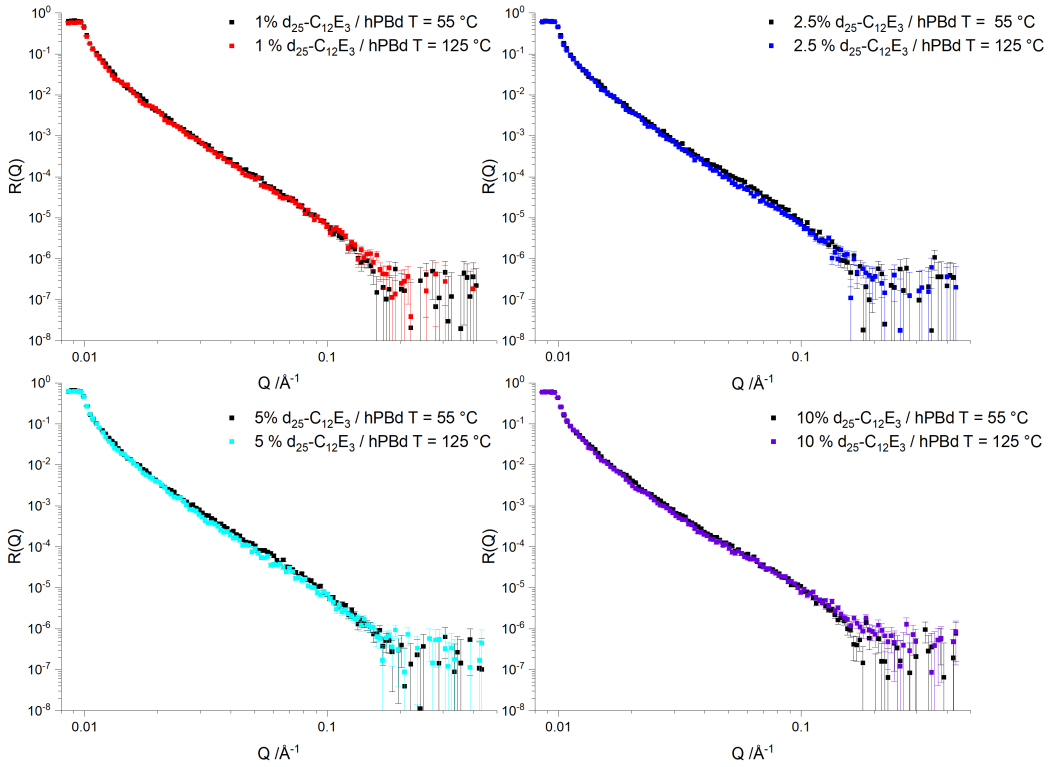

Figure 7.6: Reflectivity profiles of 1, 2.5, 5 and 10 % d_{25}-$C_{12}E_3$ / hPBd at 55 °C and 125 °C.

6.12b) were largely seen in the highest loading samples with the largest surface excess. The SLD profiles revealed that the d_{25}-$C_{12}E_5$ surface layer most likely evaporates at higher temperatures. This is not possible in d_{25}-$C_{12}E_3$ samples, where little surface enrichment is seen. Even though the smaller $C_{12}E_3$ molecule will be more volatile, as there is little surface excess initially, there is less scope for any change upon heating.

The SLD profiles of d_{25}-$C_{12}E_3$ in hPBd are shown in Fig. 7.7. From these profiles, it can be seen that there is a modest increase in the surfactant present at the film / silicon oxide interface. This suggests that as the temperature is increased, the surfactant is ejected from the film to the interfaces. It would be expected that this would also occur at the air interface, but little evidence is seen. This is likely due to the evaporation of surfactant from the surface, whereas evaporation is hindered at the silicon interface.

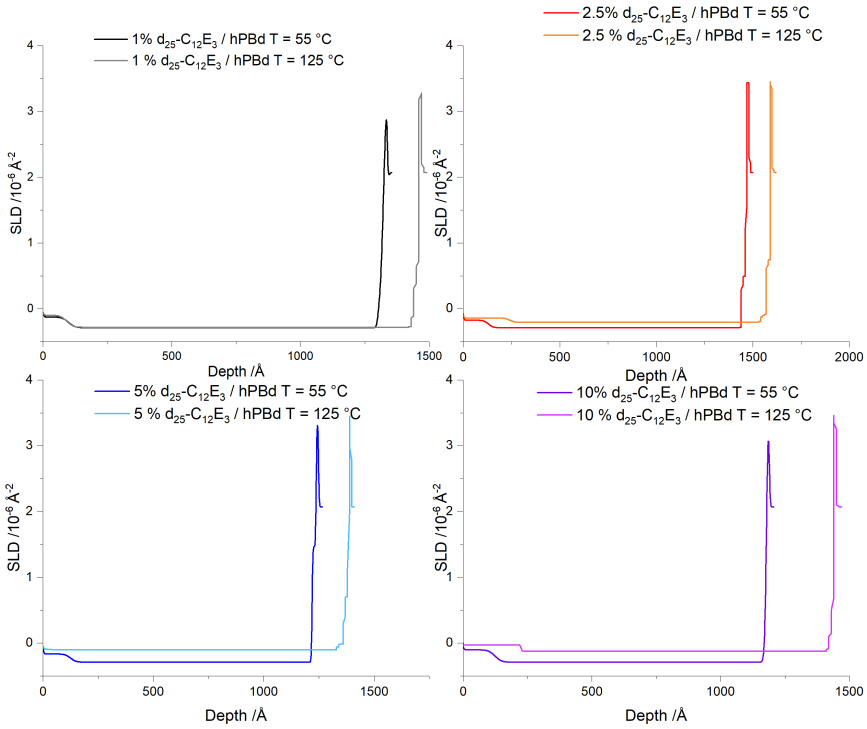

Figure 7.7: SLD profiles of 1, 2.5, 5 and 10 % d_{25}-$C_{12}E_3$ / hPBd films at 55 °C and 125 °C.

Table 7.1: Surface excesses calculated from SLD profiles of d_{25}-$C_{12}E_3$ and d_{25}-$C_{12}E_5$ in hPBd films at 55 °C as determined from NR profiles Fig. 7.2

Surfactant	z^* / Å			
	1 %	2.5 %	5 %	10 %
$C_{12}E_3$	3	3	3	5
$C_{12}E_5$	4	6	3	13

Samples containing d_{25}-DDAO in hPBd films have also been investigated using NR. The reflectivity profiles have been presented in Fig. 7.8. From this figure, it can be seen that there is little difference between reflectivity profiles at different surfactant loadings. Firstly, it appears that there are no high frequency fringes. As the high frequency Kiessig fringes arise from interference between reflection from the top and the bottom of the film, the absence of fringes indicates that there is very little reflection from the top of the film. This could be either because the film is extremely rough or because there is no surfactant at this surface. If the films are assumed to have a comparable roughness to films of the same polymer with a non-ionic surfactant, the absence of the fringes seen in $C_{12}E_5$ samples indicates that there is no enriched surface layer for d_{25}-DDAO / hPBd films. Furthermore, there is little difference in the low frequency fringe near 0.15 $Å^{-1}$. Whilst there is a small increase in the amplitude of the fringe between loadings, there appears to be no correlation between loading and the fringe amplitude, suggesting that there is no effect of loading on the buried layer SLD. The lack of any change in fringe position also appears to confirm that there is little change in the buried layer thickness either. The thickness of this buried layer ($\sim$ 25 Å) is comparable to the thickness of a DDAO monolayer ($\sim$ 20 Å),[159] which suggests that a monolayer is also present in these films.

Figure 7.9 shows data for 2.5 % *d*-DDAO in hPBd which has been fitted with a model containing no surface layer. This suggests that there is either no surface layer present or it is not possible to resolve with NR. This may mean that there are domains or droplets of surfactant on the surface as these would not be identified as a distinct layer in NR. This would be consistent with previous work, where neutron-invisible (where incomplete coverage leads to no distinct layer detectable by NR) d_{25}-$C_{12}E_5$ droplets have been identified on the surface of *cis*-PI.[201]

AFM images of the surface of these films have been collected (Figs. 7.10, 7.11, 7.12 and 7.13). These images show a similar crystalline surface structure as the hPBd surfaces seen in chapter 6. Interestingly, when the roughness parameters are calculated, Table 7.2, there appears to be no distinct change in surface roughness: both R_q and $R_{\max}$ show no correlation between loading and roughness parameters.

Furthermore, there is no difference in R_{SA} values with DDAO loading despite the presence of distinct surface features. Therefore, it would be expected that these surface features would not generate any Cassie-Baxter wetting. This is a wetting model where air pockets are trapped underneath the droplet between surface asperities. This leads to a larger contact angle due to the introduction of air-liquid interface into the contact area. One possible hypothesis for how surfactant in distributed is that the surfactant accumulates in the troughs in the surface, producing a mixed layer in NR and yielding a smoother surface. If surfactant was migrating to the surface, it would be expected that the surface roughness may decrease with surfactant loading as more of the depressions in the surface are occupied by the surfactant. This decrease in roughness has also been observed in polypropylene as an amide slip additive migrates to the surface.[202] As this does not occur, it is likely that there is little surfactant present at the surface.

It must be noted that each crystalline domain in the surface height maps appears to have a significant peak. These are present at all loadings and do not appear to change in abundance with surfactant loading. However, these are not consistently seen in films without surfactant (Fig. 6.15) or with other surfactants (Figs. 6.16a and 6.17). This suggests that these peaks are caused by the presence of DDAO. These surface features have been analysed in Fig. 7.14b and the widths and heights have been been reported in table 7.3. From these parameters, it can be seen that the heights of these features range between 26 and 50 nm. The length of a DDAO molecule has been calculated to be approximately 13 Å when in a lamellar phase,[203] meaning that if the feature is DDAO, it is between 20 and 40 molecules thick. Furthermore, the features are far wider than they are tall, with widths approximately 20 times greater than the height. This seems to suggest that the features are dome-like surfactant domains on the surface of each crystalline domain. These features only cover approximately 5 % of the surface, which is invariant across all surfactant loadings. It is also worth noting that 5 % surface coverage with a thickness of 26 nm implies that there is enough surfactant at the surface to be equal to a layer of pure surfactant that is approximately 1 nm thick. This is only possible for a 1 % film that has a thickness which is at least

1000 Å. This is in agreement with the NR fit shown in 7.9. This would justify the absence of a surface-enriched layer in NR: this is too little surface coverage to produce a recognisable interface in NR and instead may simply appear as a rough surface.

Dome-like surfactant features have been observed in latex films.[204] Within this work, the surfactant was shown to evolve over time, progressing from a uniform layer, to small, flat droplets and finally to hemispherical "blobs". However, no evolution is seen within hPBd / DDAO samples. Instead, it is likely that any evolution of the surfactant structure has occurred before the recording of these images. Additionally, the droplets observed in the work by Tzitzinou *et al.*[204] are significantly larger than the features observed in the films in this work, with droplets having widths on the order of several microns. Latex typically has much lower degrees of crystallinity than hPBd and so it is expected that the migration of surfactant within a latex film would be much quicker, allowing larger droplets to form.

Contact angle data has been collected for DDAO / hPBd films. This is given in Fig. 7.15. From these results, it can be seen that none of the films show similar wetting behaviour to $C_{12}E_5$ or $C_{12}E_3$ / hPBd films at higher loadings. Instead, the contact angle remains large, suggesting that there is little effect observed from any surfactant at the surface. This means that either the features observed are not distinct surfactant droplets or there is still insufficient surfactant at the surface to induce a decrease in surface energy.

DDAO has been shown to form moderately enriched surface layers in polymer films, with Fong *et al.* reporting a 1 – 2 nm layer over a broad range of concentrations in PVA.[159] However, the PVA matrix in these samples is much more hydrophilic polymer than hPBd. DDAO has a much smaller head group than the polyoxyethylene alkyl ether surfactants, and as this means that a larger proportion of the surfactant molecule is hydrophobic, it is reasonable to infer that DDAO is also more compatible in the hydrophobic hPBd film and so little surface segregation occurs.

As surface energy has previously been considered to be a key driver for surface

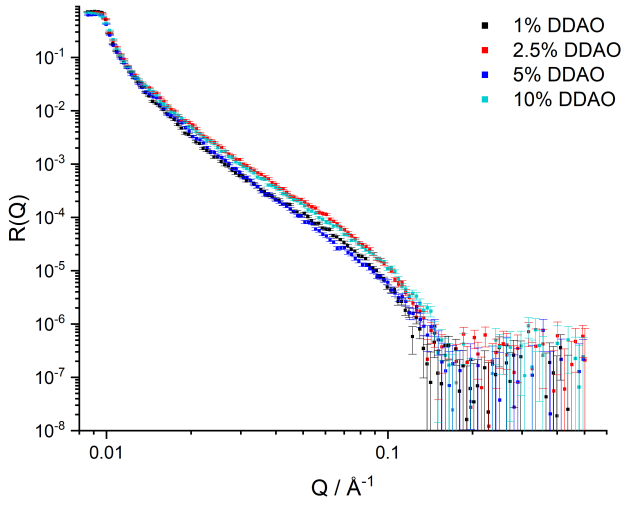

Figure 7.8: Reflectivity profiles of 1 – 10 % d_{25}-DDAO in hPBd at 55 °C. Data have been plotted without an offset to facilitate easy comparison.

Table 7.2: Roughness parameters of 1 – 10 % DDAO / hPBd films calculated from the height maps in Figs. 7.10, 7.11, 7.12 and 7.13.

DDAO loading / % wt	R_q	$R_{\max}$	R_{SA}
1	9.40	6.00	1.00
2.5	4.61	3.55	1.00
5	8.00	5.62	1.00
10	3.24	1.80	1.00

segregation, the surface tension of the surfactants should be compared. Whilst there is little work discussing the surface tension of surfactants in polymers, there is work discussing their CMCs in water. It has been shown that $C_{12}E_5$[205] has a much lower CMC than DDAO,[206] indicating that $C_{12}E_5$ is much more surface active than DDAO. Therefore, it would be expected that $C_{12}E_5$ would form a more enriched surface layer than DDAO if surface energy is a key driver for segregation. No DDAO surface layer is seen in this work, which appears to agree with the hypothesis that surface activity drives surface segregation in these samples.

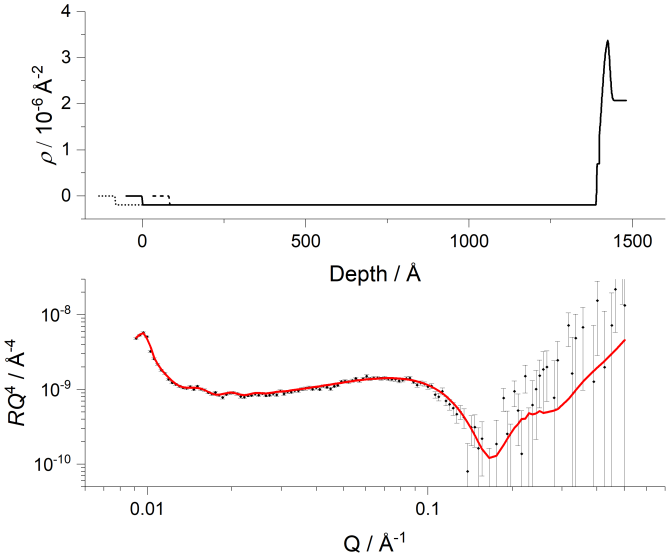

Figure 7.9: Top: SLD profile for 2.5 % DDAO in hPBd with no surface excess present. A small surfactant layer has been included in this model near the silicon interface. Bottom: Plot of RQ^4 vs. Q with the reflectivity profile generated from the model above in red and the experimental data for 2.5 % DDAO in hPBd plotted as data points.

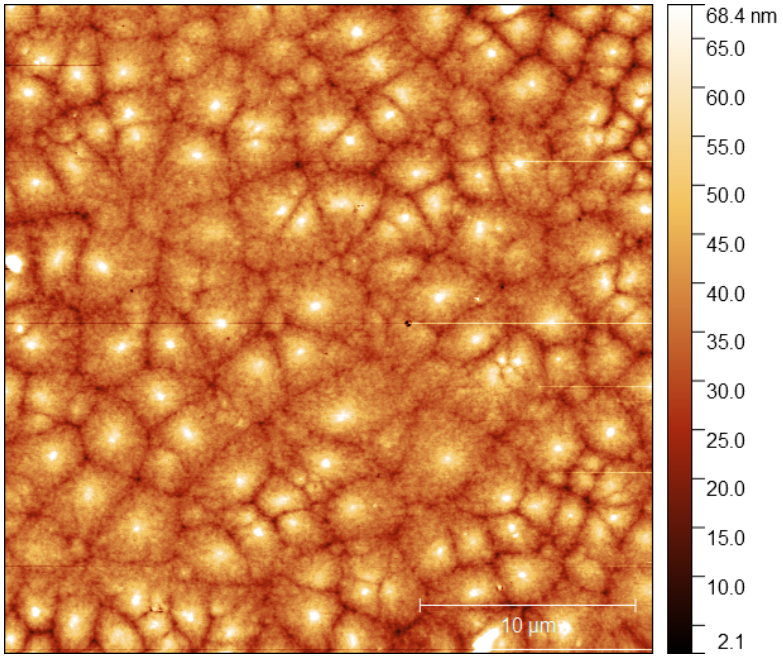

Figure 7.10: AFM height map of 1 % DDAO / hPBd at 20 °C.

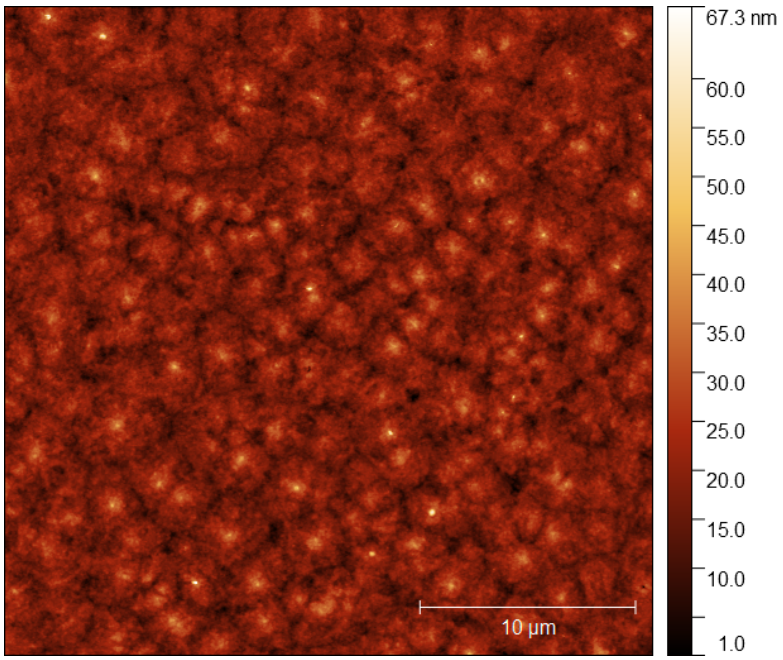

Figure 7.11: AFM height map of 2.5 % DDAO / hPBd at 20 °C.

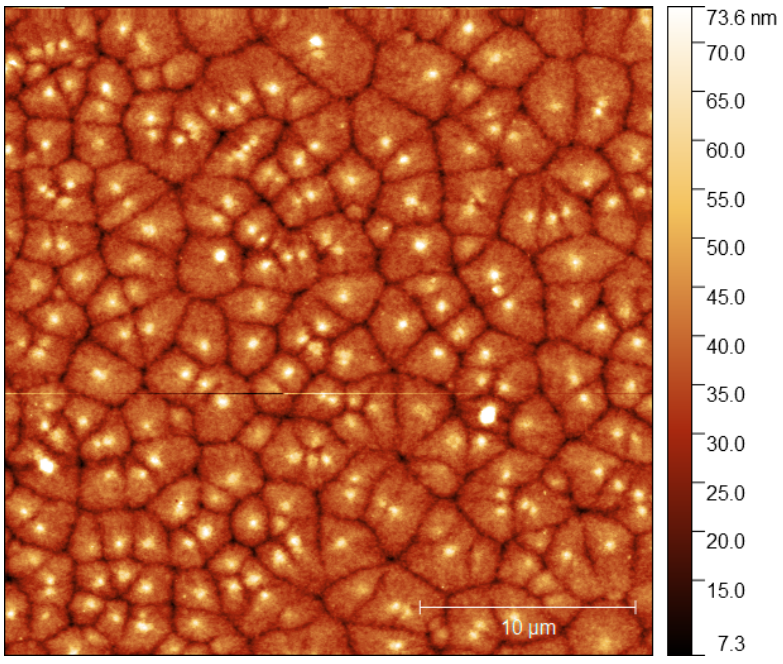

Figure 7.12: AFM height map of 5 % DDAO / hPBd at 20 °C. The same scale has been applied as the height map in Fig. 7.10.

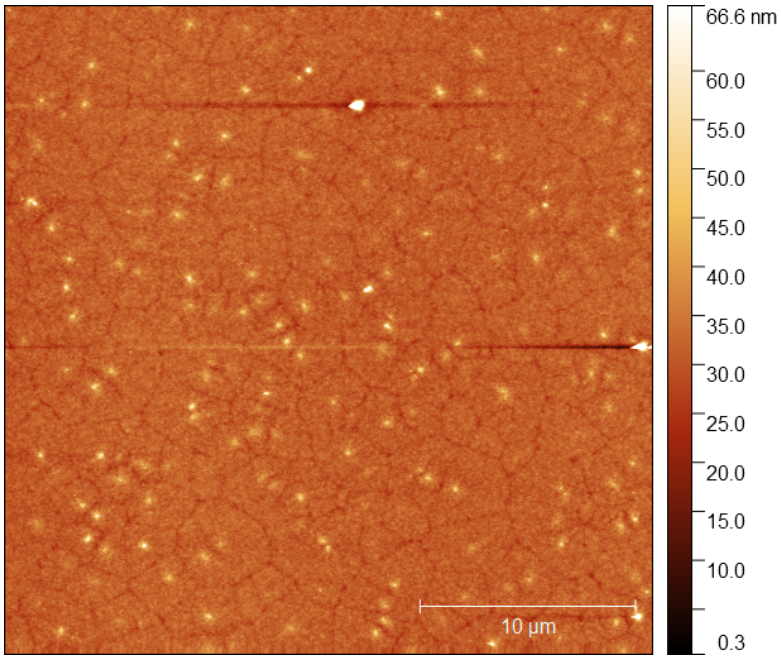

Figure 7.13: AFM height map of 10 % DDAO / hPBd at 20 °C. The same scale has been applied as the height map in Fig. 7.10.

Table 7.3: Height and widths of peaks found in Fig. 7.14a, calculated from the cross-sections given in Fig. 7.14b

line number	height / nm	width / nm
1	44	879
2	36	838
3	50	740
4	42	878
5	26	683

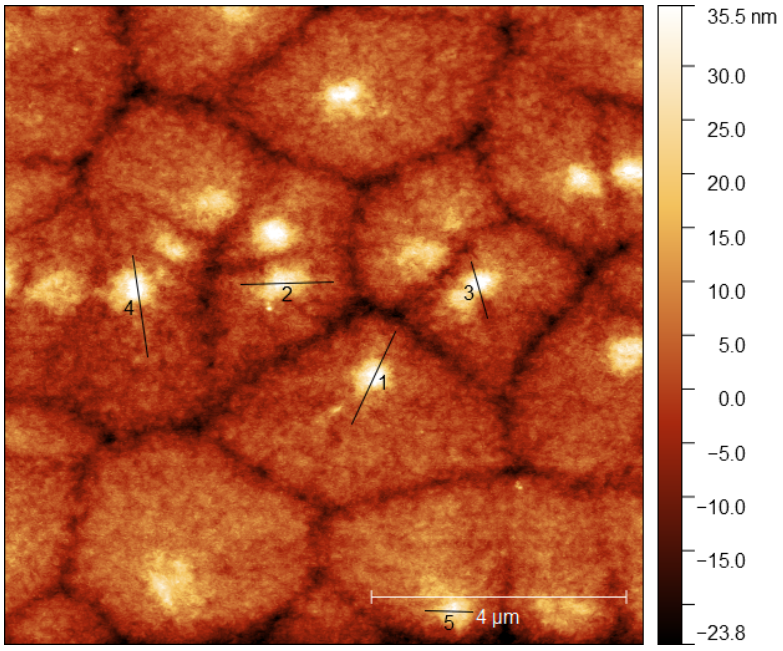

(a)

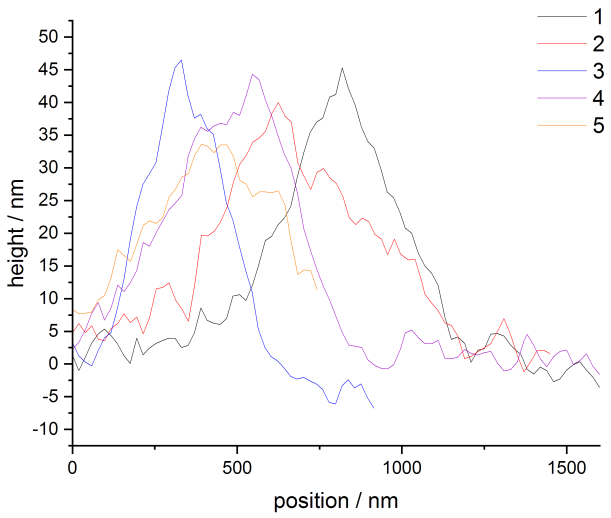

(b)

Figure 7.14: (a) 10 μm x 10 μm scan of the same 5 % DDAO / hPBd sample shown in Fig. 7.12. (b) Cross-sections along lines shown in Fig. 7.14a.

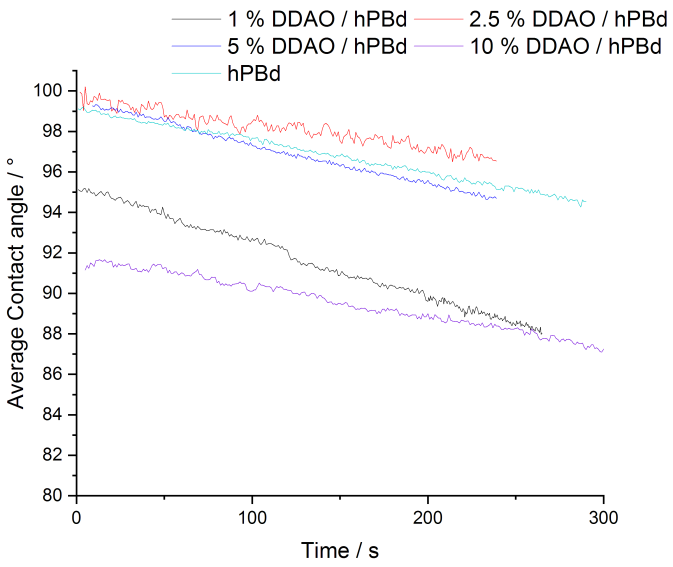

Figure 7.15: Contact angle measurements of a probe droplet of water for 1 – 10 % DDAO in hPBd. The data are plotted as a function of time, where t=0 is the time that the probe droplet is placed on the surface.

7.2.2 Effect of Surfactant Head-Group Size on Surface Properties of polymer films

The surface properties of spin-cast films of hPBd containing $C_{12}E_5$, $C_{12}E_4$ and $C_{12}E_3$ shall be compared in order to understand how the head-group influences the distribution of surfactant within amorphous polymers.

The contact angle of a droplet of water on the surface of surfactant / hPBd films are shown in Figs. 7.16 and 7.17. From these plots, it appears clear that there is little change in contact angle between 1 and 5 % for $C_{12}E_3$ samples. This is in good agreement with the NR results reported in the section above: there is little enrichment in surfactant at the surface and correspondingly, the film presents a hydrophobic surface. It must be noted that the contact angle decreases over time in all low concentration samples. This is likely to be contact angle hysteresis caused by the evaporation of the water: as volume of the droplet decreases, the contact angle decreases as it recedes.[207] In future work, this may be eliminated by the use of non-volatile liquids. An appropriate substitute for water would be an ionic liquid, these materials will not evaporate but are still polar. Furthermore, the use of additional solvents would give the capability of determining the surface energy of the films.

5 and 10 % loadings show different behaviours for each surfactant. 5 % $C_{12}E_3$ films show similar behaviour to 1 and 2.5 % loadings, with no evidence of the droplet wetting the surface. However, 5 % $C_{12}E_4$ shows a moderate decrease in contact angle over time. This appears to suggest that as the head group size is made larger, the surfactant is more responsive to the presence of a droplet of water. This change in surface hydrophilicity is likely caused by either the segregation of more surfactant to the surface, migration of the surfactant from the surface to the droplet or that the surfactant at the surface is more hydrophilic in the case of $C_{12}E_4$ than $C_{12}E_3$. The second possible mechanism is a consequence of the Young equation (equation 3.18):[208] the migration of surfactant into the droplet decreases γ_{LG}, leading to an increase in $\cos\theta_C$ (and thus a decrease in θ_C). Therefore, the movement of surfactant into the droplet and on to the water / air interface lowers

the contact angle of the droplet and allows it to spread.

10 % surfactant loadings for each surfactant show quite different behaviours. $C_{12}E_4$ shows a rapid decrease in contact angle, with the probe droplet wetting the surface in a few seconds. However, $C_{12}E_3$ shows a much slower decline, with a final contact angle of approximately 60° only being achieved at timescales longer than 200 s. This appears to show some agreement with the NR results reported above: the surfactant with the longer head group shows more surface enrichment and so the lowering of the contact angle occurs much more quickly. $C_{12}E_3$ must first migrate to the film surface and can only then lower the surface energy of the water / surface interface.

DDAO has an even smaller head group than $C_{12}E_3$ and this shows even less hydrophilicity in contact angle results, Fig. 7.15. This is surprising since Kocherbitov and söderman[209] have shown that DDAO interacts more strongly with water than some non-ionic surfactants. Unlike the other surfactants, at no loading measured is a decrease in contact angle observed. This is also in agreement with the hypothesis that a smaller head group produces much less surface enrichment and thus a much lower decrease in contact angle.

Previous work has shown that $C_{12}E_5$ and $C_{12}E_3$ can form significantly different self-assembled structures. Investigations of the surface structure of $C_{12}E_3$ in aqueous solution on a graphite surface revealed that the surfactant forms hemicylindrical micelles at the graphite surface.[210] Above the critical wetting concentration, further surfactant formed bilayers above the hemicylindrical micelles. Contrastingly, $C_{12}E_5$ has been shown to form continuous bilayers above 21 °C on mica surfaces.[162] This shows that the structure of the surfactant is important in defining the self-assembled structures at the surfaces as well as in solution. The difference in behaviour seen in these surfactants is likely caused by the difference in relative size of the head and tail groups of each surfactant. $C_{12}E_5$ has a head and tail group that are of similar lengths, whereas the tail group is much longer than the head group in $C_{12}E_3$.

The difference in surface properties is likely caused by the compatibility of the additive within the matrix. While there is little work discussing how the variation

in the size of the hydrophilic group of the surfactant affects segregation, there is some work discussing the effect of the hydrophilicity of the matrix. Squillace *et al.*[100] discussed how the segregation of an additive is affected by the degree of hydrolysis of a poly(vinyl acetate) (PVAc) matrix. As the degree of hydrolysis increases, the compatibility of a nonpolar additive decreased. Octanoic acid was shown not to segregate within PVAc with no hydrolysis, but some segregation was shown within highly hydrolysed PVAc. However, for a more polar additive, the opposite trend is exhibited. In this article, the matrix hydrophilicity is changed, which produces a similar change in compatibility to variation of the head group and thus supports the observation in the present work that increasing head group size (and thus incompatibility) increases surface segregation.

Whilst in this work the water solvent is replaced with a hPBd matrix, the previous work infers that the structures formed for the two surfactants at the polymer surface may be different.[162,203] This would rationalise the difference in surface behaviour: the $C_{12}E_5$ and $C_{12}E_4$ samples show much more uniform layers of surfactant, with distinct bilayers at the surface which may reorganise much quicker to allow surface wetting of the water droplet. The $C_{12}E_3$, however, may instead form similar hemicylindrical micelles, which may have to instead reorganise to form a uniform layer on the surface upon droplet contact. Furthermore, this may also justify the absence of a thick layer in NR: if the distribution within the layer is not uniform, it may be undetectable by NR.

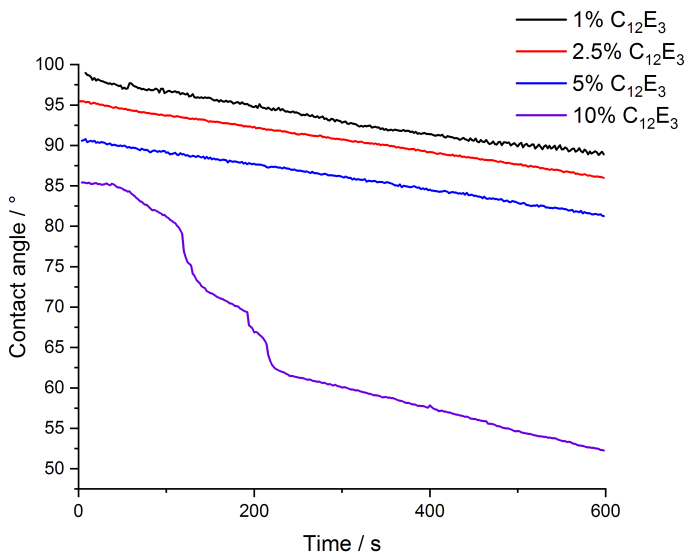

Figure 7.16: Contact angle measurements of a probe droplet of water for 1 - 10% $C_{12}E_3$ in hPBd. The data are plotted as a function of time, where $t = 0$ is the time that the probe droplet is placed on the surface.

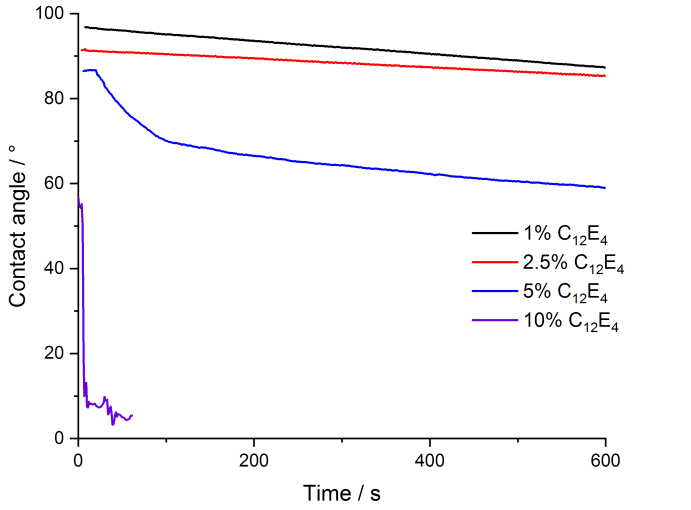

Figure 7.17: Contact angle measurements of a probe droplet of water for 1 - 10% $C_{12}E_4$ in hPBd. The data are plotted as a function of time, where $t = 0$ is the time that the probe droplet is placed on the surface.

7.3 Chapter Conclusions

The effect of varying the head group size on the behaviour of a surfactant within a hPBd film has been assessed within this chapter. This work has shown that $C_{12}E_5$ and $C_{12}E_3$ show quite different surfactant distributions within the same matrix, with $C_{12}E_3$ presenting a much smaller degree of surface enrichment. This has been attributed to the higher compatibility of surfactants with smaller head groups with hPBd. This greater compatibility has been observed in both rheology compatibility studies (chapter 4) and is expected on the basis of Flory-Huggins theory. Higher compatibility means that it is more thermodynamically favourable for the surfactant to remain mixed within the bulk and so little surface enrichment occurs for surfactants with smaller head groups.

Contact angle measurements also appeared to confirm that little surfactant was present at the surface in $C_{12}E_3$ / hPBd samples, or what $C_{12}E_3$ was at the surface had little impact on hydrophilicity. These samples showed little hydrophilicity at loadings lower than 10 %, in agreement with the observations that there is little surface enrichment. However, it was seen that in at 10 % $C_{12}E_3$ samples, the contact angle showed a decrease over approximately 200 s after the initial contact of the droplet. This was much slower than the decrease observed in $C_{12}E_5$ / hPBd and $C_{12}E_4$ / hPBd films, where the contact angle decreased rapidly upon placement of the droplet on the surface. This has shown that the arrangement of $C_{12}E_3$ at the surface in a structure which increases the wetting behaviour of a water droplet must take longer than that of $C_{12}E_5$ and $C_{12}E_4$. Since it would be expected that $C_{12}E_3$ could migrate through hPBd at least as quickly as, and probably faster than the larger homologues, this could also imply that the more rapid change in contact angle is due to surfactant that is already at the surface. The difference in surface behaviour has been related to previous work that has shown that $C_{12}E_5$ and $C_{12}E_3$ can form different structures at surfaces. From these different structures, it has been proposed that the surface structure of $C_{12}E_3$ require a more extensive organisation to allow a reduction in the contact angle.

The distribution of DDAO has also been investigated by NR and it has been

shown that little surface enrichment can be seen at any surfactant loadings. This is in reasonable agreement with previous work, where a much smaller degree of surface enrichment was seen in other films.[159] However, AFM images showed some possible evidence for surface features of DDAO. These consist of small surfactant droplets covering a small proportion of the surface. It must be noted that contact angle data presents little evidence of this surface enrichment with the contact angle remaining high and showing no change throughout the duration of experiments. Further work is required to confirm that these droplets are surfactant, with NRA experiments required to identify DDAO at the surface that does not form a homogeneous layer.

The lack of evidence for surface enrichment is somewhat surprising when compared to the the other surfactants: DDAO has the lowest surface energy of any of the surfactants and surface energy has previously been considered to be a key driver for surface segregation. However, it has instead been proposed that DDAO is more compatible than $C_{12}E_3$ or $C_{12}E_5$ in hPBd and thus there was a weaker driver for surface segregation.

Chapter 8

Effect of Shear Forces on Surfactant Behaviour in Polymer Melts

8.1 Chapter Introduction

In previous chapters, the behaviour of a surfactant within a solution-cast film has been studied. However, during manufacture of final products, these polymer blends are commonly processed in the melt. During this processing, the blend is put under a wide range of shear forces; whilst much work has been performed to investigate the distribution of additives under quiescent conditions, a much smaller body of work has considered the effect of shear on additive segregation.[211–213]

Within this chapter, a relatively novel technique shall be used to probe the distribution of small additive molecules in a polymer under flow, Rheo-NR. This is a technique involving the depth profiling of samples using neutron reflectivity whilst applying a controlled shearing force via a rheometer.

The use of a rheometer within a neutron beam is well established, with previous work demonstrating the use of a Couette cell in small-angle neutron scattering (SANS) experiments.[214,215] This work has demonstrated that it is possible to use neutrons with samples under shear and determine the bulk structure and the effect

that flow has on this. However, these experiments are performed using a Couette cell, a sample geometry which cannot be used to study composition versus depth distribution under flow: a smooth, flat surface is required and a Couette cell only presents cylindrical interfaces. Instead, a plate geometry is required along with neutron reflectometry.

Whilst both NR and rheometry are well established techniques, the combination of the two is a relatively new approach.[216] The use of a rheometer within a neutron beamline has previously been used to study other forms of soft matter such as tethered polymers in polymer melts,[217] the adsorption of asphaltenes (high molecular weight crude oil resins) to surfaces under shear[218] and the crystallisation of solids within food-based matrices.[219] These experiments, whilst using very different materials to those used within this work, present strong evidence of the utility of this promising technique in understanding the phenomena of migration and segregation within hydrophobic polymers. Specifically, neutrons have good depth penetration, with an appropriate depth resolution for molecular scale and can also be used with opaque materials.

Rheo-NR shall be used in this chapter to probe the behaviour of $C_{12}E_5$ within a deuterated hexadecane solution at the oxide interface of a silicon substrate. In this work, it is necessary to use a hydrogenous surfactant and a deuterated matrix unlike in previous chapters. This is due to the contrast requirement between the silicon oxide and any enriched layer at the interface. The neutron beam is brought up through a silicon block (SLD $= 2.06 \times 10^{-6}$ Å^{-2}) and is reflected at the interface between a solution and the silicon block. The solution is sheared by a cone-plate geometry in which the block is the plate (Fig. 8.1). A deuterated solvent or polymer matrix is necessary in order to obtain a critical edge in $R(Q)$. As a deuterated surfactant has a comparable SLD to the silicon oxide, it will not be possible to isolate each individual layer. However, if a hydrogenous surfactant is used, a much more significant contrast is obtained and any surface enriched layer can be identified with more certainty. Therefore, in order to provide contrast between an enriched layer and the bulk, a deuterated bulk material is required. It is difficult to either produce or fully deuterate polymers and so these can be

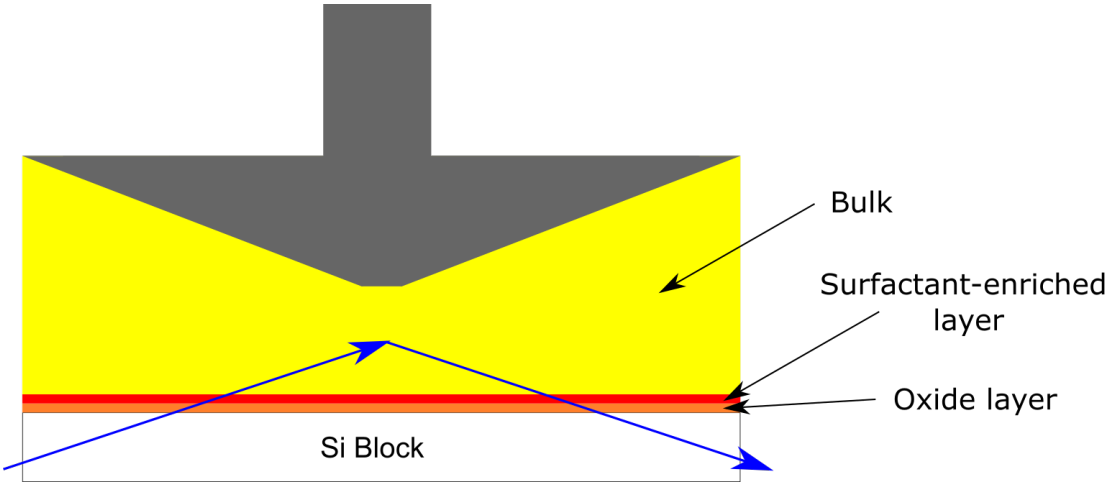

Figure 8.1: Diagram of the Rheo-NR experiment. The path of the neutron beam is shown by blue arrows and the rheometer cone is shown in grey. Layer thicknesses are not to scale.

too difficult to acquire according to the specifications required for the experiment such as the desired molecular weights or dispersities.[220] Instead an analogue, a deuterated non-polar solvent (d-hexadecane) has been selected.

8.2 Experimental setup and NR Fitting Strategy

There are some key differences between the experiments conducted in this chapter and those performed in the previous chapters. Firstly, due to the presence of the rheometer, there is no film / air interface for the neutron beam to be incident upon. Furthermore, as steel is somewhat opaque to neutrons, the beam cannot be transmitted through the rheometer plate. Instead, the neutrons are incident upon the film through the silicon block. This means that the SLD of the "fronting" is now much larger than in air and with a hydrogenous bulk would result in no critical edge, rendering fitting much more difficult. Therefore, the use of a deuterated bulk material is used as this has a higher SLD than the silicon block.

Fig. 8.2 shows the $R(Q)Q^4$ for a 1.5 % $C_{12}E_5$ in d-hexadecane. The peak at $Q \sim 0.01$ Å^{-1} corresponds to the critical edge in this data representation. As a

first step to interpreting these data, it is helpful to calculate what the reflectivity from a homogeneous mixture of the surfactant and the solvent would look like, shown in red in Fig. 8.2. In fitting the data, the aim is to represent the true physical composition profile with a minimum number of discreet layers, whose SLD and thickness dictate the form of $R(Q)$. This profile shows how it is not possible to fit the data with only an oxide layer. Instead, it is necessary to introduce layers with a lower SLD between the oxide layer and the bulk. This lower SLD can only be achieved by introducing hydrogenous material into the model in the form of $C_{12}E_5$.

The presence of a highly-enriched hydrogenated layer is justified in the simulated profiles shown in Fig. 8.3. The profile with only one layer of low $C_{12}E_5$ enriched enrichment shown in blue contains a bulge and depression between 0.02 $Å^{-1}$ and 0.1 $Å^{-1}$ that is not present within the experimental reflectivity data. It is not possible to fit this feature to the data without the introduction of a layer of lower SLD, implying enrichment in hydrogenous material (Fig. 8.4). Furthermore, inspection of NR profiles from previous chapters show that deuterated $C_{12}E_5$ shows enrichment at the silicon oxide interface in hPBd (Fig. 7.5) and thus it is possible for interfacial segregation to occur within blends containing $C_{12}E_5$.

The model used to fit the experimental data also contains an additional layer which has an SLD between the bulk and the interfacial layer Fig. 8.5). This is an additional layer that is enriched in surfactant to a lower degree than at the interface. Fig. 8.5 illustrates the need for this additional layer. Without this additional layer of decreased SLD, a peak arises near 0.07 $Å^{-1}$ that is not present in the experimental data. This can only be removed by making the enriched layer thicker. However, when this is done, the reflectivity becomes too large to fit the data, with a bulge appearing that prevents the simulated reflectivity profile matching experimental data. Therefore, it is necessary to include another layer with an SLD having an intermediate value between the enriched interfacial layer and the bulk.

Fig. 8.6 shows several simulated reflectivity profiles generated from SLD profiles with varying interfacial layer thicknesses. This demonstrates the effect of

changing this interfacial layer thickness, with the position of the minimum moving from lower to higher Q as the enriched layer thickness increases. This is accompanied by the appearance of a bulge at 0.03 Å^{-1} as the thickness is increased. Whilst this bulge is not observed in the experimental data, the large minimum seen in profiles with a thickness of 45 Å is also not present. However, with a thickness between these two values, it is possible to fit the data, reducing both the minimum and bulge to follow the curve of the data.

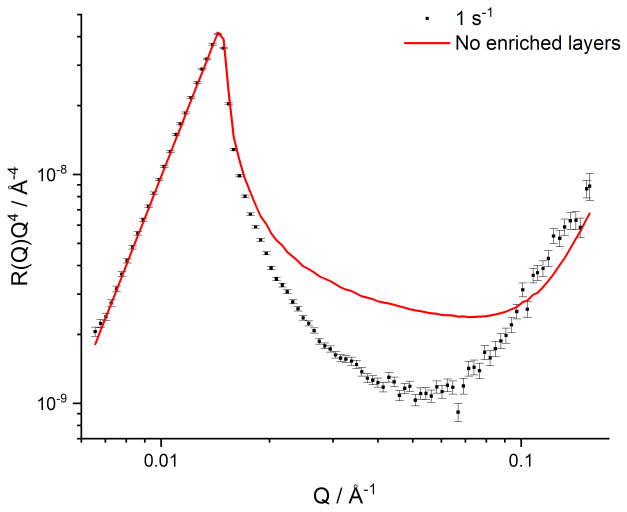

(a)

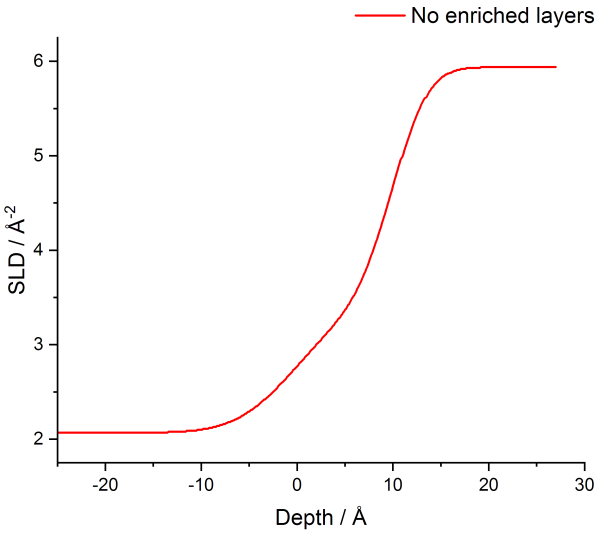

Figure 8.2: (a) NR profile of 1.5 % $C_{12}E_5$ in d-hexadecane under a 1 s^{-1} shear. Simulated reflectivity data are shown as solid lines. These data are simulated from an SLD profile containing no surfactant-enriched layers and only an oxide layer and bulk layer. (b) SLD profiles used to simulate reflectivity data above.

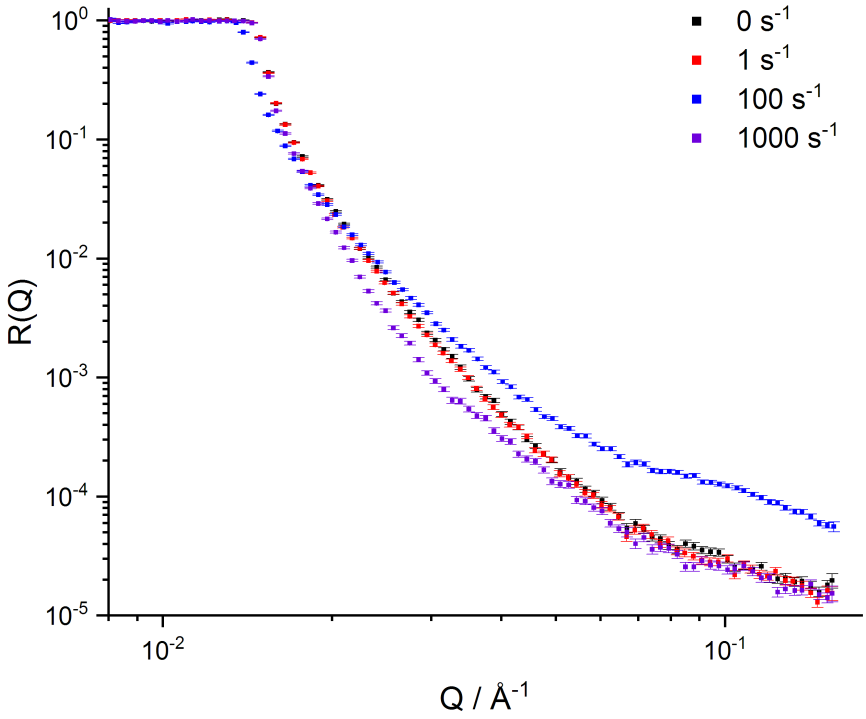

Figure 8.3: NR profiles of 1.5 % $C_{12}E_5$ in d-hexadecane at 20 °C. Samples are within a cone-plate geometry and are sheared at rates between 0 and 1000 s^{-1}.

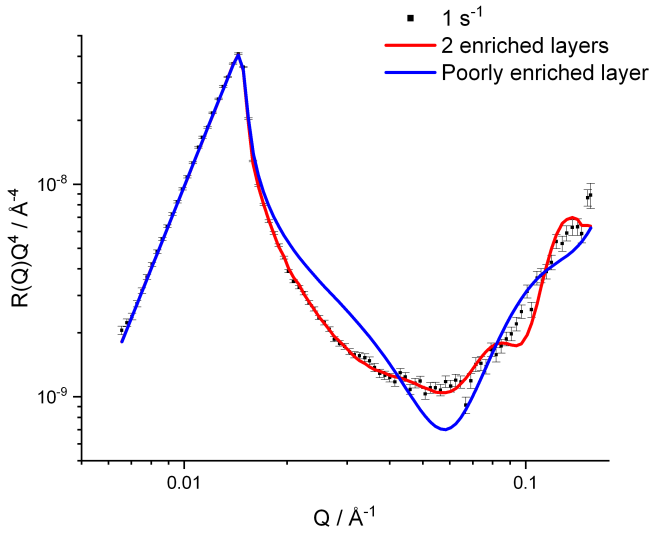

(a)

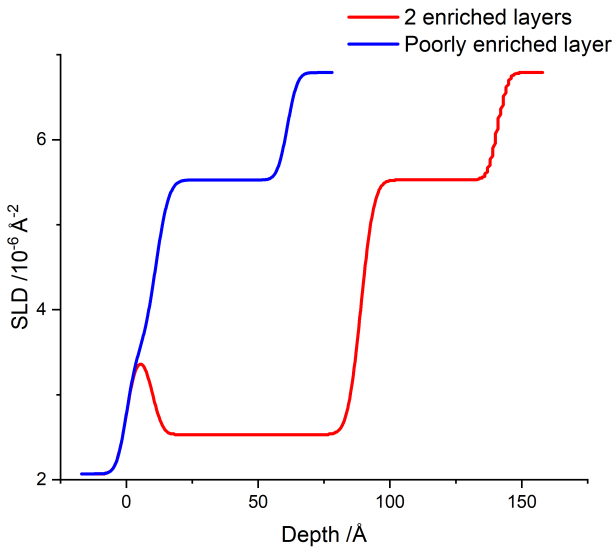

(b)

Figure 8.4: (a) NR profile of 1.5 % $C_{12}E_5$ in d-hexadecane under a 1 s^{-1} shear. Simulated reflectivity data are shown as solid lines. These data are simulated from two SLD profiles, with one containing two interfacial layers enriched in $C_{12}E_5$ and the other with only one poorly enriched layer. (b) SLD profiles used to simulate reflectivity data above. Note that the small peak near depth = 0 is the silicon oxide layer, which is only visible when the adjacent layer has a lower SLD.

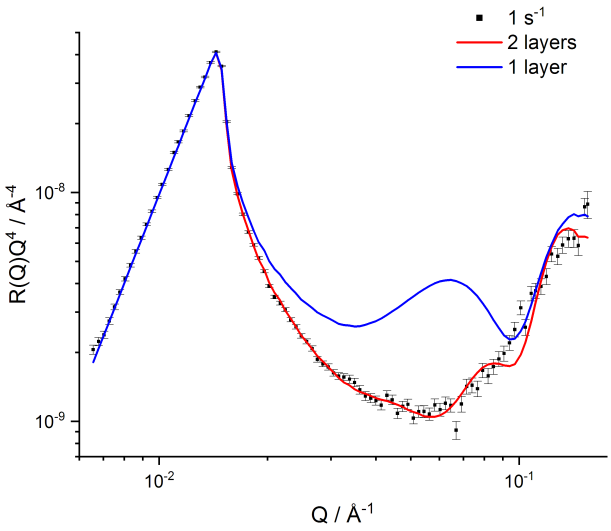

(a)

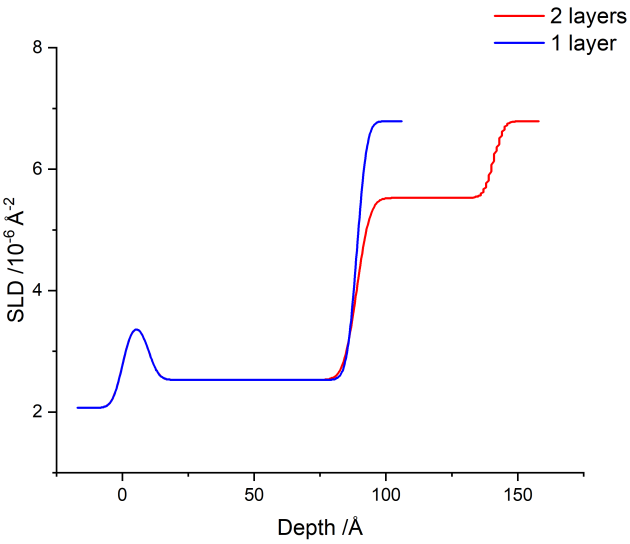

(b)

Figure 8.5: (a) NR profile of 1.5 % $C_{12}E_5$ in d-hexadecane under a 1 s^{-1} shear. Simulated reflectivity data are shown as solid lines. These data are simulated from two SLD profiles, the red line showing a fitted profile with two surfactant-enriched layers and the blue line with a single enriched layer (b) SLD profiles used to simulate reflectivity data above.

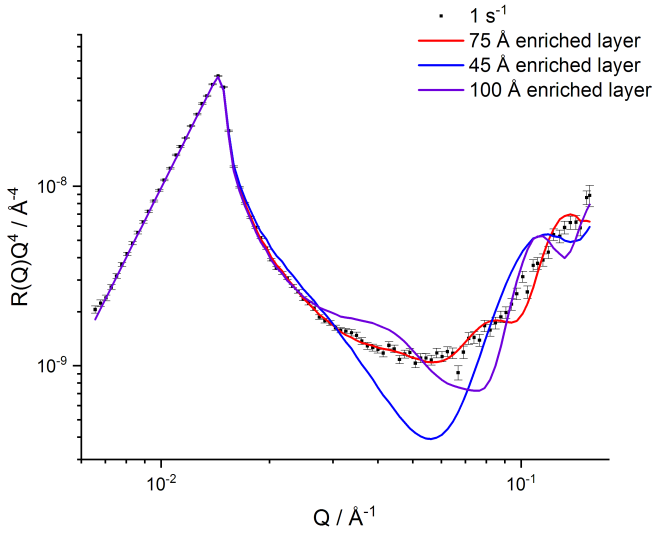

(a)

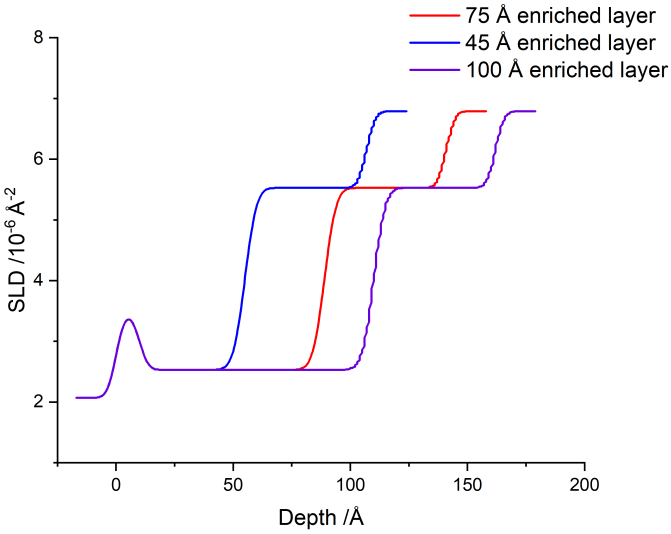

(b)

Figure 8.6: Reflectivity (a) and SLD (b) profiles of 1.5% $C_{12}E_5$ in d-hexadecane under a 1 s^{-1} shear with a range of enriched layer thicknesses.

8.3 Results and Discussion

NR reflectivity profiles for 1.5 % $C_{12}E_5$ in d-hexadecane at shear rates between 0 and 1000 s^{-1} are shown in Figs. 8.3 and 8.7. Initial inspection of these profiles reveals that there are significant similarities between the reflectivity data collected under 1 s^{-1} and no shear. However, there are some significant differences at higher shear rates, indicating that shearing has some effect on the surfactant distribution.

The reflectivity data can be fitted using using models containing a surfactant-enriched layer structure at the silicon oxide interface. These SLD profiles are presented in Fig. 8.8. These SLD profiles confirm the observation that the surfactant distribution at the interface under 1 s^{-1} and 0 s^{-1} shear are very similar. These profiles show there is a layer with a thickness of approximately 75 Å that is 64 % wt. $C_{12}E_5$. Adjacent to the interfacial layer, there is an additional surfactant-enriched layer that has a lower concentration of surfactant. The surface excess of these combined layers is 55 Å for both shear rates.

At higher shear rates, the surfactant-enriched layers change significantly. At 100 s^{-1}, the SLD of the enriched layer decreases further, indicating that the interfacial layer contains more surfactant than at lower shear rates. However, whilst this layer becomes more enriched, it also decreases in thickness. The surface excess does remain the same despite these changes in enrichment. This indicates that there is a stable interfacial layer which does not appear to remix with the bulk during shearing, in fact the extent of demixing on a local level increases with increasing shear rate.

The interfacial layer changes again at even higher shear rates. At 1000 s^{-1}, the SLD of the most surfactant-enriched layer increases, indicating that the surfactant loading decreases to 55 %. However, the total surfactant-enriched layer does become thicker and this leads to a modest increase in the surface excess (table 8.1). This suggests that larger shear rates provide a motivation for further surfactant to migrate out of the bulk and to the silicon interface. It is important to note that these shear rates are comparable to those observed within processing techniques such as injection moulding and extrusion which can often be as high as several

thousand s^{-1}.[221–223]

Fig. 8.9 shows the rheometry data that was measured alongside the NR measurements. It can be seen at low shear rates that the viscosity is quite unstable, the origin of which is unclear, but may arise from the very low torque and some problems with instrument mapping. However, it is still clear that the rheology shows an overall trend of shear thinning with increasing shear rate and that until the very highest shear rate, the viscosity does not decay with time. This latter point indicates that the sample remains intact within the geometry. Comparing the NR data and rheometry data (Fig. 8.3 and Fig. 8.9 respectively), it can be clearly seen that there is a significant difference in the NR profiles between 100 and 1000 s^{-1} that also correlates to the disappearance of oscillation in the rheometry data. Within the NR data, the 100 s^{-1} profile shows a change in the critical edge. This would be caused by a decrease in the fronting (silicon) SLD or an increase in the SLD of the backing (d-hexadecane bulk). It is not possible for the SLD of the silicon block to change between shear rates and the increase in SLD of the bulk layer would require a rapid increase in surfactant loading, which is also not possible between shear rates where the sample is not changed. Therefore, there must be some change within the sample which occurs at this shear rate, significantly affecting its rheological properties.

There is previous work which assesses the impact of shear forces on the behaviour of similar surfactants in a solvent. Kato *et al.*[224] have probed the behaviour of $C_{16}E_7$ in D_2O under shear flow. This work reveals that as the shear rate is varied, a change to the lamellar structure of the surfactant is observed. However, it is important to note that this may be a different structure to what is present in the samples in this work: the solvent has a significantly different polarity and many $C_{12}E_x$ surfactants display lyotropic behaviour, leading to a different structure at different concentrations.[114,225] This may be a similar process to what has been seen within the present work: the decrease in layer thickness that occurs at 100 s^{-1} may be caused by a rearrangement of the surfactant layer at the surface in response to the shear which leads to tilting of the molecules. It was also reported that during the rearrangement, the repeat distance of the structure de-

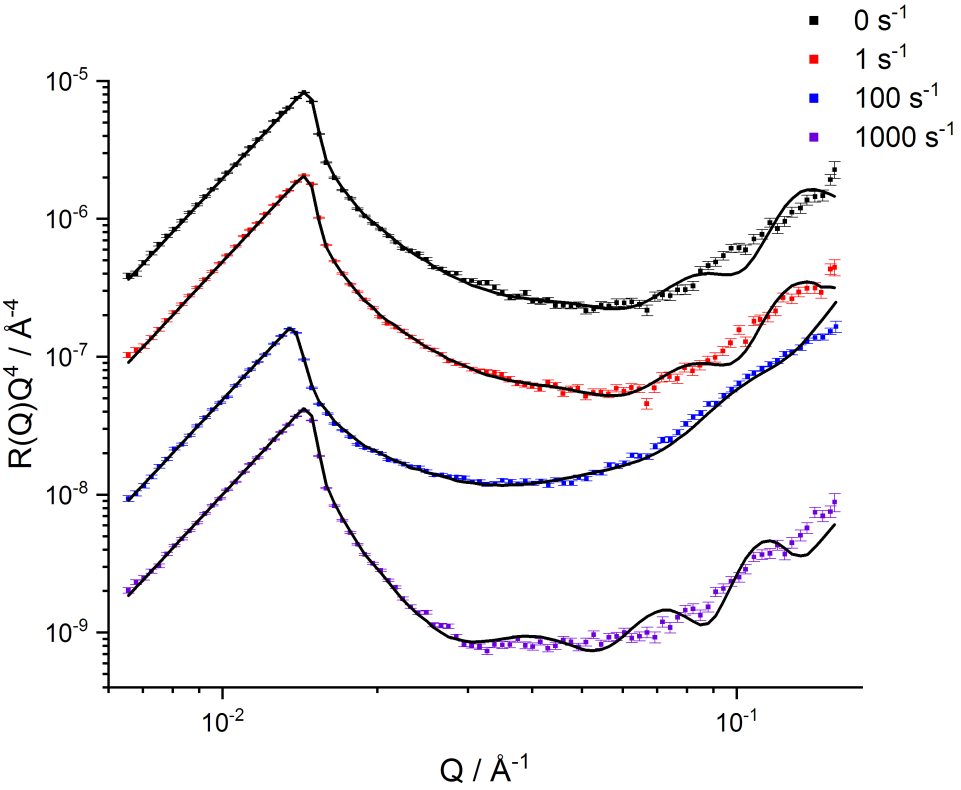

Figure 8.7: NR data and fits plotted as a function of $R(Q)^4$ at 20 °C. Samples are within a cone-plate geometry and are sheared at rates between 0 and 1000 s^{-1}. An offset has been applied to the 0 – 100 s^{-1} data series.

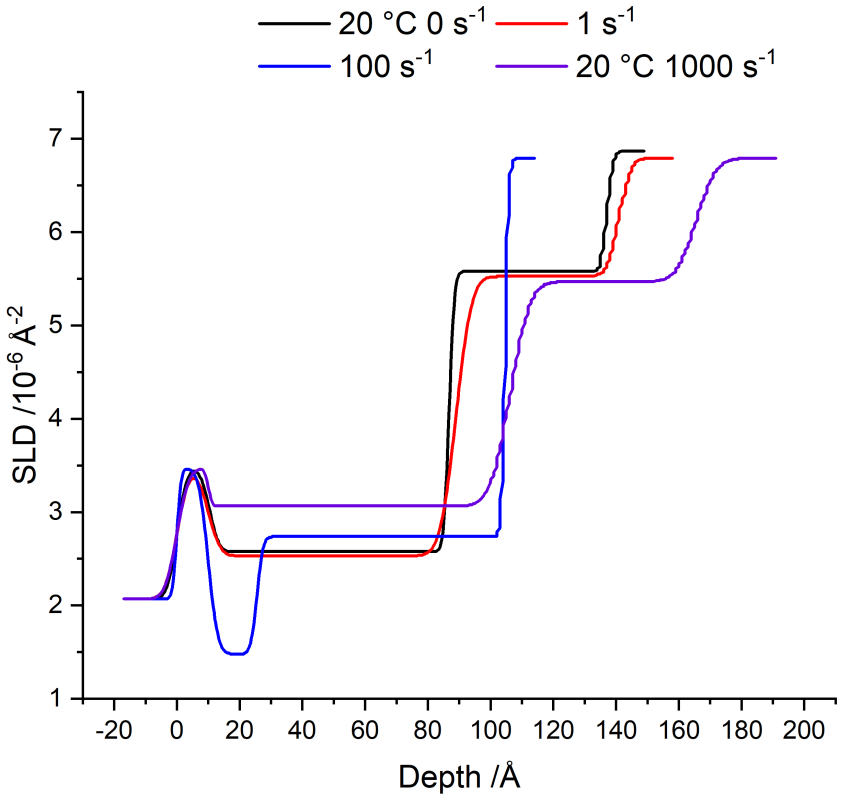

Figure 8.8: SLD profiles for 1.5 % $C_{12}E_5$ in d-hexadecane at 20 °C at shear rates between 0 and 1000 s^{-1}. SLD profiles are obtained from reflectivity profiles shown in Fig. 8.7.

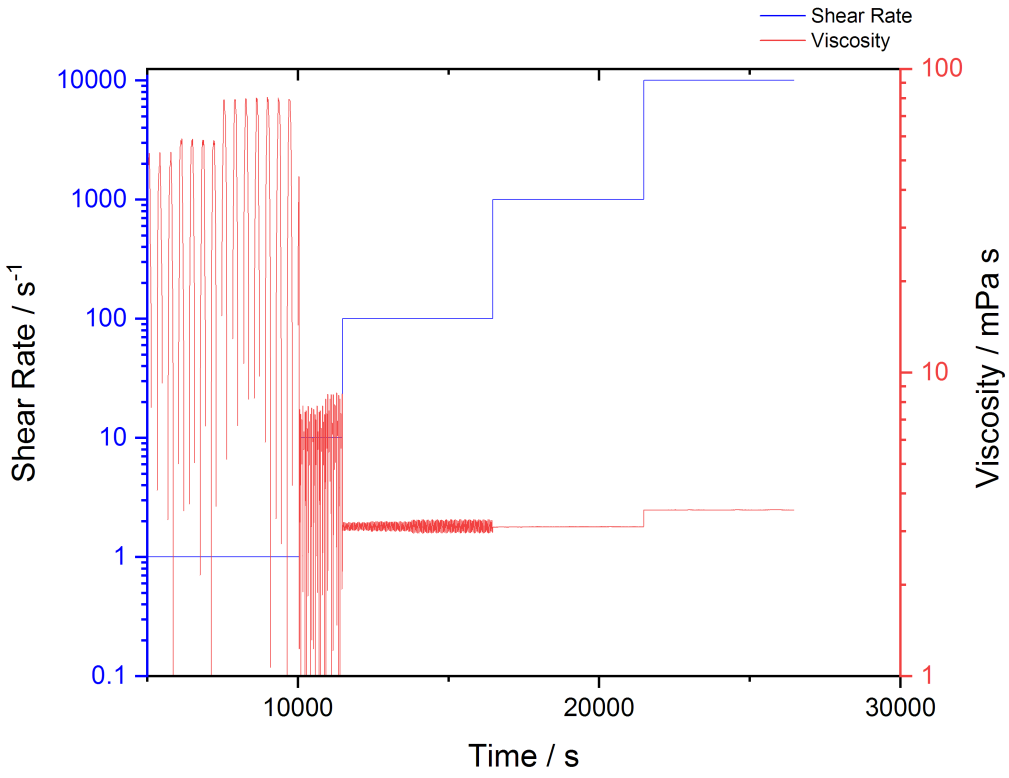

Figure 8.9: Viscosity and shear rate data collected for 1.5 % $C_{12}E_5$ in d-hexadecane at 20 °C. This data has been acquired during the NR measurements given in Fig. 8.7.

creases under shear,[224,226] which would also agree with the results in this present work.

Fig. 8.9 shows how the viscosity and shear rate of 1.5 % $C_{12}E_5$ in d-hexadecane during the rheo-NR experiment. It must first be noted that there is a large oscillation in the viscosity measurements at shear rates below 1000 s^{-1}. This is likely due to the torque limit of the instrument: at low shear rates, the shear stress of the blend is too low to be reliably measured. However, inspection of this data reveals that as the shear rate is increased, the viscosity of the sample decreases up to shear rates of 10000 s^{-1}. This is indicative of shear thinning behaviour. Previous work by Cardiel *et al.*[227] probing the effect of shear on micellar cetyltrimethylammonium bromide showed similar shear-thinning behaviour. This has been attributed to alignment of worm-like micelles within the solution, where under shear the worm-like surfactant micelles become oriented in the direction of the flow of the medium. Within previous chapters (chapter 5), strand-like structures have been observed in $C_{12}E_5$-containing polymers films and so it may be possible that these structures are also present within these $C_{12}E_5$ / hexadecane samples and that these strands are rearranging upon application of greater shear rates.

It is also important to consider another possible cause of loss of surfactant: the ejection of material out of the rheometer gap. This would lead to a decrease in the SLD of the layers as air is introduced to fill the space. It is also likely that this would be more common at higher shear rates, where the higher rotational speeds generate a greater centrifugal force. It is also possible that surfactant may be preferentially ejected from the rheometer gap, which would decrease the total surfactant loading within the blend. This can be a consequence of the edge-fracture phenomenon.[228,229] This is a process where cracks appear on a free surface of a liquid above a critical shear rate. This critical shear rate is where the second normal stress difference (the difference between the stress in the z-direction and r-direction as defined in Fig. 8.10) exceeds a value related to the surface tension of the liquid. As this second normal force increases with shear rate, ejection will occur more at higher shear rate. However, this selective ejection is unlikely when

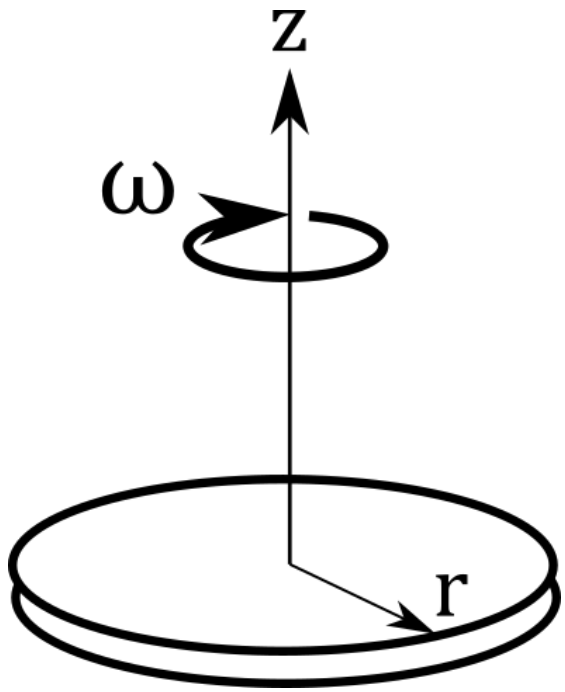

Figure 8.10: Diagram illustrating the directions of the stresses within the second normal force.

the surface excess is observed to increase at the highest shear rate and thus both hexadecane and $C_{12}E_5$ are likely ejected.

Fig. 8.11 shows the rheometry data of the same sample at 150 °C. This data shows similar behaviour at lower shear rates, with the same oscillation occurring in the viscosity data, confirming that the oscillation returns to the data after the sample is sheared at higher rates. Furthermore, at 10000 s^{-1}, the sample appears to show thixotropic behaviour, with the viscosity decreasing over time at constant shear rate. However, this is likely caused by the ejection of material from the rheometer. The absence of this apparent thixotropic behaviour in 20 °C data confirms that this ejection of material does not occur.

Table 8.1: Surface excesses calculated from SLD profiles of $C_{12}E_5$ in d-hexadecane under different shear rates. Data collected at 20 °C and 150 °C.

Temperature	z^* / Å				
/ °C	0 s^{-1}	1 s^{-1}	10 s^{-1}	100 s^{-1}	1000 s^{-1}
20	54	55	-	55	62
150	57	-	57	50	62

8.4 Surfactant Distribution Under Shear at Elevated Temperatures

Most polymer blends are processed in the melt, requiring high temperatures during extrusion. It is therefore of great interest to investigate how the surfactant behaves in blends when sheared at higher temperatures.

Fig. 8.12 shows the SLD profiles obtained by fitting NR data collected at 150 °C (Fig. 8.13). Unlike at lower temperatures, these depth profiles look remarkably similar to each other, with a similar SLD (and thus surfactant loading) in both the interfacial layer and second enriched layer. This appears to suggest that at higher temperatures, shear forces have less effect on the surfactant structure within these enriched layers.

If the SLD profiles are compared between temperatures, Fig. 8.14, it can be seen that the SLD of the interfacial layer decreases at all shear rates as the temperature increases. This indicates that the surfactant adsorption is enthalpically driven rather than entropically driven as might have been the case in an aqueous solution. However, the total thickness of the surfactant-enriched layers appear to remain similar. In chapter 6, the decrease in surface excess with increasing temperature was attributed to evaporation. In the confined geometry of the rheometer, this evaporation is impossible: the gap between the plates is 1 mm at the edge of the cone-plate geometry and the exposed surface area per volume of the sample is much lower than for much thinner films (several hundred nm thick, with a surface area of approximately 10 cm^2). Therefore, the temperature depen-

dence of the surface excess is more clearly dependent on the thermodynamics of adsorption within these samples.

Comparing the surface excesses at each loading, table 8.1, it appears that again at low shear rates, there is little change in surface excess, similar to at 20 °C. However, there is more change at higher shear rates, with a decrease at 100 s^{-1} before increasing to 62 Å at 1000 s^{-1}. This provides some evidence that the quantity of surfactant at the interface is more unstable with respect to shear at higher temperatures.

Whilst the matrix within this sample is hexadecane, not a polymer, some comparisons can be drawn to previous work within polymer blends. Sako *et al.*[212] have studied segregation in blends of polycarbonate (PC) and poly(methyl methacrylate) (PMMA) during injection moulding. Under these conditions, PMMA was observed to become more abundant at the surface of the injection moulded product than in the bulk. This was despite the demonstrated miscibility of the two polymers. The driver for segregation here was attributed to shear-induced phase separation. There was also some evidence that the segregation of the lower viscosity PMMA led to improved flow during the injection moulding and that the difference in shear viscosity played a key role in this segregation.

This segregation under shear has also been seen in polymer blends containing smaller additive molecules. Murase[230] *et al.* investigated the behaviour of ultra-high molecular weight polyethylene in paraffin wax under shear. These blends demonstrated both shear-induced phase separation and shear-induced crystallisation. This crystallisation was found above the melting temperature of the polymer, indicating that without the shear force, this crystallisation would not occur. This experiment demonstrates that the shear forces can cause a change in the structure and orientation of components within a blend, which may be similar to the observations seen in the work reported here, with a significant rearrangement occurring as evidenced by the change in rheological properties and surface excess.

This work can now be translated to the systems used in commercial applications, polymers with low molecular weight amphiphilic additives. It appears that the shear forces applied to the blend during processing may have some impact on

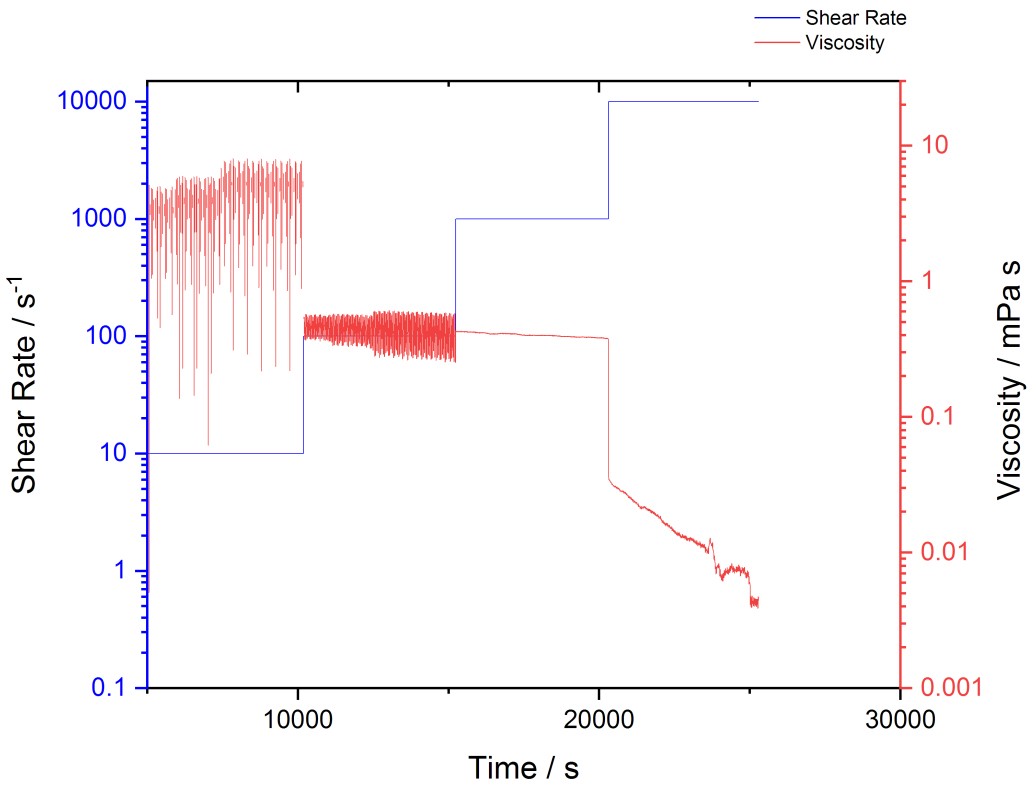

Figure 8.11: Viscosity and shear rate data collected for 1.5 % $C_{12}E_5$ in d-hexadecane at 150°C. This data has been acquired during the NR measurements given in Fig. 8.13.

the enrichment of surfactant at the interfaces of the blend. It was also shown that the processing temperature does not seem to induce a significant change in surface enrichment and so appears to be of less importance during processing. However, it must be noted that further work is required to determine whether these changes in surface enrichment remain after the shear forces are removed or, in the case of a polymer, after it has cooled to ambient temperatures.

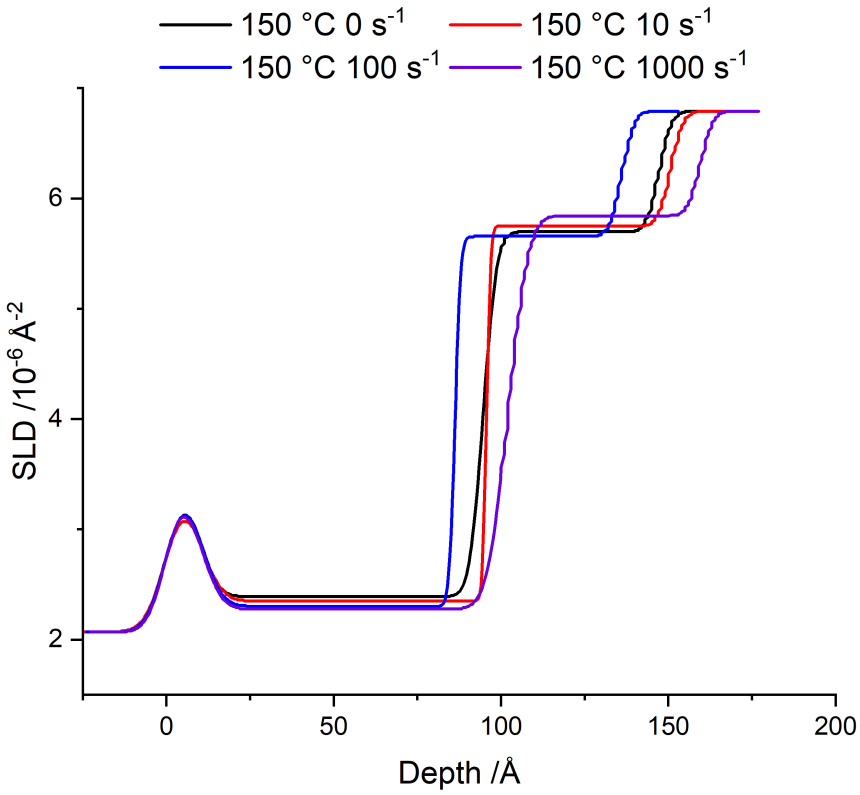

Figure 8.12: SLD profiles for 1.5 % $C_{12}E_5$ in d-hexadecane at 150 °C at shear rates between 0 and 1000 s^{-1}. SLD profiles are obtained from reflectivity profiles shown in Fig. 8.13.

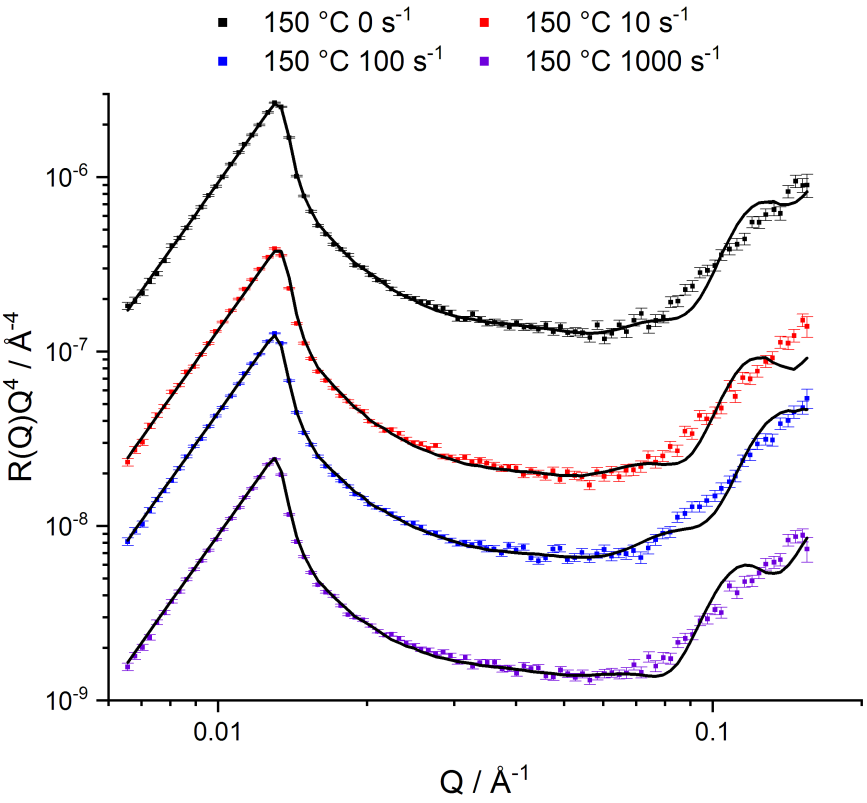

Figure 8.13: NR data and fits plotted as a function of $R(Q)^4$ at 150 °C. Samples are within a cone-plate geometry and are sheared at rates between 0 and 1000 s^{-1}. An offset has been applied to the 0 – 100 s^{-1} data series.

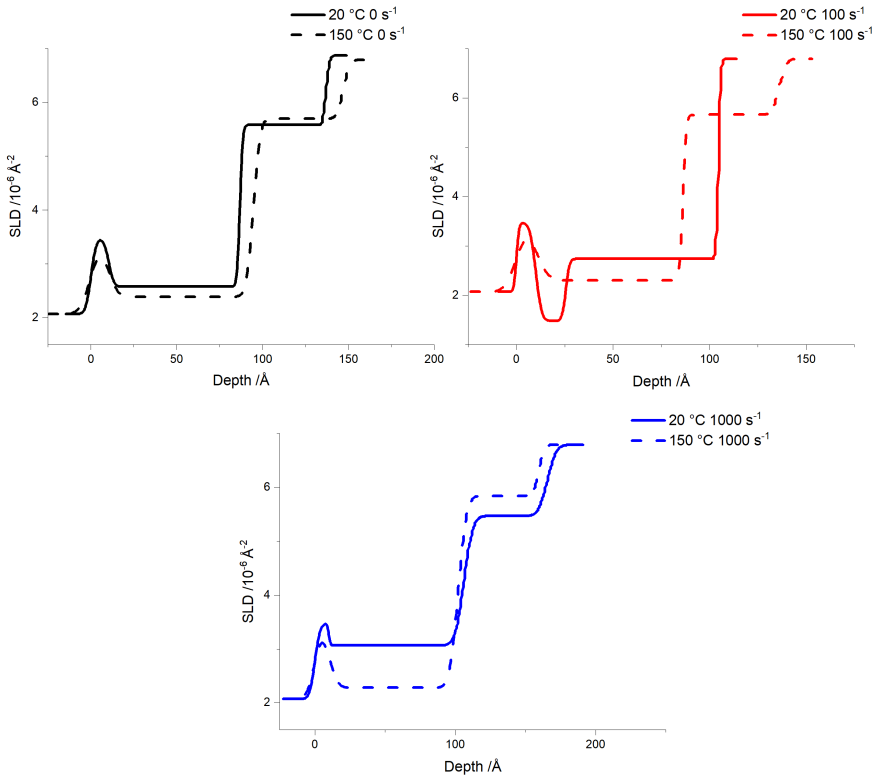

Figure 8.14: Comparison of SLD depth profiles of 1.5 % $C_{12}E_5$ in d-hexadecane at 20 °C and 150 °C at various shear rates.

8.5 Chapter Conclusions

This chapter has explored the effect of shear forces on the surfactant distribution at the liquid-solid interface in d-hexadecane. This has been achieved by using the novel technique of rheo-NR.

This work has shown that under shear, an enriched layer is still found at the silicon oxide interface. This layer has a high surfactant fraction, but is not a pure surfactant layer. However, the surface excess is approximately 55 Å, several times thicker than the molecular length of a $C_{12}E_5$ molecule.

The enriched layer appeared to be stable relative to varying shear rates at lower shear rates, with little change in the surface excess between 0 and 100 s^{-1}. However, at 1000 s^{-1} a slight increase in surface excess is seen from 55 Å to 62 Å. This change also appeared to correspond to a change in the rheological behaviour, where below this shear rate, an oscillation was observed in the viscosity data which is not present above this shear rate. It has been postulated that the change in rheological behaviour is related to the change in surfactant distribution. However, the present work does not allow further investigation of this relationship, with additional experiments required to understand the structure and orientation of the surfactant molecules within the enriched interfacial layer.

Samples were also heated to 150 °C whilst under shear in order to assess how the temperature will affect the surfactant distribution during processing. This work revealed that at high temperatures, similar behaviour was seen compared to at 20 °C, with a small increase in surface excess at 1000 s^{-1}. Unlike at 20 °C, some evidence of ejection of material from the rheometer at high shear rates is observed in the rheometry data, with the viscosity decreasing over time at 1000 s^{-1}. However, this appears to have little effect on the NR measurements, with a reflectivity profile collected at these shear rates for which a suitable fit can be found.

From these observations, it is possible to conclude that during polymer processing, a higher applied shear rate will yield a larger degree of surface enrichment. This may be more beneficial for commercial applications where increased surface

wettability is required. This work has also showed that the processing temperature has less effect on the surfactant distribution and so may not be a key factor in inducing further surface enrichment during processing. However, this work has not assessed whether this surface enrichment remains after the shear force is removed, simulating the conditions after extrusion or similar processing. This further work will be necessary to ensure that the enriched layer is still present in finished products and to understand the stability of the structures formed under shear.

Chapter 9

Conclusions and Future Directions

9.1 Conclusion

The objective of this thesis was to probe the behaviour of amphiphilic molecules within hydrophobic polymer films with the intention of gaining further understanding of the motivations of surface segregation. This required assessment of the compatibility of the amphiphile in order to consider the thermodynamic drivers for this segregation. Whilst previous techniques used for measuring compatibility were not feasible with the blends examined, DSC and rheometry were probed as more viable techniques. These techniques were used to probe the effect of head group size on compatibility. DSC examined two different thermal transitions for the two different polymers (LDPE and *cis*-PI). These were T_c and T_g respectively.

DSC showed that the compatibility of $C_{12}E_3$ was greater with both *cis*-PI and LDPE than $C_{12}E_5$. This was attributed to the shorter hydrophilic head group that produces unfavourable interactions with the hydrophobic polymers. Rheometry was also investigated as a technique to probe compatibility, with both Han plots and van Gurp-Palmen (vGP) plots produced. Whilst Han plots were more difficult to interpret, vGP plots showed strong evidence to support DSC observations that the $C_{12}E_5$ surfactant was less compatible than $C_{12}E_3$, with less overlap of data

series at different temperatures.

There were, however, key limitations with using DSC to determine compatibility. As the procedure involves the examination of a thermal transition, it only gives the compatibility at the temperature of the specific transition probed. This means that whilst it is useful for probing how different surfactants or loadings behave compared to each other, it is not useful in the construction of a phase diagram where temperature is a variable. This would be of great use in the processing of polymer / additive blends and so further work is needed to identify a technique which will allow this to be obtained.

$C_{12}E_5$ was shown to produce a surface excess on the surface of blended films comprising the surfactant and *cis*-PI. However, there was significant discrepancy between the surface layer thicknesses seen using NR and NRA, with NRA showing much more surface enrichment. This was attributed to an enriched layer which was invisible to neutrons above the detected layer. The surfactant-enriched layer also demonstrated surprising temperature resistance, with similar surface thicknesses seen at high temperatures. Water exposure also gave interesting results, with only a small decrease in surface excess thickness after rinsing (measured by NR) but with a hydrophilic-hydrophobic switch observed. This has been attributed to the neutron-invisible layer either undergoing a rearrangement or loss from the film.

These observations were not seen in hPBd films, instead much smaller surface excesses were seen and these did not remain after heating. This suggested that surface enrichment was much poorer in films with greater crystallinity. The surface excesses were far less resistant to heating, with surface excesses decreasing greatly after heating to above the melting point of the polymer. This has shown that crystallinity induces a significant change in segregation behaviour, although this present work cannot identify the mechanism by which this occurs. It is possible that whilst the surface layer is lost upon heating, the greater crystallinity impairs replenishment of the surface layer from the bulk. Furthermore, it has also been observed that strands are present on the film surfaces which are not influenced by temperature elevation, seemingly demonstrating that there is surfactant that is again present on the surface which is unaffected by ambient conditions. This

cannot be detected by neutron reflection because it lacks sufficient coherent area.

There have also been investigations conducted into the effect of head group size on segregation behaviour. It was revealed that $C_{12}E_3$ showed much less surface enrichment than $C_{12}E_5$ in hPBd films. This presented strong evidence that, when compared alongside the results found from DSC and rheometry, compatibility may be an important driver for surface segregation. It was also shown that the evolution of the contact angle was much slower upon water droplet contact for $C_{12}E_3$ than $C_{12}E_5$, suggesting that surface energy differences may play a role in directing surface segregation, with the lower surface energy difference of $C_{12}E_3$ making surfactant segregation slower and less distinct.

Preliminary work has also been conducted to probe how amphiphilic molecules behave within a hydrophobic matrix under shear. Rheo-NR has been shown to be a promising technique for the investigation of segregation during flow. $C_{12}E_5$ was shown to produce enriched layers at the silicon oxide interface and this layer appeared to be unaffected by a range of shear rates comparable to those exerted during extrusion. This work also revealed that processing temperature had little effect on the surface enrichment under flow, suggesting that within industrial processing methods, temperature may be a less important factor when producing products with surfactant-enriched layers upon extrusion.

This work shows that in order to achieve the desired surface enrichment in surfactants within industrial applications, product formulation is the most important factor. It has been shown that both temperature and shear rate, two of the more easily controlled variables during product manufacture have much less effect on surfactant distribution than the choice of surfactants to incorporate into the blend. Therefore, it is necessary in future work to further develop models which will elucidate the interactions of the surfactant and polymer matrix to move towards formulation based on predicted behaviour.

9.2 Future Directions

Whilst this thesis has probed the segregation behaviour of non-ionic surfactants within hydrophobic polymers, and has revealed some insight into the drivers for this phenomena, there is still a range of further drivers which need to be studied.

Ion beam analysis has proved to be an invaluable tool to probe surfactant distributions within polymer films. Further IBA measurements are required in order to investigate the NR invisible surfactant layer that has been seen on both hPBd and *cis*-PI films. These experiments should be conducted before and after both heating and rinsing the films with water. This will show the effect of these ambient conditions on the total surface excess and will elucidate whether the surfactant is removed upon rinsing or the whole surface layer is water-resistant.

Whilst the surface layer thickness and enrichment has been probed, there has been little attempt within this work to probe the structure of the surfactant-enriched layer. Small-angle neutron scattering (SANS) would be a useful technique for this. SANS would provide valuable data that would be required to identify if there is any ordering within the surface layer. Furthermore, it would also be possible to identify the periodicity of any features present in the surface layer. It would also be possible from this technique to identify if any surfactant remaining within the bulk forms larger scale structures such as micelles. However, SANS would be difficult to apply to the crystalline materials but could be used for molten film samples and these results would complement further rheo-NR experiments.

The technique for film preparation within this work, spin-casting, is very different to the process used to prepare films within industrial manufacturing. Extrusion does not require solvent during processing and so it would be of great interest to compare the behaviour seen within these films to the spin-cast films studied in this work. It has been proposed that the presence of a low surface energy solvent may influence surface segregation and thus elimination of this component would grant the opportunity to study this influence.

The thermodynamic motivations for migration have been probed in the exper-

iments conducted in this thesis. However, there has been no investigation of the dynamics of segregation except for time-dependent contact angle analysis. This may be studied by probing the contact angle evolution of films. If a polymer film (containing no surfactant) of defined thickness is spin-cast over a surfactant-enriched film, the time required for the surfactant to migrate to the surface (and lower the contact angle of the water droplet) can be measured. This can be used to understand how crystallinity impedes the movement of surfactant through the film.

The observations made within this work will be of greatest benefit if they can be further used in predicting surface segregation of other systems. This would require computational and theoretical work to understand how the drivers proposed for segregation in both this and other work affect the segregation. The work performed here will be of great use in corroborating simulated surfactant distributions produced by computational models. However, these computational models first require detailed parametrisation of the molecules used.

Whilst this work has shown that there is evolution of surface structures on the surface of the films upon rinsing, it is unclear how this evolution occurs. AFM can be used on surfaces under fluids and so it may be of significant interest to immerse the films in water and probe how the surface structures change in real time during water exposure.

The films produced and studied within this thesis only contain 2 components, a surfactant and polymer. However, commercial products often contain a wide range of additives. It is therefore necessary to examine the distribution of surfactant within polymers with an additional small molecule additive. Other work has shown that there can be significant interactions between segregated surfactants and small molecules and so it is important to consider how interactions may affect both the degree of segregation and the water and heat resistance of the enriched layer.

Finally, the use of Rheo-NR has been shown to be a promising technique in the investigation of surface segregation during processing. It will therefore be an interesting avenue of investigation to probe the behaviour of surfactants within

polymers. This work has probed the surfactant distribution within a hydrophobic solvent, but the use of a deuterated polymer instead of a solvent would be more similar to commercially relevant formulations. It would then be possible to couple these depth profiles with the compatibility observations made in the rheometry data presented in this thesis to identify any correlations between compatibility and surfactant segregation.

Bibliography

[1] D. Jeremic, in *Ullmann's Encyclopedia of Industrial Chemistry*, Wiley-VCH Verlag GmbH & Co. KGaA, Weinheim, Germany, 2014, pp. 1–42.

[2] D. Nwabunma and T. Kyu, *Polyolefin blends*, Wiley-Interscience, Hoboken, N.J., 2008.

[3] G. Cecchin, G. Morini and F. Piemontesi, in *Kirk-Othmer Encyclopedia of Chemical Technology*, ed. John Wiley & Sons, Inc., John Wiley & Sons, Inc., Hoboken, NJ, USA, 2003.

[4] D. B. Malpass, in *Introduction to Industrial Polyethylene*, John Wiley & Sons, Inc., Hoboken, NJ, USA, 2010, pp. 1–22.

[5] M. J. Roedel, *J. Am. Chem. Soc.*, 1953, **75**, 6110–6112.

[6] D. C. Roe, A. Chatterjee, N. E. Greening, S. I. Grenberg, C. H. Kreuzer, C. B. Martynus, M. B. O'Reilly, R. Rosati, S. Sautter, B. Simon, L. Stelzig and R. E. Walther, *Absorbent articles with channels*, 2020, US Pat. 10736794.

[7] J. Geng, Y. Sun and J. Hua, *Polym. Sci. Ser. B*, 2016, **58**, 495–502.

[8] E. G. Lovering and W. B. Wright, *J. Polym. Sci. A-1 Polym. Chem.*, 1968, **6**, 2221–2235.

[9] X. Liu, W. Li, Q. Niu, R. Wang and A. He, *Polymer*, 2018, **140**, 255–268.

[10] T. Fukui, *Process for the preparation of improved cis-1,4-polyisoprene*, 1969, US Pat. 3687925.

[11] A. K. Bhowmick, C. C. Kuo, A. Manzur, A. MacArthur and D. McIntyre, *Journal of Macromolecular Science, Part B*, 1986, **25**, 283–306.

[12] S. McIntosh, S. J. Smith, A. Jones Lang and D. L. Bergman, Jr, *Superabsorbent polymer composition coated with thermoplastics*, 2014, JP5557268.

[13] C. R. Birnie, D. Malamud and R. L. Schnaare, *Antimicrob. Agents Chemother.*, 2000, **44**, 2514–2517.

[14] N. Khan and B. Brettmann, *Polymers*, 2018, **11**, 51.

[15] F. Strubbe and K. Neyts, *J. Phys.: Condens. Matter*, 2017, **29**, 453003.

[16] K. Holmberg, B. Jönsson, B. Kronberg and B. Lindman, *Surfactants and Polymers in Aqueous Solution*, John Wiley & Sons, 2002.

[17] J. N. Israelachvili, D. J. Mitchell and B. W. Ninham, *J. Chem. Soc., Faraday Trans. 2*, 1976, **72**, 1525.

[18] S. Schrödle, G. Hefter, W. Kunz and R. Buchner, *Langmuir*, 2006, **22**, 924–932.

[19] P. J. Flory, *The Journal of Chemical Physics*, 1942, **10**, 51–61.

[20] K. H. Meyer, *Zeitschrift für Physikalische Chemie*, 1939, **44B**, 383–391.

[21] M. Rubenstein and R. H. Colby, *Polymer Physics*, Oxford University Press, 2003.

[22] P. J. Flory, *Principles of polymer chemistry*, Cornell Univ. Press, Ithaca, NY, 19th edn., 2006.

[23] M. L. Huggins, *J. Chem. Phys.*, 1941, **9**, 440–440.

[24] V. S. Minnikanti and L. A. Archer, *Macromolecules*, 2006, **39**, 7718–7728.

[25] V. M. Datla, E. Shim and B. Pourdeyhimi, *Polymer Engineering and Science*, 2012, **52**, 1920–1927.

[26] J. S. Higgins, J. E. G. Lipson and R. P. White, *Phil. Trans. R. Soc. A.*, 2010, **368**, 1009–1025.

[27] E. Patyukova, E. Xi and M. R. Wilson, *Macromolecules*, 2021, **54**, 2763–2773.

[28] R. A. L. Jones, L. J. Norton, E. J. Kramer, F. S. Bates and P. Wiltzius, *Physical Review Letters*, 1991, **66**, 1326–1329.

[29] M. Geoghegan, R. A. L. Jones and A. S. Clough, *The Journal of Chemical Physics*, 1995, **103**, 2719–2724.

[30] R. C. Ball and R. L. H. Essery, *Journal of Physics: Condensed Matter*, 1990, **2**, 10303–10320.

[31] K. Tanaka, A. Takahara and T. Kajiyama, *Macromolecules*, 1998, **31**, 863–869.

[32] H. Lee and L. A. Archer, *Macromolecules*, 2001, **34**, 4572–4579.

[33] M. R. Wattenbarger, H. S. Chan, D. F. Evans, V. A. Bloomfield and K. A. Dill, *The Journal of Chemical Physics*, 1990, **93**, 8343–8351.

[34] J. Baschnagel and K. Binder, *Macromolecules*, 1995, **28**, 6808–6818.

[35] P. Sakellariou, *Polymer*, 1993, **34**, 3408–3415.

[36] A. M. Mayes, D. G. Walton and J. F. Hester, *Polymeric Membranes and Other Polymer Articles Having Desired Surface Characteristics and Method for Their Preparation*, 2002, US Pat. 6413621.

[37] K. A. Houghton, *Thesis (Doctoral)*, Durham University, Durham, UK, 2005.

[38] F. Welle and R. Franz, *Polymer Testing*, 2012, **31**, 93–101.

[39] Z.-W. Wang, B. Li, Q.-B. Lin and C.-Y. Hu, *Packaging Technology Science*, 2018, **31**, 277–295.

[40] J. Crank, *The Mathematics of Diffusion*, Clarendon Press, Oxford, 2nd edn., 1975.

[41] I. S. Arvanitoyannis and L. Bosnea, *Critical Reviews in Food Science and Nutrition*, 2004, **44**, 63–76.

[42] N. L. Thomas and A. H. Windle, *Polymer*, 1982, **23**, 529–542.

[43] C.-Y. Hui, K.-C. Wu, R. C. Lasky and E. J. Kramer, *Journal of Applied Physics*, 1987, **61**, 5129–5136.

[44] D. Bucknall, J. Higgins and S. Butler, *Chemical Engineering Science*, 2001, **56**, 5473–5483.

[45] A. Briddick, P. Li, A. Hughes, F. Courchay, A. Martinez and R. L. Thompson, *Langmuir*, 2016, **32**, 864–872.

[46] D. I. Bower, *An Introduction to Polymer Physics*, Cambridge University Press, 2002.

[47] A. Satti, R. Quijada, J. Pastor and E. Vallés, *Polymer Testing*, 2018, **67**, 450–456.

[48] X. Xu, J. Xu, L. Feng and W. Chen, *J. Appl. Polym. Sci.*, 2000, **77**, 1709–1715.

[49] M. Hedenqvist, A. Angelstok, L. Edsberg, P. Larsson and U. Gedde, *Polymer*, 1996, **37**, 2887–2902.

[50] B. Marcato, S. Guerra, M. Vianello and S. Scalia, *International Journal of Pharmaceutics*, 2003, **257**, 217–225.

[51] B. H. Mahlman, *Polyphase compositions and process for their preparation*, 1970, US 3664981.

[52] S. Mäkipirtti, M. Ojanen and H. Bergholm, *Method of Regulating the Internal Transport of Adjuvants and Additives of a Polymer*, 1997, EP 0753606.

[53] S. Al-Malaika, M. D. R. J. Goonetileka and G. Scott, *Polymer Degradation and Stability*, 1991, **32**, 231–247.

[54] A. Reynier, P. Dole, S. Humbel and A. Feigenbaum, *Journal of Applied Polymer Science*, 2001, **82**, 2422–2433.

[55] M. T. Scholz, M. R. Berrigan and T. P. Klun, *Hydrophilic Polypropylene Melt Additives*, 2010, WO/2010/111491.

[56] J. Grebowicz, S.-F. Lau and B. Wunderlich, *J. polym. sci., C Polym. symp.*, 2007, **71**, 19–37.

[57] G. Dlubek, K. Saarinen and H. M. Fretwell, *Journal of Polymer Science, Part B: Polymer Physics*, 1998, **36**, 1513–1528.

[58] P. D. Calvert and N. C. Billingham, *Journal of Applied Polymer Science*, 1979, **24**, 357–370.

[59] G. S. Smith, C. B. Skidmore, P. M. Howe and J. Majewski, *Journal of Polymer Science, Part B: Polymer Physics*, 2004, **42**, 3258–3266.

[60] A. D. Schwope, D. E. Till, D. J. Ehntholt, K. R. Sidman, R. H. Whelan, P. S. Schwartz and R. C. Reid, *Food and Chemical Toxicology*, 1987, **25**, 317–326.

[61] W. M. Heiserman, S. Z. Can, R. A. Walker, T. H. Begley and W. Limm, *Journal of Colloid and Interface Science*, 2007, **311**, 587–594.

[62] J. Rosen-Kligvasser, R. Y. Suckeveriene, R. Tchoudakov and M. Narkis, *Polymer Engineering and Science*, 2014, **54**, 2023–2028.

[63] T. Young, *Philosophical Transactions of the Royal Society of London*, 1805, **95**, 65–87.

[64] R. L. Thompson, S. J. Hardman, L. R. Hutchings, A. Pillay Narrainen and R. M. Dalgliesh, *Langmuir*, 2009, **25**, 3184–3188.

[65] D. R. Iyengar, S. M. Perutz, C.-A. Dai, C. K. Ober and E. J. Kramer, *Macromolecules*, 1996, **29**, 1229–1234.

[66] E. F. D. Sabattié, J. Tasche, M. R. Wilson, M. W. A. Skoda, A. Hughes, T. Lindner and R. L. Thompson, *Soft Matter*, 2017, **13**, 3580–3591.

[67] E. F. D. Sabattié, *Thesis (Doctoral)*, Durham University, Durham, UK, 2018.

[68] A. Briddick, R. J. Fong, E. F. D. Sabattié, P. Li, M. W. A. Skoda, F. Courchay and R. L. Thompson, *Langmuir*, 2018, **34**, 1410–1418.

[69] I. Mršić, A. Lorenz, R. J. Lehnert, G. Lorenz and T. Chassé, *Applied Surface Science*, 2022, **578**, 151957.

[70] H. Raval, Y. P. Singh, M. H. Mehta and S. Devi, *Polymer International*, 1991, **24**, 99–104.

[71] D. F. S. Petri, *J. Braz. Chem. Soc.*, 2002, **13**, 695–699.

[72] D. W. Schubert, *Polymer Bulletin*, 1997, **38**, 177–184.

[73] P. Saxena, P. Shukla and M. S. Gaur, *Polymers and Polymer Composites*, 2020, **29**, S11–S18.

[74] J. Rieger, *Polymer Testing*, 2001, **20**, 199–204.

[75] T. G. Mezger, *The Rheology Handbook*, European Coatings Tech Files, 4th edn., 2014.

[76] T. Chatterji, in *Neutron Scattering from Magnetic Materials*, ed. T. Chatterji, Elsevier, Amsterdam, The Netherlands, 2006, pp. 1–25.

[77] D. S. Sivia, *Elementary Scattering Theory For X-ray and Neutron Users*, Oxford University Press, 2011.

[78] S. K. Peace and R. W. Richards, in *Applications of Neutron Scattering to Soft Condensed Matter*, ed. B. J. Gabrys, Gordon and Breach Science Publishers, Amsterdam, The Netherlands, 2000, pp. 163–204.

[79] N. F. Berk, *Journal of Research of the National Institute of Standards and Technology*, 1993, **98**, 15–30.

[80] J. Penfold and R. K. Thomas, *Journal of Physics: Condensed Matter*, 1990, **2**, 1369–1412.

[81] V. F. Sears, *Neutron News*, 1992, **3**, 26–37.

[82] J. S. Higgins and H. C. Benoît, *Polymers and Neutron Scattering*, Oxford University Press, 1994.

[83] O. S. Heavens, *Optical properties of thin solid films*, Dover Publications, 1965.

[84] J. Penfold and R. K. Thomas, *Current Opinion in Colloid & Interface Science*, 2014, **19**, 198–206.

[85] C. Flood, T. Cosgrove, D. Qiu, Y. Espidel, I. Howell and P. Revell, *Langmuir*, 2007, **23**, 2408–2413.

[86] A. R. J. Nelson and S. W. Prescott, *J Appl Crystallogr*, 2019, **52**, 193–200.

[87] M. Litwinowicz, C. Gibson and R. Thompson, *MUSCtR*, 2021, `https://sourceforge.net/projects/musctr/`.

[88] D. Kwok and A. Neumann, *Advances in Colloid and Interface Science*, 1999, **81**, 167–249.

[89] D. K. Owens and R. C. Wendt, *Journal of Applied Polymer Science*, 1969, **13**, 1741–1747.

[90] A. F. Stalder, G. Kulik, D. Sage, L. Barbieri and P. Hoffmann, *Colloids and Surfaces A: Physicochemical and Engineering Aspects*, 2006, **286**, 92–103.

[91] P. P. Pronko and J. G. Pronko, *Phys. Rev. B*, 1974, **9**, 2870–2878.

[92] G. Vizkelethy, in *Handbook of Modern Ion Beam Materials Analysis*, ed. J. R. Tesmer and M. Nastasi, Materials Research Society, Pittsburgh, Pennsylvania, 1995, pp. 139–166.

[93] W. Möller, *Nuclear Instruments and Methods*, 1978, **157**, 223–227.

[94] N. P. Barradas and C. Jeynes, *Nuclear Instruments and Methods in Physics Research Section B: Beam Interactions with Materials and Atoms*, 2008, **266**, 1875–1879.

[95] H.-J. Butt, B. Cappella and M. Kappl, *Surface Science Reports*, 2005, **59**, 1–152.

[96] M. N. Jones, *Journal of Colloid and Interface Science*, 1967, **23**, 36–42.

[97] K.-W. Zhang, G. Karlström and B. Lindman, *Colloids and Surfaces*, 1992, **67**, 147–155.

[98] B. Lindman and G. Karlström, *Comptes Rendus Chimie*, 2009, **12**, 121–128.

[99] C. O. Kerobo, E. Attiogbe, A. Wang, C. Rocafort and J. A. Randolph, *Method of Influencing the Surface Energy of a Non-Woven Fabric*, 2015, WO/2015/143352.

[100] O. Squillace, R. Fong, O. Shepherd, J. Hind, J. Tellam, N. J. Steinke and R. L. Thompson, *Polymers*, 2020, **12**, 205.

[101] P. H. Daniels and A. Cabrera, *Journal of Vinyl and Additive Technology*, 2015, **21**, 7–11.

[102] J. Li, Y. Zhang, Y. Jiacuo, Y. Shang, H. Huo and S. Jiang, *Polymer Bulletin*, 2012, **68**, 1405–1423.

[103] D. Vlassopoulos, A. Koumoutsakos, S. H. Anastasiadis, S. G. Hatzikiriakos and P. Englezos, *Journal of Rheology*, 1997, **41**, 739–755.

[104] C. R. López-Barrón and C. W. Macosko, *Journal of Rheology*, 2012, **56**, 1315–1334.

[105] C. R. López-Barrón and C. W. Macosko, *Journal of Rheology*, 2014, **58**, 1935–1953.

[106] C. D. Han and J. Kim, *Journal of Polymer Science Part B: Polymer Physics*, 1987, **25**, 1741–1764.

[107] F. Walha, K. Lamnawar, A. Maazouz and M. Jaziri, *Polymers*, 2016, **8**, 61.

[108] M. van Gurp and J. Palmen, *Rheology Bulletin*, 1998, **67**, 5–8.

[109] H. Chen, X. Shi, Y. Zhu, Y. Zhang and J. Xu, *Journal of Applied Polymer Science*, 2009, **114**, 2461–2468.

[110] P. Reichert, B. Hoffmann, T. Bock, R. Thomann, R. Mülhaupt and C. Friedrich, *Macromolecular Rapid Communications*, 2001, **22**, 519–523.

[111] D. R. Burfield, *J. Chem. Educ.*, 1987, **64**, 875.

[112] H. Iino, T. Usui and J.-i. Hanna, *Nature Communications*, 2015, **6**, 6828–.

[113] A. Tonegawa, K. Ohno, H. Matsuura, K. Yamada and T. Okuda, *The Journal of Physical Chemistry B*, 2002, **106**, 13211–13223.

[114] V. V. Klochkov, I. Z. Rakhmatullin, K. A. Il'yasov and A. V. Klochkov, *BioNanoScience*, 2020, **10**, 690–695.

[115] D. J. Mitchell, G. J. T. Tiddy, L. Waring, T. Bostock and M. P. McDonald, *J. Chem. Soc., Faraday Trans. 1*, 1983, **79**, 975–1000.

[116] S. Masatoki, K. Ohno, H. Yoshida and H. Matsuura, *Chemistry Letters*, 1996, **25**, 149–150.

[117] S. Masatoki, K. Ohno, H. Yoshida and H. Matsuura, *The Journal of Physical Chemistry*, 1996, **100**, 8487–8498.

[118] J. A. Bouwstra, D. A. van Hal, H. E. J. Hofland and H. E. Junginger, *Colloids and Surfaces A: Physicochemical and Engineering Aspects*, 1997, **123-124**, 71–80.

[119] P. C. Schulz, J. F. A. Soltero and J. E. Puig, in *Thermal Behavior of Dispersed Systems*, ed. N. Garti, Taylor & Francis Group, London, United Kingdom, 2000, pp. 121–182.

[120] D. J. Blundell, *Polymer*, 1987, **28**, 2248–2251.

[121] F. Chen and M. P. Wolcott, *European Polymer Journal*, 2014, **52**, 44–52.

[122] A. Linares and J. L. Acosta, *Journal of Applied Polymer Science*, 1998, **67**, 997–1004.

[123] M. M. Sander, A. Nicolau, R. Guzatto and D. Samios, *Polymer Testing*, 2012, **31**, 1077–1082.

[124] P. Sharma, S. Roy and H. A. Karimi-Varzaneh, *Macromolecular Theory and Simulations*, 2019, **28**, 1900003.

[125] E. H. Immergut and H. F. Mark, in *Plasticization and Plasticizer Processes*, ed. N. A. J. Platzer, American Chemical Society, Washington DC, USA, 1965, vol. 48, pp. 1–26.

[126] J. Jang and D. K. Lee, *Polymer*, 2003, **44**, 8139–8146.

[127] P. W. Atkins and J. De Paula, *Atkins' Physical chemistry*, Oxford University Press, Oxford ; New York, 9th edn., 2010.

[128] W. Wu, H. Tian and A. Xiang, *J Polym Environ*, 2012, **20**, 63–69.

[129] Y. Kong and J. N. Hay, *European Polymer Journal*, 2003, **39**, 1721–1727.

[130] L. Mandelkern, A. L. Allou and M. R. Gopalan, *J. Phys. Chem.*, 1968, **72**, 309–318.

[131] P. J. Flory, *The Journal of Chemical Physics*, 1949, **17**, 223–240.

[132] L. Mandelkern and R. G. Alamo, in *Physical Properties of Polymers Handbook*, ed. J. E. Mark, AIP Press, New York, USA, 1st edn., 1996, pp. 119–137.

[133] P. J. Flory and A. Vrij, *J. Am. Chem. Soc.*, 1963, **85**, 3548–3553.

[134] F. A. Quinn and L. Mandelkern, *J. Am. Chem. Soc.*, 1958, **80**, 3178–3182.

[135] F. Chen and J. Qian, *Fuel*, 2002, **81**, 2071–2077.

[136] A. R. Arnold and P. Evans, *J. nat. Rub. Res.*, 1991, **6**, 75–86.

[137] M. Kapnistos, A. Hinrichs, D. Vlassopoulos, S. H. Anastasiadis, A. Stammer and B. A. Wolf, *Macromolecules*, 1996, **29**, 7155–7163.

[138] B. Wang, Z. Tu, C. Wu, T. Hu, X. Wang, S. Long and X. Gong, *Polymers*, 2019, **11**, 846.

[139] Y. Chen, H. Zou, Y. Cao and M. Liang, *Polym. Sci. Ser. A*, 2014, **56**, 630–639.

[140] K. Rinawa, S. N. Maiti, R. Sonnier and J.-M. Lopez Cuesta, *Polym. Bull.*, 2015, **72**, 3305–3324.

[141] C. Weis, J. Leukel, K. Borkenstein, D. Maier, W. Gronski, C. Friedrich and J. Honerkamp, *Polymer Bulletin*, 1998, **40**, 235–241.

[142] P. Agrawal, M. H. A. Silva, S. N. Cavalcanti, D. M. G. Freitas, J. P. Araújo, A. D. B. Oliveira and T. J. A. Mélo, *Polym. Bull.*, 2021, **79**, 2321–2343.

[143] A. K. Dordinejad and S. H. Jafari, *Polymer Engineering & Science*, 2014, **54**, 1081–1088.

[144] R. Li, W. Yu and C. Zhou, *Journal of Macromolecular Science, Part B*, 2006, **45**, 889–898.

[145] S. Trinkle and C. Friedrich, *Rheologica Acta*, 2001, **40**, 322–328.

[146] S. Trinkle, P. Walter and C. Friedrich, *Rheologica Acta*, 2002, **41**, 103–113.

[147] N. F. A. Zainal, S. A. Lai and C. H. Chan, *Polymers*, 2020, **12**, 724.

[148] M. Iza, M. Bousmina and R. Jérôme, *Rheol. Acta*, 2001, **40**, 10–22.

[149] M. Doi and T. Ohta, *J. Chem. Phys.*, 1991, **95**, 1242–1248.

[150] E. Mor and N. Vasanthakumar, *Wettable polymer fibers, compositions for preparaing same and articles made therefrom*, 2000, US 6146757.

[151] S. Zhu and D. E. Hirt, *Journal of Vinyl and Additive Technology*, 2007, **13**, 57–64.

[152] M. Litwinowicz, S. Rogers, A. Caruana, C. Kinane, J. Tellam and R. Thompson, *Macromolecules*, 2021, **54**, 9636–9648.

[153] M. Morita, T. Ohmi, E. Hasegawa, M. Kawakami and M. Ohwada, *Journal of Applied Physics*, 1990, **68**, 1272–1281.

[154] H. Kuhn and H. Rehage, *Physical Chemistry Chemical Physics*, 2000, **2**, 1023–1028.

[155] L.-H. Lee, *Journal of Polymer Science Part A-2: Polymer Physics*, 1967, **5**, 1103–1118.

[156] C. J. v. Oss, M. K. Chaudhury and R. J. Good, *Advances in Colloid and Interface Science*, 1987, **28**, 35–64.

[157] D. W. v. Krevelen and Hoftyzer, *Properties of Polymers: their Estimation and Correlation with Chemical Structure*, Elsevier, 2nd edn., 1976.

[158] S. Wu, *The Journal of Physical Chemistry*, 1968, **72**, 3332–3334.

[159] R. J. Fong, O. Squillace, C. D. Reynolds, J. F. K. Cooper, R. M. Dalgliesh, J. Tellam, F. Courchay and R. L. Thompson, *Langmuir*, 2020, **36**, 4795–4807.

[160] W. Xie, L.-T. Weng, K. L. Yeung and C.-M. Chan, *Surface and Interface Analysis*, 2018, **50**, 1302–1309.

[161] M. Wahlgren, J. Kedström and T. Arnebrant, *Journal of Dispersion Science and Technology*, 1997, **18**, 449–458.

[162] J. Dong and G. Mao, *Langmuir*, 2000, **16**, 6641–6647.

[163] S. Shirai and Y. Einaga, *Polymer Journal*, 2005, **37**, 913–924.

[164] V. M. Datla, E. Shim and B. Pourdeyhimi, *Journal of Applied Polymer Science*, 2011, **121**, 1335–1347.

[165] S. Zhu, N. Welsh and D. E. Hirt, *Journal of Plastic Film and Sheeting*, 2007, **23**, 187–201.

[166] S. Goffri, C. Müller, N. Stingelin-Stutzmann, D. W. Breiby, C. P. Radano, J. W. Andreasen, R. Thompson, R. A. J. Janssen, M. M. Nielsen, P. Smith and H. Sirringhaus, *Nature Mater*, 2006, **5**, 950–956.

[167] A. Babel and S. A. Jenekhe, *Macromolecules*, 2004, **37**, 9835–9840.

[168] D. M. Bieliński and ł. Kaczmarek, *J. Appl. Polym. Sci.*, 2006, **100**, 625–633.

[169] N. Lützow, A. Tihminlioglu, R. P. Danner, J. Duda, A. De Haan, G. Warnier and J. M. Zielinski, *Polymer*, 1999, **40**, 2797–2803.

[170] A. S. Michaels, H. J. Bixler and H. L. Fein, *Journal of Applied Physics*, 1964, **35**, 3165–3178.

[171] K. Vorotilov, V. Petrovsky and V. Vasiljev, *J Sol-Gel Sci Technol*, 1995, **5**, 173–183.

[172] B. T. Chen, *Polym. Eng. Sci.*, 1983, **23**, 399–403.

[173] J. Danglad-Flores, S. Eickelmann and H. Riegler, *Engineering Reports*, 2021, **3**, e12390.

[174] Y. Yan, J. Li, Q. Liu and P. Zhou, *Coatings*, 2021, **11**, 1322.

[175] M. Shanahan and C. Bourgès, *International Journal of Adhesion and Adhesives*, 1994, **14**, 201–205.

[176] N. Kumar, K. Varanasi, R. D. Tilton and S. Garoff, *Langmuir*, 2003, **19**, 5366–5373.

[177] B. Frank and S. Garoff, *Colloids and Surfaces A: Physicochemical and Engineering Aspects*, 1996, **116**, 31–42.

[178] T. C. Schulz and R. P. Danner, *Polym Eng Sci*, 2015, **55**, 688–692.

[179] V. Kanellopoulos, M. A.-h. Ali, S. Sundvall and S. Das, *Ind. Eng. Chem. Res.*, 2013, **52**, 15855–15862.

[180] X.-F. Wei, E. Linde and M. S. Hedenqvist, *npj Mater Degrad*, 2019, **3**, 18.

[181] C. A. Ward and G. Fang, *Phys. Rev. E*, 1999, **59**, 429–440.

[182] L. Maringer, M. Grabmann, M. Muik, D. Nitsche, C. Romanin, G. Wallner and W. Buchberger, *International Journal of Polymer Analysis and Characterization*, 2017, **22**, 692–698.

[183] T. Cherdhirankorn, V. Harmandaris, A. Juhari, P. Voudouris, G. Fytas, K. Kremer and K. Koynov, *Macromolecules*, 2009, **42**, 4858–4866.

[184] J. P. Greene, in *Automotive Plastics and Composites*, Elsevier, 2021, pp. 27–37.

[185] F. Zhang, E. Mohammadi, X. Luo, J. Strzalka, J. Mei and Y. Diao, *Langmuir*, 2018, **34**, 1109–1122.

[186] B. Suresh, S. Maruthamuthu, M. Kannan and A. Chandramohan, *Polym J*, 2011, **43**, 398–406.

[187] J. J. Gilman, *Journal of Applied Physics*, 1960, **31**, 2208–2218.

[188] D. C. Bassett, *Journal of Macromolecular Science, Part B*, 2003, **42**, 227–256.

[189] S. J. Hardman, L. R. Hutchings, N. Clarke, S. M. Kimani, L. L. E. Mears, E. F. Smith, J. R. P. Webster and R. L. Thompson, *Langmuir*, 2012, **28**, 5125–5137.

[190] F. Julienne, F. Lagarde and N. Delorme, *Polymer Degradation and Stability*, 2019, **170**, 109012.

[191] J. Rams, A. López, M. Sánchez, A. Ureña, V. Leal, B. Sánchez-Mariscal and P. Lafuente, *Polymer Testing*, 2012, **31**, 136–148.

[192] D. Gubała, N. Taylor, R. Harniman, J. Rawle, H. Hussain, E. Robles, M. Chen and W. H. Briscoe, *Langmuir*, 2021, **37**, 6521–6532.

[193] E. R.-v. Dorp, B. Möginger and B. Hausnerova, *Polymer*, 2020, **191**, 122249.

[194] R. S. Nohr and J. G. MacDonald, *Surface-Segregatable Melt-Extrudable Thermoplastic Composition*, 1992, US 5120888.

[195] D. Hu, A. Mafi and K. C. Chou, *J. Phys. Chem. B*, 2016, **120**, 2257–2261.

[196] X. Ye, B. Zuo, M. Deng, Y. Hei, H. Ni, X. Lu and X. Wang, *Journal of Colloid and Interface Science*, 2010, **349**, 205–214.

[197] G. W. Ehrenstein and R. P. Theriault, *Polymeric materials: structure, properties, applications*, Hanser ; Hanser Gardner Publications, Munich : Cincinnati, OH, 2001.

[198] V. R. Gundabala, W. B. Zimmerman and A. F. Routh, *Langmuir*, 2004, **20**, 8721–8727.

[199] B. E. Rapp, in *Microfluidics: Modelling, Mechanics and Mathematics*, Elsevier, 2017, pp. 243–263.

[200] S. Yada, T. Suzuki, S. Hashimoto and T. Yoshimura, *Journal of Molecular Liquids*, 2018, **255**, 208–214.

[201] C. P. Gibson, M. A. Litwinowicz, J. P. Tellam, R. J. L. Welbourn, M. W. A. Skoda, J. Claussen and R. L. Thompson, *Polymers*, 2021, **13**, 3407.

[202] J. S. Won, J. M. Lee, P. G. Lee, H. Y. Choi, T. J. Kwak and S. G. Lee, *J Mater Sci*, 2022, **57**, 1489–1505.

[203] G. Orädd, G. Lindblom, G. Arvidson and K. Gunnarsson, *Biophysical Journal*, 1995, **68**, 547–557.

[204] A. Tzitzinou, P. Jenneson, A. Clough, J. Keddie, J. Lu, P. Zhdan, K. Treacher and R. Satguru, *Progress in Organic Coatings*, 1999, **35**, 89–99.

[205] B. P. Binks, P. D. I. Fletcher, V. N. Paunov and D. Segal, *Langmuir*, 2000, **16**, 8926–8931.

[206] Y. Imaishi, R. Kakehashi, T. Nezu and H. Maeda, *Journal of Colloid and Interface Science*, 1998, **197**, 309–316.

[207] L. Gao and T. J. McCarthy, *Langmuir*, 2006, **22**, 6234–6237.

[208] M. E. Schrader, *Langmuir*, 1995, **11**, 3585–3589.

[209] V. Kocherbitov and O. Söderman, *J. Phys. Chem. B*, 2006, **110**, 13649–13655.

[210] T. Svitova, R. Hill and C. Radke, *Colloids and Surfaces A: Physicochemical and Engineering Aspects*, 2001, **183-185**, 607–620.

[211] I. Rychkov, *Macromol. Theory Simul.*, 2005, **14**, 207–242.

[212] T. Sako, A. Ito and M. Yamaguchi, *J Polym Res*, 2017, **24**, 89.

[213] D. R. M. Williams and F. C. MacKintosh, *Macromolecules*, 1994, **27**, 7677–7680.

[214] G. Straty, C. Muzny, B. Butler, M. Lin, T. Slawecki, C. Glinka and H. Hanley, *Physica B: Condensed Matter*, 1997, **241-243**, 74–76.

[215] M. Lin, H. Hanley, C. Muzny and G. Straty, *Physica B: Condensed Matter*, 1997, **241-243**, 990–992.

[216] A. J. Armstrong, T. M. McCoy, R. J. L. Welbourn, R. Barker, J. L. Rawle, B. Cattoz, P. J. Dowding and A. F. Routh, *Sci Rep*, 2021, **11**, 9713.

[217] L. A. Sasa, E. J. Yearley, C. F. Welch, M. A. Taylor, R. D. Gilbertson, C. Hammeter, J. Majewski and R. P. Hjelm, *Review of Scientific Instruments*, 2010, **81**, 055102.

[218] Y. Corvis, L. Barré, J. Jestin, J. Gummel and F. Cousin, *Eur. Phys. J. Spec. Top.*, 2012, **213**, 295–302.

[219] F. Nemoto, N. L. Yamada, F. Takabatake and H. Seto, Proceedings of the 3rd J-PARC Symposium (J-PARC2019), Tsukuba, Japan, 2021.

[220] L. Li, J. Jakowski, C. Do and K. Hong, *Macromolecules*, 2021, **54**, 3555–3584.

[221] G. Titomanlio, V. Speranza and V. Brucato, *International Polymer Processing*, 1997, **12**, 45–53.

[222] M. Yousfi, T. Dadouche, D. Chomat, C. Samuel, J. Soulestin, M.-F. Lacrampe and P. Krawczak, *RSC Adv.*, 2018, **8**, 22023–22041.

[223] Y. Li, B. Huang and X. Qu, *Powder Metallurgy*, 1999, **42**, 86–90.

[224] T. Kato, K. Miyazaki, Y. Kawabata, S. Komura, M. Fujii and M. Imai, *J. Phys.: Condens. Matter*, 2005, **17**, S2923–S2928.

[225] G. Salamat and E. W. Kaler, *Langmuir*, 1999, **15**, 5414–5421.

[226] F. Nettesheim, J. Zipfel, U. Olsson, F. Renth, P. Lindner and W. Richtering, *Langmuir*, 2003, **19**, 3603–3618.

[227] J. J. Cardiel, A. C. Dohnalkova, N. Dubash, Y. Zhao, P. Cheung and A. Q. Shen, *Proc. Natl. Acad. Sci. U.S.A.*, 2013, **110**, E1653–E1660.

[228] E. J. Hemingway and S. M. Fielding, *Journal of Rheology*, 2019, **63**, 735–750.

[229] M. Keentok and S.-C. Xue, *Rheologica Acta*, 1999, **38**, 321–348.

[230] H. Murase, T. Kume, T. Hashimoto and Y. Ohta, *Macromolecules*, 2005, **38**, 8719–8728.